Devising computational tools to quantify the actin cytoskeleton and pavement cell shape using network-based approaches

Jacqueline Nowak

Student ID: 797700 (UoM), 750310 (UP)
nowakj@student.unimelb.edu.au

ORCID: 0000-0002-2881-7384

Submitted in total fulfilment of the requirements of the jointly awarded degree of

Doctor of Philosophy

April 2020

Date of Defense: 20^{th} November 2020

School of Biosciences
University of Melbourne

Institute of Biochemistry and Biology
University of Potsdam

Abstract

Recent advances in microscopy have led to an improved visualization of different cell processes. Yet, this also leads to a higher demand of tools which can process images in an automated and quantitative fashion. Here, we present two applications that were developed to quantify different processes in eukaryotic cells which rely on the organization and dynamics of the cytoskeleton. In plant cells, microtubules and actin filaments form the backbone of the cytoskeleton. These structures support cytoplasmic streaming, cell wall organization and tracking of cellular material to and from the plasma membrane. To better understand the underlying mechanisms of cytoskeletal organization, dynamics and coordination, frameworks for the quantification are needed. While this is fairly well established for the microtubules, the actin cytoskeleton has remained difficult to study due to its highly dynamic behaviour. One aim of this thesis was therefore to provide an automated framework to quantify and describe actin organization and dynamics. We used the framework to represent actin structures as networks and examined the transport efficiency in *Arabidopsis thaliana* hypocotyl cells. Furthermore, we applied the framework to determine the growth mode of cotton fibers and compared the actin organization in wild-type and mutant cells of rice. Finally, we developed a graphical user interface for easy usage. Microtubules and the actin cytoskeleton also play a major role in the morphogenesis of epidermal leaf pavement cells. These cells have highly complex and interdigitated shapes which are hard to describe in a quantitative way. While the relationship between microtubules, the actin cytoskeleton and shape formation is the object of many studies, it is still not clear how and if the cytoskeletal components predefine indentations and protrusions in pavement cell shapes. To understand the underlying cell processes which coordinate cell morphogenesis, a quantitative shape descriptor is needed. Therefore, the second aim of this thesis was the development of a network-based shape descriptor which captures global and local shape features, facilitates shape comparison and can be used to evaluate shape complexity. We demonstrated that our framework can be used to describe and compare shapes from various domains. In addition, we showed that the framework accurately detects local shape features of pavement cells and outperform contending approaches. In the third part of the thesis, we extended the shape description framework to describe pavement cell shape features on tissue-level by proposing different network representations of the underlying imaging data.

Abstract

Aktuelle Entwicklungen in der Mikroskopie haben zu einer verbesserten Visualisierung von verschiedenen Zellprozessen geführt. Dennoch führt das auch zu einem höheren Bedarf an Werkzeugen, die Bilder in einer automatisierten und quantitativen Weise bearbeiten und analysieren können. Hier präsentieren wir zwei Anwendungen, die entwickelt wurden, um verschiedene Prozesse in eukaryotischen Zellen zu quantifizieren, welche von der Organisation und Dynamik des Zytoskeletts abhängig sind. In Pflanzenzellen bilden Mircotubuli und Aktinfilamente das Rückgrat des Zytoskeletts. Diese Strukturen unterstützen die Zytoplasmaströmung, die Organisation der Zellwand und den Transport von zellulärem Material zu und von der Plasmamembran. Um die zugrundeliegenden Mechanismen der Organisation, Dynamik und Koordination des Zytoskeletts zu verstehen, sind Hilfsmittel zur Quantifizierung notwendig. Während das ziemlich ausführlich für Microtubuli getan wurde, bleibt das Aktin-Zytoskelett schwer zu studieren aufgrund seines hoch dynamischen Verhaltens. Das erste Ziel dieser Arbeit war es daher, einen automatisierten Framework zu entwickeln, der die Aktin-Organisation und Dynamik quantifiziert und beschreibt. Wir haben diesen Framework genutzt, um Aktin-Strukturen als Netzwerke zu repräsentieren und haben damit die Transporteffizienz in *Arabidopsis thaliana* Hypocotylzellen untersucht. Des Weiteren haben wir den Framework genutzt, um den Wachstumsmodus in Baumwollfasern zu bestimmen und um die Aktin-Organisation in Reis-Wildtyp und Mutanten zu vergleichen. Zuletzt haben wir eine grafische Benutzeroberfläche zur einfacheren Benutzung entwickelt. Microtubuli und das Aktin-Zytoskelett spielen auch eine große Rolle in der Morphogenese von epidermalen Blattzellen. Diese Zellen haben hochkomplexe und interdigitale Formen, welche sehr schwer in einer quantitativen Art zu beschreiben sind. Während die Beziehung zwischen Microtubuli, dem Aktin-Zytoskelett und Formgestaltung der Zellen in vielen Studien untersucht wurde, ist es immer noch nicht ganz klar wie und ob die Zytoskelettkomponenten die Ein- und Ausbuchtungen in Blattzellen vorherbestimmen. Um die zugrundeliegenden Zellprozesse zu verstehen, die die Zellmorphogenese koordinieren, sind quantitative Beschreiber von Formen notwendig. Daher war das zweite Ziel dieser Arbeit die Entwicklung eines netzwerkbasierten Gestaltbeschreibers, welcher globale und lokale Gestaltmerkmale erfasst, einen Gestaltvergleich ermöglich und die Komplexität von Formen evaluieren kann. Wir haben nachgewiesen, dass unser Framework benutzt werden kann, um Formen aus verschiedenen Bereichen zu beschreiben und zu vergleichen. Darüber hinaus haben wir gezeigt, dass der Framework lokale Gestaltmerkmale in Blattzellen akkurat ermittelt und andere konkurrierende Methoden hinter sich lässt. Im dritten Teil der Arbeit haben wir den Gestaltbeschreiber erweitert, um Gestaltmerkmale von Blattzellen, bezogen auf das ganze Zellgewebe, zu beschreiben, indem wir verschiedene Netzwerkrepräsentationen der zugrundeliegenden Bilddaten vorstellen.

Declaration

The work descibed in the thesis was performed in the School of Biosciences of The University of Melbourne and the Institute of Biochemistry and Biology of the University of Potsdam between September 2016 and April 2020. The scientific work was performed solely by the author, with the exception of the assistance which has been specifically acknowledged. The thesis is less than 100.000 words in length, exclusive of tables, figures, references and appendices. No part of this thesis has been submitted for any other degree or diploma.

.....

Jacqueline Nowak

20^{th} April 2020

Preface

Works in this thesis were carried out under the supervision of Prof. Dr. Staffan Persson at the University of Melbourne and Prof. Dr. Zoran Nikoloski at the University of Potsdam. Below is a summary of publications which are relevant for the thesis chapters.

The approach proposed in Section 2.2.1 was published in:

- Breuer D, **Nowak J**, Ivakov A, Somssich M, Persson S and Nikoloski Z (2017). System-wide organization of actin cytoskeleton determines organelle transport in hypocotyl plant cells.
  PNAS, **114**(28): E5741-5749.

The results presented in the publication are introduced in Section 2.3.1 of this thesis. Data representation were reprinted from the publication and the published Supplementary Material. The author contributed to the development of the proposed framework and analyzed supplementary data.

The results presented in Section 2.3.2 were achieved in collaboration with Prof. Dr. Zhaosheng Kong from the Chinese Academy of Sciences, Beijing and were published in:

- Yu Y, Wu S, **Nowak J***, Wang G, Han L, Feng Z, Mendrinna A, Ma Y, Wang H, Zhang X, Tian J, Dong L, Nikoloski Z, Persson S and Kong Z (2019). Live-cell imaging of the cytoskeleton in elongating cotton fibres.
  Nature Plants, **5**: 498-504.
  *first co-author

The results and figure in Section 2.3.2 were cited and reprinted from this publication. Additional unpublished data was shown. The author used the framework described in Section 2.2.1 to extract networks from actin cytoskeleton imaging data and analyzed the network properties.

The resuts presented in Section 2.3.3 were achieved in collaboration with Prof. Dr. Dabing Zhang fron the University of Adelaide and were published in:

- Song Y, Li G, **Nowak J**, Zhang X, Xu D, Yang X, Huang G, Liang W, Yang L, Wang C, Bulone V, Nikoloski Z, Hu J, Persson S and Zhang D (2019). The rice actin-binding protein RMD regulates light-dependent shoot gravitropism.
  Plant Physiology, **181**: 630-644.

Part of the visualized data in Section 2.3.3 was reprinted from this publication. Additional unpublished data were shown. The author used the framework described in Section 2.2.1 to extract networks from actin cytoskeleton imaging data and analyzed the network properties.

The graphical user interface proposed in Section 2.4 was published in:

- **Nowak J**, Gennermann K, Persson S and Nikoloski Z (2020). CytoSeg 2.0: automated extraction of actin filaments.
  Bioinformatics, btaa035.

The author developed the graphical user interface and analyzed additional data.

The framework proposed in Chapter 3 and consequential results were summarized in a manuscript and submitted for publication:

- **Nowak J**, Eng RC, Matz T, Waack M, Persson S, Sampathkumar A and Nikoloski Z. A network-based framework for shape analysis enables accurate characterization and classification of leaf epidermal cells.
  Submitted to *Nature Communications* (accepted 30.11.20).

The author implemented the proposed framework, analyzed the data presented in Chapter 3 and developed the graphical user interface.

The work in Chapter 4 is unpublished material that was not yet submitted for publication.

The author's PhD candidature, during which the works in this thesis were carried out, was funded by a Melbourne International Engagement Award scholarship including tuition fees offset and stipend.

Acknowledgements

First and foremost, I would like to thank my two supervisors, Prof. Dr. Staffan Persson and Prof. Dr. Zoran Nikoloski for the great opportunity to obtain my doctorate degree in two labs at opposite sides of the world. I highly appreciate the detailed discussions and helpful comments during my candidature and the expertise in their respective areas. In addition, I'm very grateful for the wonderful and friendly atmosphere in both groups, which helped me a lot to feel home wherever I stayed.

I would like to thank the University of Melbourne for the scholarship I received. Furthermore, I would like to thank Ina Talke, who always tried to help with the processes of the newly established Joint PhD program between the University of Melbourne, the University of Potsdam and the MPIMP. I also thank the IMPRS program for the opportunities to advance my scientific skills and career. I thank Prof. Dr. Zhaosheng Kong from Beijing and Prof. Dr. Dabing Zhang from Adelaide and their respective groups for the fruitful collaborations and the opportunity to apply our framework. Furthermore, I would like to thank all the open-source software and the great community behind it, without whom I wouldn't have achieved the things presented in this thesis.

A big thank you goes to Cassie Watts, who gave me a home and a family in Australia and provided me with delicious food, wonderful sightseeing trips and introduced me to the Australian culture. I'd also like to thank all the people in both labs for their help in scientific or personal matters and the many lunch breaks we spend together. A special thanks goes to all my colleagues who became close friends during my time as a PhD student. I appreciate all the times we spend together to watch movies, bake cakes, play games or win with the best trivia team at PA's. Last but not least, I would like to thank my closest friends and family for always being there and taking care of things, even when I was at the other end of the world.

Abbreviations

ABP	actin-binding protein
BHI	biological homogeneity index
TMK	transmembrane kinase
ADF	actin-depolymerizing factors
ADP	adenosine diphosphate
ARP	actin-related protein
ATP	adenosine triphosphate
CesA	cellulose synthase
CP	capping proteins
ER	endoplasmatic reticulum
fABD2	second actin binding domain
F-actin	filamentous actin
G-actin	globular actin
GDP	guanosine diphosphate
GFP	green fluorescent protein
GTP	guanosine triphosphate
GUI	graphical user interface
GWAS	genome-wid association studies
LatB	latrunculin B
MAP	microtubule-associated protein
MBD	microtubule-binding domain
MMC	moving median center
MTOC	microtubule organizing centre
PCA	principal component analysis
PIN	peptidyl-prolyl cis-trans isomerase NIMA-interacting
PPB	preprophase band
PPB	preprophase band
QTL	quanitative trait loci
RIC	Rop-Interactive Crib motif-containing protein
RMD	rice morphology determinant
RMSE	root mean square error
ROI	region of interest
ROP	Rho of plants
SNPs	single-nucleotide polymorphism
TGN	trans-Golgi network
+TIP	plus end tracking proteins
TUB	tubulins

Contents

List of Figures

List of Tables

Chapter 1

Introduction

1.1 Research Aims

To understand the coordination of cytoskeletal components and its underlying molecular mechanisms, frameworks are necessary which enable the quantification of cytoskeleton organization. While this is fairly well established for the microtubules, the actin cytoskeleton has remained difficult to define due to its highly dynamic behaviour. Therefore, I propose an image-based framework which allows for:

1. Automated extraction and analysis of actin filaments on a system-level.
2. Quantification of actin network properties to understand underlying transport principles.

Furthermore, to understand how the cytoskeleton is involved in the formation of lobes and necks in pavement cells, I propose a novel shape descriptor that enables:

4. Quantitative description of pavement cell shape on a global and local scale.
5. Shape comparison based on global and local properties.
6. Quantification of pavement cell complexity.
7. Classification of plants into their respective phylogenetic clades.

In addition, I aimed to extend such shape description framework to investigate pavement cell shape on a tissue-wide level and thus allowing for:

8. Identification of stomata cells.
9. Analysis of pavement cell complexity and growth over time.
10. Internal validation of different lobe detection tools, by correlating lobes and necks in adjacent cells.

1.2 The Cytoskeleton

In plant cells, the cytoskeleton is a three-dimensional network that connects cytoplasmic elements, nucleus, organelles and the plasma membrane. To be more precise, the cytoskeleton is comprised of microtubules, actin filaments and intermediate filaments. The cytoskeleton has many functions and is involved in, e.g. cell division, cell growth, morphogenesis, endo- and exocytosis, as well as transport and trafficking of cytoplasmic components [227, 116, 241, 89, 96, 245]. While the presence of intermediate filaments in plants is debated, microtubules and actin filaments, as well as their associated proteins, have been more thoroughly investigated [126]. Plant cells are surrounded by a rigid, yet flexible cell wall that provides strength and structure, but also protects them from biotic and abiotic stresses. Furthermore, the cytoskeleton is an important structure for cell wall deposition.

1.3 The Actin Cytoskeleton

Actin filaments are assembled from globular actin (G-actin) monomers forming helical structures which are 5-7 nm in diameter [33, 185, 186]. Three G-actin monomers create a seed which nucleates the assembly of additional monomers at one end. The head-to-tail assembly of asymmetric subunits causes polarity of the filament, with the assembled monomers often in different nucleotide-bound states [139]. At the fast-growing, barbed end of the actin filament, ATP-bound monomers are preferentially added, while at the slow-growing pointed end ADP-bound subunits tend to be lost or disassembled. Only seconds after subunits are added to the barbed end, nucleotide hydrolysis occurs and transforms the bound ATP to ADP-P_i. After another lag period the P_i is released, leaving behind the ADP-bound subunits that define the older regions of the actin filament (Fig. 1.1). The assembly at the barbed filament end and the loss of subunits at the pointed end exhibit a treadmilling behaviour, meaning that the flux of subunits is balanced through the backbone over time [139].

Quantitative analyses of filament initiation in epidermal plant cells showed that the majority of new filaments originate from the sides of pre-existing actin filaments (40-50%), while only 28-34% of new filaments are assembled de novo in the cytoplasm. The remaining 20-22% of new filaments are assembled from filament ends which have ceased growing [105, 140, 141, 220, 228]. A large pool of available subunits in the cell (50-100 μM) and a fast assembly rate of 1.6-3.4 μm/s enables actin filaments to assemble and grow with impressive speed [105, 106, 109, 140, 141, 220, 228, 237]. The average actin filament can reach a length of 10-15 μm before it is disassembled and has a relatively short lifetime of 15-30 s [139].

The actin cytoskeleton can appear either as fine, single filaments or as actin bundles in the cell [108, 220, 228]. Single filaments are more randomly arranged and exhibit dynamic

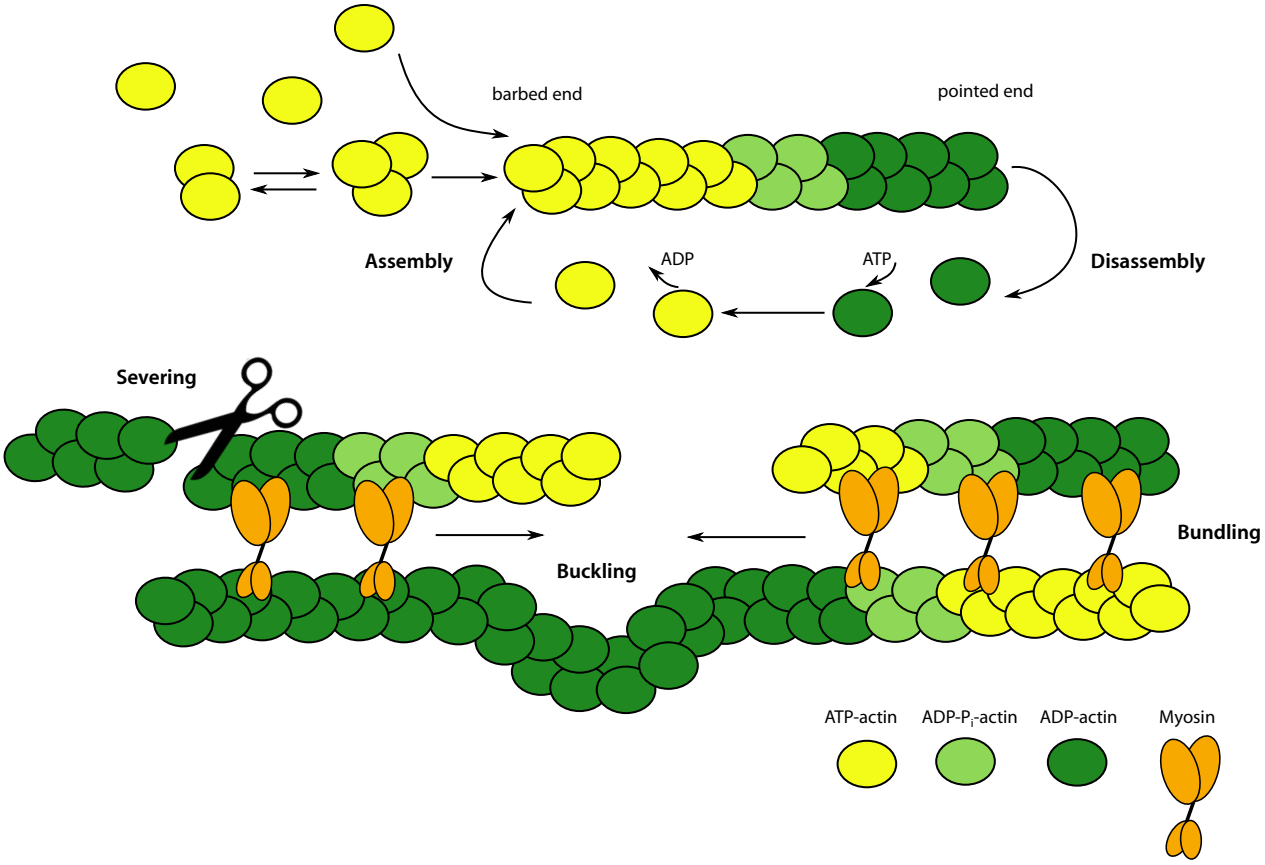

Figure 1.1: Assembly and architecture of actin filaments. G-actin monomers are assembled to polar actin filaments with a barbed and a pointed end. The assembly and disassembly of subunits is balanced through the backbone over time in a treadmilling behaviour [139]. The architecture of the actin cytoskeleton can be influenced by different proteins that enable severing or bundling of actin filaments [220, 228].

behaviour, constantly changing between assembling, disassembling, rearranging and fusing into larger bundles [228]. By contrast, actin bundles, which emerge from two or more single filaments, are thicker and straighter, resulting in a longer lifetime, and a more axially orientation in the cell [220, 228]. Besides these actin architectures, the filaments can furthermore change their shape by buckling and straightening events [220, 228].

The organization and assembly of actin filaments is choreographed by a plethora of different actin-binding proteins (ABPs) with distinct functions [33, 72, 187]. The ABPs can either bind to the G-actin, the F-actin or both. Monomer-binding proteins like profilin, actin-depolymerizing factors (ADF) or cyclase-associated proteins (CAP) regulate the activity and size of the subunit pool [139]. The actin-related protein (ARP) 2/3 complex and formins act as nucleation factors, determining the nucleation place and time, by initiating "seeds" from G-actin or profilin-actin complexes for the filament assembly [139, 257]. In addition, severing proteins like ADF/cofilin and villin trigger the shortening of actin

filaments by creating breaks in the backbone. This process generates new ends at which monomers can assemble or disassemble. To limit the addition or loss of subunits, capping proteins (CP) and villin bind with high affinity to the barbed ends of the filaments. The cross-linking and bundling of filaments are initiated by villin, fimbrin and LIM-domain containing proteins, which stabilize the cytoskeleton against disassembly [34, 234, 115]. Lastly, myosins are responsible for actin filament-based motility as they generate the force for vesicle movement along actin filaments or bundles [180].

Different inhibitors may provoke significant changes in the actin cytoskeleton organization. Such drugs can either inhibit the actin cytoskeleton polymerization by depolymerizing, rearranging or interfering in different ways, or stabilize the actin structures [179]. An example of an inhibiting drug is cytochalasin D, which binds the barbed end of actin filaments and acts in direct competition with capping proteins which limit the loss of subunits [242]. Another inhibitor is the marine toxin latrunculin B (LatB) which forms 1:1 complexes with the G-actin monomers, thus inhibiting the polymerization of actin filaments [60, 224, 98, 154, 228]. LatB is effective in diverse cell types in higher land plants [13] and in smaller concentration than cytochalasin D [242]. By contrast, there are also substances that stabilize and polymerize actin filaments, such as jasplakinolide, phalloidin and chondramides [111]. Both jasplakinolide and phalloidin bind competitively to F-actin, thus stabilizing the filaments [44]. However, further studies revealed that jasplakinoide in high concentration actually disrupt actin filaments, resulting in the complete disappearance of F-actin [223, 172].

During plant cell growth, cell wall matrix material-containing vesicles are secreted to the plasma membrane. These secretory vesicles contain materials, produced in the Golgi apparatus, for new and expanding cell walls [5, 117]. Golgi bodies are seemingly organized in random patterns throughout the cytosplasm and exhibit a stop-and-go motion due to pauses at endoplasmatic reticulum (ER) export sites [161]. Together, this may increase the transport efficiency of secretory vesicles, because the travel distances from the Golgi to the plasma membrane, as well as from ER export sites to Golgis, are reduced [161]. The Golgi positioning and movement is an actomyosin-based process, which therefore depends on the actin cytoskeleton organization. Whereas slow and undirected Golgi body movement is typically co-localized with fine F-actin, fast and directional movements are often co-localized with actin bundles [161, 5]. More precisely, the actin cytoskeleton is a network of tracks that guide the movement of Golgi, and exocytic and endocytic vesicles [123, 219]. Hence, the actin cytoskeleton substantially contributes to membrane trafficking in plants, and therefore has quite different functions than in animal cells [246, 126]. In addition to steering the secretion of cell wall material from the Golgi, typically via the trans-Golgi network (TGN), the actin cytoskeleton has also been shown to impact protein distribution at the plasma membrane, for example the cellulose synthesizing protein complexes [205].

1.4 Microtubules

Microtubules are about 25nm in diameter and are assembled from heterodimers consisting of α- and β-tubulin, two members of the tubulin superfamily [54]. The asymmetric structure of the α/β-tubulin heterodimer is reflected in its polarity and forms the basic building block for the assembly of microtubule filaments (Fig. 1.2). The polymerization of heterodimers into protofilaments is regulated by the hydrolysis of the β-tubulin-bound GTP [4], whereby the dimers are assembled in a head-to-tail array, thus creating polar structures with distinct ends [54]. Thirteen such protofilaments are subsequently arranged in parallel with the same polarity around a hollow core, forming a microtubule. The end of the microtubule that exposes the α-subunits and the β-subunits, are defined as the minus and the plus end, respectively. Elongation of a microtubule is possible at both ends, although it was shown *in vitro* that the minus end grows slowly, while the plus end grows more rapidly [70, 166].

The plus end of the microtubule is stabilized by a GTP cap which is formed by GTP-bound tubulin dimers where GTP hydrolysis has not yet occurred [212]. Soon after the incorporation of the dimer into the microtubule, the β-tubulin hydrolyses GTP to GDP, which has a lower affinity for other tubulin dimers and therefore destabilizes the microtubule. Once the microtubule growth is slowed down because of low concentrations of tubulin dimers, the GTP hydrolysis catches up with the incorporation of dimers and depolymerization is favoured [4, 54]. Instead of growing steadily, microtubules alternate between growing, stopping and shrinking, a behaviour that is called dynamic instability and is determined by the rate of tubulin incorporation relative to the GTP hydrolysis rate [54]. The transition from growing to shrinking is called catastrophe, while the transition from shrinking to growing is called rescue [94]. Another term to explain the dynamic behaviour of microtubules is treadmilling, which describes the loss of GDP binding tubulin from the minus end and the addition of GTP bound tubulin to the plus end.

Microtubules may transition between different microtubule conformations to control dynamics. Polymerizing plus ends are straight and the protofilaments have varying lengths. By contrast, depolymerizing plus ends are strongly curved and the protofilaments are peeled outwards [43]. A third conformation that is halfway between the curved and the straight conformation has also been described [243]. Depending on the conformation, assembly or disassembly of the microtubule is promoted.

Microtubule-associated proteins (MAPs) regulate microtubule dynamics, but molecular motor proteins are also involved [4]. One type of MAPs is the microtubule polymerase, a member of the plus end tracking proteins (+TIP) family that binds to the plus end to promote microtubule growth by recruiting tubulin dimers. The end tracking proteins of the +TIP family are able to detect the tips of the microtubules and may steer the direction of

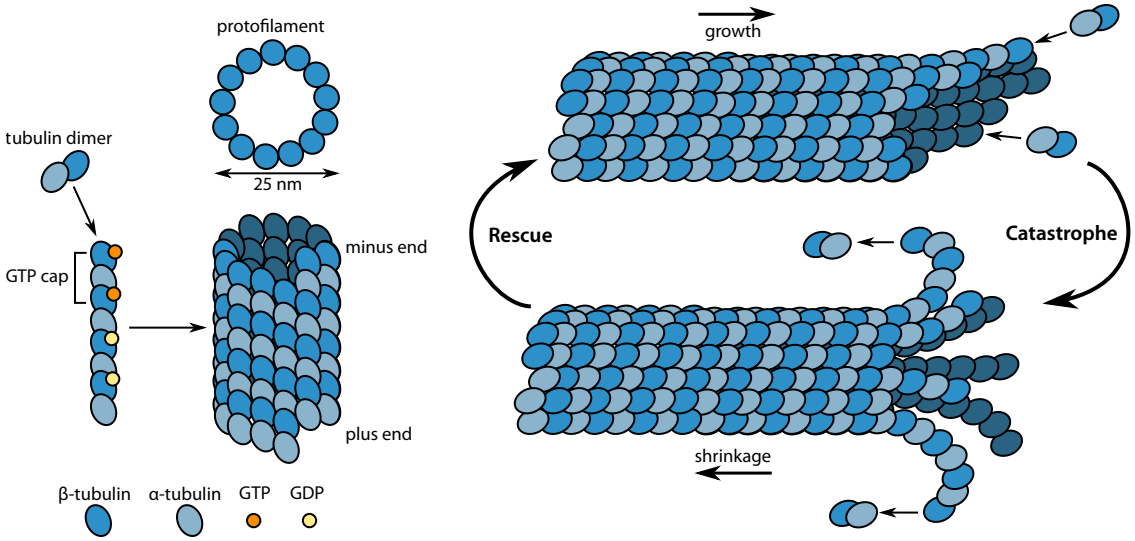

Figure 1.2: Microtubule structure and assembly. Left: microtubules are built from α- and β-tubulin heterodimers, which assemble into protofilaments. 13 of these protofilaments form a microtubule, which has a hollow core in the inside and is about 25nm in diameter [54]. Right: The assembly and disassembly are controlled by the dynamic instability of the microtubule [54, 94].

microtubule polymerization. In general, the +TIPs can be separated into autonomous tip trackers and hitchhikers. The autonomous tip trackers are able to recognize the tips independently, contrary to hitchhikers, which are proteins with low affinity for microtubules, wherefore they bind mainly to autonomous tip trackers that are concentrated at the microtubule ends [4]. Microtubule shrinkage is controlled by microtubule depolymerases belonging to the kinesin family, which remove terminal dimers at the microtubule tip by using the energy of ATP hydrolysis [4]. Besides the regulation of microtubule assemble and disassembly, MAPs and molecular motors also guide the microtubule-microtubule growth via cross-linking and facilitate microtubule-actin co-alignment.

In growing cells, microtubules are parallelly arranged at the cell cortex, typically transverse to the direction of cell expansion [30]. Reorientation of the array can occur in response to developmental cues, cytoplasmic streaming or can be influenced by external cues, such as mechanical stress or hormone gradients [155]. An example of external impact on microtubule reorganization is the exposure of etiolated hypocotyls to blue light. Here, blue light stimulates the reorientation of microtubules by katanin-mediated severing at microtubule crossover sites to support new growth regimes [143].

1.5 Microtubules and the Cell Wall

Plant cells are surrounded by a polysaccharide-rich cell wall, which provides the cell with rigidity and mechanical strength. Cell walls are involved in the regulation of cell expan-

sion, as well as in cell-cell adhesion and in providing a physical barrier against pathogens [76, 205]. The cell expansion is regulated by two interdependent processes, namely the irreversible yielding of the cell wall and the subsequential water absorption to increase the cell volume [56, 57]. Before the expansion the turgor pressure is reduced due to the relaxation of the cell wall, but is reestablished by the passive water influx.

Furthermore, cell walls are typically characterized as two types; the primary and the secondary walls, which are identified by different structures, compositions and functions [47]. Primary cell walls are composed of carbohydrate-based polymers, including cellulose, hemicellulose and pectins. They are built during cell division, are modified during cell growth and are regulated by ion distribution and enzyme activity [76]. Although strong, primary cell walls are also plastic and therefore not sufficient to provide the plant with enough stability and strength. The mechanical strength needed for vertical growth to substantial heights is provided by secondary cell walls, built after the termination of cell growth. They can be found inside primary cell walls in certain cell types (e.g., fibres and tracheary elements). Secondary cell walls are composed of cellulose and hemicellulose just like primary cell walls, with the slight difference that the pectin is largely substituted by polyphenolic lignin structures. Due to this arrangement of components the cell wall provides a rigid, settled shape which confers mechanical strength to the plant [267].

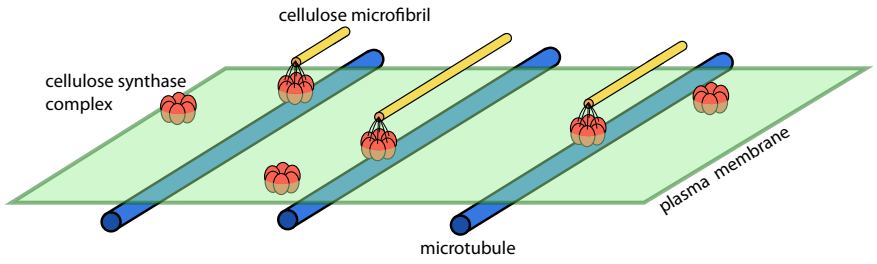

Figure 1.3: Deposition of cellulose microfibrils synthesised by CesAs at the plasma membrane. Cellulose synthase complexes, hexameric rosette-like structures, synthesize cellulose microfibrils at the plasma membrane. The deposition of cellulose microfibrils is directed by microtubules [178].

The main component in both primary and secondary walls is cellulose, which is made of parallel, unbranched β-1,4-glucan chains. These chains are arranged into microfibrils induced by Van der Waals forces and hydrogen bonds. Furthermore, cellulose is characterized by hydrogen-bonded stretches of crystalline cellulose and less ordered amorphous regions. The synthesis of cellulose takes place at the plasma membrane and is achieved by the hexameric rosette-like structure of the cellulose synthase (Fig. 1.3). The deposition of cellulose microfibrils is directed by microtubules, which provide guiding rails for the newly synthesized cellulose microfibrils and help them orient themselves and organize the cell wall construction [178]. Yet, CesAs are able to self-organize themselves even in the

absence of microtubules [50]. There is even evidence that microtubules are not essential for cellulose microfibrils to orient in expanding cells [248].

1.6 The Interplay Between the Actin Cytoskeleton and Microtubules

Microtubules and actin filaments can be cross-linked and build an integrated system in plant cells [69]. The organization of cytoskeletal components is dependent on the developmental state of the cell and its growth mode. In interphase cells, actin filaments are randomly arranged in networks and are responsible for the positioning of cell organelles in the cell through cytoplasmic streaming. By contrast, microtubules are typically arranged in parallel and perpendicular to the growth axis [126]. The cytoskeletal organization in growing cells depends on the growth mode: cells can be diffuse or tip growing, or have a growth mode that is somewhere in between [222]. Through these distinctive growth modes and other growth patterns, cells acquire their different shapes, ranging from very simple to more complex shapes of pavement cells in the upper leaf epidermis [221].

Diffuse growth is the expansion in all directions, driven by the turgor pressure. In cells with a directed diffuse growth, the cell is growing preferentially along one axis. Cellulose microfibrils are transversely orientated to the axis of elongation and are in alignment with cortical microtubules (Fig. 1.4A) [99, 10]. The pattern of the microfibrils resembles hoops around a barrel which guides the anisotropic growth of the cell by resisting certain directions of cell expansion [101]. The microtubules are important for the orientation of the expansion in diffuse growing cells, as they guide material for new cell walls to the appropriate sites at the plasma membrane via secretory vesicles [221]. Moreover, the actin cytoskeleton seems to have an effect on the rate of cell expansion [195, 151]. Actin bundles in diffuse growing cells are longitudinally oriented to the major cell axis, while fine actin filaments in the cortex of the expanding cell are oriented transversely in co-alignment with the microtubules (Fig. 1.4A) [14, 31]. The main function of the actin cytoskeleton in diffuse growing cells is the transport of secretory vesicles to the cell surface [71, 18].

In tip-growing cells, such as pollen tubes or root hairs, the cell wall is extended on a single site of the cell surface. The driving force of this unidirectional growth is the turgor pressure [129]. Actin filaments are arranged in longitudinal bundles along the length of the cell and guide the growth direction by determining the location of newly delivered cell wall material (Fig. 1.4B) [107]. Moreover, at the tip of the growth site, fine actin filaments are organized in a sub-apical network. As a result, secretory vesicles can be directly transported along the actin cytoskeleton to the vicinity of the growth site [107]. Furthermore, the actin cytoskeleton might have a role in initiating the tip growth by selecting the growth site for the initial bulging of the cell wall in root hairs [197]. Microtubules are longitudinally oriented in tip-growing cells, similar to the actin bundles (Fig. 1.4B).

The array of microtubules may guide the deposition of cellulose at the growth site in Arabidopsis root hairs [221]. In addition, the microtubules may play a role in stabilizing the growth site and regulating the directionality of tip growth [25].
Cytoplasmic calcium (Ca^{2+}), which appears as a Ca^{2+} gradient in tip-growing systems, has been identified to regulate the development and growth [146, 17]. The control of the growth is mediated by the regulation of actin filaments through actin-binding proteins. In particular, the actin-binding proteins profilin and villin/gelsolin are influencing the organization of the actin cytoskeleton in a calcium-dependent manner [17]. Microtubules may be responsible for the restriction of the Ca^{2+} gradient location to a single site.

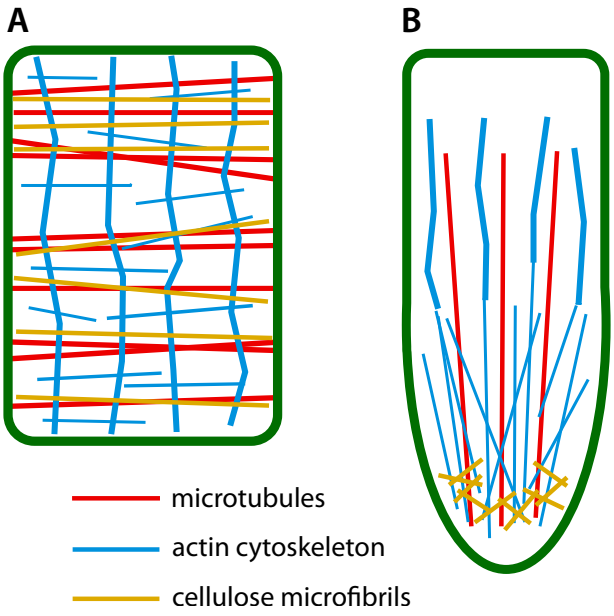

Figure 1.4: Overview of different growth modes in plant cells. (**A**) In cells with diffuse growth, microtubules are transverse oriented (red), similar to fine actin filaments (blue, thin) [99, 31]. Cellulose microfibrils (orange) are in alignment with the microtubule. Actin bundles are longitudinal arranged (blue, thick) [14]. (**B**) In tip-growing cells, both microtubules and actin filaments and bundles are logitudinal arranged, whereby fine actin filaments are concentrated at the tip of the cell [221]. Cellulose microfibrils are oriented in a random network at the growth site [221].

Although actin filaments and microtubules are controlled by different mechanisms, the dynamics between both components are highly dependent on each other and require dynamic interaction. Actin filament dynamics are associated with the orientation and position of cortical microtubules. For instance, during reassembly of the actin cytoskeleton, actin fragments coincide with microtubules, indicating that microtubules might influence the orientation of newly formed actin filaments and are required for the actin reassembly [207]. Furthermore, this study demonstrated that the disturbance of one component will

also affect the other component and vice versa. Different proteins might be involved in the interaction between microtubules and actin filaments. For instance, AtFH4, an actin-nucleating protein from the *Arabidopsis thaliana* formin family, also has a microtubule-binding region [66]. The protein co-aligned with microtubules, suggesting that there is a local cross-talk between actin filaments and microtubules. Such coordination is necessary during the PPB formation, the interdigitation of epidermal cells or for the cytoskeletal polarisation in response to a pathogen attack [66]. In addition, another formin (AFH14) directly binds to and bundles actin filaments and microtubules during the PPB formation [142]. If both microtubules and actin filaments are present, AFH14 has a higher affinity to bind to microtubules. Furthermore, an excessive AFH14 concentration promotes the cross-linking of microtubules and actin filaments.

Notably, the kinesin 14-type molecular motor AtKinG localizes to both microtubules and actin filaments in PPB of Arabidopsis [45]. Indeed, class-14 kinesins contain a calponin homology domain (KCHs) that acts as cross-linker of microtubules and actin filaments [125, 182]. The coordination of microtubules and actin filaments might also be coordinated by the interaction of microtubule- actin-associated proteins. For example, +TIPs, which control the dynamics and organization of microtubules, can interact with actin-nucleating factors, such as formins [182].

The dynamic communication between the cytoskeletal components is instrumental to respond to changing environmental factors, leading to a restructuring of the cytoskeleton by influencing the way in which cell wall material is deposited in expanding cells. These structural responses can be the defence against other organisms like pathogens, but can also be a cellular response after wounding or responses to light or gravitational cues [233].

1.7 Quantification of Cytoskeletal Organization and Dynamics

Instigated by advances in molecular biology and microscopy techniques, the quantification of cytoskeletal organization and dynamics and the study of effects of mutations and environmental perturbations became more feasible [173]. Microtubules can be imaged by immunolabelling of tubulin or the fusion of green fluorescent protein (GFP) to different proteins including various tubulins (TUB), the microtubule-binding domain (MBD) of mammalian MAP4, EB1 and MAPs [48]. With this, the shrinkage and growth of microtubules can be observed in near real-time using the appropriate imaging platforms [215, 49, 121]. Due to the slower growth rate of microtubules (0.2-0.4 μm/s) compared to the growth rate of actin filaments (1-2 μm/s), there are plenty of frameworks for quantitative analyses of microtubule dynamics and organization [8, 79, 119, 120, 263]. The frameworks are often fully automated and also allow for tracking of both plus- and minus-ends of the microtubules [120].

Actin filaments can be visualized with genetically encoded fluorescent F-actin reporters of which several were engineered in the last years. The first marker for visualization of the actin cytoskeleton was expressed from the C-terminus of mouse talin and fused to GFP [127]. The C-terminus has an F-actin-binding domain which, unlike in the full-length talin, cannot nucleate actin polymerization. mTalin-GFP binds and visualizes the actin cytoskeleton in different plant cell types by stabilizing the actin filaments [127]. Subsequently, a fusion protein between GFP and the second actin-binding domain (fABD2) was published and later further improved [173]. In contrast to mTalin-GFP, the GFP-fABD2 labelling provided more structurally detailed insights of dynamic and dense actin network organizations in different species and cell types [216]. The most recent F-actin marker Lifeact-GFP was extracted from a *Saccharomyces cerevisiae* actin-binding domain [196]. Due to the small size of the 17-amino-acid-peptide it is an ideal actin marker especially for eukaryotes.

In parallel to the development of actin-visualizing markers, there has been a growing need for software solutions able to extract quantitative information from imaging data. Different frameworks use parameters such as skewness, F-actin orientation, thickness, eccentricity or complexity of filaments to describe the actin organization [173]. Frameworks to describe the actin dynamics revert to changes in filament intensity between time points or the lateral motility of filaments [173]. The underlying requirement for quantitative frameworks is the accurate extraction of actin filaments from image data. It should be noted here, that due to the restrictions of conventional optical microscopy, the majority of imaged actin structures are actin bundles, since the fine, single actin filaments might be too thin and low in intensity to be properly detected or analyzed. The extraction of filamentous objects is not only studied for cytoskeletal components, but also in for example fungal networks, retinal and blood vessels, leaf vein networks, solar filaments and street topology [162, 16, 168, 190, 128, 22, 217]. In addition, several actin filament extraction algorithms are available, although not all of them are automated and therefore need manual intervention [200, 192, 20, 39, 40, 6, 264, 253, 199, 1]. Furthermore, the extraction of filaments alone is not informative, so proper descriptors of filament properties are necessary to understand actin organization. Currently, a framework which is fully automated and quantitatively describes the actin cytoskeleton organization on a system-wide level is lacking.

1.8 The Cytoskeleton and its Involvement in Cell Shape

The shape of cells is important for different cellular processes, such as organ and tissue development, morphogenesis, cell function and behaviour [90]. While the mechanisms of morphogenesis were thoroughly investigated in unicellular systems [134], those in multicellular organisms are more challenging since there is a need for coordination between

adjacent cells. In animal cells, the relationship between cytoskeletal components, cell shape and growth is fairly well understood [52, 133], whereas in plant cells the relationship is a bit more complex due to the contribution of the cell wall in shape formation [58]. The expansion of the plant cell wall is driven by the relaxation of the cell wall which is controlled by mechanical cell wall properties [97]. The turgor pressure is reduced due to the cell wall relaxation and subsequently reestablished by passive water influx. The mechanical properties of the plant cell wall are determined by its biochemical composition and the interaction between its components. For instance, pectin regulates the growth process on a spatial and temporal level [174]. Through biochemical changes of the pectin composition, different developmental processes might be triggered. Indeed, the anisotropic growth of cells might be induced by modulations of the pectin chemistry, which lead to a non-uniform softening that precedes cell wall stiffening through cellulose [27]. A recent study outlined that cell shape is not only driven by turgor-driven growth, but also by the cell wall itself [102]. Pectin nanofilaments that are contained in the cell wall are able to chemically induce the local expansion of the cell wall and are thus actively shaping plant cells, although the validity of these results is highly discussed [59].

An interesting system to study the mechanisms for cell shape formation in more detail are pavement cells of the upper leaf epidermis [193, 67, 221, 249]. In Arabidopsis, the development of pavement cells can be defined by three distinct stages [91]. In the first stage, small, pentagonal cells expand along the leaf axis and might form elongated polygons. In the second stage, indentations form due to local growth restriction, while outgrowths appear where there is no restriction. These shallow concave and convex regions of the cell are termed necks and lobes, respectively. In the last step, the lobes expand, forming highly complex and interlocked cells (Fig. 1.5). Here, the formation of lobes in one cell corresponds to the formation of a neck in the adjacent cell, showing that there might be a cell-to-cell signalling which coordinates the growth and inhibition of cell regions, although it was found that mechanical stress might be a key driver for the morphogenesis of pavement cell shape [209]. Further, it was inferred that both the physical connectivity of adjacent cells and the turgor pressure might provide the driving force of pavement cell morphogenesis [232, 26, 28]. The complex shape of the pavement cells may ensure mechanical stability, as the interlocking of cells increases the resistance to tension and ensures that the structural integrity of the leaf surface is maintained [147, 169, 203].

The cytoskeletal components seem to play a major role in the control of pavement cell development, but the underlying molecular and biomechanical mechanisms are still debated [221, 91, 90, 249]. Many studies assume that there is a correlation between the microtubule localization and local growth restrictions, leading to the common idea that microtubules define lobe initiation sites [177, 11]. Moreover, anticlinal microtubules concentrate at concave regions in highly lobed cells [250, 261], and were also observed along growing flanks and tips of pavement cell lobes [193, 261]. This led to the conclusion that pavement cells

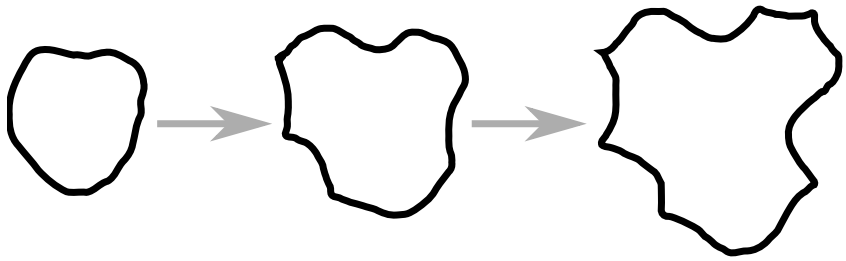

Figure 1.5: Morphogenesis of pavement cell. Pavement cells start as simple, round shapes and develop into highly complex cells over time. During morphogenesis, indentations and protrusions are formed, also called necks and lobes, respectively [91].

have alternating regions of microtubule-free and microtubule-rich zones, whereby the cell wall growth is greater in the microtubule-free regions [78]. In addition, cortical fine actin filaments were localized in microtubule-free zones of pavement cells and were suggested to promote local lobe outgrowth by delivering new cell wall materials [85, 91]. Since microtubules are known to pattern cellulose microfibril deposition [178] it was hypothesized that anticlinal microtubules generate cell wall thickenings which resist the local strain during lobe formation [177, 80, 256]. In more detail, these cell wall thickenings are evoked by the local enrichment of pectin and microfibrils which causes a modulation of the cell wall stiffness and consequently restrict its local growth [7, 26]. Yet, the proposed idea of a cell wall thickness gradient was challenged by the fact that no such gradients were found in Arabidopsis pavement cells [24]. In addition, some studies even question the involvement of microtubules in pavement cell lobing; rather, it was proposed that the microtubule patterning is a consequence of the local cell geometry and cell wall stress patterns [24, 206]. Nevertheless, different drug studies imply that for the lobe formation in pavement cells both microtubules and actin filaments are essential [78]. To understand how the cytoskeletal components are coordinated, it is important to understand the underlying molecular mechanisms.

Rho of Plants (ROP) proteins control both microtubule and actin filament organization in pavement cells [91, 90, 258]. There are two ROP-mediated pathways which countersignal the cell wall expansion with opposing effects (Fig. 1.6) [2]. To promote lobe growth, ROP2 activates RIC4, a protein which mediates the local assembly of fine cortical actin filaments [90]. As a consequence, RIC1, responsible for the organization of cortical microtubules, is inactivated. For the neck formation however, the RIC1 pathway is activated by the antagonistic ROP6, leading to a repression of ROP2 activation, therefore restricting cell expansion [92]. It was proposed that the activation of these antagonistic ROP pathways is coordinated by auxin, a hormone that is involved in many developmental processes in plant cells [254]. The auxin flow is directed by plasma membrane-localized pin formed

(PIN) proteins and it was found that PIN1 is preferentially localized at lobe tips, thus being involved in the ROP-mediated interdigitation pathway [254, 160]. An ABP1-TMK1 complex at the cell surface was proposed to sense auxin and activate ROP signalling for the interdigitation of pavement cells [21, 254]. However, the function of *ABP1* in developmental processes was challenged by recent findings of the complete loss-of-function mutants, which showed no obvious developmental defects [93]. In fact, *ABP1's* role in auxin signalling is questioned and consequently its role in plant growth and development.

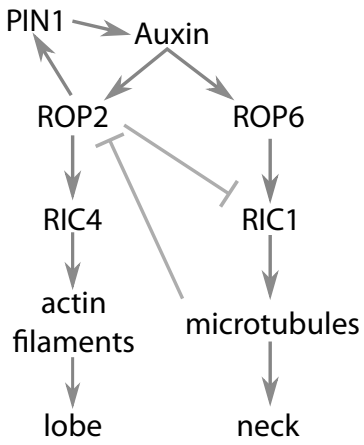

Figure 1.6: Molecular mechanism for lobe and neck formation of pavement cells. Different ROPs promote two antagonistic pathways to promote either the formation of lobes or restricting cell growth, hence promoting neck formation [91, 90, 258].

The molecular mechanism underlying the formation of lobes and necks in pavement cells can be formulated as a reaction-diffusion model using the Turing equation [238, 153]. Turing suggested that mobile, interacting diffusible components produce heterogenous spatial patterns, whereby one component is the activator which activates the other components, the inhibitor. The inhibitor in turn, is mobile and is able to move into adjacent cells to repress the activator. Through the combination of local activation and inhibition the spatial patterns are organized. Other examples for patterning following the reaction-diffusion model are the patterning of stomata pores in the leaf epidermis or the pattering of skin stripes in zebrafish [236]. To fully understand the molecular mechanisms of pavement cell morphogenesis, frameworks are needed which enable the quantification of cytoskeletal components in the cell while simultaneously quantifying global cell shape and local features such as lobes and necks.

1.9 Quantification of Cell Shape and Local Pavement Cell Features

There are two classes of descriptors that can be used to compare shapes. Region-based descriptors quantify key shape properties, such as the area, convex hull, eccentricity, media axis or combinations thereof, while boundary-based descriptors, like the classical Fourier analysis, use the shape's contour [83]. To obtain the shape descriptors one of two principal approaches can be followed: global (continuous) approaches, which analyse shapes in their entirety and structural (discrete) approaches, which divide the shapes into subparts [262]. Depending on the descriptor's properties, bias might be introduced when comparing shapes. For example, for distances between region-based descriptors the comparison is size-dependent, rendering them unsuitable for developmental studies [46, 132, 226, 252]. Using the ratios of region-based descriptors overcomes this issue, yet they are not very informative for shape comparison [124, 135, 138, 254]. A better comparison of shapes can be achieved by using landmarks which are placed along the shape boundary. However, to account for rotation, scaling and translation of different shapes, the landmarks have to be superimposed [29, 75]. In addition, cell shapes often lack common landmarks, so points have to be placed along the boundary either manually or by arbitrary sampling.

The Fourier Transform offers a classical, boundary-based descriptor used for shape comparison which decomposes a closed two-dimensional shape boundary into a set of ellipses [55, 88]. In contrast to the previous mentioned descriptors, this descriptor is similarity invariant, meaning its independent of the rotation, orientation and scaling of the shape [81]. Another boundary-based shape descriptor which is size- and orientation-invariant, characterizes a two-dimensional shape as a linear combination of sequential boundary samples following the autoregressive model approach [74]. Furthermore, for the global comparison of shapes, similarity of local shape descriptors, i.e. shape context, representing neighbourhoods of points sampled from the boundary, have been used [23].

While the presented approaches mainly focus on the general description and comparison of global shape features, there are also plenty of approaches which focus on local shape features. Here, we discuss different approaches which were used to identify local pavement cell features, namely the convex and concave regions of the boundary, termed lobes and necks, respectively. The detection of lobes and necks has been used in many studies to compare differences in pavement cell shape [240, 145, 252, 156]. Very simple region-based tools reduce the shape to a one-pixel representation, called the skeleton or medial axis, which preserves topological and size characteristics of the shape (Fig. 1.7A) [226]. The medial axis is described by a set of symmetry axes which are positioned equidistant between points along the shape's boundary [12]. However, a disadvantage of the skeleton-based is the sensitivity to small perturbations of the shape. Lobes are quantified by the number, length and angle of the skeleton branches; however, this approach is not very accurate

when identifying necks or weak-defined lobes. The usage of landmarks was also applied to identify lobe regions, by using fluorescent microbeads on the leaf epidermis surface (Fig. 1.7B) [75]. The lobes were defined as sectors which are created as polygons from multiple landmarks to describe the growth of lobes over time. The downside of this approach is that the accuracy of detected lobes depends on the number and placement of artificial landmarks, which is hard to control.

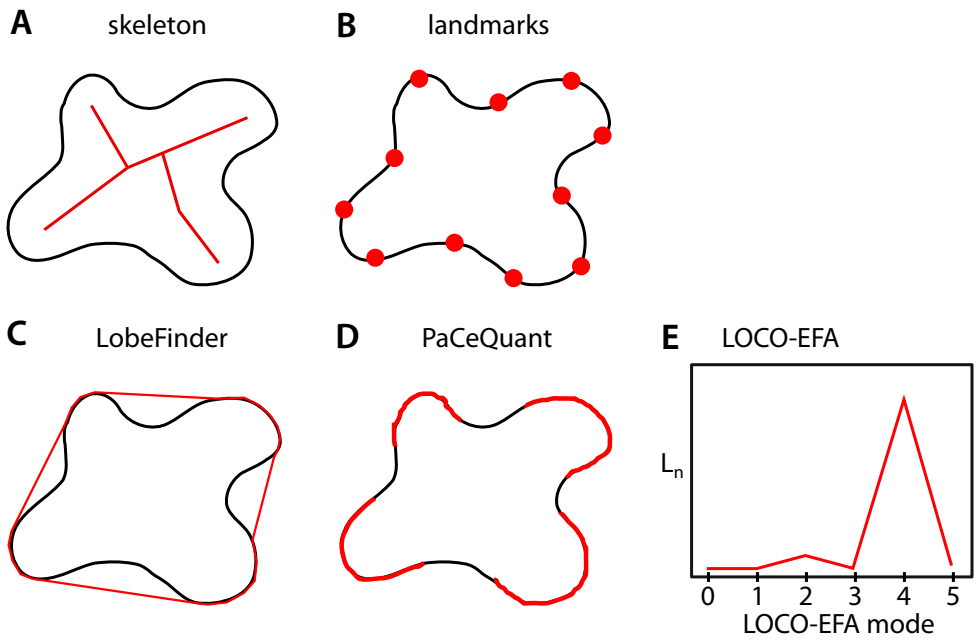

Figure 1.7: Overview of different pavement cell shape quantification methods. Local shape features of pavement cells, namely lobes and necks, are used in many studies to compare differences in pavement cell shape. Prominent approaches are (**A**) the skeleton-based medial axis of a cell [226], (**B**) landmark-based [75], and (**D-E**) outline-based methods. (**C**) Lobefinder uses a modified convex hull to identify lobes and necks [252], while (**D**) PaCeQuant uses changes in the contour curvature for lobe detection [156]. (**E**) LOCO-EFA uses a modified Fourier Transform to estimate the number of lobes [208]. Besides the depicted approaches, other parameters for the description of pavement cell shape include the circularity which describes the degree of roundness of a shape, the number of lobes per circumference, or the lobe amplitude.

More sophisticated detection tools use the shape boundary to identify lobes and necks of pavement cells. LobeFinder operates on the cell boundary coordinates to create a modified convex hull, a minimal polygon surrounding the whole set of coordinates (Fig. 1.7C) [252]. The convex hull is used to identify key points of the cell shape, which correspond to lobes. LOCO-EFA also uses an outline-based method, but here the Elliptic Fourier Analysis (EFA) is used to quantify complex pavement cell shapes by providing a set of metrics that relate directly to morphological features (Fig. 1.7D) [208]. Here, the cell shape is

decomposed into an infinite series of ellipses, which can be represented as a unique combination of coefficients. From the contribution of certain ellipses, it is then possible to infer the number of lobes present in the shape. Lastly, the toolbox PaCeQuant offers an automatic segmentation and feature extraction for pavement cells (Fig. 1.7E)[156]. Lobes and necks are defined according to their local curvature orientation: a negative and positive curvature correspond to convex and concave segments, respectively. To detect lobes, the point of change in signs of the local curvature are determined. A neck point corresponds to the centre point of a concave curvature, whereas a lobe is defined as the contour segment between two adjacent neck points.

Despite efforts to devise descriptors that simultaneously identify differences between pavement cells across different taxa and accurately characterize their local shape features, comparative analyses that assess the performance of existing solutions based on a gold standard is lacking. Such efforts can be regarded as a necessary step towards understanding the contribution of cellular processes, beyond mechanical stresses, in the emergence of complex cell shapes [209].

Chapter 2

CytoSeg: Automated Extraction of Actin Filaments

2.1 Research Questions and Aims

The actin cytoskeleton is important for many cellular processes, such as cell movement, cell growth, cytoplasmic streaming and transport processes [178, 205, 232, 62, 95]. Depending on how the actin cytoskeleton is connected by cross-linking proteins, it can occur as bundles or networks of filaments. To better understand cell wall patterning it is important to know how the cytoskeletal structures are organized and how they are modified over time. While answers to these questions have been obtained for the microtubules, the actin cytoskeleton has remained difficult to study due to its highly dynamic behaviour. Nevertheless, while there are theoretical models that describe the actin cytoskeleton organization, there are no frameworks to describe and quantify the actin cytoskeleton based directly on imaging data and to investigate how such organization underpins trafficking of cytoplasmic components.

To address these issues, the first part of the thesis deals with the organization of the actin cytoskeleton and how we can quantify its key features. We describe the development of a powerful automated framework to extract and represent the actin cytoskeleton as networks and we used this framework to show that the actin cytoskeleton has structural properties facilitating efficient transport [42]. Furthermore, we applied the developed frameworks to different biological systems to compare the actin cytoskeleton organization of different cell types and between wild-type and mutant cells [259, 222]. Finally, we further improved our framework and its usability by developing a graphical user interface [167].

2.2 Materials and Methods

2.2.1 An Approach to Quantify the Cytoskeleton Organization

The actin cytoskeleton is a highly dynamic cellular component and its quantification has proven as challenging. Here, we propose a fully automated framework which represents the

actin cytoskeleton as a network and enables the quantification of the actin organization on a system-level. The input of the framework were image stacks of fluorescently tagged actin filaments.

Image pre-processing.
To extract networks from the actin filaments, the recorded images were first pre-processed using the image processing software Fiji [210]. The Fiji pipeline includes different correction steps, such as the correction for cell drift (stack registration), uneven illuminated background (background subtraction) and loss of fluorescence due to long light exposure (bleach correction). To manually select the region of interest (ROI), the image stacks were Z-projected using the maximum intensity to highlight actin filaments. After selecting the ROI, the Z-projected images were not used for further analysis and were discarded. The network extraction was continued on the pre-processed image stacks.

Network extraction and randomization.
The pre-processed image was smoothed using a Gaussian filter and a Gaussian kernel of size v_{width} (Fig. 2.1A). To enhance the filamentous-like structures of the actin filaments, we applied a tube filter which was defined by the same parameter v_{width} (Fig. 2.1B). The resulting image was used for the binarization into background and actin filaments using an adaptive threshold v_{thres} (Fig. 2.1C). The binary image was cleaned of small particles which were below the size of v_{size}; further, actin filaments which were below the average filament intensity v_{int} were removed. Due to the thinness and low intensity of single actin filaments, they might have been removed during this step. Following this, the majority of segmented actin structures will be actin bundles. Afterwards, the binary structure was reduced to a one-pixel width using the skeletonization approach (Fig. 2.1D) [104].

We next created a network by placing nodes at all crossings and end points of the skeleton, which were identified by a 3x3 pixel sliding window. This sliding window checks how many neighbouring pixels the selected skeleton pixel has. If only one neighbour was found, the skeleton pixel was defined as an end point. In contrast, skeleton pixels with three or more neighbours were defined as a crossing. All other skeleton pixels were not considered as network nodes (Fig. 2.2).

Once all nodes were identified, the edges between two nodes were added if the pair of nodes was directly connected via the skeleton. For each edge, we assigned edge weights which store information about the underlying filament intensity and edge length. For this, we tracked the skeleton pixels between two connected nodes in the Gaussian filtered image and stored the summed filament intensity along these pixels and their surrounding pixels in a 3x3 periphery in a seperate image. The edge length was calcuated as the Euclidean distance d_E:

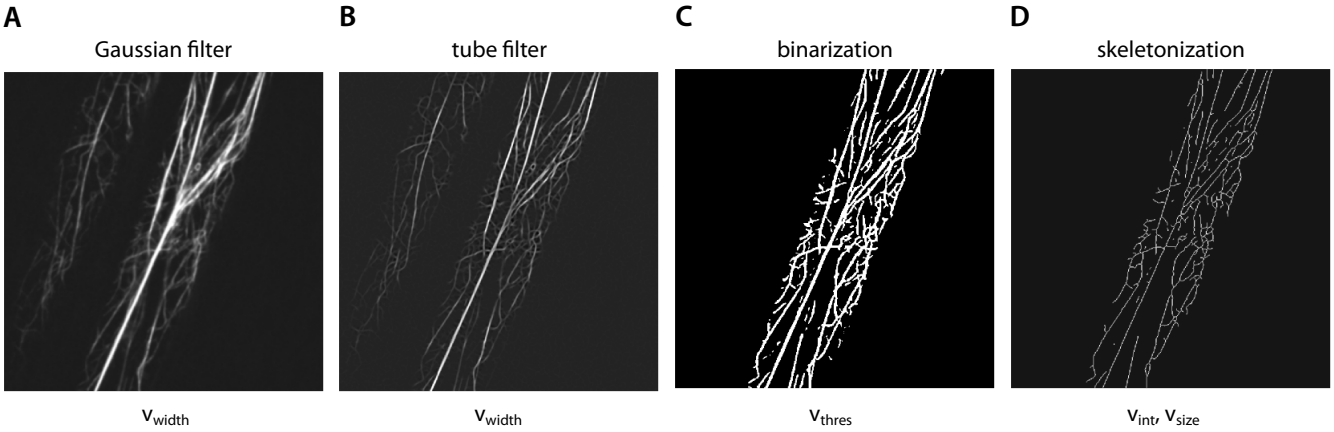

Figure 2.1: Image processing pipeline to segment actin filaments. (**A**) A Gaussian filter is used for image smoothing using the v_{width} parameter. (**B**) A tube filter is used to enhance tube-like structures using the same parameter as before. (**C**) The image is binarized using v_{thres} to separate into background (black) and actin filament (white). (**D**) The binarized image is reduced to a one-pixel width using skeletonization. Particles smaller than v_{size} are removed, as well as filaments with an intensity below v_{int}.

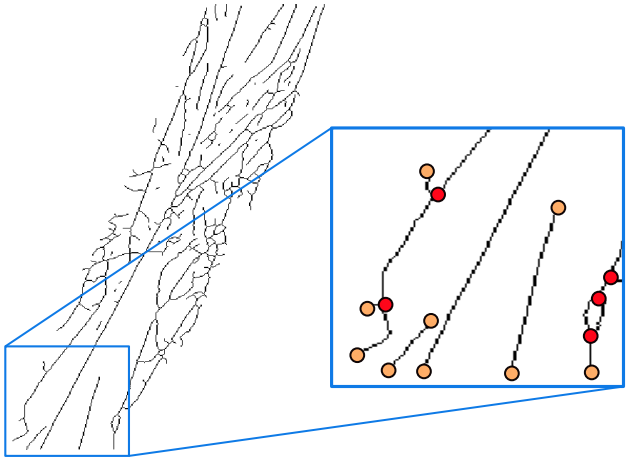

Figure 2.2: Detection of network nodes and edges from the segmented skeleton. The nodes are detected by identifying crossings (red) and end points (orange) of the skeleton. Afterwards, edges are tracked from one node until another node is found.

$$d_E(x,y) = \sqrt[2]{(x_1 - y_1)^2 + (x_2 - y_2)^2}, \tag{2.1}$$

where x and y are defined as the coordinates of the graph nodes.
In addition, we designed and implemented an algorithm for the creation of randomized networks that keep the number of nodes and edge length distribution (Fig. 2.3). To this end, we removed all edges from the graph and sorted them into bins according to their edge length. The node positions were shuffled within the defined ROI and edges were added back to the graph such that their length was preserved.

Parameter gauging.

As mentioned in the previous section, the network extraction depends on the four parameters v_{width}, v_{thres}, v_{size} and v_{int}. The selection of these parameters will determine the quality of the image segmentation into background and actin filaments. To find the set of optimal parameters set we used parameter gauging. For this, we extracted the skeletonized actin filaments from a selection of images by using the automated framework and using manual segmentation (Fig. 2.4). For the automated segmentation we defined specific ranges of ten values for each parameter. Trying each possible combination of parameter values, we extracted the skeleton of the actin filaments. To this end, we calculated the distance between the manual and automated segmentation and identified the parameter set that resulted in the average minimum Euclidean distance between the pixels of both segmentations. The selected set of parameters can then be used for the image segmentation of this specific experiment.

Transport-related network properties.

Following the extraction of networks from the image data, seven different network properties were computed to quantify the cytoskeletal phenotype as well as evaluating the transport efficiency in these networks. Extracted networks were represented as weighted,

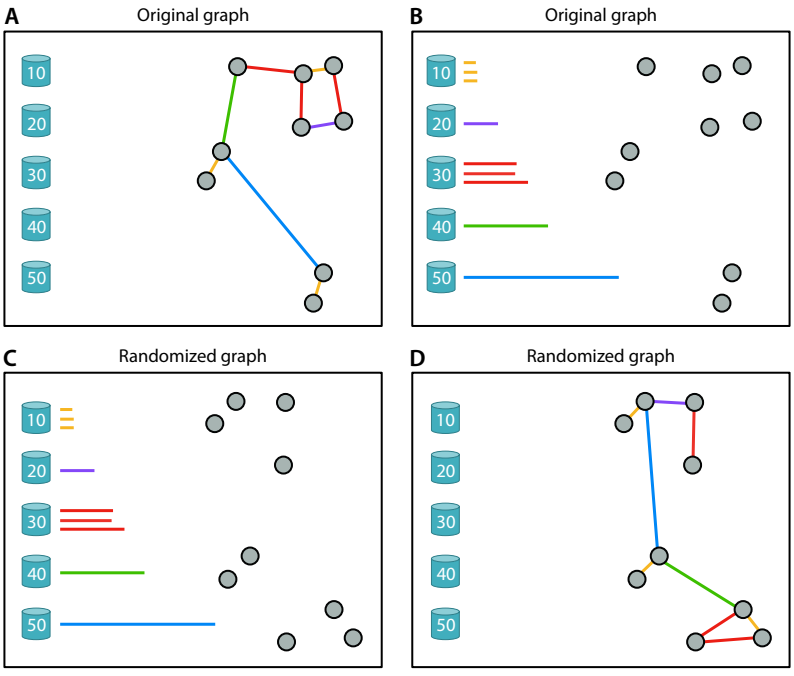

Figure 2.3: Randomization of networks while keeping the number of nodes and edge length distribution the same. (**A-B**) The edges are removed from the graph and sorted into bins according to their edge length (bins were given by [0, 10, ..., 190, 200,∞] pixels). (**C-D**) The position of nodes is shuffled and the edges from the bins are placed between nodes that match their weights (i.e. length).

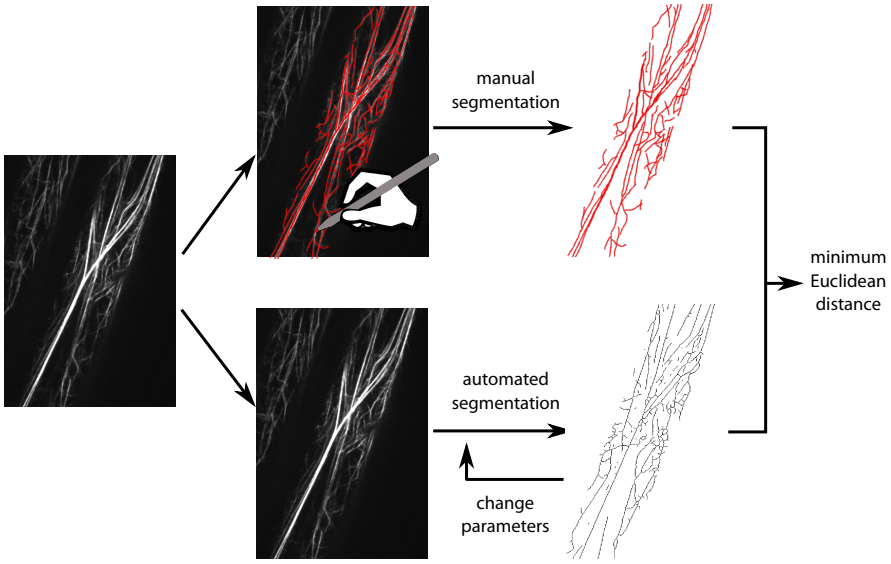

Figure 2.4: Gauging of parameters for the optimal image segmentation. The actin cytoskeleton is both manually extracted and using the automated framework. For each parameter were defined a range of ten values and used each possible combination of parameter values for the extraction. The set of parameters of the automatically segmented skeleton with the minimum Euclidean distance to the manual detected skeleton is selected for the final segmentation.

undirected graphs $G = (V, E)$ with $|V|$ vertices and $|E|$ edges. The average edge capacity was calculated as a measure of actin bundling by

$$EC = |E|^{-1} \sum_{e=1}^{|E|} a_{e,capa}, \tag{2.2}$$

where $a_{e,capa}$ is the edge capacity which captures the filament thickness by measuring the average edge weight per filament segment.
The connectedness of the networks was measured by removing all edges with edge capacities below the 50^{th} percentile and computing the average fraction of nodes per connected components CC. For the evaluation of the transport efficiency, we chose the average shortest path length

$$ASPL = \frac{1}{2|N|(|N|-1)} \sum_{u \neq v} d(u, v), \tag{2.3}$$

with $u, v \in V$ and $d(u, v)$ the shortest distance between the nodes u and v. Furthermore, we calculated the coefficient of variation of the shortest path lengths

$$CV_{ASPL} = \frac{SD(ASPL)}{\overline{ASPL}}, \tag{2.4}$$

where SD is the standard deviation and $\overline{ASPL}$ is the mean of shortest path lengths of all

nodes. Additionally, we computed the algebraic connectivity as a measure for robustness of the network against disruptions

$$AC = \lambda_2, \tag{2.5}$$

where λ_2 is the second smallest Eigenvalue of the graph Laplacian $L = D - A$. Here, D is the diagonal matrix of capacity-weighted nodes and A is the graph's adjacency matrix. The assortativity was calculated as measure of heterogeneity by

$$AS = \frac{1}{2|E|} \sum_{n=1}^{N} \sum_{m=1}^{N} (a_{(n,m),capa} - \frac{d_n d_m}{2E} d_n d_m. \tag{2.6}$$

The assortativity reflects the heterogeneity of the actin distribution by quantifying whether two adjacent nodes are of a similar degree, indicated by a positive assortativity. Thus, regions of spatially clustered actin bundles can be detected.

Edge angles between filament segments and the major cell axis x_{cell} were calculated as

$$ANG = arccos(\frac{(x_n - x_m)x_{cell}}{||x_n - x_m||||x_{cell}||}). \tag{2.7}$$

2.2.2 Applications to Different Biological Questions

Examining the transport effectiveness of the actin cytoskeleton.
Growing and fully elongated *Arabidopsis thaliana* etiolated seedlings were imaged using a spinning-disk confocal microscope as described in Breuer et al., 2017 [42]. The hypocotyls of the seedlings were either treated with LatB, a drug inhibitting the actin polymerization, or not treated (control). For every image the hypocotyl was scanned through at 1 μm intervals, resulting in 100 image slices per image stack. Networks were extracted and randomized from every z-stack of each image. To test for statistical significance, we used an independent two-sample t-test.

Determining the growth type of cotton fibers.
Images of the actin cytoskeleton in cotton fibers, hypocotyl epidermal cells, root epidermal cells and root hairs were imaged by our collaborators with a spinning-disc microscope as described in Yu et al., 2019 [259]. In addition, we imaged the actin cytoskeleton in *Arabidopsis thaliana* Columbia-0 35S:FABD-GFP labelled elongating hypocotyls and root hairs. We used the proposed framework to process the images and extract networks of the actin cytoskeleton. For the comparative analysis of cell types, we calculated the following network properties: number of connected components, average edge capacity, assortativity, average path length, CV of path length and CV of edge angles. In addition, we compared the extracted networks of each cell type against an ensemble of randomized null model networks. For statistical testing we applied an independent two-sample t-test and

corrected for multiple testing using the Bonferroni adjustment.

Actin cytoskeleton organization of rmd2 mutants in rice.
Images of light-grown, 5-day-old rice seedlings were captured using a confocal laser scanning microscope as described in Song et al., 2019 [222]. For the analysis we selected 14 replicates of wild type rice seedlings and 15 replicates for the *rmd-2* mutant. We used the network extraction pipeline as described in Section 2.2 and slightly adjusted the preprocessing pipeline. Therefore, we used a Fiji pipeline and first corrected for drifting of cells, bleaching and uneven illuminated background [210]. Each image stack was comprised of multiple slices taken at different focal distances. To account for this, we used a maximum intensity Z-projection to combine the slices into a single composite image. The network extraction was done as described Section 2.2.1. For the analysis of network properties, we selected the number of connected components, average edge capacity and the average shortest length. In addition, we calculated the diameter of the networks which we normalized by the expected diameter following Moore's bound $D_{exp} = log_{\Delta} n$, where n is the largest number of network edges and Δ is the maximum degree. To test the statistical difference between the wild type and *rmd-2* rice seedlings we used an independent two-sample t-test.

2.3 Results

We applied our proposed framework to investigate the actin cytoskeleton organization in different biological systems. First, we addressed the question whether our framework indeed is capable of describing the actin cytoskeleton organization on a system-wide level. Therefore, we investigated if the actin cytoskeleton is tuned towards efficient transport in plants by comparing the actin cytoskeleton in Arabidopsis hypocotyls against depolymerized actin cytoskeletons and randomized actin networks. In addition, we used the framework to quantify the actin organization in cells in which growth mode was unknown or assumed. To do so, we investigated the actin cytoskeleton in cotton fibers to deduce their growth mode by comparing the actin organization with cells that typically exhibit tip growth and diffuse growth. In another study, we investigated the mutual influence between the actin cytoskeleton and cellular processes. To this end, we compared the actin cytoskeleton in rice seedlings for wild-type cells and a mutant line to investigate the influence of the actin cytoskeleton on negative gravitropism in plants. Finally, we built a graphical user interface for the proposed framework to allow for an easy distribution and usage, and show that the framework is also applicable to problems in other fields.

2.3.1 Examining the Transport Effectiveness of the Actin Cytoskeleton

To investigate the system-wide coordination of cellular transport in plant cells, we imaged the actin cytoskeleton in Arabidopsis hypocotyls [42]. The hypocotyls are highly suitable to study individual actin filaments, as the cytoskeleton is localized close to the plasma

membrane due to the large central vacuole. We compared control cells with cells which were treated with LatB, a drug that inhibits the actin polymerization [242].

We first analysed the extracted networks of the growing hypocotyls. The comparison of control and LatB treated cells revealed that control cells have a smaller number of connected components ($p < 10^{-50}$), indicating that the actin cytoskeleton is largely connected in the control conditions (Fig. 2.5D). This can also be inferred from the visual inspections of the extracted networks (Fig. 2.5A,C). The average edge capacity was lower in LatB treated cells ($p < 10^{-38}$) and corresponds to a reduction in actin bundling (Fig. 2.5D). The assortativity was larger in control cells ($p < 10^{-50}$) and suggests that the control cells have large patches of actin bundles which are surrounded by finer actin filaments (Fig. 2.5D). We further investigated the distribution of edge angles and found that the edges in control cells are preferentially oriented in parallel to the major cell axis (Fig. 2.5G). Together, the results show that the extracted networks indeed capture biological relevant information.

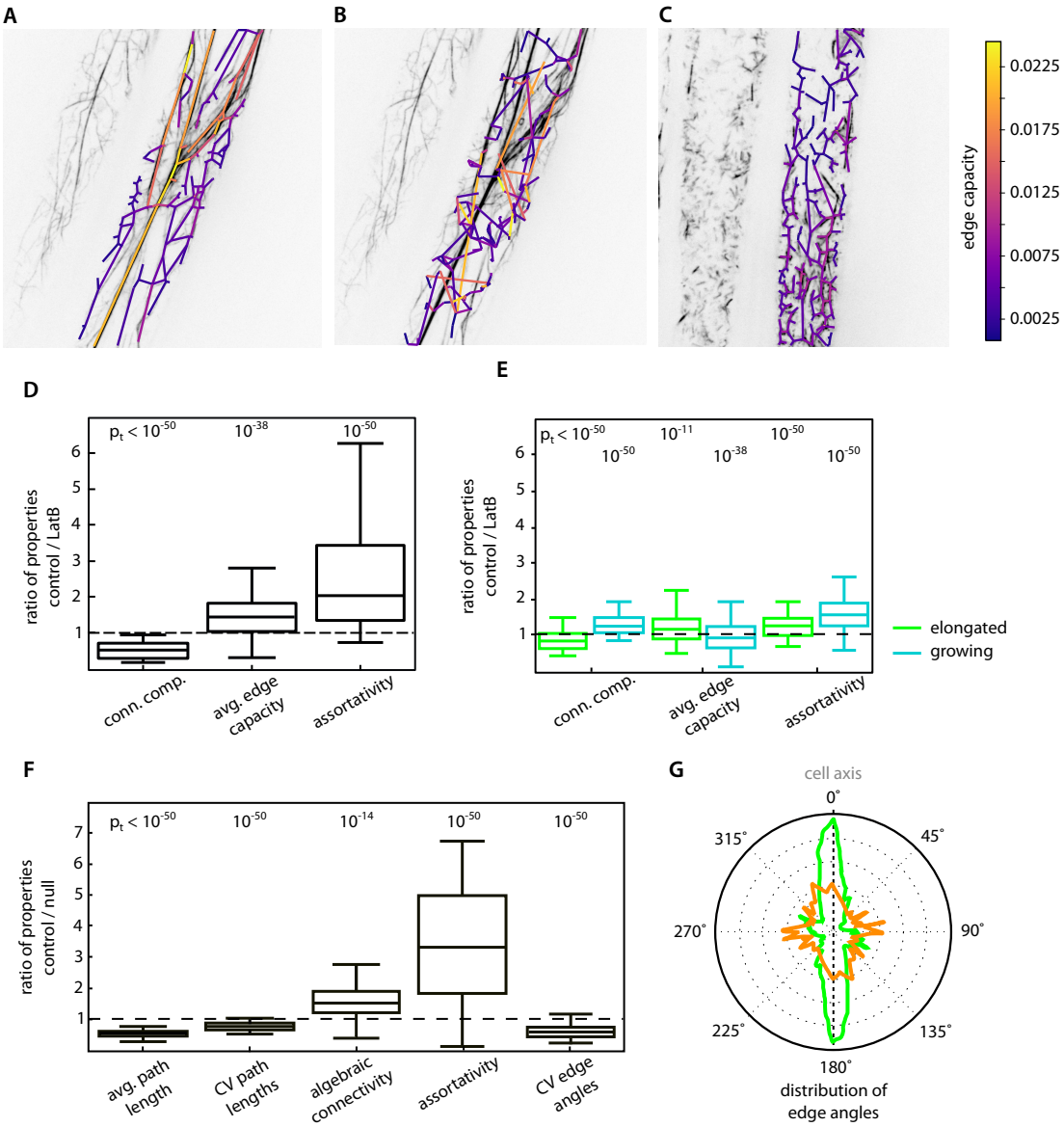

Figure 2.5: The actin cytoskeleton captures biological signals and reveals transport efficiency. Extracted and overlayed actin network of (**A**) control cells, (**B**) control cells (randomized) and (**C**) LatB-treated cells. The color of the extracted networks corresponds to the edge capacity. (**D**) Extracted actin networks of elongated control cells have a lower number of connected components ("fragmentation") and edge capacity ("bundling") and a larger assortativity ("heterogeneity") than LatB treated cells. (**E**) The actin cytoskeleton of growing cells has similar properties as elongated cells but are more evenly distributed in the cell and are structurally more branched, indicated by a lower average edge capacity and higher number of connected components. (**F**) The extracted actin networks support efficient transport as shown by a smaller average shortest path length ("reachability"), small coefficient of variation of path length, higher algebraic connectivity ("robustness") and assortativity and lower coefficient of variation of edge angles for the extracted networks when compared to randomized networks. (**G**) Edges in elongated and growing actin networks are oriented parallel to the major cell axis for control cells, LatB treated cell have a more random distribution. Reprinted from Breuer et al., 2017 [42]

We obtained similar results for the comparison of control and LatB treated cells for the growing cells, but also found that the control cells showed a stronger fragmentation of the actin network which is displayed by a larger number of connected components (Fig. 2.5E). In addition, the control cells had a lower average edge capacity, which indicates that growing cells have actin bundling. These findings lead to the conclusion that the actin cytoskeleton in growing cells has a strongly branched structure and the actin is more evenly distributed in the cell.

Finally, we compared the extracted networks with the randomized networks and analysed the transport efficiency of the actin cytoskeleton (Fig. 2.5F). The shortest average path length was smaller in the extracted networks ($p < 10^{-50}$), showing that cells are tuned towards short path lengths. Furthermore, fluctuation in path length were at a low level, as shown by the coefficient of shortest path lengths which was lower in the extracted networks ($p < 10^{-50}$). The algebraic connectivity was higher in the extracted networks ($p < 10^{-14}$) stating that the actin cytoskeleton is transport efficient by design. Finally, we found that the bundling of actin filaments is functionally relevant which was shown by the higher assortativity, suggesting that there are well connected regions of actin bundles, and lower CV of edge angles, implying minimal contortion of the actin bundles, for the extracted networks ($p < 10^{-50}$ and $p < 10^{-50}$, resp.). Taken together, the results indicate that the actin cytoskeleton supports efficient transport in plant cells.

2.3.2 Determining the Growth Type of Cotton Fibres

Cotton fibers are single cells of the seed epidermis which elongate in a highly polarized manner. Their unicellular morphology and distinct stages of cell wall synthesis render cotton fibers a powerful model for cell wall research [103, 122]. Furthermore, cotton fibers produce an extensive amount of cellulose and are therefore highly important for the textile industry [148]. To understand how cotton fibers elongate, we investigated the mechanisms behind the polarized growth. Studies on this topic revealed that the cytoskeleton might control the fiber development, but it remains unclear how this is achieved by the cytoskeleton organization [244, 191, 231]. Cells have two distinct growth modes which are directly dependent on, or related to, the structure of the cytoskeleton network: they can expand either via diffuse growth or via tip growth. However, the dispute whether cotton fibers are diffuse or tip growing remains inconclusive [191, 231, 235]. The quantitative analysis of the cytoskeleton is therefore important to shed light upon the subject. While previous studies were limited by difficulties in visualizing the cytoskeleton, e.g. by using beads to estimate the growth rate yielding unsatisfactory results, here we were able to image the cytoskeleton by using stable cotton fiber transformants expressing fluorescent markers of actin [259].

Actin cytoskeleton organization of different cotton cell types.
To investigate the growth mode of cotton fibres grow, we compared the actin cytoskeleton organization in different cell types of cotton plants expressing the ABD2-GFP marker.

Therefore, we analyzed different actin properties in cells that use either diffuse or tip growth and compared them to actin properties of cotton fibres [259]. As an example for diffuse growing cells, we imaged root epidermal cells of the elongation zone and elongating etiolated hypocotyl cells (Fig. 2.6F-I). In addition, we imaged root hair cells as an example for tip-growing cells (Fig. 2.6J, K). As described in Breuer et al., we processed and extracted the actin networks from the imaged cell types (Fig. 2.6A-D).

We calculated different properties of the extracted networks as described in Section 2.2.1 and used those to compare similarities of network properties between the different cell types. To estimate the overall connectedness of the actin network, we examined the number of connected components (Fig. 2.6L). Here, a large number of connected components suggest that there are large patched of unconnected actin structures. We found that the cotton fibres exhibited a significantly smaller number of connected components than the root epidermal cells (independent two-sample t-test, p-value $< 10^{-46}$) and the elongating hypocotyl cells (p-value $< 10^{-41}$), but significantly larger than that of root hairs (p-value $< 10^{-39}$).
The average edge capacity, a measure for the degree of actin bundling, was significantly larger in cotton fibres than in root epidermal cells (p-value $< 10^{-35}$) and elongating hypocotyl cells (p-value $< 10^{-48}$), but significantly smaller than in root hairs (p-value $< 10^{-44}$, Fig. 2.6M).
Furthermore, we calculated the assortativity of the networks to assess the heterogeneity of the networks, which indicate the degree of clustering of F-actin and actin bundles (Fig. 2.6N). The cotton fibres had a significantly higher assortativity, and therefore a higher degrees of clustering, than all of the other cell types (root epidermal cells, p-value $< 10^{-51}$; elongating hypocotyls, p-value $< 10^{-53}$; root hairs, p-value $< 10^{-26}$).
To quantify the reachability of the actin networks from one point to another, we calculated the average shortest path lengths (Fig. 2.6O). The cotton fibres showed a similar average shortest path lengths than both root epidermal cells (p-value $< 10^{-3}$) and elongating hypocotyls (p-value $< 10^{-3}$), although it was significantly smaller than that of root hairs (p-value $< 10^{-26}$).
In addition, the coefficient of variation of the shortest path lengths, a measure for the fluctuation in the path lengths, was significantly larger in cotton fibers compared to root epidermal cells (p-value $< 10^{-12}$) and elongating hypocotyls (p-value $< 10^{-16}$), but similar to that of root hairs (p-value < 0.2, Fig. 2.6P).
Finally, the coefficient of variation of the edge angles was calculated to assess the degree of actin bundling, as actin bundles tend to be organized along the longitudinal axis of the cell (Fig. 2.6Q). Cotton fibres displayed a significantly smaller metric than the root epidermal cells (p-value $< 10^{-57}$) and the elongating hypocotyls (p-value $< 10^{-72}$), but were similar than that of the root hairs.

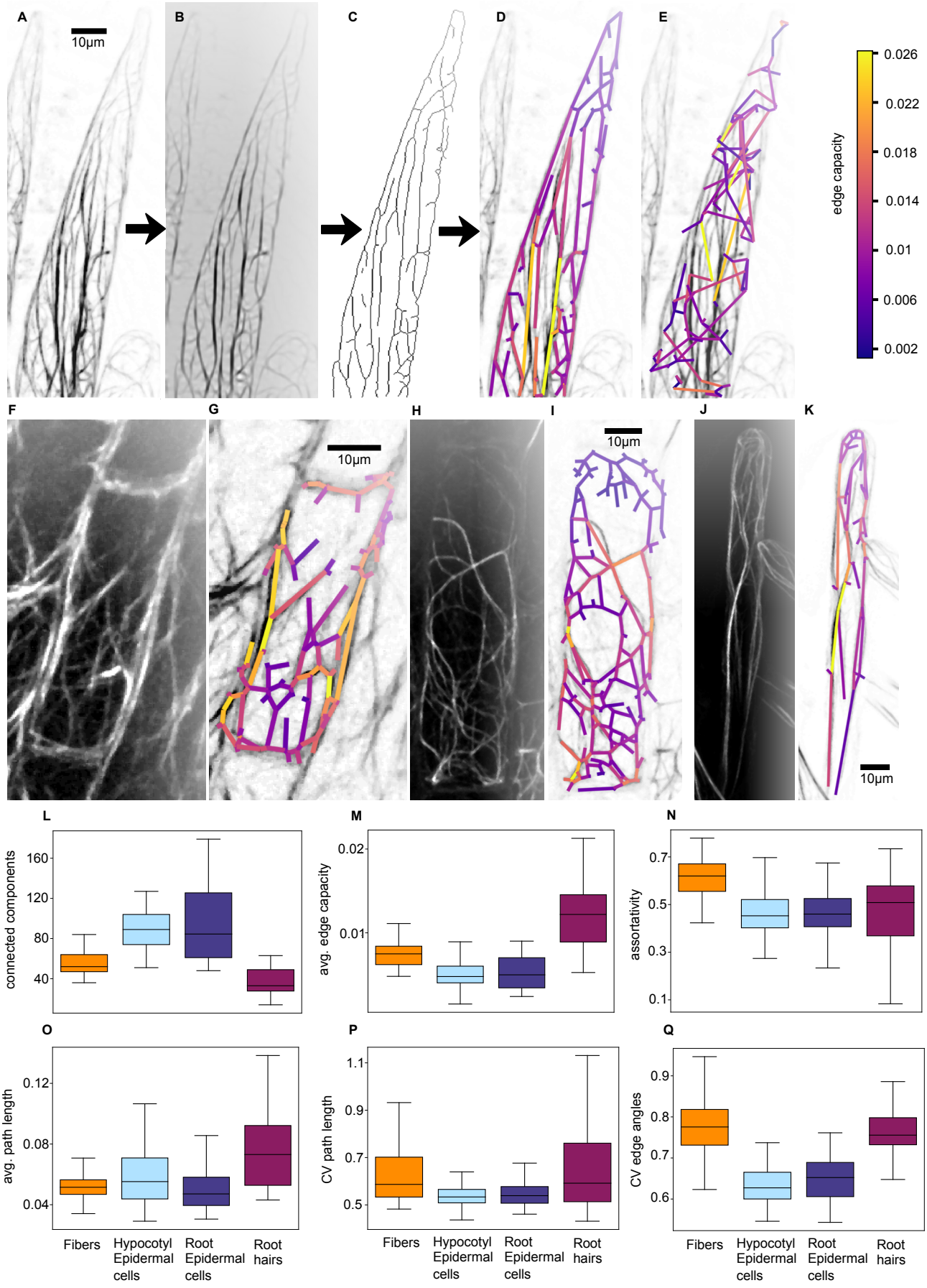
A
10µm
B
C
D
E
edge capacity
0.026
0.022
0.018
0.014
0.01
0.006
0.002
F
G
10µm
H
I
10µm
J
K
10µm
L
connected components
160
120
80
40
M
avg. edge capacity
0.02
0.01
N
assortativity
0.7
0.5
0.3
0.1
O
avg. path length
0.12
0.08
0.04
P
CV path length
1.1
0.9
0.7
0.5
Q
CV edge angles
0.9
0.8
0.7
0.6
Fibers
Hypocotyl Epidermal cells
Root Epidermal cells
Root hairs

Figure 2.6: *(Previous page.)***Automated network extraction analysis shows that the F-actin organization in cotton fibres blends features of that in tip- and diffuse-growth cells.** (**A-E**), Automated extraction of networks from actin cytoskeletal image data from cotton fibres. (**A**) A greyscale confocal image of cotton fibre after bleach correction, background subtraction and stack registration. (**B**) Enhanced tube-like structures after application of a tubeness filter. (**C**) A skeletonized cytoskeleton image after elimination of small or low-intensity objects. (**D**) A greyscale cytoskeleton image with the extracted network overlaid, with the edges colour-coded according to their capacity. (**E**) A greyscale cytoskeleton image with a randomized network overlaid. The edge capacities are indicated as per the colour scheme to the far right. (**F-K**) Single-frame and greyscale cytoskeleton images with the extracted network overlaid, with the edges colourcoded according to their capacity from different cell types: elongating cotton hypocotyl epidermal cells (**F, G**), elongating cotton root epidermal cells (**H, I**) and cotton root hairs (**J, K**). For each cell type (**A, F, H, I**), representative images of 12 fibre cells from five independent replicates were imaged and networks were extracted. (**L-Q**) Different properties of extracted networks from cotton fibres (orange), elongating hypocotyl epidermal cells (light blue), elongating root epidermal cells (dark blue) and root hairs (magenta). We then calculated the properties from 250, 161, 150 and 132 extracted networks of cotton fibres, elongating cotton hypocotyl epidermal cells, elongating cotton root epidermal cells and cotton root hairs, respectively. The properties are indicated on the y axes of the graphs. The box plots are shown with median (horizontal line), 25th and 75th percentiles (box edges) and 1.5x interquartile range (whiskers). Reprinted from Yu et al., 2019 [259].

Taken together, the analysis of the different transport-related networks properties indicates that some of the properties of the cotton fibres are more similar to that of diffuse growing cells, while others are more similar to properties of tip-growing cells. For example, the average shortest path length of the actin networks in cotton fibres and diffuse growing cells was smaller than in root hairs, indicating that these cell types exhibit an actin organization which is more efficient for transport. In contrast, other network properties of the cotton fibres were more similar to that of tip-growing cells, like the coefficient of variation of the edge angles. This indicates, that both cotton fibres and root hair cells exhibit actin networks with regions of aligned actin bundles, whereby root hairs show a slightly higher degree of bundling than cotton fibres (average edge capacity). Other network properties of the cotton fibres were distinct from both diffuse and tip-growing cells. For example, the actin networks of cotton fibres were less well connected than actin networks in tip-growing cells, but better connected than in diffuse growing cells. Moreover, cotton fibres displayed a stronger network heterogeneity than the other cell types, suggesting that there are well-defined regions of bundled actin which are surrounded by actin filaments.

Comparison of actin cytoskeleton organization in Arabidopsis and cotton.
We compared the network properties of the cotton actin cytoskeleton with elongating hypocotyls and root hairs from *Arabidopsis thaliana*. For all investigated network properties, we found that the Arabidopsis cell types are similar to the corresponding cell types of cotton (Fig. 2.7A-D). For example, the number of connected components was highest in the cotton hypocotyl epidermal and root epidermal cells and also in the Arabidopsis hypocotyl cells. Both cotton and Arabidopsis root hairs had the lowest number of connected components, while the cotton fibers were somewhere in between.
We further performed a clustering analysis based on the network features and calculated the pairwise distances between network properties of the different cell types and plant species. To this end, the calculated network properties of each sampled cell were log- and z-transformed to put the different network properties on a common scale. For hierarchical clustering of the transformed data the Euclidean distance between two sample pairs was used to quantify the distance between pairs of observations, obtained from hierarchical average linkage clustering (Fig. 2.7E). We found two clusters largely corresponding to root hairs and the joined group of hypocotyl and root epidermal cells. Once again, the Arabidopsis root hairs and hypocotyls were clustered together with the corresponding cotton cell types. Yet, we found that the cotton fibers were clustered closer with the root hairs of both plant species.
We tested this observation by calculating the pairwise Euclidean distance between the means of the different network properties of cotton fiber cells and the other cell types. The results demonstrated that the pairwise distance between cotton fibers and hypocotyl cells for both cotton and Arabidopsis were larger than between the cotton fibers and root hairs of both species (Fig. 2.7F). This shows that the root hairs and hypocotyls of both plant species have a similar actin cytoskeleton organization and are distinct from the cotton fibers, but are closer to tip growing cells than to cells that expand via diffuse growth.

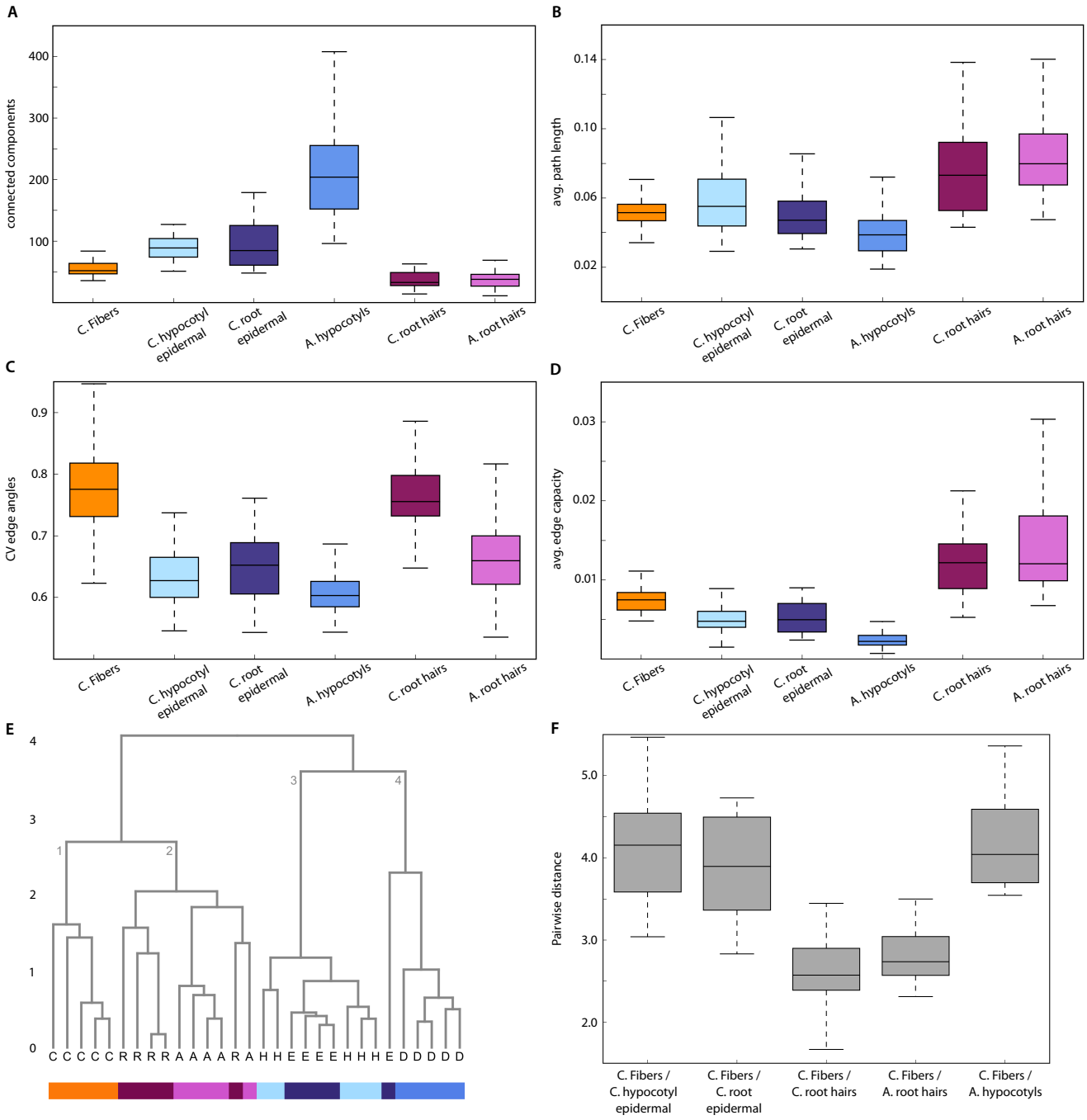
A
connected components
400
300
200
100
C. Fibers
C. hypocotyl epidermal
C. root epidermal
A. hypocotyls
C. root hairs
A. root hairs
B
avg. path length
0.14
0.10
0.06
0.02
C
CV edge angles
0.9
0.8
0.7
0.6
D
avg. edge capacity
0.03
0.02
0.01
E
4
3
2
1
0
C C C C C R R R R A A A A R A H H E E E E H H H E D D D D D
F
Pairwise distance
5.0
4.0
3.0
2.0
C. Fibers / C. hypocotyl epidermal
C. Fibers / C. root epidermal
C. Fibers / C. root hairs
C. Fibers / A. root hairs
C. Fibers / A. hypocotyls

Figure 2.7: *(Previous page.)***Automated network extraction analysis shows that the F-actin organization in cotton fibres and Arabidopsis cells is similar.** (**A-D**), Different properties of extracted networks from cotton fibres (orange), cotton elongating hypocotyl epidermal cells (light blue), cotton elongating root epidermal cells (dark blue), cotton root hairs (magenta), Arabidopsis root hairs (pink) and Arabidopsis hypocotyls (blue). The properties are indicated on the y axes of the graphs. The box plots are shown with median (horizontal line), 25th and 75th percentiles (box edges) and 1.5x interquartile range (whiskers). (**E**), Average linkage clustering (E: cotton hypocotyl epidermal cells, C: cotton fibers, R: cotton root hairs, A: Arabidopsis root hairs, D: Arabidopsis hypocotyls) and (**F**), pairwise Euclidean distance between different cell types.

2.3.3 Actin Cytoskeleton Organization of *rmd-2* Mutants in Rice

Two key factors that contol the growth direction of plants are light and gravity. The coordinated sensing of these factors ensures that plant roots grow downwards in response to the gravity, while the shoots grows upwards towards the light. This process, termed gravitropism, is defined by gravisensing, signal initiation, transduction and asymmetric cell growth [32]. The starch-filled amyloplasts in columella and endodermal cells of roots and shoot, respectively, are considered as statoliths which sediment according to the gravity vector [32, 158].
How light and gravity signalling and perception are coordinated remains unclear, although there is evidence for interaction between both factors and other environmental signals. In Arabidopsis, light-grown hypocotyls grow less anisotropic, while dark-grown hypocotyls display a strong gravitropism [188].

There is an ongoing debate about whether the actin cytoskeleton is involved in negative gravitropism. To test this, we took a closer look at the actin-binding Rice Morphology Determinant (RMD) which controls the actin cytoskeleton organization in rice (*Oryza sativa*) [265, 113, 255, 175, 204]. Using light-grown *rmd-2* mutants, that display an agravitropic bending growth pattern, we show that RMD indeed has an effect on the actin cytoskeleton organization in light-grown rice seedlings and also influences the distribution of amyloplasts in the cells [265, 222].

We investigated the difference of the actin cytoskeleton organization in light-grown seedlings for wild type and *rmd-2* rice seedlings. Examples of extracted networks for wild-type and the *rmd-2* mutant are shown in Figure 2.8A and 2.8B, respectively. From these images we can already infer that the actin filaments are distributed across the whole cell in the wild type (Fig. 2.8A), but are organized mainly along the cell walls for the *rmd-2* mutant (Fig. 2.8B).
We then analyzed different network properties to quantify and interpret the differences. We found that the number of connected components is higher in the wild-type (independent t-test, p-value: $p < 10^{-4}$), indicating that the *rmd-2* mutant networks are less well connected than the wild-type networks (Fig. 2.8D). Furthermore, we compared the aver-

age edge capacity, which is smaller in the wild-type networks ($p < 10^{-4}$) and confirms that there is a higher actin bundling in the *rmd-2* mutant. The average shortest path length and the diameter, both smaller in the wild-type ($p < 10^{-7}$ and $p < 10^{-3}$, respectively), show that the wild-type networks are more compact, and nodes are in a closer proximity to each other (Fig. 2.8D, E). In addition, we calculated the ratio of actin cytoskeleton and the total cell area (Fig. 2.8C). As expected, the proportion of the cytoskeleton is higher in the wild-type than in the mutant ($p < 10^{-2}$). To summarize, these properties may imply the possibility for more efficient transport in the wild-type compared to the *rmd-2* mutant. Further observations showed that the effect on the actin cytoskeleton organization also influences the distribution and dynamics of the amyloplasts, which are abnormal in *rmd-2* cells [222].

2.4 Building a GUI for the Automated Extraction of the Cytoskeleton

Description of the framework pipeline.
We showed that the CytoSeg framework is suitable for quantitative analysis of the actin cytoskeleton for different biological questions. Our framework was written in Python and needs manual adjustment for the algorithm's input and output, as well as for the gauging of parameters for the optimal image segmentation. Since biologists, often with little programming experience, are the target users of our framework, we decided to develop a simple-to-use graphical user interface (GUI). We developed the GUI in Fiji, an image processing software which is widely used by biologists [210]. The GUI is provided as a Fiji plugin which can be simply downloaded and copied to the Fiji plugins folder (https://github.com/jnowak90/CytoSeg2.0). The plugin still needs Python 3 and related modules to be installed, but needs no further interaction with the code base.

The input of the GUI are images of fluorescently-tagged or immuno-labelled actin filaments in TIFF format. Below we show that our framework is also applicable for other types of filamentous structures. Due to its dynamic behaviour, the preferred input are image stacks, e.g. for different time points. We enabled the usage of single images, too, but results warrant caution. To automate the analysis as much as possible, we allow the user to choose a single image stack or a whole image folder as input. The project's Github page provides a set of demo images which were used for testing the GUI and are guaranteed to be working with the framework. We split the pipeline of the CytoSeg GUI into four distinct steps of image pre-processing, parameter gauging, image segmentation and network extraction (Fig. 2.9A). The whole pipeline, as well as distinct steps can be chosen by the user and require different inputs depending on the selected analysis step. The pre-processing step takes the original images as input and applies the different correction steps described in 2.2. The user-defined ROI is afterwards stored as an image mask (Fig.

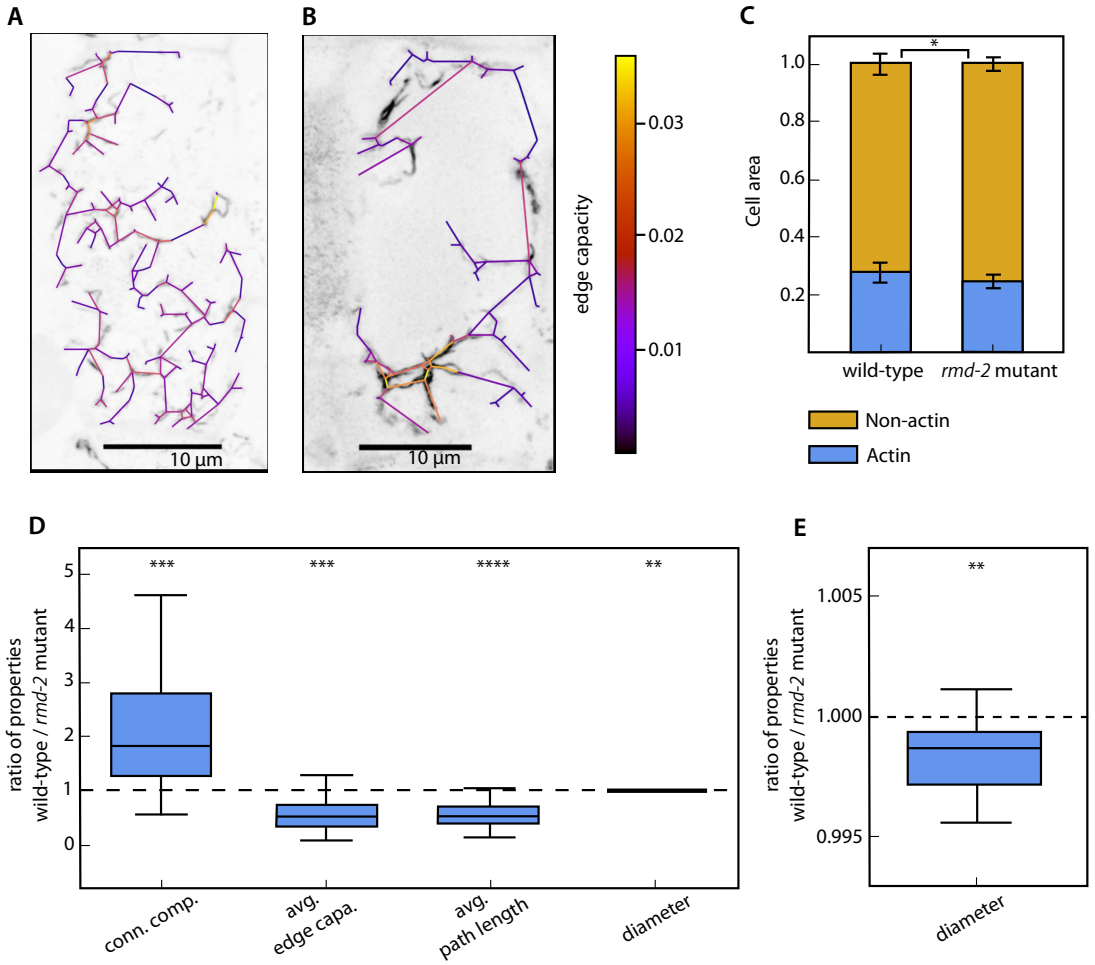

Figure 2.8: Automated extraction of actin cytoskeleton networks from wild-type and *rmd-2* mutants. (**A**) Actin cytoskeleton with over-layed extracted network for light-grown (**A**) wild type and (**B**) *rmd-2* mutant. The networks are colored according to their edge capacity (colorbar). (**C**) Average proportion of actin in the cells. (**D**) Boxplot of selected property ratios between wild-type and *rmd-2* mutants. (**E**) Magnified boxplot of the ratio between wild-type and *rmd-2* mutant for the diameter. Boxplots are shown with median (horizontal line), 25th and 75th percentiles (box edges) and 1.5x interquartile range (whiskers). $*$ Significant at $p < 0.05$, $**$ significant at $p < 0.01$, $***$ significant at $p < 0.001$, $****$ significant at $p < 0.0001$. Reprinted from Song et al., 2019 [222].

2.9C). This selected mask enables the user to select specific cells in the image or exclude non-filamentous structures and is a necessary input for both parameter gauging and the image segmentation.

The set of parameters which were described in Section 2.2.1 for the optimal image segmentation can be deduced from the parameter gauging for which we also built a GUI (Fig. 2.9B). Using the parameter gauging GUI, the user has to select a previously pre-processed image for which an image mask exists. Selecting an original image instead of a pre-processed image for the parameter gauging should be prevented, as it will later lead

to discrepancies in the segmentation which uses the pre-processed image as input. The parameter gauging GUI has four sliders which correspond to the four aforementioned parameters. Dragging the sliders will show the resulting segmented skeleton of the input actin cytoskeleton (red, Fig. 2.9B) and can be used for visual evaluation of the segmentation. Once the optimal segmentation was found, the corresponding parameters can be saved for the next steps of the pipeline. The parameter gauging should be done for each experiment separately and multiple images should be tested with the selected parameters to make sure that the segmentation is working equally well for all of them.

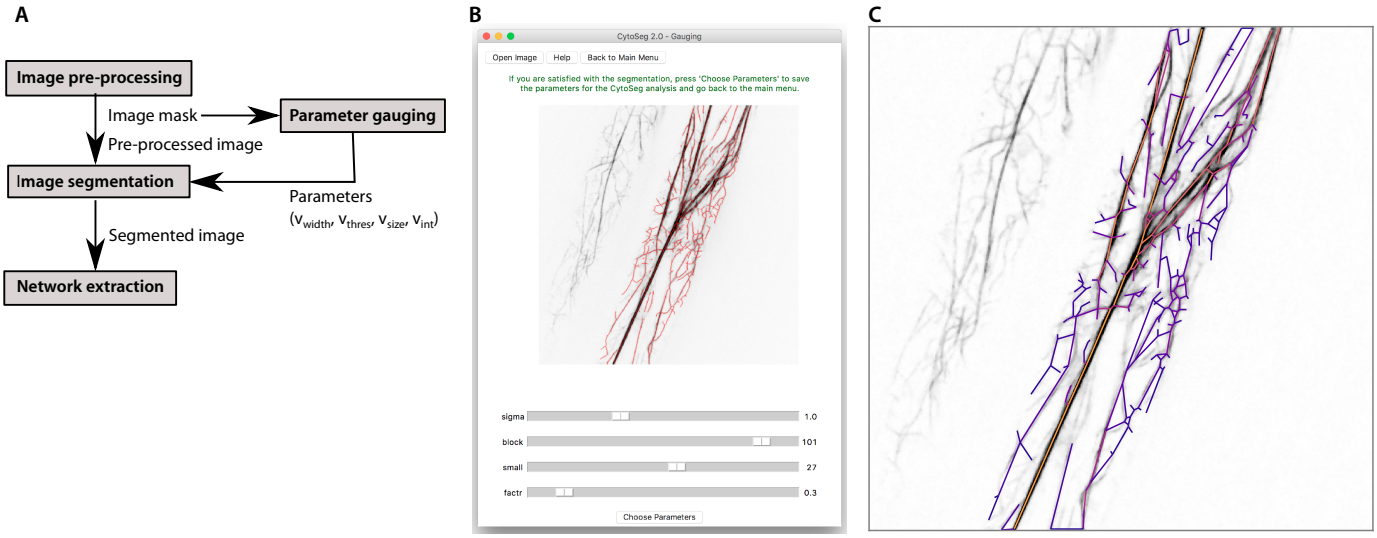

Figure 2.9: Overview of the CytoSeg 2.0 workflow. (**A**) Scheme of the four different steps of the image-processing pipeline. (**B**) GUI for the parameter gauging and resulting segmented actin cytoskeleton (red). (**C**) Pre-processed image with the selected region of interest (blue) and overlaid extracted network (purple/orange). Reprinted from "CytoSeg2.0: automated extraction of actin filaments." by Nowak et al., 2020 [167].

The selected parameters are used for different steps of the image segmentation as described in Section 2.2.1. First, the pre-processed is smoothed using a Gaussian filter, where v_{width} is used for the standard deviation of the Gaussian kernel. The same parameter is used for the enhancement of tube-like structures in the image. Afterwards, the image is binarized using an adaptive threshold for which v_{thres} defines the size of the pixel neighborhood used for the threshold value calculation. Finally, the image is cleaned, segmented and reduced to a one-pixel width using skeletonization [104] using the parameters as described in Section 2.2.1. From the segmented image the final networks are extracted by defining specific points, namely crossings and end points of the segmented skeleton as nodes of the network. Two nodes are connected by an edge if they are directly connected on the skeleton. The edge itself is weighted by its edge capacity which is calculated from the edge length and width of the underlying filament (Fig. 2.9C). In addition to the extracted network we also implemented an algorithm to create randomized networks which maintain the number of nodes and the edge length distribution of the originally extracted network.

Different transport-related network properties are calculated and saved in tables in a results folder for each analysed image. These calculated properties include the average edge capacity, assortativity, number of connected components, average path length, algebraic connectivity and edge angles. The user can calculate other network properties or compare properties between different conditions, time steps or test for statistical significance utilizing the saved extracted or randomized networks.

Application to other types of filamentous structures.
To show that our framework is also applicable for the extraction and quantitative analysis of filamentous structures of other organisms, we selected images from three publicly available databases. The first image was selected from the DRIVE database which provides images of blood vessels in the retina [225]. The architecture of the blood vessels can be used to detect ocular or systemic diseases in a direct and noninvasive way. A method for an automated and reliable segmentation is therefore important and many processing pipelines were proposed [3]. We furthermore selected an image of a dragonfly wing from *Didymops transversa* by Phil Myers from the Animal Diversity Web for extraction [159]. The wing shows an intricate pattern created by the wing veins. The differentiation of the individual shapes of those patterns are object of many studies to create developmental models of the pattern formation [110]. The last image we selected from the Cleared Leaves database which collects leaf images with enhanced veins [64]. Here, we choose a micro CT image of *Quercus faginea* (CLID_image_420_95918) which was provided by the Senckenberianum Herbarium (Department of Botany and Molecular Evolution, Senckenberg Research Institute and Museum, Frankfurt/Main, Germany). The venation pattern is highly correlated with the leaf shape and can be used to distinguish different plant species [202]. We processed the selected images individually using the same procedures as mentioned in Section 2.2. Due to different image compositions, we adjusted the image pre-processing pipeline to ensure that the selected features were recognized. The extracted networks of the selected images are shown in Figure 2.10, displaying that the extraction of networks also works well with other organisms.
To summarize, we aimed to show that the network representation of the actin cytoskeleton captures biological relevant features and can be used to quantify the actin cytoskeleton organization. We showed this by demonstrating that the actin cytoskeleton is tuned for efficient transport by comparing extracted actin networks with randomized networks. Furthermore, we demonstrated that the framework can be used to compare different cell types, time points or mutants and is a first step to understand the actin cytoskeleton organization.

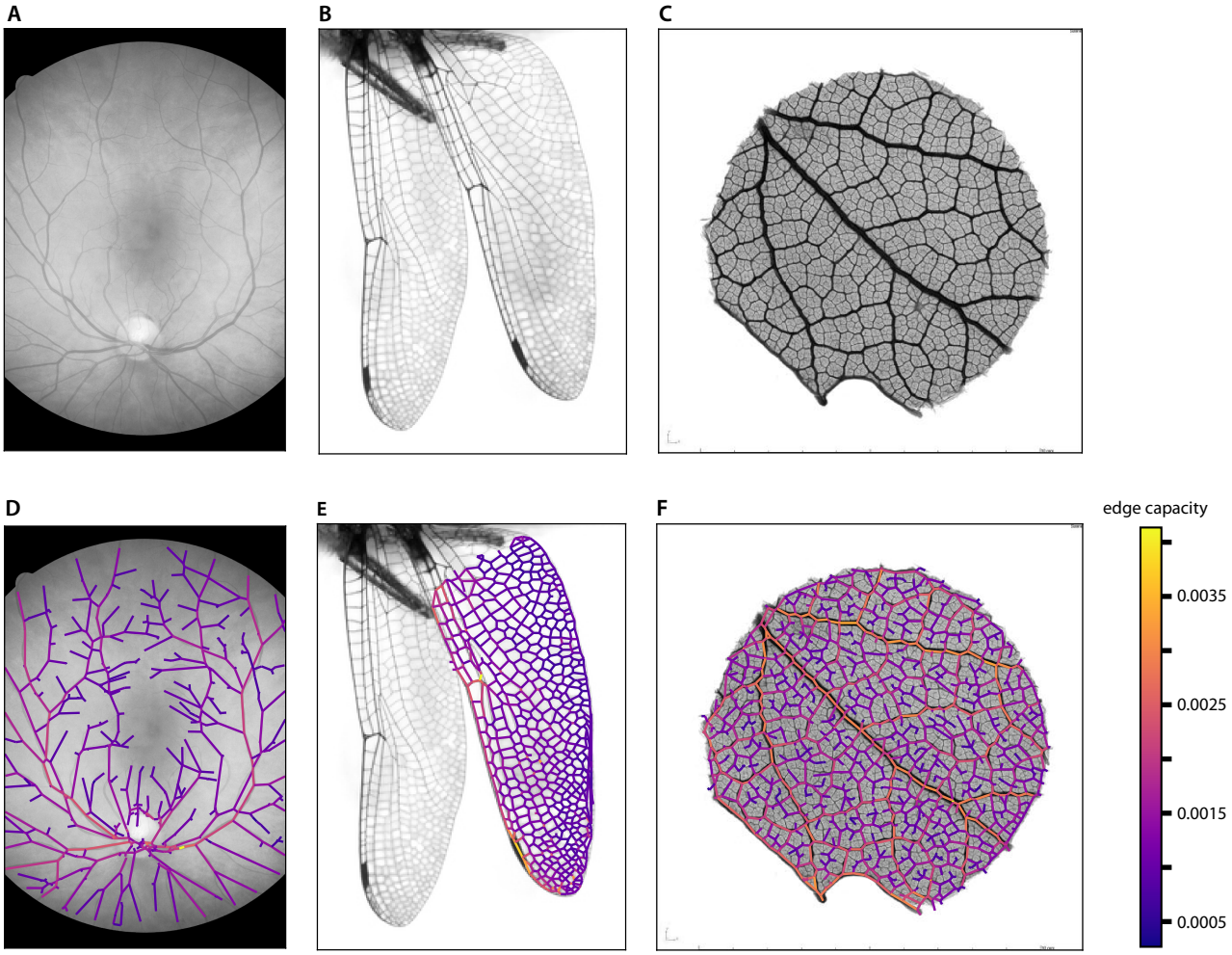

Figure 2.10: Network extraction for different organisms. (**A**) Retina image from the DRIVE database, (**B**) image of dragonfly wings from the Animal Diversity Web and (**C**) leaf image from the Cleared Leaf Image Database. The corresponding, overlaid extracted networks are shown (**D-F**) The networks are colored according to their edge capacity (see color bar). Reprinted from Supplementary Material of "CytoSeg2.0: automated extraction of actin filaments." by Nowak et al., 2020 [167].

Chapter 3

GraVis: a Pavement Cell Shape Descriptor

3.1 Research Question and Aims

Cells can have a variety of different shapes, yet the origin and evolution of the shape geometries remain unknown [15]. During morphogenesis the cell shape can change from very simple to highly complex shapes, caused by forces acting on the cell and subcellular processes [84, 176, 213]. Furthermore, cell shape can also dictate cellular functions [51]. To understand the relationship between cell shape and underlying cell processes, and effects of shape on cellular functions, it is therefore important to quantify cell shape features via descriptors. Such descriptors should allow to distinguish global differences among shapes, but also allow the characterization of key features of individual shapes and their precise reconstruction in silico. While there are multiple shape descriptors available, their functionality is often limited to either shape comparison, detection of certain shape properties or the evaluation of shape complexity, but do not combine multiple of these functionalities.

We selected pavement cells of the upper leaf epidermis as model to investigate cell shape, as those cells have a highly complex, jigsaw puzzle-like shape with specific local features [77, 90, 118]. The features are defined by the concave and convex regions of the cell boundary that are termed necks (invaginations) and lobes (protrusions), respectively. The detection of lobes and necks was used in many studies to compare differences in pavement cell shape between mutants with shape defects or between pavement cells across different plant taxa [240, 145]. In addition, different tools that allow for accurate characterization of local shape features of pavement cells have been developed [156, 208, 252]. Yet, some of the tools require manual intervention and a gold standard to precisely assess how the tools perform is missing.

Here, we present an automated, network-based framework that describes cell shapes using visibility graphs. Our proposed framework does not only allow for global description of

shapes, but also enables the detection of local shape features and outperforms contending tools. In addition, our framework enables the comparison of different shapes and evaluation of their complexity. The development of such a framework is an important step to understand how cell shape is intertwined with certain cell functions.

3.2 Results

3.2.1 A Network-Based Approach for Shape Description

To describe the shape of an object, we used the concept of the visibility graph, a structure that was previously used for different applications in computational geometry. The visibility graph represents the visibility relation between a set of objects, which can be used to reconstruct, recognize or characterize those objects, depending on how they are defined (Fig. 3.1) [170, 171]. One application for visibility graphs is in robotics, where the visibility graphs are used to find the shortest path through a set of polygonal objects by forming the visibility graphs on the vertices of the object polygons [144]. Another example is the usage of visibility graphs to characterize properties of time series by corresponding the graph nodes to amplitudes of particular time points [130]. Finally, visibility graphs have been used for shape decomposition by placing nodes along a piecewise approximation of a shape [214, 82].

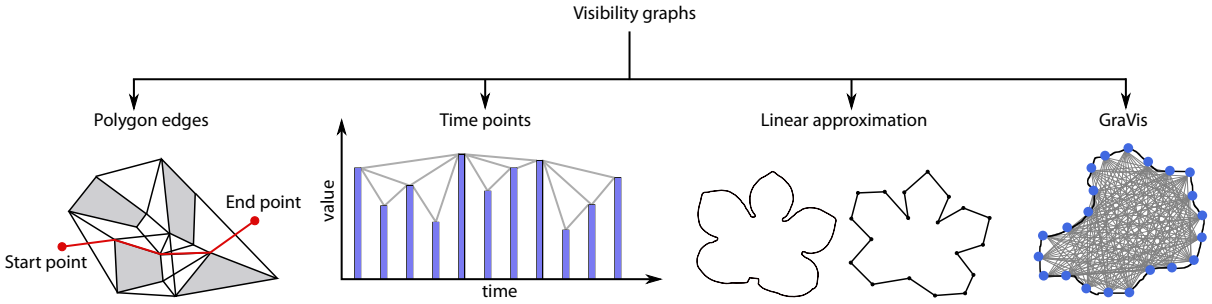

Figure 3.1: Different types of visibility graphs. The visibility graph represents a set of objects along with a visibility relation between them. One type of visibility graph is formed on the vertices of multiple polygons; it is applied in robotics, where it can be used to find the shortest path among polygonal obstacles. In another type of visibility graphs the nodes correspond to the amplitude (i.e. value) at time points and edges are placed between nodes if they can see each other, and this type of visibility graphs has been used to deduce properties of time series. In addition, visibility graphs can be used for shape decomposition by placing nodes along a piecewise linear approximation of a shape. The here proposed approach GraVis places nodes along the shape contour and connects nodes which are visible to each other.

However, visibility graphs have not yet been used for shape comparison and characterization of local and global properties of shape, which is the main contribution of our study. Shapes in our study are defined by their contour which is a one-pixel description of the shape boundary. To create the visibility graph of a shape, we firstly placed nodes along the shape contour in an equidistant manner (Fig. 3.2A). To add edges to the graph we

applied the concept of visibility by linking all node pairs which can see each other. We say that two nodes see each other if the segment between the nodes does not align with or crosses the shape boundary (Fig. 3.2A). This condition was tested for all possible node pairs along the contour and resulted in the final visibility graph of the analysed shape. The visibility graph can be weighted according to the Euclidean distance between the two nodes (Fig. 3.2B). Here, longer edges have a higher weight than shorter edges.

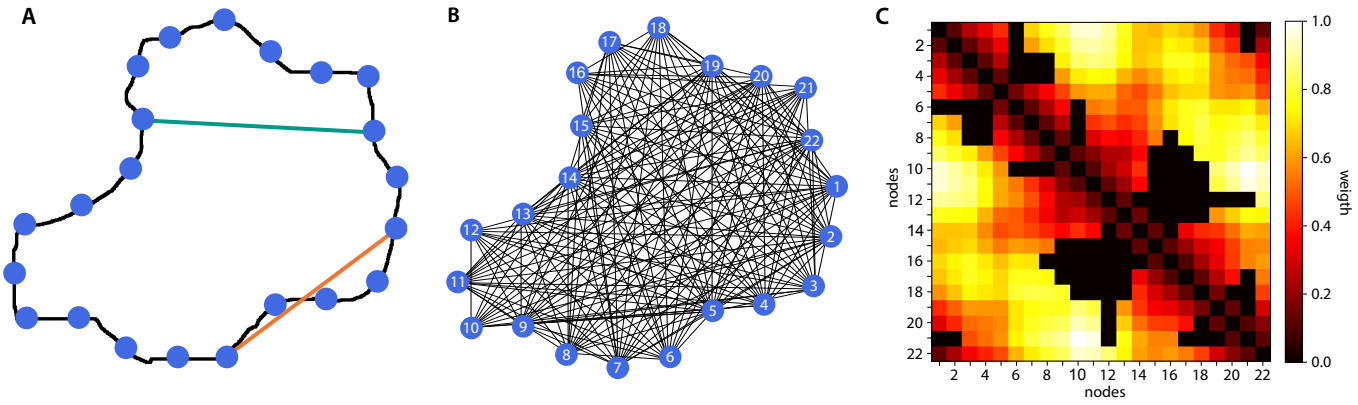

Figure 3.2: Visibility graphs as descriptor of shape. (**A**) Contour of an illustrative shape. Nodes (blue) are placed equidistantly along the contour and used to create a visibility graph. Two nodes are connected in the visibility graph if they can "see each other", i.e. the segment connecting them does not cross or align with the contour (teal edge); otherwise, the nodes cannot see each other (orange edge). The edges between nodes can be weighted according to their edge length. (**B**) Visualization of the visibility graph for the selected cell. (**C**) Heatmap of the weighted and scaled adjacency matrix of the visibility graph.

We can further represent the visibility graph by its adjacency matrix A, in which the rows and columns correspond to the nodes. The entries of the adjacency matrix corresponded to edges between two nodes and had the value of 1 if this edge exists in the unweighted graph, or the scaled weight of the graph edge if the graph was weighted (Fig. 3.2C). Both the scale-weighted and unweighted visibility graphs were size-, orientation- and rotation-invariant, i.e. visibility graphs of the same object which were rotated or of different size were isomorphic. The size of the graph was only dependent on its number of nodes which is defined by the distance between nodes placed along the contour. We were able to represent the shape in one-to-one correspondence when placing the nodes at each pixel on the boundary. To approximate the optimal distance between nodes, we based the distance between nodes on the image resolution and contour length (see Section 3.2.5 for more details). Following this, the number of nodes may be different for the visibility graphs of two distinct shapes with different image resolution and contour length.

3.2.2 Comparing shapes

The comparison of shapes and their extracted visibility graphs depends on whether they have the same or different number of nodes. To illustrate different approaches for measuring the similarity between two graphs, we created a set of 20 simple, synthetic shapes from three distinct groups: triangular (i.e. right-angled, equilateral, obtuse), rectangular (i.e. square, rectangle, trapeze, rhombus), and circular (i.e. circle, ellipse, rotated ellipse) shapes. For each shape we manually defined uniformly spaced coordinates for two different shape sizes. In addition, we created a set of shapes with equal number of nodes and another where the number of nodes varies depending on the shape size and type (see Section 3.3 for details). The defined coordinates were used as node positions and the corresponding visibility graphs were created to test various distance measurements.

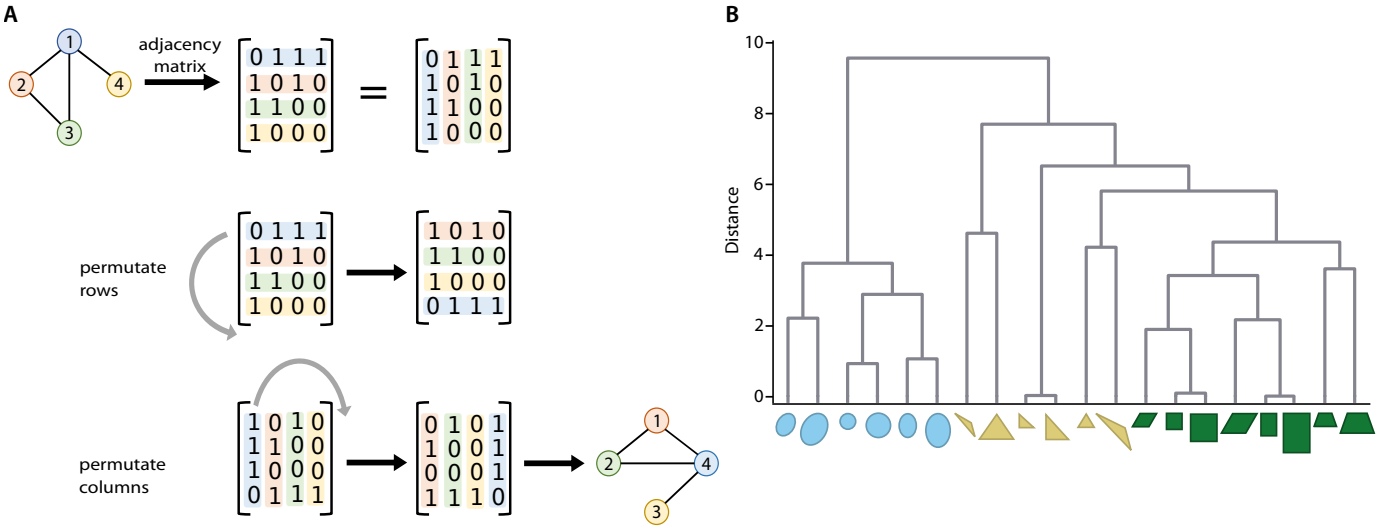

Figure 3.3: Rotational permutation of a graph. (**A**) To circularly permute a graph, the corresponding adjacency matrix is used. The first row and column of the matrix are rotated to the end of the matrix, decreasing the row- and column- indices by one. (**B**) Shapes are compared by calculating the rotational distance between their corresponding visibility graphs. The resulting distance matrix is used for hiererchical complete-linkage clusterting of a set of synthetic shapes with same number of nodes, on which the rotational distance can be readily applied.

Visibility graphs with equal number of nodes can be easily compared using the rotational distance. For this purpose, we used the corresponding unweighted adjacency matrices and fixed one of them while the other matrix was circularly permuted. This was accomplished through setting the last row and column of the adjacency matrix to be the first row and column in the circularly rotated matrix and reducing the respective row- and column-indices by one (Fig. 3.3A). The Euclidean distance was afterwards calculated between the fixed and the permutated matrix. This was repeated for all circular rotations of the

permuted matrix to determine the smallest distance which corresponds to the best overlay between two visibility graphs.

We used the set of synthetic shapes with equal number of nodes to test the proposed approach. The calculated distance between the synthetic shapes were saved in a distance matrix which we further used for hierarchical complete-linkage clustering. The clustering shows that the shapes were accurately grouped into their respective rectangular, triangular and circular shapes (Fig. 3.3B).

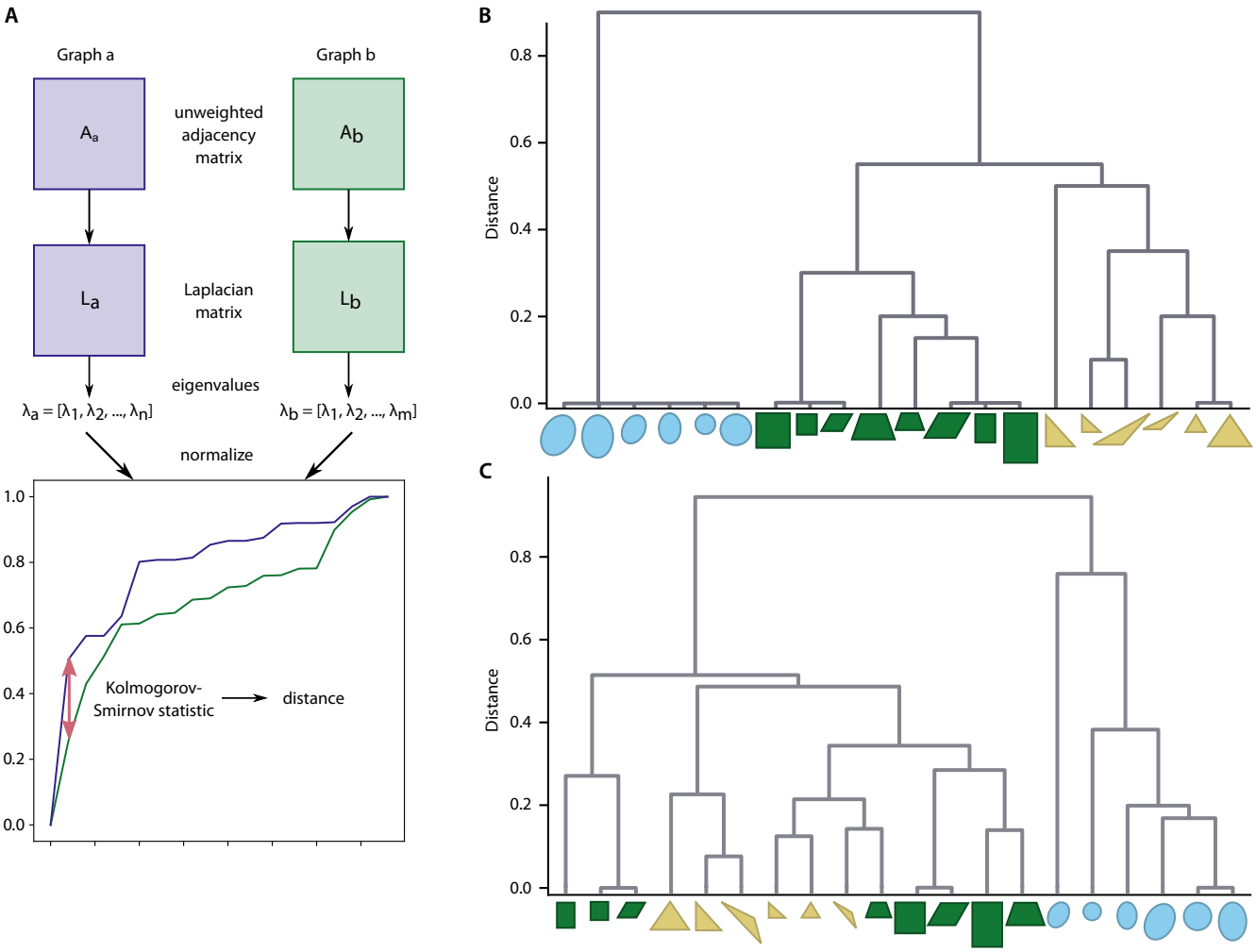

Figure 3.4: Comparison of visibility graphs. (**A**) Two visibility graphs are compared based on the spectrum (i.e. distribution of eigenvalues) λ of the Laplacian L obtained from the unweighted adjacency matrices A. The Kolmogorov-Smirnov statistic is used to quantify the difference between the distributions of two spectra [229]. (**B-C**) Clustering dendrogram obtained by the procedure for a set of synthetic, simple triangular, circular, and rectangular shapes with (**B**) the same number of nodes and (**C**) variable number of nodes between the network representation of the shapes.

By contrast, visibility graphs with unequal number of nodes are harder to compare because of their different matrix dimensions and therefore require a different distance measure, which we introduce here. It should be noted here, that we used the unweighted visibility graphs for the comparison of shapes. To calculate the distance between two unweighted graphs, we compared the distributions of the eigenvalues of their Laplacian matrices $L = D - A$, with D denoting the diagonal matrix of node degrees (Fig. 3.4A). The distribution of eigenvalues of a Laplacian matrix, which are guaranteed to be non-negative, have already been used for comparison of images prior to this [251]. In particular, the Laplacian matrix was found to capture information about the graph topology, which is why the distribution of the Laplacian eigenvalues has been studied to analyze and compare the structure of graphs [53, 61]. The distance between the eigenvalue distributions of two visibility graphs was quantified with the Kolmogorov-Smirnov statistic (Fig. 3.4A) [229]. As before, the resulting distances were saved in a distance matrix and used for clustering.

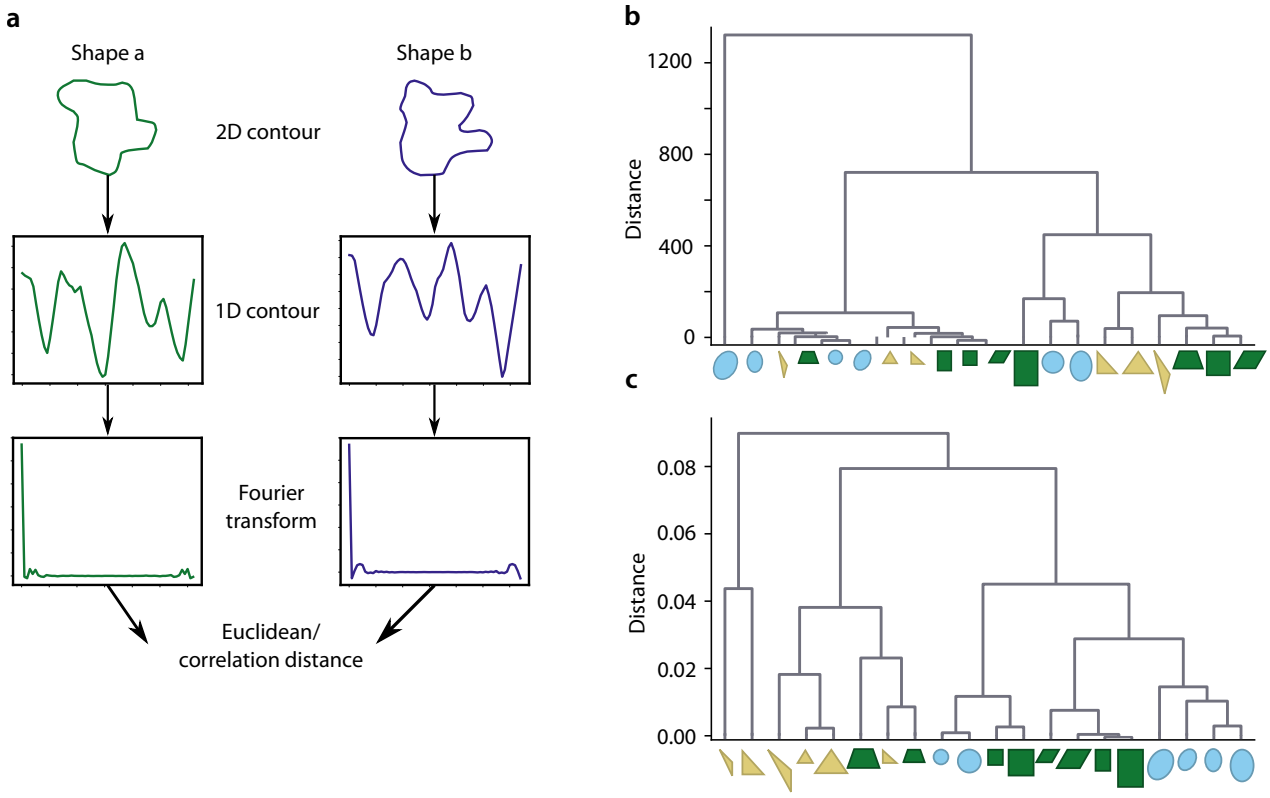

Figure 3.5: Comparison of synthetic shapes using the Fourier transform. (**A**) Two shapes are compared based on their Fourier transforms obtained from their one-dimensional contour which is calculated by the difference of the shape centroid and its coordinates. The difference between two Fourier transforms is determined by the Euclidean distance or the correlation distance. (**B-C**) Resulting clustering dendrogram for a set of synthetic, simple triangular, rectangular and circular shapes with equal number of coordinates using (**B**) the Euclidean distance and (**C**) the correlation distance.

We tested the proposed approach by calculating the pairwise distances using the synthetic set of shapes with both equal and different number of nodes (Fig. 3.4B-C). The hierarchical complete-linkage clustering shows that the shapes with equal number of nodes were grouped accurately into the corresponding classes, demonstrating that this approach performs as well as the rotational distance (Fig. 3.3B). On top of this, we show that our distance measure even provides a good clustering for shapes with unequal number of nodes (Fig. 3.4C). Together, the results manifest that the eigenvalue-based distance measure is accurate in quantifying the distance between two graphs and also allows the comparison of different-sized matrices.

We further assessed the performance of our approach with the Fourier transform, another prominent method for shape comparison [260, 208, 37]. For this, we used the synthetic set with the same number of nodes and employed the classical contour representation of the distances of contour points from the shape centroid (Fig. 3.5A). We used the resulting profile as input to the discrete Fourier transform and compared the resulting descriptors by using the Euclidean distance and the correlation distance. Again, we used hierarchical complete-linkage clustering and found that the shapes are not separated well into the respective classes for both distance methods, although the approach is widely used for shape characterization (Fig. 3.5B).

In addition, we utilized the set of synthetic shapes with the same number of nodes to investigate the sensitivity of the algorithm to the spatial resolution of node placement. To illustrate the clustering quality based on different node densities, we selected the large synthetic shapes with each the equal number of nodes (n=20). We implemented a node reduction method based on modularity clustering to stepwise reduce the number of nodes of each graph to 12 nodes (Fig. 3.6, Materials and Methods).

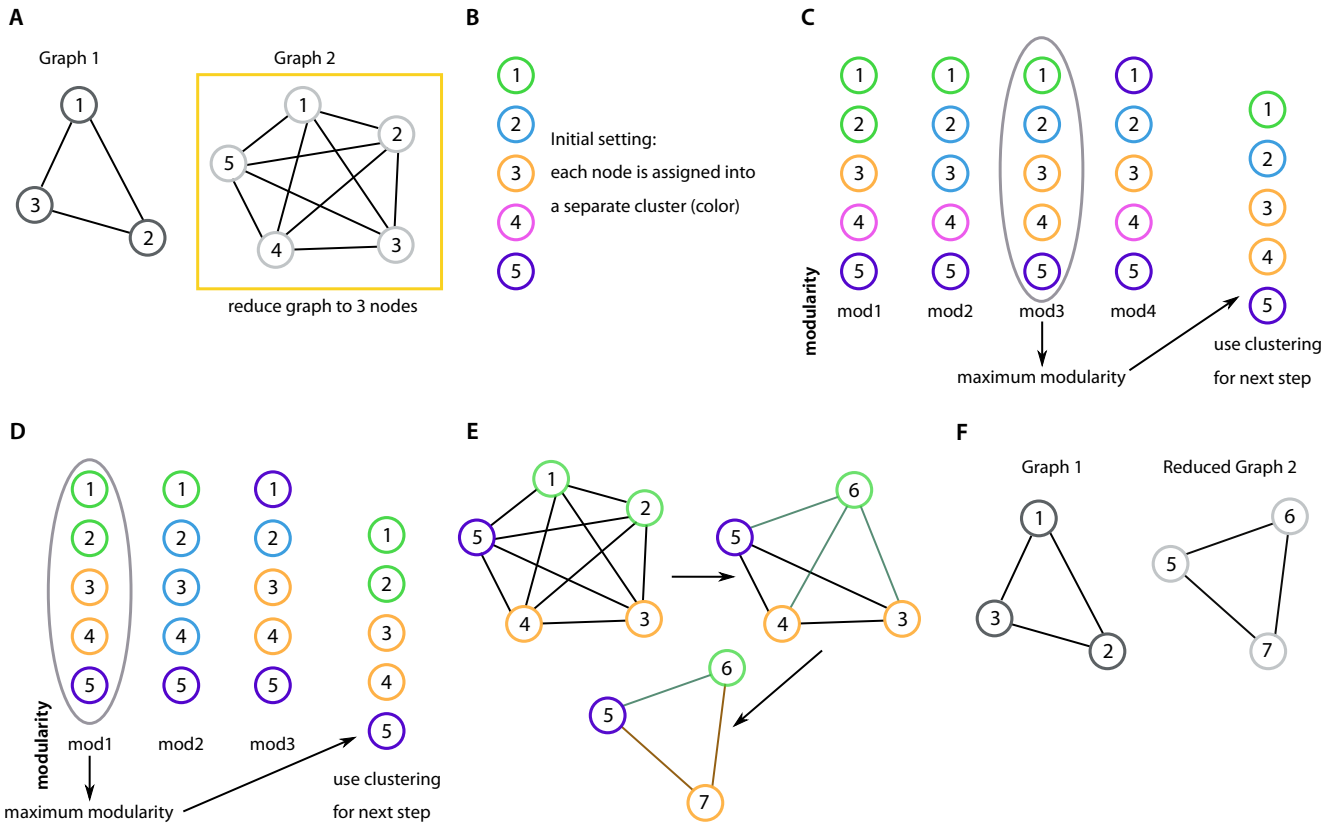

Figure 3.6: Comparison of visibility graphs based on a node-reducing method using modularity clustering. (**A**) Given two graphs, the graph with the larger number of nodes is identified to be reduced to the order of the smaller graph. The number of nodes in the larger graph are reduced by partitioning the graph into as many network clusters as there are nodes in the smaller graphs, whereby we rely on modularity as a network cluster quality index. (**B**) Initially, the nodes of the larger graph are each assigned to a cluster. (**C**) New clusters are created by assigning two consecutive nodes to the same cluster. All possible combinations of two consecutive merged nodes are created. The combination with the maximum modularity is selected. (**D**)This reduction method is applied until the final number of clusters equals the order of the smaller graph. (**E**) Nodes which belong to the same cluster are represented by a single new node, which position is determined by the geometric median of the merged nodes. (**F**) The smaller graph and the reduced larger graph can be used for comparison approaches that require the same number of nodes for two graphs.

We created the visibility graphs for each set of reduced graphs and calculated the distance matrices, which we further used for hierarchical complete-linkage clustering (Fig. 3.7). To assess the homogeneity of the resulting clusters, we computed the Biological Homogeneity Index (BHI) (Materials and Methods) [65]. We found that the BHI decreased for visibility graphs with reduced number of nodes (Fig. 3.8). The visibility graphs with 20 and 19 nodes per graph had a perfect score of 1.0 for all clusters, thus showing that the corresponding node density of 10-14 pixel/nodes is optimal for the detection of distinguishing global shape features. In addition, we observed that the BHI score is slightly below 0.9 for 17 and 18 nodes, demonstrating the robustness of our approach for small differences

in node numbers. Changes in BHI for number of nodes that differed by one is not larger than 36%.

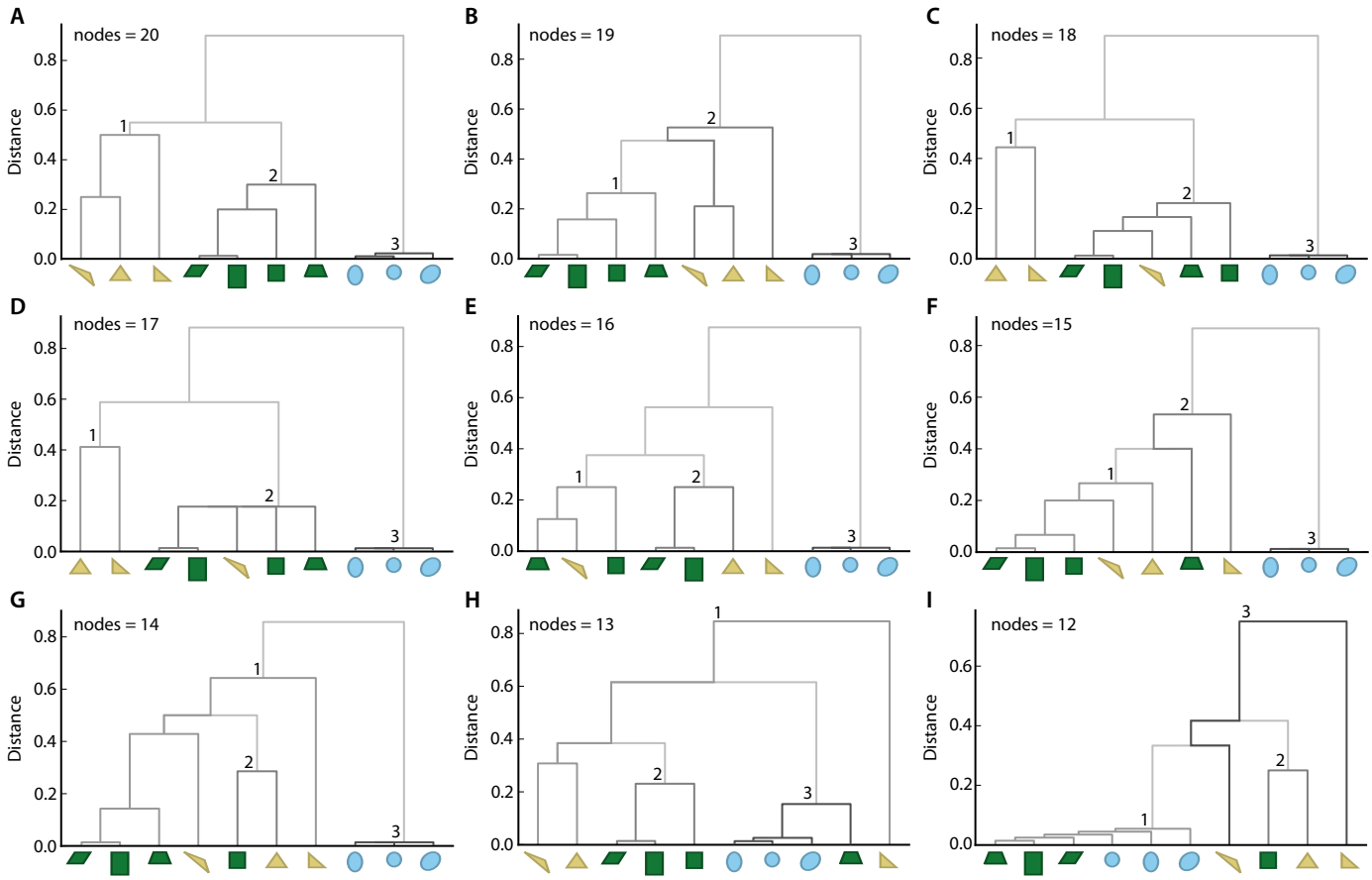

Figure 3.7: Comparison of visibility graphs with different node densities. (**A-I**) The visibility graphs of a set of synthetic shapes with the same number of nodes (20) were reduced stepwise by one node and used to calculate the distance matrix to use for hierarchical clustering. To measure the quality of the clustering, the BHI was calculated for the resulting clusters (see Fig. 3.8).

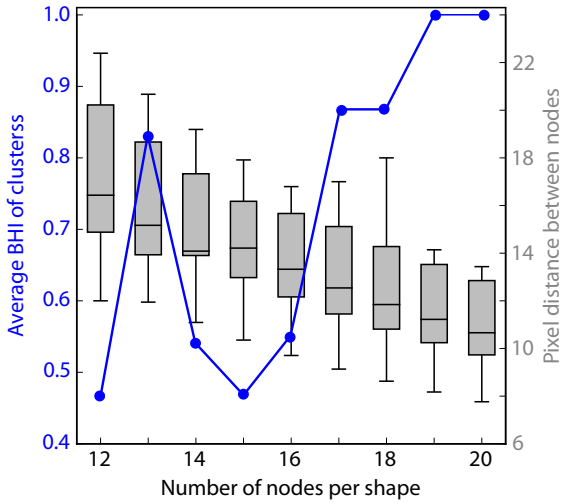

Figure 3.8: Sensitivity of the number of nodes on the performance of shape comparison. Visibility graphs with equal number of nodes were compared against each other for the synthetic shapes. The number of nodes were decreased in a stepwise fashion using the node-reducing method. The distance matrix was calculated for the resulting graphs and used for hierarchical clustering whose quality we quantified with the BHI (blue). The highest average BHI was calculated with graphs that have a distance between of 10-14 pixels between nodes (gray). Boxplots are shown with median (horizontal line), 25th and 75th percentiles (box edges) and 1.5-fold of the interquartile range (whiskers).

3.2.3 Application of Approach to Shapes from Different Domains

To test how well the visibility graphs serve as global descriptors of shape, we selected various objects from different domains including fish shapes from the WoRMS database [35], leaf shapes provided by Vőfely et al. (2018)[240] and images of sand grains from the Australian coast. We created the corresponding visibility graphs and calculated the distance matrix for the shapes of each domain. Afterwards, we used principal component analysis (PCA) to show that our approach is able to distinguish shapes based on their complexity (Fig. 3.9). Taking the PCA of the distance matrix of fish shapes as example (Fig. 3.9B), we can see that the shapes were split into groups analogous to their complexity. In the upper left corner one can find the most complex shapes, such as the seahorse and swordfish. By contrast, the simple and smooth shapes can be found in the upper right corner (i.e. turbot, eelpout). At the bottom, the shapes which were intermediates of the two extremes were grouped and also show a gradient of complexity from right to left, transitioning from smoother, simpler shapes to more complex fish with defined fins. The PCAs of the distance matrix of sand grains (Fig. 3.9A) showed a similar trend, while the trend was laterally reversed for the leaf shapes (Fig. 3.9C). The U-shape of the shapes in the PCA for the different domains shows that the underlying data structure is not linear. Therefore, the components of the PCA cannot be easily used to describe the changes in shape. Nevertheless, it can be concluded from these facts that the visibility graphs are a powerful tool to describe diverse shapes from different domains on a global scale.

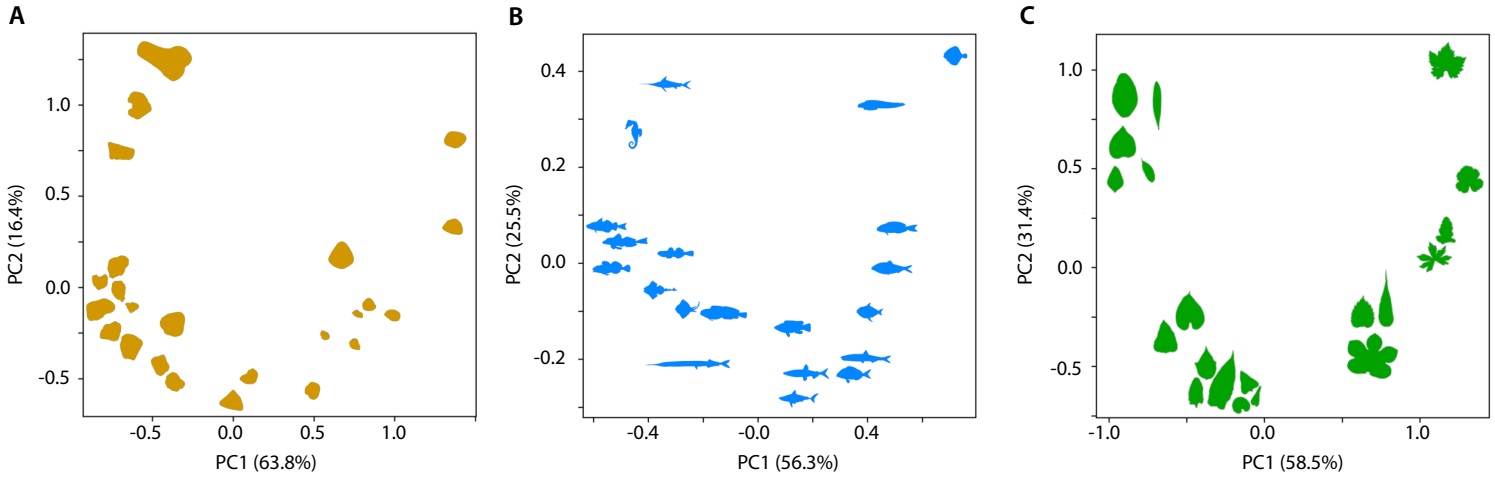

Figure 3.9: Comparison of shapes from different domains based on their visibility graphs. The distances between visibility graphs based on the spectra of their Laplacians can be used in multivariate analyses and visualizations to distinguish different groups of similar shapes. We show the principal component analyses of shapes from three different domains: (**A**) sand grains, (**B**) fish shapes and (**C**) leaf shapes [35, 240].

3.2.4 Displaying Shape Complexity in a Heatmap

As shown in the previous section, the visibility graphs can be used to quantify the complexity of shapes. To further illustrate this point, we applied our framework to leaf epidermal pavement cells, which are highly complex cells often used for morphological studies. Pavement cells undergo morphogenesis from quite simple, polygonal shapes to complex shapes which are defined by invaginations (necks) and protrusions (lobes). Here, we aimed to depict how the cell complexity is distributed and changed over time by calculating the relative graph completeness of the corresponding visibility graphs. The (relative) graph completeness was quantified for an undirected graph by the ratio between the graph edges and the maximum number of graph edges on the given number of nodes:

$$\sigma = \frac{2|E|}{|V|(|V|-1)} \tag{3.1}$$

where $|E|$ and $|V|$ were the numbers of all edges and nodes in the graph, respectively. In a dense graph, the number of edges is close to the maximum number of edges. We can then conclude that for round cells, where each node is visible to all other nodes, i.e. a complete graph, the visibility graphs will be very dense, while more complex cells will yield sparser graphs. We can use this global network property to investigate the complexity of cell shape, as depicted in the complexity heatmap in Figure 3.10. Stomatal pores (white, Fig. 3.10B) are easily detected, as they are formed by two, typically round guard cells. More complex pavement cells can be distinguished from stomatal pores by using the graph completeness as measure of complexity (dark orange, Fig. 3.10B). In

addition, we calculated the solidity for each cell, a shape feature which is often used to describe pavement cell shape and found that stomata cells could be well distinguished from very complex pavement cells, but the distinction between stomata and simple pavement cells is not as distinct as using the relative graph completeness (Fig. 3.10).

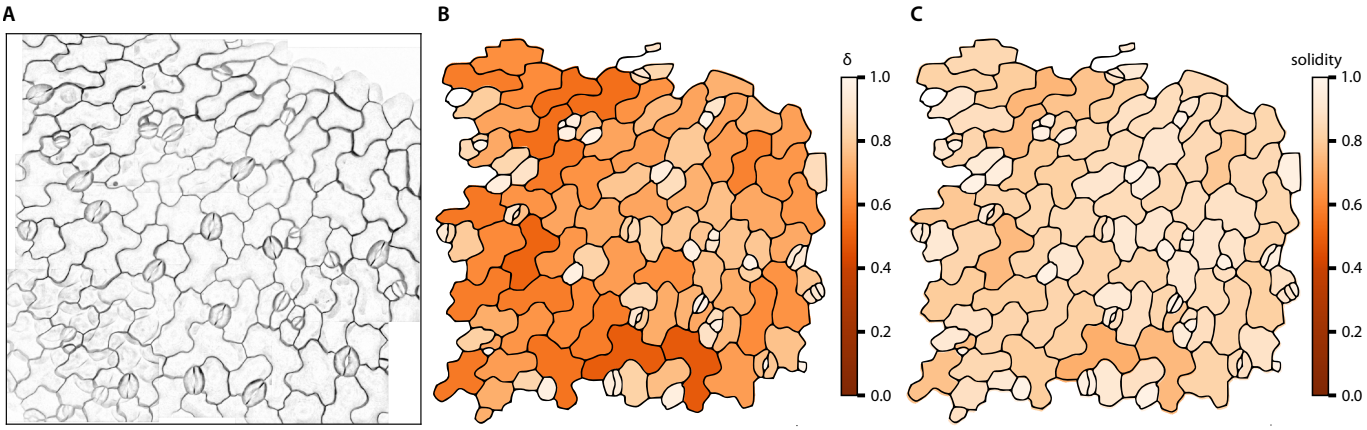

Figure 3.10: Heatmap of Arabidopsis pavement cell complexity. (**A**) Microscopy image of Arabidopsis pavement cells. (**B**) The original microscopy image can be recreated by plotting the extracted visibility graphs of all detected pavement cells and weighting them according to their complexity, which is calculated by the relative completeness of the corresponding visibility graphs. Simple, round shapes like stomata have a smaller complexity (white) than the more complex pavement cell shapes (dark orange). (**C**) Heatmap of pavement cells weighted by their solidity, a commonly shape feature to describe pavement cell shape.

3.2.5 Comparison of Different Lobe Detection Tools

In addition to the global graph properties, we can also use properties of graph nodes to quantify local shape features. Here, we used the visibility graphs that are weighted by their edge lengths. We tested this idea on pavement cells for which we determined the node centralities to detect lobes and necks. While there was a variety of different centrality measures that could be used for the characterization of node positions in the graph [131], we selected the closeness centrality, as nodes in neck regions are expected to be closer to other nodes in comparison to nodes in lobe regions. We calculated the closeness centrality of node as:

$$C(v) = \frac{|V| - 1}{\sum_{u \in V} d(u, v)}, \tag{3.2}$$

where $d(u, v)$ was the distance of the shortest path between the nodes u and v (Fig. 3.11A-B). The likelihood that a node corresponds to a lobe or neck was quantified by the local minima and maxima of the closeness centrality along the contour, respectively (Fig. 3.11C). Furthermore, we can discriminate detected lobes as either true lobes (protrusion between two cells) or as tri-cellular junction which are created at places where three cells

meet [7]. We did so by superimposing the node positions of the detected lobe with positions of detected tri-cellular junctions.

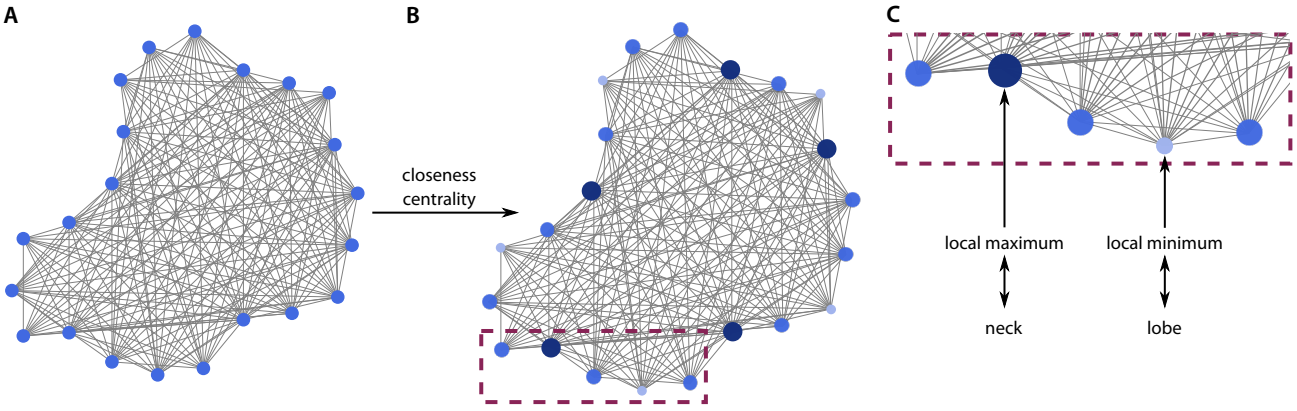

Figure 3.11: Detection of lobes and necks in pavement cells based on visibility graphs. (**A-B**) The closeness centrality is calculated for the nodes of a visibility graph, visualized by different node size. (**C**) Lobes (light blue nodes) and necks (dark blue nodes) correspond to the local minima and maxima along the contour, respectively.

To compare the performance of our framework GraVis, we selected the three contending lobe detection tools LobeFinder, PaCeQuant and LOCO-EFA [156, 208, 252]. Like GraVis, all of the selected tools use a boundary-based lobe detection approach. LobeFinder detects lobes using a modified convex hull-based approach, while PaCeQuant detects lobe based on local changes of the contour curvature orientation. LOCO-EFA uses an advanced version of the elliptical Fourier analysis by decomposing the contour into a set of unique coefficients. From the resulting ellipse profiles, the number of lobes can be inferred by quantifying the contribution of specific modes.

We created a gold standard of manually curated lobes of pavement cell shapes and used it to quantify the performances of the selected lobe detection tools. Thus, we selected ten pavement cells each from three different *Arabidopsis thaliana* lines, including wild-type, oryzalin-treated wild type and the *clasp-1* mutant. Oryzalin is an inhibitor of microtubule polymerization [19] and known to inhibit de novo lobe formation and growth of established lobes [11]. The *clasp-1* mutant encodes an allele of the *CLASP* gene which encodes a regulator of microtubules and impacts the morphology of pavement cells [9]. We used the set of selected pavement cells for manual detection of lobes by 20 experts (see Fig. 3.12). Here, we provided the experts with the cell contours of individual cells, outside of the tissue context, and thus provided no information about cell wall segments with neighbouring cells (tri-cellular junctions). However, we manually distinguished true lobes and tri-cellular junctions after the manual detection by the experts.

The consensus of detected lobes of example cells for each condition among the 20 experts

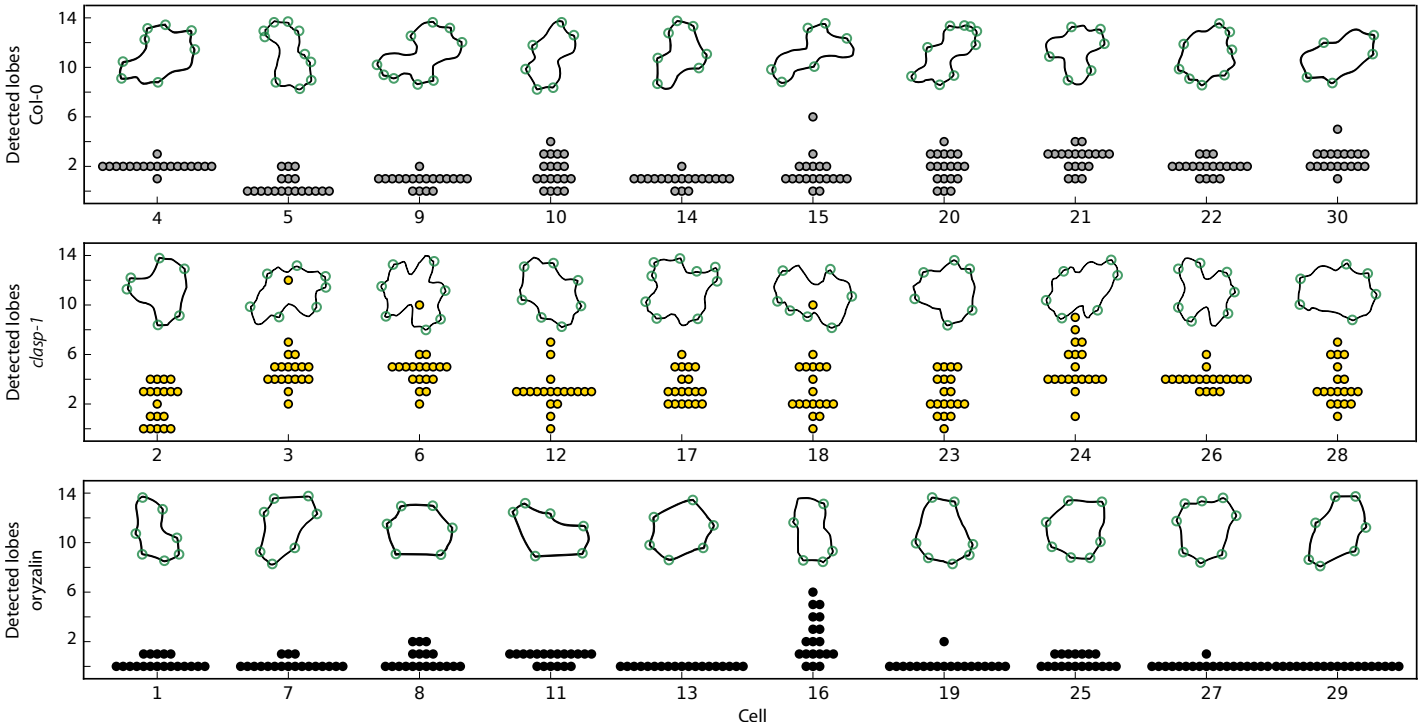

Figure 3.12: Bee swarms of manually detected lobes by 20 experts. The number of detected lobes (without tri-cellular junctions) for the 30 cells of the gold standard that were selected from three different conditions (Col-0: gray, clasp-1: yellow, oryzalin: black) are shown as bee swarms. The position of tri-cellular junctions is indicated by green circles.

is depicted in Figure 3.13 and reveals that the majority of detected lobes and tri-cellular junctions were detected by the majority of experts. Smaller protrusions were detected by single or only a few individuals. For the evaluation of the tool performances, we used the number of lobes from the gold standard which were detected manually by 20 experts and compared them to the number of lobes detected by the tools for each scenario (Fig. 3.14A). For each tool except LOCO-EFA, we specified which of the detected lobes were true lobes and tri-cellular junctions.

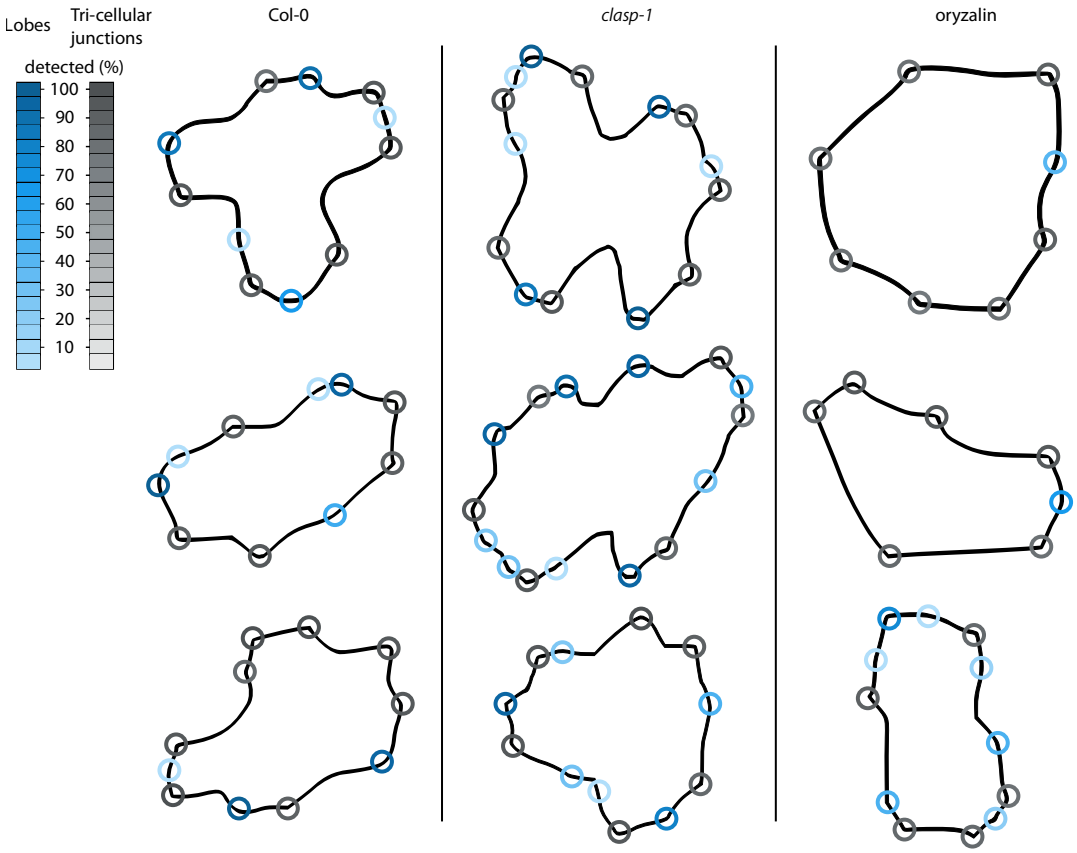

Figure 3.13: Consensus of manually detected lobes by 20 experts.. Three cells for each condition are selected from the gold standard to visualize the consensus among the experts regarding the positions of lobes (blue) and tri-cellular junctions (gray). The consensus of experts is indicated by the hue of the colored circles. Light circles indicate a low percentage of consensus (true lobes: light blue, tri-cellular junctions: light gray), while dark circles indicate a high percentage of consensus among the experts (true lobe: dark blue, tri-cellular junctions: dark gray).

When comparing the number of lobes in which we excluded tri-cellular junctions (Fig. 3.14A-C), we found that the number of detected lobes by GraVis is closer to the mean of the gold standard compared to the other tools, PaCeQuant and LobeFinder. In addition, there is no significant difference between the gold standard mean and the detected lobes by GraVis. The comparison of detected lobes including tri-cellular junctions shows similar results, whereas here the results of LOCO-EFA are included (Fig. 3.14E-G). To further show the accuracy of the approaches in respect to the gold standard, we determined the root mean square error (RMSE) of expected number of lobes based on the number of manually detected and predicted lobes (Fig. 3.14D, H). We used a two-sample t-test to the significance of the RMSE between GraVis and the other tools and found that the mean RMSE of PaCeQuant is 5.2 times higher (p-value $< 10^{-7}$), and the mean RMSE of LobeFinder is 4.3 times higher (p-value $< 10^{-9}$ than that of GraVis, excluding tri-cellular junctions (Fig. 3.14D). The comparison based on number of lobes including tri-cellular junctions shows similar findings, with the addition that LOCO-EFA has a RMSE that is 3.9-fold higher in comparison to that of GraVis (p-value $< 10^{-7}$) (Fig. 3.14H).

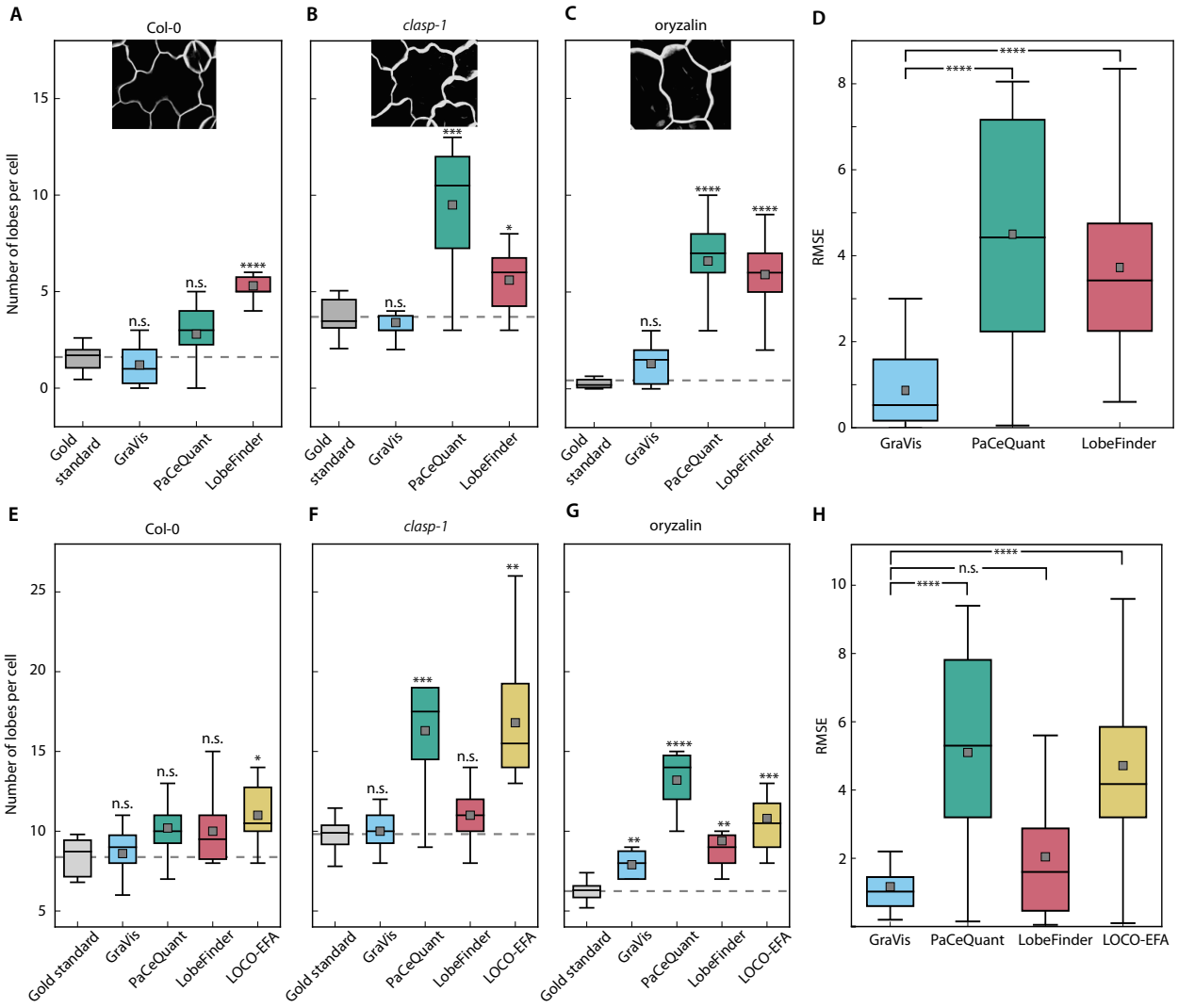

Figure 3.14: Comparison of visibility graphs with other contending approaches to count number of lobes without tri-cellular junctions in leaf pavement cells. The comparison involves three computational approaches: PaCeQuant [156], based on the contour curvature, LobeFinder [252], based on convex hull, and LOCO-EFA ([208]), based on elliptical Fourier analysis. Since LOCO-EFA does not distinguish between true lobes and tri-cellular junctions, it was removed from the comparison based on (**A-D**) true lobes, but is included in the comparison of tools based on (**E-H**) number of lobes including tri-cellular junctions. The quantitative comparison is based on a gold standard that includes 30 Arabidopsis pavement cells obtained from each of the three scenarios: (**A, D**) wild type, (**B, E**) oryzalin treatment, and (**C, F**) *clasp-1* mutant, all with manually annotated lobes by 20 experts. The dotted line denotes the mean of the gold standard, i.e. manual detection by 20 experts, for the respective scenario. GraVis outperforms all three contenders based on the residual mean square error (RMSE) for the analysis of (**D**) true lobes and (**H**) performs as well as LobeFinder when including tri-cellular junctions. ($*$ significant at p-value < 0.01, $**$ significant at p-value < 0.001, $***$ significant at p-value $< 10^{-4}$, $****$ significant at p-value $< 10^{-5}$, two sample t-test). Boxplots are shown with median (horizontal line), 25th and 75th percentiles (box edges) and 1.5x of the interquartile range (whiskers).

Using the gold standard, we also tested the performance of other node centralities for the detection of lobes and necks with GraVis. To this end, we used the extracted visibility graphs of the gold standard and calculated a variety of different node centralities which are described in Table 3.1. Let $u, v, t \in V$ be nodes in an undirected graph $G = (V, E)$ with $|V|$ vertices and $|E|$ edges. We defined $deg(v)$ as the degree of node v and $d(u, v)$ as the length of shortest path connecting nodes v and u. Furthermore, we definded $\sigma(v, u)$ as the number of shortest path and $\sigma_v(u, t)$ as the number of shortest paths connecting nodes u and t through node v. The adjacency matrix was denoted by $A = (a_{v,u})$ where $a_{v,u} = 1$ if an edge connects nodes v and u, and $a_{v,u} = 0$ otherwise. The effective resistance between the nodes v and u corresponded to the term $p_{uv}(v) - p_{uv}(u)$ and $\tau_{ut}(v)$ was defined as the information throughput of node v. Lastly, we denoted λ as the eigenvalue and $\theta_{u,t}(v)$ as the overall commodity sent from node u to t and forwarded by node v.

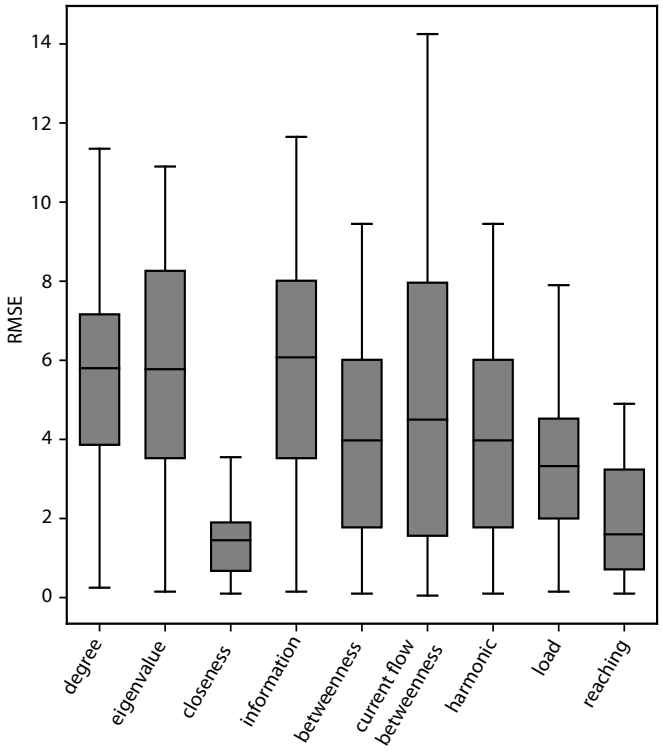

Figure 3.15: RMSE of detected pavement cell lobes for different centralities. The RMSE was calculated from the number of lobes detected using different centralities of the visibility graphs and the mean of manually annotated nodes.

Like in the case of closeness centrality, we detected lobes by identifying the local minima of the centralities and subsequently computed the RMSE to measure the difference to the mean of the gold standard (Fig. 3.15). The closeness centrality had the lowest RMSE and therefore predicted the number of lobes and necks with the highest accuracy, closely followed by the local reaching centrality that uses a similar algorithm as the closeness

Centrality measure	Definition	Reference
Degree	$C_D(v) = \frac{deg(v)}{\|V\|-1}$	[87]
Eigenvector	$C_E(v) = \frac{1}{\lambda} \sum_{u \in V} a_{u,v} C_E(u)$	[36]
Closeness	$C_C(v) = \frac{\|V\|-1}{\sum_{u \in V} d(u,v)}$	[201]
Information	$C_I(v) = \frac{\|V\|-1}{\sum_{u \in V} p_{uv}(v) - p_{uv}(u)}$	[230]
Betweenness	$C_B(v) = \frac{2}{(\|V\|-1)(\|V\|-2)} \sum_{s,t \in V} \frac{\sigma_v(s,t)}{\sigma(s,t)}$	[86]
Current flow betweenness	$C_{CFB}(v) = \frac{2}{(\|V\|-1)(\|V\|-2)} \sum_{s,t \in V} \tau_{st}(v)$	[165]
Load	$C_L(v) = \frac{2}{(\|V\|-1)(\|V\|-2)} \sum_{s,t \in V} \theta_{s,t}(v)$	[100]
Harmonic	$C_H(v) = \frac{\sum_{u \in V} \frac{1}{d(u,v)}}{\|V\|-1}$	[149]
Local reaching	$C_R(v) = \frac{1}{\|V\|-1} \sum_{u \in V} \frac{1}{d(u,v)}$	[157]

Table 3.1: Definitions of graph centralities used for analysis of local shape features of pavement cells. Each listed centrality measure was used to identify lobes of the 30 manually annotated graphs of the gold standard.

centrality. Hence, we confirmed that the closeness centrality is the best of the tested centrality measures to accurately detect local features of pavement cells.

Moreover, we used the extracted visibility graphs of the gold standard to determine the

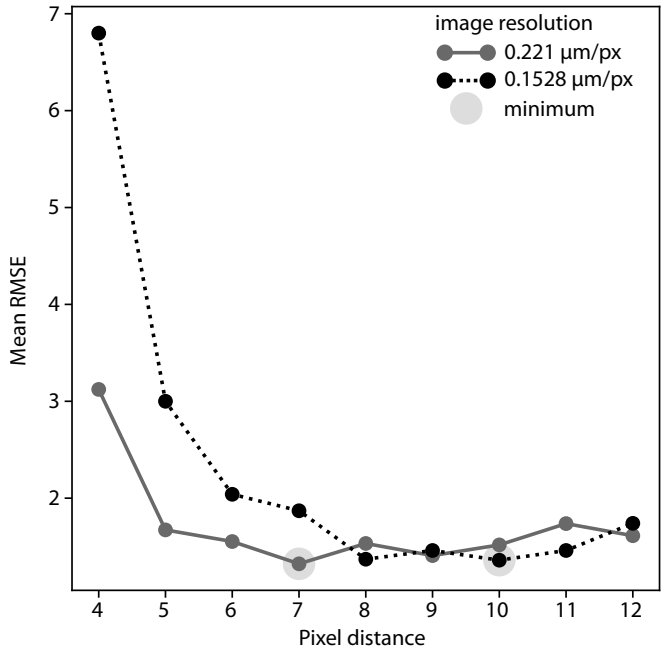

Figure 3.16: Determining the optimal pixel distance for visibility graph node placement. The visibility graphs of the 30 cells from the gold standard were created using different pixel distances between nodes. The mean RMSE was computed for each pixel distance. The minimum of all mean RMSE was then detected for cells from two different image resolutions.

optimal distance between visibility graph nodes using various pixel distances. The cells selected for the gold standard were derived from three different image, from which the image of the *clasp-1* mutant had a different resolution than the images of wild-type and oryzalin-treated cells (Table 3.2). Lobes were detected as local minima of the closeness centrality for each visibility graph and subsequently compared to the mean of manually detected lobes using the RMSE. We predefined a range of pixel distances which were used to create the gold standard visibility graphs. Afterwards, the mean RMSE was computed for each of the pixel distances and for the different image resolutions. We determined the lowest mean RMSE for both image resolutions and found that this corresponds to a distance of seven pixels and ten pixels between visibility graph nodes for the wild-type/oryzalin-treated cells and the *clasp-1* mutant, respectively (Fig. 3.16). Given the image resolution, we can calculate the optimal distance, termed node coverage, as:

$$nodecoverage = \frac{1}{resolution * pixel\ distance}. \tag{3.3}$$

Calculating the node coverage for the two different image resolutions resulted in a node coverage 0.65 node/μm for both images, thus defining the optimal pixel distance implemented into the algorithm to create visibility graphs in GraVis.

Image	**Cells**	**Resolution** $[\frac{\mu m}{px}]$	**Pixel distance** $[\frac{px}{node}]$	**Node coverage** $[\frac{node}{\mu m}]$
Col-0 oryzalin-treated	10	0.221	7	0.65
clasp-1	10	0.1528	10	0.65

Table 3.2: Calculated node coverage for cells from the gold standard. For the gold standard we selected 10 cells from wild-type (Col-0), oryzalin-treated wild-type and the *clasp-1* mutant and used their corresponding image resolution and different pixel distances to calculate the node coverage.

3.2.6 Detecting Lobes of Different Pavement Cell Shape Mutants

We showed that GraVis can identify local features in pavement cells. Next, we asked if GraVis is efficiently detecting differences of these features. To test this, we selected different genetically modified lines in which the number and size of lobes and necks were affected (Fig. 3.17C). We selected 20 pavement cells from each line and generated the corresponding visibility graphs and distance matrices. In the PCA plot, we could separate three distinct regions that describe the complexity of the pavement cells. In the lower left corner, we identified the two lines which show defects in lobe formation resulting in a reduced shape complexity (*RIC1-OX*, *CA-ROP2*, Fig. 3.17A) [90, 91]. In contrast, on the right, we identified a cluster of the two wild-type ecotypes that had highly complex pavement cells (Col-0, Ws, Fig. 3.17A). The pavement cells of the remaining lines can be found between these extremes, with an increase of cell complexity from left to right (*DN-ROP2*, *clasp-1*, *dek1-4*, *lue1*, *ric1-1*, *rop4-1*, *spr2-2*, Fig. 3.17A). We next plotted the number of detected lobes excluding tri-cellular junctions for each line and found a similar result as in the PCA (Fig. 3.17B). Once more, the wild-type ecotypes had the highest number of detected lobes, whereas *RIC1-OX* and *CA-ROP2* showed the lowest number of detected lobes. To conclude, we demonstrated that GraVis can be used to distinguish lines based on their pavement cell shapes and could be a powerful tool for phenotyping different genetic backgrounds. In contrast to other studies, which used various manual methods to quantify and assess these phenotypes [7, 11, 240], GraVis enables an automated analysis of pavement cell shape which can be used for genotype comparison, quantitative shape analysis and genetic screening to identify lines with shape defects.

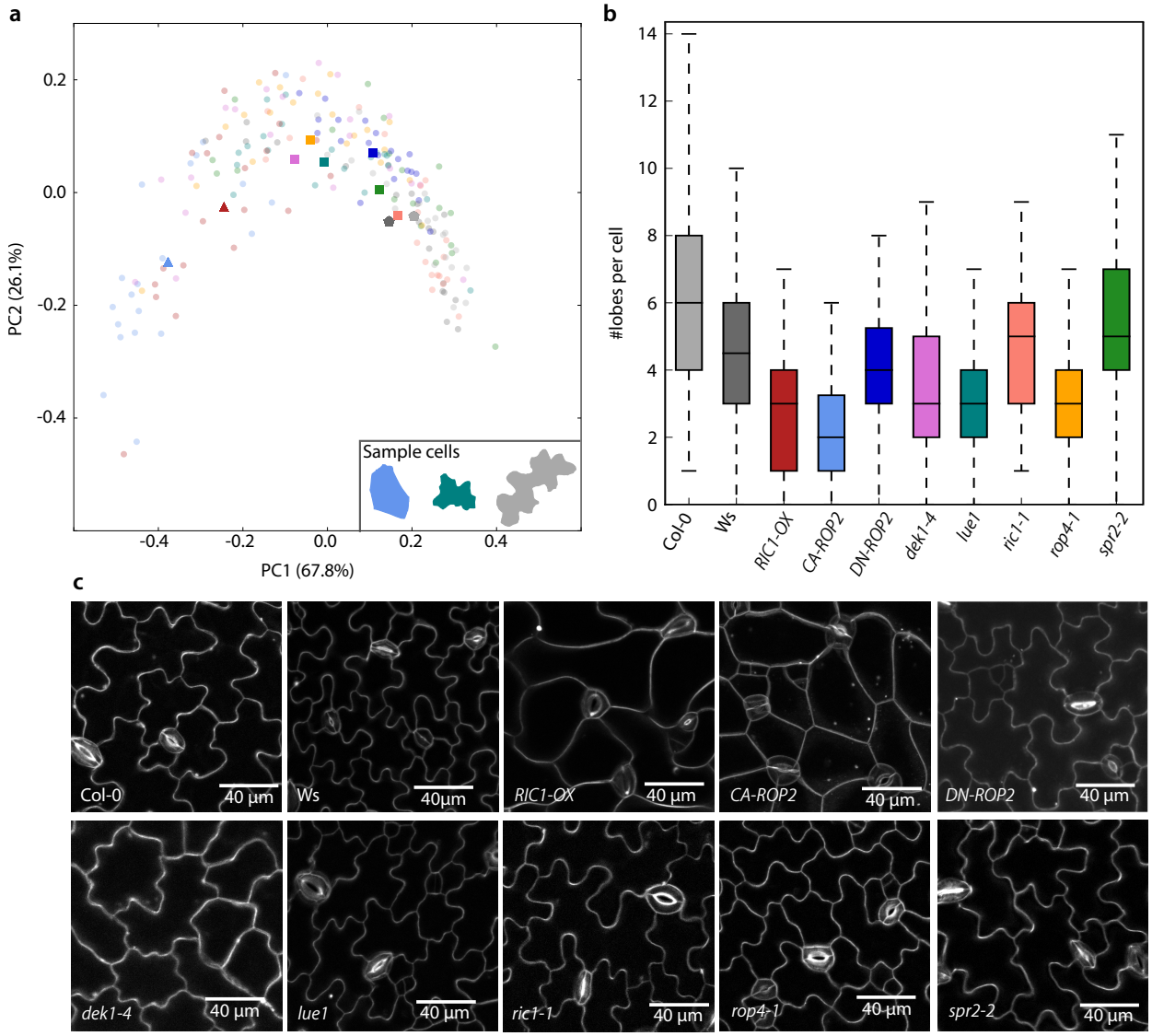

Figure 3.17: Comparison of pavement cells based on visibility graphs distinguishes Arabidopsis wild-type and genetically modified lines. (**A**) PCA of distances (20 pavement cells per sample) between pavement cells of wild-type Col-0 and WS (light gray and dark gray, respectively) and expression lines: *RIC1-OX* (red), *CA-ROP2* (light blue), *DN-ROP2* (dark blue), *dek1-4* (pink), *lue1* (teal), *ric1-1* (salmon), *rop4-1* (orange) and*spr2-2* (green). The circles correspond to selected cells, and the other shapes denote the center of mass for the corresponding expression lines. Sample cells for *CA-ROP2* (light blue), *lue1* (teal) and Col-0 (light gray) are shown in the lower right corner. (**B**) Boxplot of number of detected lobes excluding tri-cellular junctions for wild-type and mutants (80 pavement cells per sample). Boxplots are shown with median (horizontal line), 25th and 75th percentiles (box edges) and 1.5-fold of the interquartile range (whiskers). Outliers (circles) are data points past the end of the whiskers. (**C**) Images of LTi6b-GFP expressing Arabidopsis thaliana wild-type (Col-0, WS) and genetic lines (*RIC1-OX*, *CA-ROP2*, *DN-ROP2*, *clasp-1*, *dek1-4*, *lue1*, *ric1-1*, *rop4-1*, *spr2-2*).

3.2.7 Using Machine Learning Approaches to Classify Pavement Cells of Different Plant Clades

Plants of different clades were shown to have differences in leaf morphology which can be recognized using various classifiers like moving median center (MMC) hypersphere, plant feature similarity, centroid-contour distance curves or elliptic Fourier analysis to name a few [73, 112, 163, 266, 247]. While the classification works accurately on the level of leaves, it is still unknown if the same is applicable on the level of individual cells. To address this issue, we used a data set of manually extracted pavement cells from 278 different plant taxa published by Vőfely et al. for classification of plant clades [240].

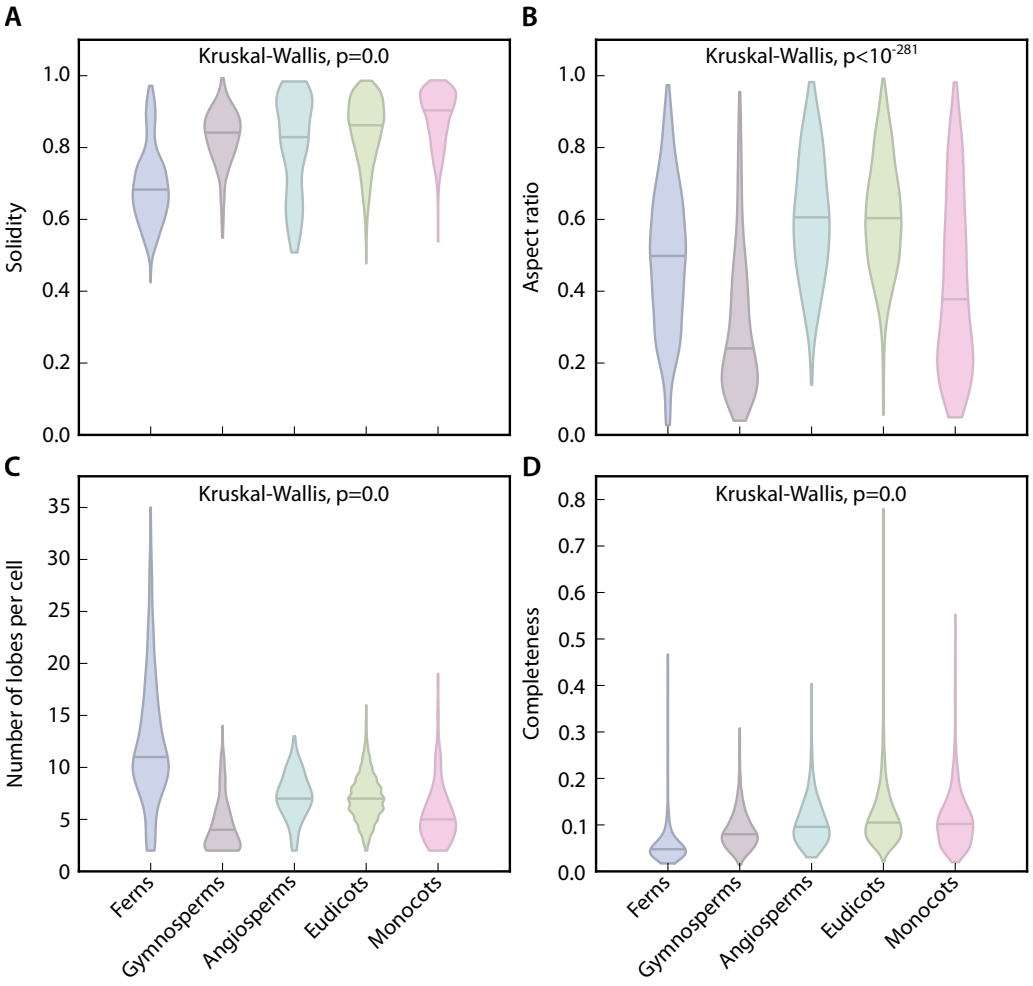

Figure 3.18: Violin plots of selected shape features for pavement cells of different plant clades. The selected cells of 213 different plant species are used to display the distribution of the (**A**) solidity, (**B**) the aspect ratio, (**C**) the number of lobes per cell and (**D**) the relative completeness. The five major clades of the plant species are shown with their corresponding centroid: eudicots (green), monocots (pink), ferns (blue), gymnosperms (purple) and angiosperms (light blue). The lines in the violin plots indicate the median of the data. The Kruskal-Wallis test was used to test whether there is a difference in means between the clades for the shown shape features.

We used GraVis to create the visibility graphs of adaxial pavement cells of five phylogenetic clades: eudicots, monocots, angiosperms, gymnosperms and ferns.

First, compared features we extracted with GraVis, e.g. the number of lobes per cell and the relative completeness, with shape features that were previously used by Vőfely et al., e.g. the solidity and aspect ratio (Fig. 3.18). To test if there are significant differences in means between the five clades, we used the Kruskal-Wallis test and found that there are indeed significant differences on the four compared shape features (see Fig. 3.18).
Following this, we used Dunn's post-hoc test to compare pairwise differences between the five clades. The test indicated that the solidity could not distinguish differences between gymnosperms and angiosperms (Table 3.3). Furthermore, the aspect ratio and the number of lobes per cell could not seperate eudicots and angiosperms and the relative completeness could not seperate monocots and angiosperms. In summary, the four compared shape features can be used to distinguish most of the pairs. However, this analysis is based solely on the comparison of means between clades and thus does not allow for a classification of pavement cells into the respective clade. A better staretgy to distinguish the different plant clades coud be the joint analysis of multiple shape features.

Solidity

	Ferns	Gymnosperms	Angiosperms	Eudicots
Gymnosperms	10^{-82}			
Angiosperms	10^{-37}	0.84		
Eudicots	10^{-274}	10^{-6}	10^{-3}	
Monocots	10^{-276}	10^{-29}	10^{-16}	10^{-25}

Aspect ratio

	Ferns	Gymnosperms	Angiosperms	Eudicots
Gymnosperms	10^{-56}			
Angiosperms	10^{-12}	10^{-61}		
Eudicots	10^{-59}	10^{-199}	0.77	
Monocots	10^{-11}	10^{-21}	10^{-27}	10^{-111}

Number of lobes per cell

	Ferns	Gymnosperms	Angiosperms	Eudicots
Gymnosperms	10^{-296}			
Angiosperms	10^{-29}	10^{-37}		
Eudicots	10^{-173}	10^{-94}	0.17	
Monocots	10^{-255}	10^{-11}	10^{-18}	10^{-53}

Completeness

	Ferns	Gymnosperms	Angiosperms	Eudicots
Gymnosperms	10^{-56}			
Angiosperms	10^{-53}	10^{-5}		
Eudicots	0.0	10^{-32}	10^{-3}	
Monocots	10^{-160}	10^{-13}	0.52	10^{-4}

Table 3.3: Adjusted p-values of the pairwise differences for each pair of clades. The shape metrics listed in Figure 3.18 are used to do a pairwise comparison using Dunn's post-hoc test between the different clades for the solidity, aspect ratio, number of lobes per cell and relative completeness. Non-significant adjusted p-values (p-value < 0.01) are highlighted in gray.

Second, we calculated the distance matrix of the extracted visibility graphs and used PCA to decompose the data (Fig. 3.19). The ferns (blue) could be easily distinguished, while the other clades were harder to differentiate. The gymnosperms (purple) were slightly separated from the cluster of monocots (pink), eudicots (green) and angiosperms (teal). Nevertheless, the centroids of the gymnosperms and angiosperms were closest, reflecting their close phylogenetic relationship.

Next, we used the extracted visibility graphs for classification using machine learning approaches. To this end, we first joined the cells of angiosperms and gymnosperms due to

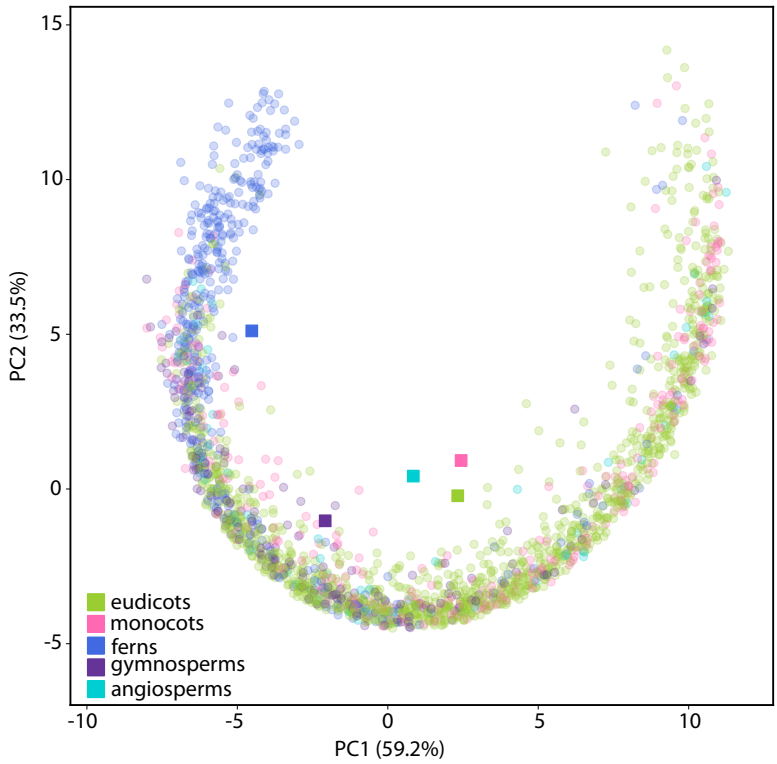

Figure 3.19: PCA of visibility graphs from different plant clades. The distance matrix of visibility graphs from manually segmented pavement cells of 213 different plant species was calculated [240]. The five major clades of the plant species are shown with their corresponding centroid: eudicots (green), monocots (pink), ferns (blue), gymnosperms (purple) and angiosperms (light blue).

their small sample sizes and close phylogenetic relationship and treated them as a single class (Table 3.4). The provided pavement cells were used to create the corresponding visibility graphs, from which multiple features were calculated, such as the number of lobes, and the minimum, maximum, mean, median, skewness and kurtosis of the different centrality measures we introduced earlier. We used multiclass support vector machine (SVM) with a Gaussian kernel and trained a model with 80% of the data set. To build the multiclass SVM, we used the well-established one-against-all strategy with accuracy as a measure of performance (see Section 3.3).

We showed that ferns are the first to be distinguished from the rest of the clades with a high accuracy of 84%. Carrying on with the one-against-all strategy, we removed the fern samples from the training set and repeated the procedure with the samples from the remaining clades. The last SVM was built based on the training data for monocots and the merged samples of angio- and gymnosperms. Finally, we used the remaining 20% of the data set as test set to evaluate the overall performance of the SVM models. The average accuracy on the test set was 85%, while the average precision and recall were 57% and 51%, respectively (Table 3.4).

Clade	Samples	Training set	Accuracy			Test set	Acc.	Pre.	Rec.
			SVM1	SVM2	SVM3				
Ferns	1176	919	0.84	-	-	257	0.92	0.87	0.72
Eudicots	3534	2841	0.78	0.75	-	693	0.78	0.76	0.89
Angio-/ Gymnosperms	209+ 570	167+ 468	0.72	0.71	0.74	42+ 102	0.86	0.55	0.30
Monocots	870	692	0.74	0.73	0.73	178	0.83	0.11	0.12
Total	**6359**	**5087**				**1272**	**0.85**	**0.57**	**0.51**

Table 3.4: Prediction of plant clades using nested SVMs. Pavement cells of five different plant clades were used for prediction. The two minority classes angiosperms and gymnosperms were merged. The multi-class SVM was trained on 80% of the total dataset, the remaining 20% were used as test set to evaluate the resulting SVMs. (Acc.: Accuracy, Pre.: Precision, Rec.: Recall).

3.3 Materials and Methods

Creation of visibility graphs. The visibility graph was created from the shape contour by placing equidistant nodes along it. The optimal pixel distance was calculated from the optimal number of nodes per μm and the image resolution (see below). After positioning the nodes, edges were drawn between each pair of nodes if the corresponding segments did not cross the contour. If a segment between two nodes lay on the contour, we allowed an edge to be drawn if there was no additional node on the segment. Edges were weighted according to the Euclidean distance between nodes.

Comparison of visibility graphs. A graph was transformed into its corresponding unweighted adjacency matrix. The Laplacian matrix was computed as $L = D - A$ with D the diagonal matrix and A the adjacency matrix of the graph. The eigenvalues of the Laplacian matrix were calculated and normalized to the largest eigenvalue. The Kolmogorov-Smirnov statistic was used to calculate the maximum distance between the distribution of Laplacian eigenvalues. The resulting distance between each pair of graphs was stored in a distance matrix which can be used for clustering or for dimension-reducing techniques like principal component analysis.

Synthetic data set of simple shapes. We created a synthetic set of simple shapes including three types of triangular (right-angled, equilateral, and obtuse), three types of circular (circle, ellipse, and rotated ellipse) and four types of rectangular shapes (square, rectangle, trapeze, rhombus). For each object, we created a smaller and a larger shape by using equal and unequal numbers of nodes for each graph (Table 3.5).

Shape			Equal				Unequal			
			Small		Large		Small		Large	
			$\|V\|$	$\|E\|$	$\|V\|$	$\|E\|$	$\|V\|$	$\|E\|$	$\|V\|$	$\|E\|$
Triangular	Rectangular	◣	20	132	20	112	14	64	28	256
	Equilateral	▲	20	128	20	128	16	84	24	192
	Obtuse	◣	20	125	20	138	14	63	29	276
Rectangular	Square	■	20	150	20	150	12	54	32	384
	Rectangle	■	20	148	20	148	16	91	40	592
	Trapeze	▲	20	146	20	144	14	69	34	424
	Rhombus	◆	20	150	20	148	12	54	32	384
Circular	Circle	●	20	190	20	190	24	276	32	496
	Ellipse	⬭	20	190	20	190	22	231	32	496
	Rotated ellipse	⬭	20	190	20	190	20	190	33	528

Table 3.5: Properties of the visibility graphs of the synthetic set with equal and unequal number of nodes. Each shape in the synthetic set was used to generate a smaller and a larger visibility graph. The number of input coordinates (nodes) and the corresponding edges are shown. V and E denote the set of nodes and edges, respectively, and $||$ denotes set cardinality.

Comparison of visibility graphs based on a node-reducing method using modularity clustering. To compare two graphs of different order (i.e. number of nodes), we implemented an algorithm that reduces the number of nodes to that of the compared graphs with the smaller order. The algorithm is based on modularity clustering and includes the following steps (Fig. 3.6): Given two graphs, we identify which graph has the larger number of nodes and reduce this graph to the order of the smaller graph (Fig. 3.6a). We reduce the number of nodes by partitioning the larger graph into as many network clusters (intuitively, subgraphs which are more densely connected within than to the rest of the network) as there are nodes in the smaller graph. To do the partitioning we rely on the modularity, as a network cluster quality index [38]. Since optimizing modularity is an NP-hard problem, here we use greedy approximation algorithm widely used in the network research community [164], which also allows us to control the number of clusters. Initially, each node is assigned to a cluster (Fig. 3.6b). In the next step, new clusters are created by assigning two consecutive nodes to the same cluster and calculating the modularity. The consecutiveness property needs to be respected, since the reduced graph should maintain the properties of the original visibility graph. Here, all possible combinations of two consecutive merged nodes are created and the combination with the maximum modularity is selected (Fig. 3.6c-d). The nodes which belong to the same cluster are merged and represented by a single new node, whose position is determined by the geometric median of the merged nodes, which minimizes the sum of distances to all node positions (Fig.

3.6e). The merging of nodes is repeated until the larger graph has the same number of nodes as the smaller graph (Fig. 3.6f).

Homogeneity of the derived clusterings of shapes. To compare the quality of clusters derived from the different comparison methods, we calculate the Biological Homogeneity Index (BHI), which provides a measure of homogeneity of the determined clusters [65]. Let $B(i)$ and $B(j)$ be functional classes containing shape i and j, respectively. We assign the indicator function $I(B(i) = B(j)$ the value 1 if $B(i)$ and $B(j)$ match. Thus, for a given statistical clustering partition C_k, the BHI is defined as:

$$BHI = \frac{1}{K} \sum_{k=1}^{K} \frac{1}{n_k(n_k - 1)} \sum_{i \neq j \epsilon C_k} I(B(i) = B(j)), \tag{3.4}$$

where K is the number of clusters and n_k is the number of annotated shapes in a cluster. A value of 1 for the BHI denotes perfect clustering, in which all shapes assigned to a cluster belong to the same group (provided as a priori knowledge). Smaller values for the BHI denote larger departure from homogeneity and point at issues of the resulting clusterings. To do so, we use the dendrogram derived from the comparisons of the synthetic shapes and cut them into three clusters by using the dendrogram distance, since we compare three different shape types. To prevent clusters with a single shape, we merged single shape clusters with the closest cluster according to the dendrogram distance.

Shape data sets from different domains. We used shape data sets from three different domains: fish, sand grains, and leaves for which we chose 20 open-access images of fish drawings from different subfamilies from the marine species database WoRMS [35, 184]. Furthermore, we selected 20 images of leaf shapes collected from 278 different vascular plant taxa which were openly accessible [240, 239]. We also collected sand from different beach locations at the Australian coast. Images were captured using a brightfield microscope and a dark background (Leica M205 FA stereomicroscope, 8.2X). Here, we selected 24 unique shapes from a single image for further processing. All selected images were segmented by converting them to grayscale and binarizing them using either a mean or Otsu thresholding. Small particles and holes were then removed. Furthermore, the petioles of leaves were removed to focus only on the shape of the leaf lamina. The visibility graphs for all shapes were created and compared within their corresponding data sets (see Table 3.6).

Microscopy images of pavement cells (wild-type and mutants).
For imaging of the 96 hour post-dissection cotyledons, seeds in the wild-type and *clasp-1* background expressing 35Spromotor:LTi6b-GFP [63] were sterilized in 70% ethanol and rinsed three times with sterilized dH20 before being stored in dH20 in the dark at $4°C$ for three days. Samples were then prepared according to Peterson and Torii (2012) [181] with samples being mounted under 0.5% micro-agar supplemented with or without 1 μm oryzalin (Sigma-Aldrich). Samples were moved to a $21°C$ growth cabinet with a 16-hour light regiment. Z-stacks (0.3 μm step sizes) of adaxial cotyledon surfaces proximal to

Sand grains		Fish		Leaves	
$\|V\|$	$\|E\|$	$\|V\|$	$\|E\|$	$\|V\|$	$\|E\|$
15	100	211	7871	304	20168
30	405	186	8307	231	18470
41	649	253	7238	169	10087
25	287	172	6078	83	2983
20	186	178	7668	297	10970
42	766	184	10902	124	5581
39	683	118	2732	95	3536
28	376	100	3342	105	3118
30	434	160	6960	106	3692
14	88	197	6686	172	6594
34	512	120	2836	52	363
43	706	103	2720	199	9615
29	377	146	4810	144	8887
74	2032	171	4412	113	4247
41	780	184	7592	147	8381
39	735	160	5582	81	2308
36	561	184	8354	97	4006
33	499	169	5510	125	5860
27	305	150	3992	207	12323
30	388	159	7062	175	13400
25	275				
18	146				
19	150				
21	206				

Table 3.6: Details of visibility graphs for different domains. We selected shapes from three different domains (sand grains, fish, leaves) and created the corresponding visibility graphs. For each graph, the number of edges, $|E|$ and nodes, $|V|$ are provided.

the petiole were acquired 96 hours post-dissection on a spinning-disk confocal microscope (Roper Scientific) with a 60x objective lens. Overlapping regions of interests were stitched together using the stitching plug-in [189] for ImageJ [210].

For imaging of the wild-type (Col-0, Ws eco-types), *RIC1-OX*, *CA-ROP2*, *DN-ROP2*, *dek1-4*, *ric1-1*, *spr2-2*, *rop4-1*, *lue1* and *clasp-1* lines [9, 90, 136, 152, 198, 218], seeds were sterilized as previously mentioned and plated onto half-strength Murashige and Skoog

media with 1% micro-agar. Plates were stored in the dark at $4°C$ for three days before being grown vertically in a $21°C$ growth cabinet with a 16-hour light regiment for five days. Seedlings were incubated in 0.2 mg/mL of propidium iodide (Sigma-Aldrich) for 2 minutes followed by two rinses with dH20. Z-slices (0.5 μm step sizes) of adaxial cotyledon surfaces were imaged with a SP8 confocal light microscope (Leica) using a 20x objective lens.

Pre-processing of pavement cell images.
Imported images of pavement cells were converted to grayscale and screened for necessary image cleaning steps, such as removal of artificial edges caused by image stitching, image denoising or image rescaling. The need for the cleaning steps was evaluated in an automated manner; however, it can also be specifically selected in the GUI. Artificial edges were detected by using a Sobel filter as well as probabilistic Hough lines and were consequently removed. Noisy images were detected by calculating the percentage of white images pixels after binarization and were subjected to total variation denoising, white top hat transform and histogram equalization.

After cleaning, the image intensity WAs rescaled, and a Gaussian filter and a tube filter were used for image smoothing and enhancement of tube-like structures, respectively. This was followed by image binarization, where the threshold for the binarization was selected by calculating the mean of the global threshold using Otsu's method and the maximum of the pixel intensity histogram. The image was separated into background and pavement cell contours, which were skeletonized after removing small objects and holes. The skeleton was examined for small gaps which were closed if the gap was small enough and the skeleton endings were tilted at a similar angle. To ensure that only whole cells are used for the creation of visibility graphs, protruding branches of the skeleton were detected and removed. The final image was labelled to guarantee that each detected pavement cell has its own label which was used to create the corresponding visibility graph.

Detection of lobes as local features of pavement cells.
The closeness centrality was calculated for each node in the graph. Lobes and necks were identified by the local minima and maxima of the closeness centrality along the contour. To distinguish true lobes from tri-cellular junctions, we correlated the lobe positions with the positions of detected tri-cellular junctions, allowing for a difference of three pixels in x- and y-direction. Tri-cellular junctions were identified in the skeletonized image of the pavement cells by searching for crossing of the skeleton.

Comparison of lobe detection tools.
The contours of 30 pavement cells were selected from microscopy images of *Arabidopsis thaliana* epidermal tissues 96 hours after germination for three different scenarios (Wild type (Col-0 background), oryzalin-treated, *clasp-1* mutant). Lobes of these 30 cells were

detected manually by 20 experts in a blind study and used as a gold standard. Lobes were also detected using the tools PaCeQuant, LobeFinder, LOCO-EFA and GraVis. For PaCeQuant and LobeFinder, the outlines were saved as Region of Interest files (.roi). For LOCO-EFA, the outlines of the selected pavement cells were converted into their corresponding x- and y-pixel positions. The number of detected lobes was provided in table format for GraVis, PaCeQuant and LobeFinder. In contrast, we selected the number of detected lobes from LOCO-EFA's output as the highest modus number with a lambda that drops by more than 0.5 compared to the lambda of the next mode.

The root mean square error (RMSE) was calculated to quantify the difference between the number of lobes detected by the tools and the mean of the number of manually detected lobes. Furthermore, to calculate the optimal pixel distance between visibility graph nodes for GraVis, we created visibility graphs using node distances ranging from 4 to 12 pixels for the 30 pavement cells. We computed the RMSE between the detected lobes and the mean of the gold standard. To this end, we chose the pixel distance with the lowest RMSE and the image resolution to calculate 0.65 nodes/μm as the optimal number of nodes (see Fig. 3.16).

Prediction of plant clades.
We used the dataset of epidermal cell outlines from Vőfely et al. (2018)[240, 239] to predict plant clades using different properties of extracted visibility graphs. The manually traced outlines of pavement cells were provided as coordinate files from which we selected all adaxial cells to create the corresponding visibility graphs. In total, we selected 6359 cell outlines from five different plant clades (monocots, eudicots, ferns, gymnosperms, angiosperms; see Table 3.4).

For each visibility graph we calculated the number of lobes and a range of different graph centralities (see Table 3.1) for which we further computed the mean, median, minimum, maximum, kurtosis, and skewness. These were used as features of the SVM. Non-negativity of the features was ensured by subtracting the minimum value from each property. We used 80% of the data for training of a nested SVM, while the remaining 20% were used as a test set. We optimized the SVM by testing different parameter combinations using grid search.

The multiclass SVM was built using the one-against-all strategy [114]. To account for the imbalance of class sizes, we balanced class sizes by down sampling the majority class to the size of the minority class. This process was repeated ten times for each class. For each sampling, the training data was again split into test and training subsets using 5-fold cross validation. The resulting accuracy, precision, and recall were calculated and averaged for each sampling and used to determine the best predicted class. The final multiclass SVM model was evaluated using the test set that we put aside. After the performance evaluation of the model, we used the entire data set to retrain the SVMs.

Requirements for GraVis.

GraVis can be downloaded as an executable file for all major operating systems from Github: https://github.com/jnowak90/GraVisGUI. We implemented the described features of GraVis in a simple-to-use graphical user interface (GUI) using Python 3. The GUI can be launched by clicking the downloaded executable file (for Windows, Linux or MacOS) without the need of a Python installation. The GUI is split into two major parts: the shape description, where visibility graphs are extracted from segmented shapes, and the shape comparison, where a distance matrix of selected visibility graphs is computed. For the shape description part, the user can upload images of pavement cells which are firstly pre-processed to segment the individual cells. For each of the detected cells, visibility graphs are created and stored in a results folder. We further implemented a pipeline for the description of shapes from other domains, which require the input of binary images. For the shape comparison part, the user can select visibility graphs from a single image or multiple images to compute a distance matrix which can be used for further analysis, such as PCA or clustering. A more detailed description of the GUI functions, as well as sample images and example workflows can be found on the Github page.

Chapter 4

A Tissue-Wide Description of Pavement Cells

4.1 Research Question and Aims

In Chapter 3, we proposed a network-based framework for the description of shapes and showed that we can accurately quantify shapes of individual pavement cells. Yet, the development of individual pavement cells is highly coordinated with its adjacent cells by cell-to-cell signalling [90]. To understand how the coordination is regulated between cells, it is important to investigate pavement cell shape development on a tissue-level. To address this issue, we extended our shape description framework and investigated network-based representations of adjacent cells. Here, we determined the complexity of the visibility graph derived from two neighbouring cells which contours were joined and, together with the information about the number of cell neighbours, used it to identify stomata cells in pavement cell tissues. Furthermore, we propose a polygonal representation of pavement cells on a tissue level that allows the investigation of changes to the morphogenesis progression. Since a neck in one cell is a lobe in the adjacent cell, we use the polygonal representation for internal validation of different lobe detection approaches by correlating detected lobes and necks in adjacent cells.

4.2 Results

4.2.1 Identification of Stomata

Stomata cells are small pores in the leaf epidermis which enable the gas exchange necessary for photosynthesis. In *Arabidopsis thaliana*, stomata appear as small pores which are surrounded by two kidney-shaped guard cells (Fig. 4.1A). They are widely scattered between pavement cells and show random orientations in eudicot leaves [194]. In contrast to pavement cells, they have quite simple, round shapes and can be easily detected by eye. To identify stomata in an automated fashion, we used GraVis, our network-based shape descriptor, which uses the visibility graph concept to represent shapes (see Chapter 3). As

illustrated in Section 3.2.4, we can determine the complexity of a shape by calculating the (relative) graph completeness and identify stomata according to their high graph densities (Fig. 4.1B).

However, as can be seen in Figure 4.1B, depending on the segmentation quality during image pre-processing, stomata were present as single, round cells (Type I, Fig. 4.1, orange), or they were segmented into two guard cells (Type II, Fig. 4.1B, green) or even two guard cells and the pore (Type III, Fig. 4.1B, blue). While Type I stomata cells can be easily detected by their corresponding complexity values which were close to one, the other types were more difficult to identify, as the complexity values (as quantified by the graph completeness) varied and their distribution sometimes overlaped with that of pavement cells (see Fig. 4.1C).

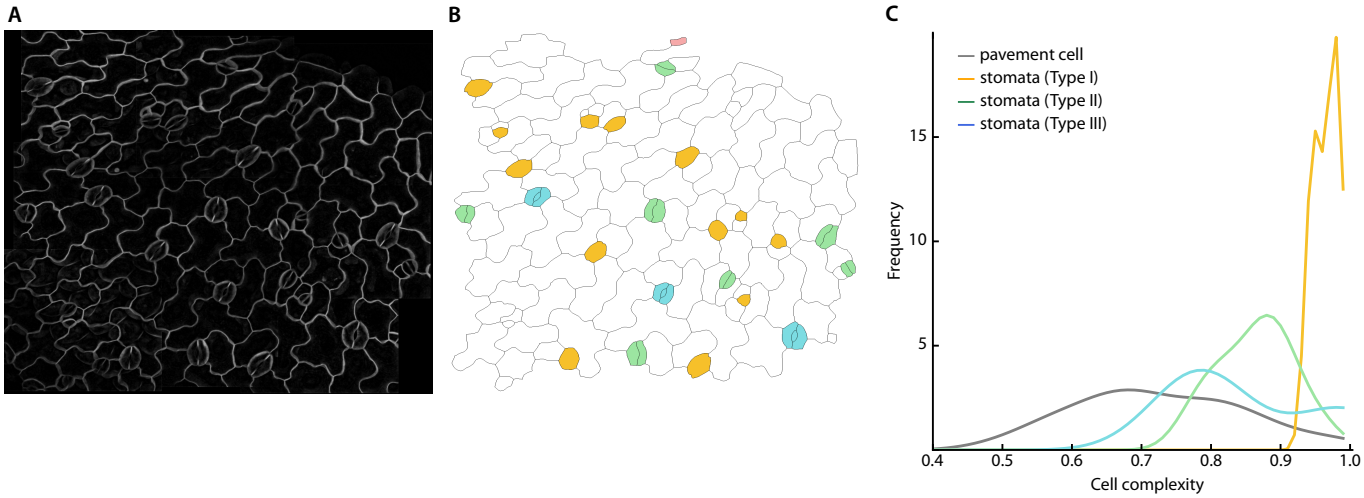

Figure 4.1: Stomata cells in the upper leaf epidermis. (**A**) Spinning-disk confocal microscopy image of the upper leaf epidermis of Arabidopsis wild-type (Col-0). (**B**) Segmented cells and manually identified stomata cells: single stomata (Type I, orange), stomata separated into two guard cells (Type II, green) and stomata separated into two guard cells and the pore (Type III, blue). Isolated cells which are not connected to neighbouring cell are shown in red. (**C**) Density plot of complexity values, quantified by the relative graph completeness, for pavement cells and the three different stomata types.

To allow for an automated detection of Type III stomata cells, we represented the pavement cell tissue as a neighbour graph. Here, each cell was defined as a node and two nodes were connected by an edge if the corresponding cells were direct neighbours (Fig. 4.2). Furthermore, we added a node that represents the image background (i.e. all pixels not belonging to pavement cells) and connected the node to all cells which were directly facing the background. First, we used this graph representation to identify isolated cells, i.e. cells which were not directly adjacent to other cells due to improper segmentation. Because these cells have no neighbouring cells, they do not have any edges and can be

identified by searching for nodes with a node degree of one, as they will be only connected to the background (Fig. 4.2A, blue).

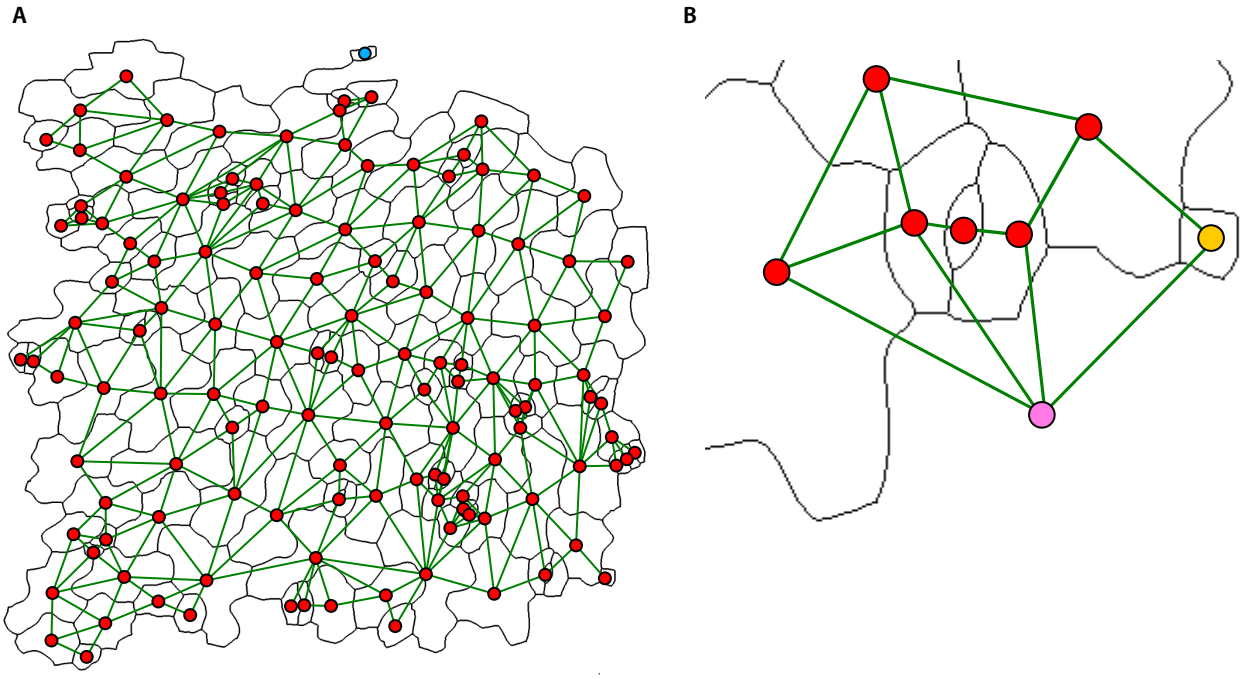

Figure 4.2: Neighbour graph of pavement cell tissue. (**A**) Segmented cells are represented by nodes (red) connected by an edge (green) if two cells are adjacent. Isolated cells are not connected to other cells, i.e. have no edges and can be easily distinguished (blue). (**B**) Stomata pores can be identified by searching for cells with a node of degree two, whereby none of the connected neighbours represents the background (pink); otherwise, the cell faces the background (orange).

Next, we attempted to detect Type III stomata, or more specifically stomata pores, by identifying cells which had exactly two neighbours, whereby no neighbour was background. Stomata pores are surrounded by two guard cells and have no direct contact to the background (Fig. 4.2B). Further, small cells at the border of the tissue might also have two connections, with one of them to the background. These rules can help to identify stomata pores. In addition, we can identify all guard cells since these are direct neighbours to stomata pores. To standardize the appearance of all stomata, we can further merge the pore and the guard cells into one cell and assign a new node to the cell.

Finally, we also attempted to identify Type II stomata which are built by two guard cells, whereas the pore is included in one of the cells (Fig. 4.1B). Here, we used an extension of our network-based approach, GraVis by applying the visibility graph concept to two neighbouring cells. For each pair of neighbouring cells, we merged the corresponding contours into one (Fig. 4.3A-B). We then created the visibility graph as described in Section

3.2.1 and calculated the graph completeness. As before, we can now detect stomata by identifying merged cells with a graph completeness that is close to one (orange, Fig. 4.3C). Combining the results of all steps, we can identify different kinds of segmented stomata cells in an automated and accurate fashion. Ultimately, this enables the analysis of stomata patterns not only in pavement cell tissue of wildtype Arabidopsis, but also in mutants that are defective in stomatal functions, for example the *too many mouths* (*tmm*) mutant in which stomata are aggregated in groups [183].

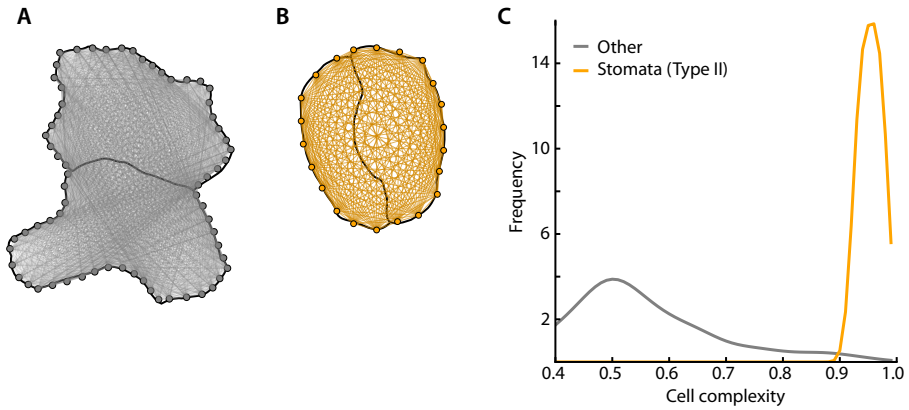

Figure 4.3: Visibility graphs of two merged cell contours. The contour of two (**A**) pavement cells and (**B**) two guard cells are merged and the visibility graphs is created for the resulting contour. Cells with a complexity close to one, like in (**B**) are identified as stomata. (**C**) Complexity values for merged guard cells (orange) and merged cells, which can either be two pavement cells, or a pavement cell and a stomata cell of different types (gray).

4.2.2 Polygonal Representation of Pavement Cells

Yet another way to study the development of pavement cells on tissue-level is to use polygons that describe the cell shape. The polygonal description of cell shapes can be used to investigate the growth of cells and cell shape change over time. To create the polygons, we first identified all tri-cellular junctions between cells, i.e. places where three or more cells meet.

During pre-processing, pavement cell images were binarized, where the cell membrane was defined as foreground and the rest as background. The cell membrane was then reduced to a one-pixel-wide skeleton, and branches belonging to cut-off cells were removed by additional cleaning steps (see Section 3.4). This branchless skeleton was used to identify tri-cellular junctions by detecting skeleton crossings (Fig. 4.4A). Furthermore, we detected additional junctions by using the information of cut-off cells from the uncleaned skeleton. All identified junctions were defined as the nodes of the polygonal graph. If two junctions were connected by an anticlinal cell wall segment, they were connected by an edge. The resulting polygonal graph is shown in Figure 4.4B.

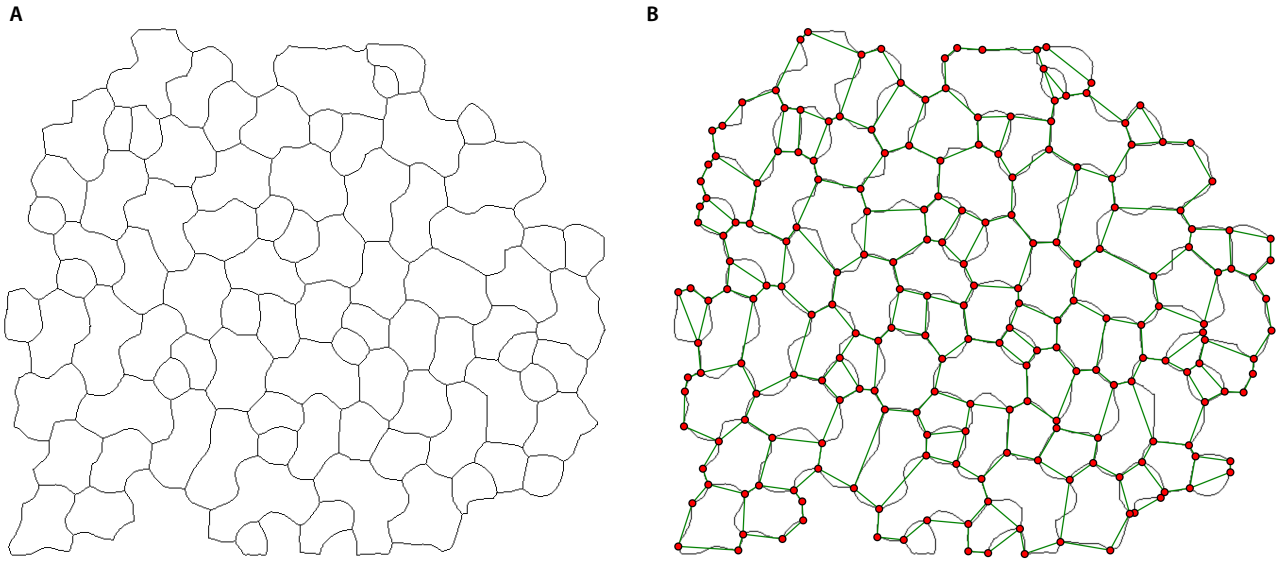

Figure 4.4: Polygonal graph of pavement cells. The skeleton (**A**) of the binarized cell membrane is used to detect tri-cellular junctions as crossings and defined as nodes (red) of the polygonal graph representation (**B**). Edges (green) are drawn between two nodes if the corresponding junctions are connected by a cell membrane segment in the skeletonized image.

Interestingly, the majority of stomata cell polygons (small, round cells) were quadrangular, with two exceptions which were trigonal and pentagonal. The majority of pavement cells was at least pentagonal. During development of pavement cells, the cells grow and differentiate, thus creating new tri-cellular junctions which will create new polygons and add sides to existing polygons. The information about the change of the size and shape of the polygons is therefore a way to study progression of pavement cell morphology. In Figure 4.5A-D, it can be seen that during the development of pavement cells the size of the polygons WAs increasing for each consecutive time point and lobes and necks were more indented in later time points. Nevertheless, the overall number of polygon sides was not changing much over time for most cells in the shown examples, as new polygon sides are only introduced if cells divide (Fig. 4.5E).

4.2.3 Lobe Calling

We further used the polygonal graph to evaluate the accuracy of identified lobes and necks by different lobe detection tools including GraVis, PaCeQuant and LobeFinder [156, 252]. In pavement cells, the lobe of one cell corresponds to a neck in the adjacent cell. Therefore, we aim to evaluate how well this one-to-one calling of lobes and necks in adjacent cells is achieved by the selected lobe detection tools.

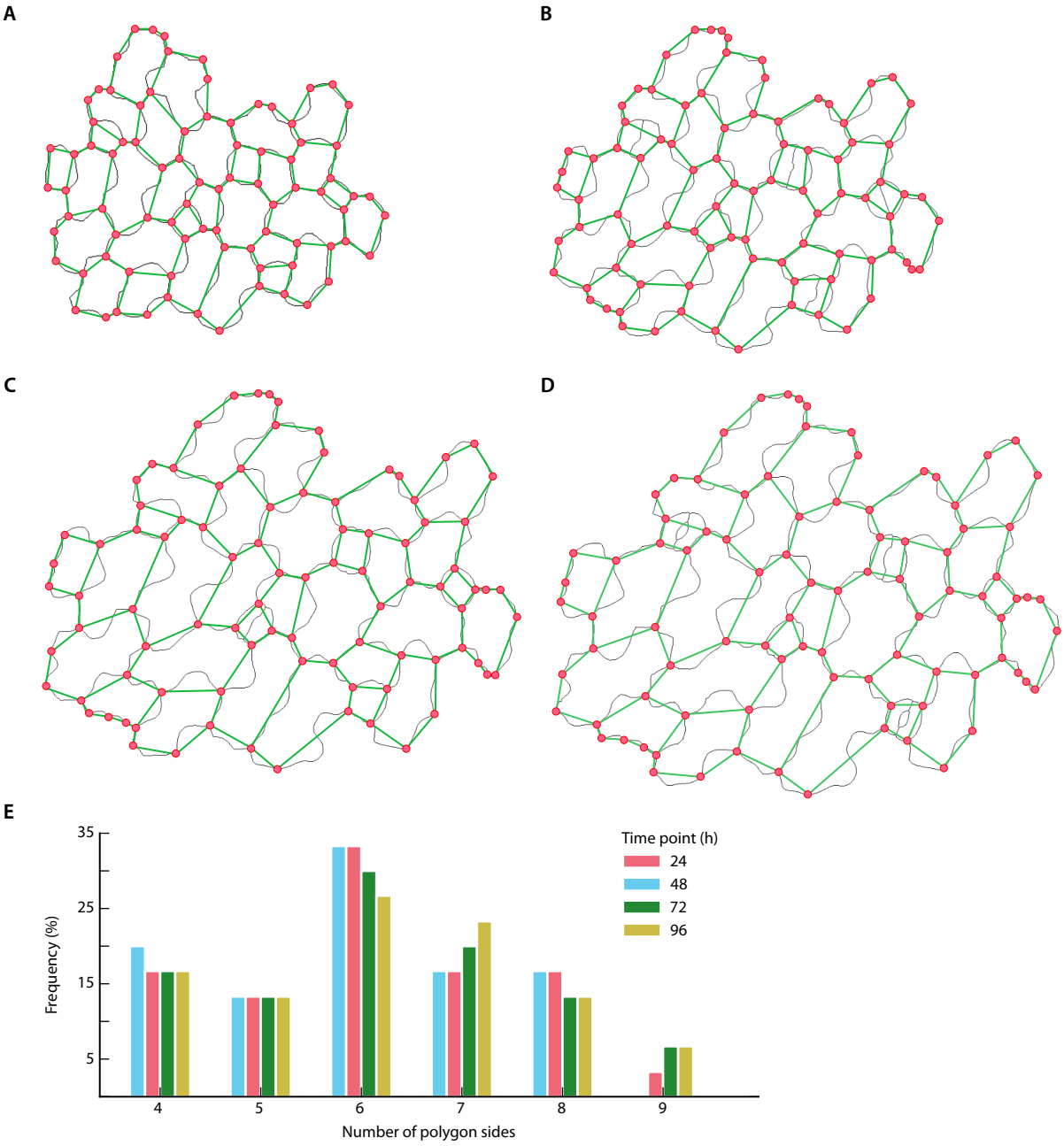

Figure 4.5: Polygonal graphs of pavement cells over time. The polygonal graphs were created for the same set of pavement cells over four different time points: (**A**) 24h, (**B**) 48h, (**C**) 72h and (**D**) 96h. tri-cellular junctions are denoted by nodes (red) which are connected by edges (green) if they are connected by cell membrane. (**E**) Distribution of different n-sided polygons in pavement cell tissue at different time points (**A-D**).

Creating a manual curation for lobe calling.

To facilitate the evaluation of the performance for the three different approaches and corresponding tools for lobe calling, we created a manual curation of detected lobe and neck pairs using the tissue of pavement cells at a specific time point. To this end, we identified all tri-cellular junctions of the skeletonized image and created the polygonal graph. For

each pair of junctions (nodes, Fig. 4.6A) that was connected by an edge, we first identified the two adjacent cells and the pixels of the contour connecting them. Afterwards, we counted the number of lobes and necks for each of the adjacent cells and created lobe/neck pairs by combining the number of detected lobes in one cell (cell 1) with the number of detected necks in an adjacent cell (cell 2), and vice versa (Fig. 4.6B). To detect lobes and necks for each of the adjacent cells, we first determined all coordinates of the line which connects the corresponding junction nodes (green edge, Fig. 4.6B). For each coordinate along this line, we located the closest pixel on the actual contour between junctions and calculated the Euclidean distance between the line and selected contour pixel. Whenever this distance equaled zero, the line crossed the contour. Thus, we split the contour into segments, defined by the crossings of the line and the contour (yellow, Fig. 4.6B). For each segment we finally localized in which cell the maximum distance between the line and the contour was found. To evaluate whether the maximum corresponded to a lobe or neck, we ensured that the magnitude of the indentation was significant enough by setting a threshold for the maximum distance. Depending in which cell the maximum was discovered, we created the lobe/neck pairs. This process was then repeated for the remaining junction pairs.

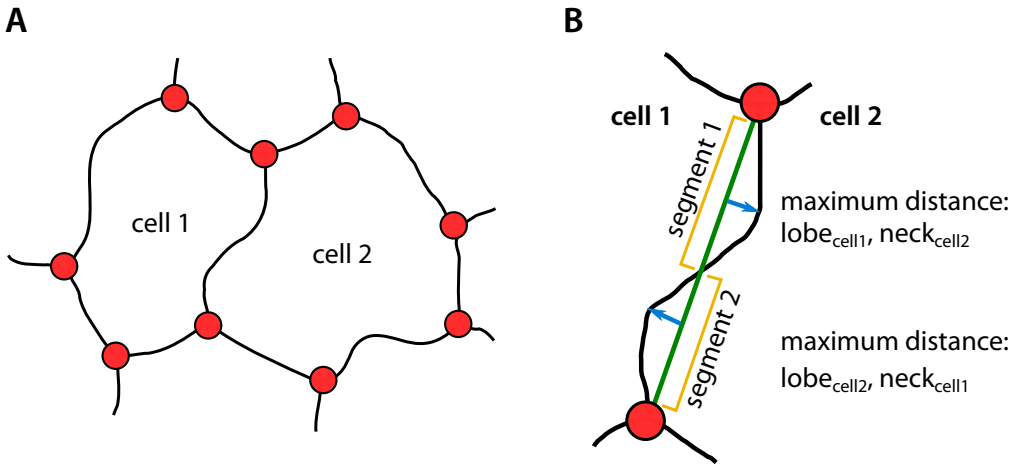

Figure 4.6: Automated detection of lobes and necks using the polygonal graph. (**A**) The contour between two adjacent cells is used to detect lobes and necks. (**B**) The coordinates of the line (green) connecting two junction nodes (red) are determined and the closest pixel on the contour located. The Euclidean distances between the line and the selected contour pixels are calculated and split into segments (yellow) whenever the distance equals zero (the line crosses the contour). The maximum distance of each segment is used to identify whether a lobe or neck was detected for the adjacent cells (blue).

Lobe detection output of the different tools.

We compared the lobe calling performance of GraVis with the performances of PaCeQuant and LobeFinder. Unlike LOCO-EFA [208], all of these tools provide locations of detected

lobes, albeit in different ways. Due to the visibility graph representation of shapes in GraVis, we can define specific positions of both lobes and necks for single cells, but also with respect to the whole tissue. In contrast, LobeFinder only provides positions of lobes for single cells, whereas the position of necks has to be inferred from the area between two detected lobes (Fig. 4.7C). Likewise, PaCeQuant only provides lobe positions, although here whole lobe regions instead of point-specific positions are provided (Fig. 4.7B).

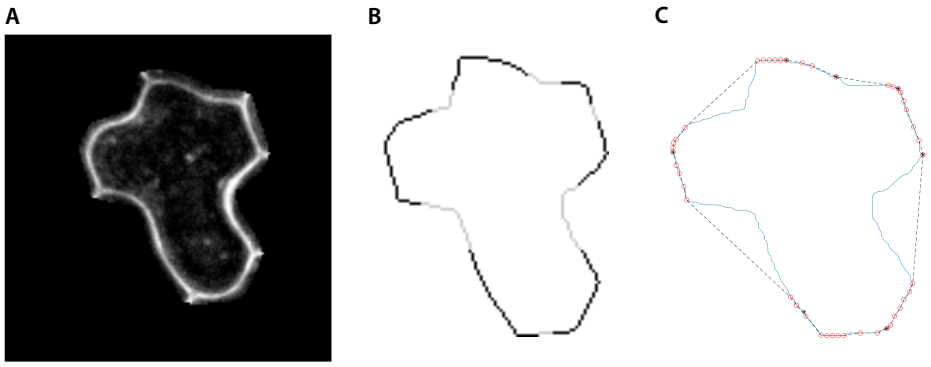

Figure 4.7: Output of lobe detection tools. (**A**) Imaged cell membrane of the input pavement cell. (**B**) Output of detected lobes for PaCeQuant. Lobes are depicted by dark areas, while brighter regions define neck regions. (**C**) Output of detected lobes for LobeFinder. Detected lobes are marked by circles with asterisks.

Lobe calling for different lobe detection tools.
We used GraVis to automatically segment cells and extract the corresponding visibility graphs. We saved the contours of all segmented cells and converted them into ROI files which we used as input for PaCeQuant and LobeFinder. To account for detected lobe/neck pairs in GraVis, we used the visibility graphs of two adjacent cells. To this end, we identified the visibility graph nodes which were closest to the pair of junction nodes defining the border between two adjacent cells. Along this defined region of visibility graph nodes, we then counted the number of detected lobes and necks, excuding tri-cellular junctions, and created the corresponding lobe/neck coordinates. Since both LobeFinder and PaCeQuant only provided relative positions of lobes in single cells as depicted in Figure 4.7B-C, we had to manually determine the number of detected lobes and necks, excluding tri-cellular junctions, of each pair of adjacent cells, by bringing their lobe output face to face. For PaCeQuant, the regions between two lobes were defined as neck regions. We applied the same definition to the output of LobeFinder, although we did not define specific positions of necks, but rather identified neck regions. Finally, we plotted the occurrences of all lobe/neck pairs for the manual curation and the three investigated tools (Fig. 4.8).

The manual curation illustrated nicely the one-to-one correspondence of detected lobes and necks of adjacent cells described by the diagonal on Figure 4.8A. For the majority

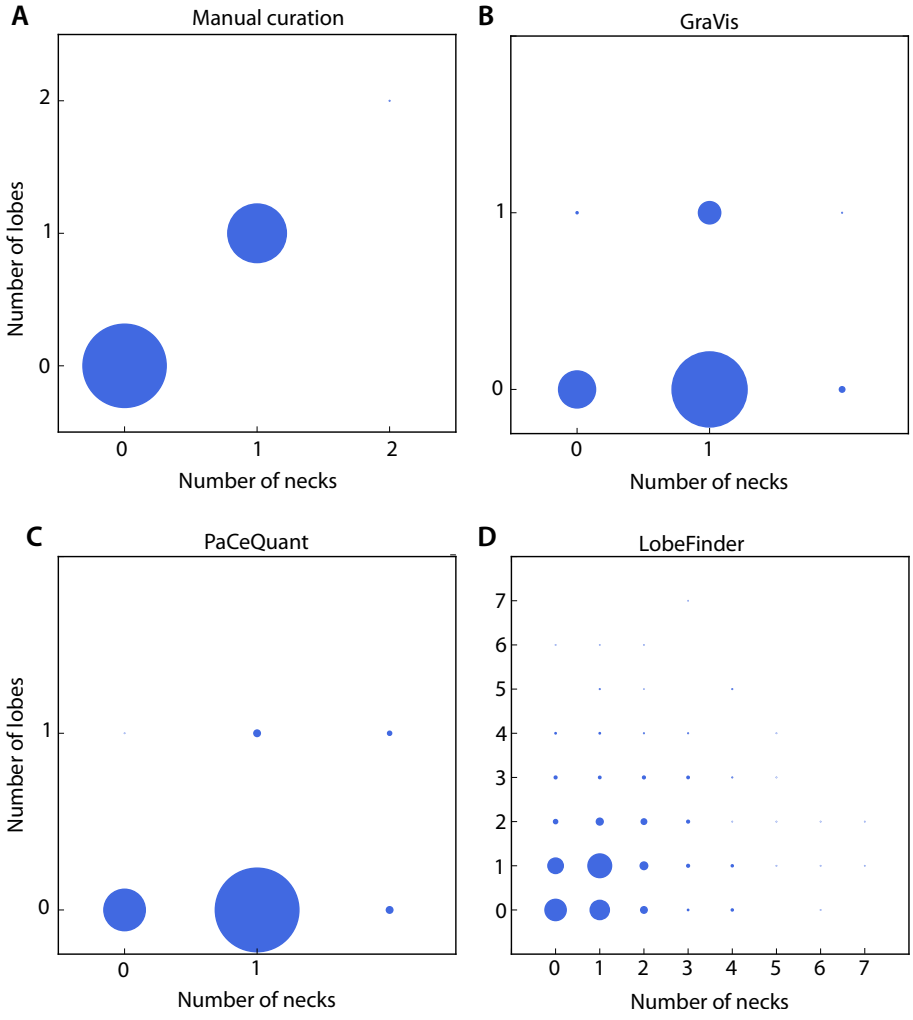

Figure 4.8: Occurrences of lobe/neck pairs for the manual curation and different tools. (**A**) Manual curation, (**B**) GraVis, (**C**) PaCeQuant and (**D**) LobeFinder. The size of the dots corresponds to the number of occurrences of lobe/neck pairs (total number of lobe and neck pairs is 416).

of adjacent cells, neither lobes nor necks were detected, showing that pavement cells at this time points have not yet developed a highly complex shape. In addition, for a large fraction of cells one lobe and neck were detected, whereas for only a few cells two, and in one case three, lobes and necks were identified. Both GraVis and PaCeQuant identified no lobes and one neck for the majority of adjacent cells, showing that there is a discrepancy to the one-to-one correspondence of lobes and necks (Fig. 4.8B-C). For PaCeQuant this behaviour can be explained by the fact that lobe regions, rather than specific positions are employed in the quantification. We note that prior to counting detected lobes and necks, we removed points (in the case of PaCeQuant, regions), which directly corresponded to junctions. As a result, there was often no lobe region left which could be detected by the lobe calling (Fig. 4.9).

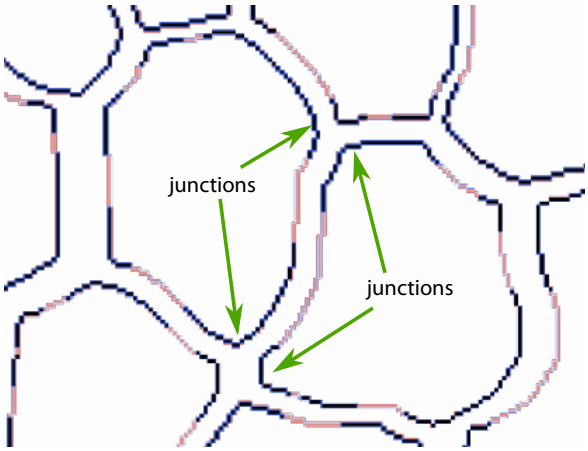

Figure 4.9: Lobe calling for PaCeQuant. Lobes (blue) are defined as regions which are interrupted by neck (pink) regions. Lobe regions including the junction nodes are removed for the lobe calling.

For GraVis, the discrepancy in the number of detected lobes and necks could be due to the mismatched positions of visibility graph nodes for the adjacent cells. In GraVis, the global structure of each visibility graph affects the detection of lobes and necks. Therefore, while a lobe is detected in one cell, it could happen that the corresponding neck in the other cell is not detected because in relation to the global structure of the visibility graph the signal for a neck is not strong enough. To overcome this, identified lobes and necks could be examined after the initial detection and put into correspondence for the selected section of the adjacent cell's contour. Nonetheless, the occurrences of lobe-and-neck pairs along the diagonal were greater for GraVis compared to PaCeQuant. The worst performance was found for LobeFinder (Fig. 4.8D). Here, the occurrences of lobe-and-neck pairs were spread across all possible combinations, although the majority of occurrences seemed to be centred along the diagonal. Moreover, the maximum number of seven detected lobes and necks illustrated quite clearly that LobeFinder tended to overpredict the number of lobes.

Next, we quantified the lobe calling performances for the different tools by calculating the mean square error between the manual curation and the findings from the compared tools. To this end, we represented the occurrences of lobe/neck pairs in a matrix, where each row corresponded to the number of detected lobes and each column to the number of detected necks. To calculate the mean square error, we computed the sum of squares of the difference between the manual curation matrix and the matrix resulting from a respective tool. Finally, we divided the result by the total number of segments. We repeated the mean square error calculation for lobe-and-neck pairs with and without consideration of tri-cellular junctions (Table 4.1). The results showed that GraVis had the lowest mean square error compared to the manual curation, followed by LobeFinder and PaCeQuant. Furthermore, it showed that including the junctions into the analysis, decreased the error

for all tools.

Mean square error	With tri-cellular junctions	Without tri-cellular junctions
GraVis	169.4	186.8
PaCeQuant	232.1	235.7
LobeFinder	208.4	213.3

Table 4.1: Mean square error of lobe calling. For each tool we calculated the mean square error to the manual curation using all detected lobe/neck pairs including detected tri-cellular junctions and without.

Correlation between closeness centralities along segments.
To obtain a better insight into the correspondence of lobes and necks, we next had a detailed look at the correlation of closeness centralities between two cells, obtained from GraVis. This analysis, too, was based on the fact that a lobe in one cell should correspond to a neck in the adjacent cell. This implies that the local maxima of centrality values of one cell (neck) should correspond to the local minima of centrality values of the adjacent cell (lobe), which must result in negative correlation of the closeness centralities of nodes in a given segment.

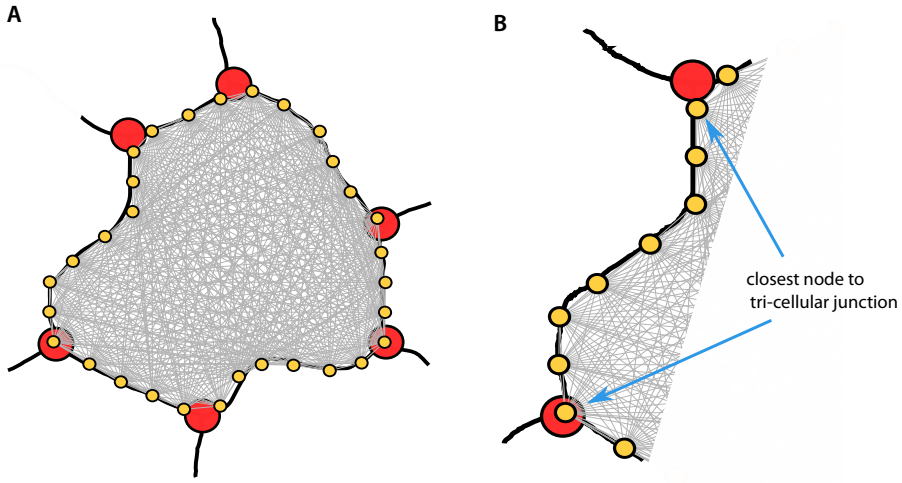

Figure 4.10: Matching of tri-cellular junctions and nodes of visibility graphs. (**A**) Visibility graph nodes (orange) of a pavement cells are superimposed with detected tri-cellular junctions (red). (**B**) For each segment between two adjacent cells, the closest nodes of the visibility graph to the corresponding tri-cellular junctions along this segment are identified by calculating the Euclidean distance between the coordinates of the tri-cellular junctions and the visibility graph nodes.

For a segment shared by two adjacent cells, we first identified the nodes in the corresponding visibility graphs that were closest to the tri-cellular junctions (Fig. 4.10). Therefore,

we calculated the Euclidean distance between the coordinates of the segment-defining tricellular junctions and the nodes of the visibility graphs for each adjacent cell. The visibility graph nodes with the minimal Euclidean distance were then used to define the graph nodes along the segment. We then extracted the corresponding closeness centrality values of the selected nodes and calculated the correlation between the centralities of the adjacent cells using the Pearson and Spearman correlation coefficient. As before, we calculated the correlation between centralities excluding and including the centrality values of the junction nodes. Figure 4.11 showed that the Spearman correlation was more effective in detecting a negative correlation between centralities (Fig. 4.11C-D). Furthermore, the exclusion of closeness centrality values of the junctions greatly improved the correlation. Yet, there were also segments where no correlation was detected at all between the centralities and segments where there was a positive correlation. An explanation for this finding is that for quite a few cells no lobes and necks where detected (manual curation), hence we would expect to find a positive or no correlation here.

In conclusion, we showed that there is a one-to-one correspondence between necks and lobes of two adjacent pavement cells by manual curation. We used the manual curation data to evaluate the accuracy of detected lobes and necks of different lobe detection tools and found that GraVis performed best compared to LobeFinder and PaCeQuant. Indeed, when we evaluated the lobe-neck correspondence using GraVis, we found that there is a negative correlation of closeness centrality values between the visibility graph nodes of two adjacent cells, implying that a local maximum of centrality values in one cell (neck) corresponds with a local minimum in the other cell (lobe). This shows that we can correlate local shape features of pavement cells on a tissue-wide level and can use the lobe calling approach to further improve the detection of lobes and necks in GraVis.

4.3 Materials and Methods

Processing of pavement cell images.
We used images of pavement cells from cotyledons of wild-type Arabidopsis plants at 24-, 48-, 72- and 96-hours post-dissection. A detailed description of the imaging is found in Section 3.3. The images were cleaned, binarized and skeletonized to segment the individual cells in the tissue. We cleaned branches from the skeletonized image to remove cut off cells. All of the remaining cells were assigned a unique label.

Neighbour graph representation.
To create the neighbour graph, we calculated the centre of each labelled cell and placed the nodes at these positions. Two nodes of two cells were connected if they were direct neighbours, sharing a segment of the contour. An additional node was added for the background and edges added if cells were directly facing the background. Isolated cells were identified by detecting nodes with a node of degree zero. Stomata pores were detected by

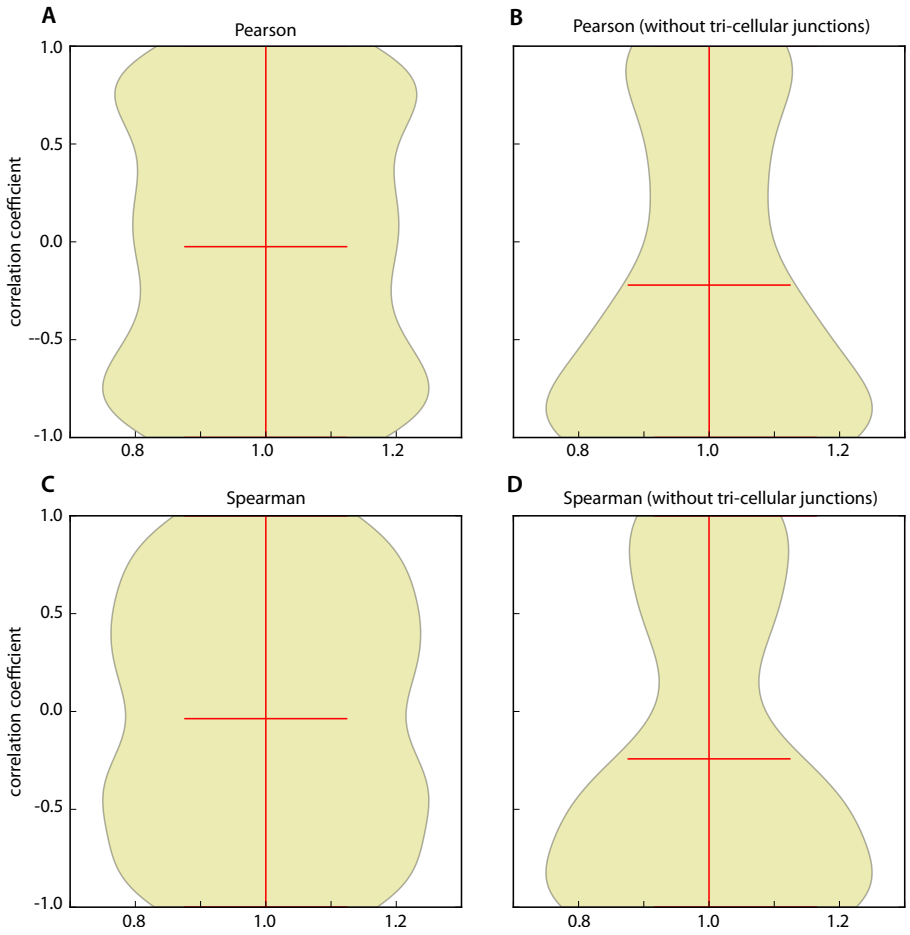

Figure 4.11: Correlation between closeness centralities along a segment. Visibility graph nodes along the segments were determined for two adjacent cells and the closeness centralities extracted. We then calculated the correlation between the closeness centralities along a segment using the (**A, B**) Pearson and (**C, D**) Spearman correlation coefficient. For (**B, D**) we excluded the closeness centralities for the nodes that correspond to tri-cellular junctions. The correlation values over all segments are visualized by violin plots where the mean is indicated as red line.

identifying the nodes with degree two and no edge to the background.

Polygonal graph representation.

We used the skeletonized image of pavement cells to detect all tri-cellular junctions and used additional information from previously removed branches to detect junctions at the tissue border facing the background. Nodes were placed at the junction positions and edges added between nodes, if the selected junctions were connected by a cell contour. For each edge, the identities of the corresponding adjacent cells were saved.

Lobe calling manual curation.

For each segment between two adjacent cells, we selected the corresponding contour pixels delimited by the corresponding junctions. Furthermore, we identified the pixel positions of

the edge between the tri-cellular junctions and calculated the Euclidean distance between all edge pixels and the contour pixels. For each edge pixel we then selected the contour pixel with the minimum distance. Positions where the contour crossed the edge (distance = 0) were used to cut the contour into smaller segments. For each segment we again calculated the Euclidean distance between the corresponding edge and contour pixels to determine the position of the maximum distance. To determine whether the maximum corresponds to a neck or lobe, we checked in which cell it was found.

Lobe calling for the different tools.
We used GraVis to create ROI files for each segmented cell which we then employed to detect lobes using PaCeQuant and LobeFinder. For each segment we determined the number of lobes and necks by counting either automatically (GraVis) or manually (PaCeQuant, LobeFInder) how many lobes were detected for that segment. Junctions were not counted as lobes. For two adjacent cells, we created the coordinate of a lobe-and-neck-pair by pairing lobes of one cell with necks of an adjacent cell and vice versa. The occurrences of all pairs were saved in a matrix, where rows and columns corresponded to number of lobes and necks, respectively. For the evaluation of the lobe calling performance, we calculated the mean square error between the tools and the manual curation.

Correlation of closeness centralities.
For each edge in the polygonal graph we selected the corresponding junctions and determined the closest nodes in the visibility graphs of the adjacent cells. Then, we extracted the closeness centralities for the selected nodes and correlated the values using Pearson and Spearman correlation for every segment. The correlations were computed with and without consideration of the tri-cellular junctions.

Chapter 5

Conclusion

5.1 Summary

In this thesis, we introduced two frameworks for automated and quantitative analyses of different cell processes. In the first part, we aimed to get new insights into how the organization and dynamics of cytoskeletal components are coordinated in plant cells (Chapter 2). Due to its highly dynamic behaviour, the description of the actin cytoskeleton organization has proven very challenging. To this end, we developed a framework which automatically extracts actin bundles from images and represents them as networks at a system, i.e. cell, level [42].

We demonstrated the power of our proposed approach to study the actin cytoskeleton by investigating transport-related network properties, and showed that the actin cytoskeleton is indeed tuned towards efficient transport in Arabidopsis hypocotyl cells. Furthermore, we applied our framework to different biological systems to highlight that the framework can be used to compare the actin cytoskeleton organization between different mutants, treatments and time points. For example, we investigated the actin cytoskeleton organization in cotton fibers and found that they have a unique growth mode which has similarities to both diffuse and tip growing cells [259]. In addition, we examined the influence of the actin cytoskeleton in gravitropism signalling and found that mutants with a defect in gravitropism sensing had an altered cytoskeleton organisation, e.g. by quantifying and comparing the number of connected components, the average shortest path length, the edge capacity and diameter [222]. Finally, we proposed a GUI for easy usage of our framework [167].

The cytoskeleton is involved in the development of cell shapes, although the underlying mechanism is still not fully understood. A first step towards mechanism identification is the development of frameworks which enable an accurate description of cell shape. These frameworks build the foundation for the analysis of how specific cytoskeletal components are coordinated during cell morphogenesis. Thus, in the second part of the thesis, we

developed a network-based framework, termed GraVis, for the quantitative analysis and description of shapes using the concept of visibility graphs (Chapter 3). We demonstrated that our framework facilitates accurate description and comparison of shapes from different domains. Furthermore, we showed that our framework can quantify global, e.g. complexity, but also local shape features, such as lobes and necks in pavement cells of the upper leaf epidermis. We demonstrated that GraVis outperforms all state-of-the-art contenders for lobe detection and also facilitates accurate classification of plants into respective phylogenetic clades based on their pavement cell shapes.

In the last part, we proposed different network representations to describe the shape of pavement cells on a tissue-level (Chapter 4). We utilized information of neighbouring cells in the tissue to set up a pipeline which enables the automated detection of stomata in the leaf epidermis. In addition, we introduced a polygon-based description of pavement cells which allows for the analysis of pavement cell shape over time. Moreover, we used the polygonal representation to test and validate the accuracy of different lobe detection approaches by correlating detected lobes and necks of adjacent cells. Once again, we could demonstrate that GraVis outperforms other contending approaches, although shortcomings, which will be addressed in future research were also outlined.

5.2 Advantages and Contributions

Our proposed frameworks represent important steps towards quantifying cellular processes and identifying the underlying molecular mechanisms in plant cells in an automated manner. We demonstrated that the combination of image data and graph-theoretic analysis is powerful in capturing various aspects of the underlying systems [42, 259, 222]. There are many different ways to define the nodes and edges in a graph. However, the greatest advantage of a graph-based analysis is the fact that different attributes may be assigned to graph nodes and edges, thus enabling the quantification and comparison of diverse graph properties which can be employed in not only comparative, but also predictive analysis. For instance, graph nodes may be assigned specific coordinates, while edges may be assigned directions or weights.

With our first framework, we showed that we can quantitatively assess the transport efficiency of the actin cytoskeleton on a system level (Chapter 2). Moreover, we demonstrated that the extracted graph properties enable the comparison of the actin cytoskeleton organization of different treatments, mutants or over time, thus paving the way for efficient genetic screenings. Furthermore, the extracted networks can be employed in combination with other quantitative analysis, such as tracking data from Golgi which move along the actin filaments [42]. The analysis of such trafficking data enables the prediction of Golgi speed, directionality or potential exchange sites of Golgi-related material.

With GraVis we introduced a framework which facilitates: (1) quantification of global and local shape features, (2) shape comparison and (3) the characterization of cell shape complexity based on underlying biological imaging data (Chapter 3). While other frameworks often focus on only one aspect of the aforementioned analysis steps, we combined all of these steps using a graph-based approach. To this end, we extended the concept of the visibility graph which was previously used to analyse time-series data [130]. Here, point locations in a timeline or in space are represented by a node, whereas edges represent a visible connection between nodes. For our approach, we applied this concept by placing nodes along an object's contour to finally characterize the shape. In doing so, we are able to calculate different local and global network properties which allow for the extraction of relevant shape characteristics, shape comparison or can be used as features in machine learning approaches.

In the last part of the thesis, we extended the GraVis framework by introducing different graph representations to analyse shape of pavement cells not only on a single cell basis, but on a tissue-level (Chapter 4). With the creation of the neighbour graph we depicted the relationship between adjacent cells. Together with the calculation of the relative graph completeness of the merged visibility graphs of two adjacent cells, we allowed for the automated detection of stomata cells. In addition, we created a polygonal graph to investigate the correspondence of lobes and necks along a segment that is shared by adjacent cells.

The usage of the proposed graph representations further motivated the investigation of different network properties, and establishing their correspondence to relevant biological properties. For instance, in our cytoskeleton extracting framework the average shortest path length describes how fast and efficient cargo can be transported along actin filaments and bundles, while the algebraic connectivity facilitates assessment of how robust the actin networks are against disruptions. Moreover, the edge capacity gives insights into the architecture of the actin cytoskeleton by describing the filament thickness, thus indicating whether actin filaments or filament bundles preferably occur.

Lastly, we ensured that our proposed frameworks are usable for a large community by implementing graphical user interfaces [167]. With this, we allow for easy usage of the proposed algorithms and the automatization of image analysis processing. In addition, our proposed frameworks for filament extraction and shape description can be readily applied to various problems from other domains, such as for the quantitative description of retinal blood vessels, slime mould veins or street topology, but also for the comparison and classification of shapes from different biological organisms, e.g. insect wing, leave, seed or fish shapes.

5.3 Limitations of the Network-Based Extraction of Actin Filaments

In our extracted networks, filament crossings or end points are defined as nodes, while actin filaments and bundles are represented as edges. For straight, thick actin bundles, the representation of edges properly describes the underlying bundle orientation. Albeit, for fine actin filaments the representation might lead to some drawbacks, as the filaments can be considerably curved. Therefore, an extension of the framework which enables the accurate description of curved filaments would be a huge improvement of the framework. To this end, one solution could be the automated detection of curved filaments and subsequently splitting of the corresponding edge in the extracted network into smaller segments, such that the curve of the filament is described by successively connected edges.

In addition, our framework is limited to bi-directional transport of organelles along the actin cytoskeleton due to undirected edges in the network. To allow for the analysis of unidirectional transport, such as the movement of motor proteins, the edge directionality has to be incorporated into the framework. The tracking of the directionality could be achieved by using imaging techniques which allow the tracking of the barbed and pointed ends of the filaments; an approach that was already published for microtubules [211]. Another way to solve this problem could be done by tagging myosin motor proteins with a red fluorescent protein, as myosin travels along the cytoskeleton, thus providing information about the directionality. Finally, a third approach would be akin to the classical orientation of an undirected graph such that a particular property is optimized. The latter can then be validated by the findings from the tracking of filaments over time.

Furthermore, there are some limitations to our proposed network randomization approach. For the randomization, we shuffle the node positions while keeping the edge length distribution the same. After node shuffling, the edges are added back to the graph such that their edge length is preserved. However, if the original graph has a large number of very short edges, there are sometimes no proper solutions for the placement of edges preserving their edge length. To overcome this problem, a better randomization algorithm is needed that ensures that there is always an edge of a certain length. An approach that could be used for this problem is the Delaunay triangulation [68]. Here, a set of points (nodes in the network) is connected such that they create triangles, whereby no triangle is inside or crosses another triangle. To create the randomized graph, one could then remove edges from the Delaunay graph until the edge length distribution of the original graph is matched.

For the analysis of the actin cytoskeleton organization we focused on transport-related network properties, such as the average shortest path length, connected components or the assortativity. Nonetheless, there might be other relevant network properties which could be helpful in understanding the underlying mechanism of the actin cytoskeleton.

Future efforts should be directed towards establishing connections between the physiology of a cell and how certain aspect of it can be described on the network-level.

Recent advances in super-resolution microscopy allowed for an increased spatio-temporal resolution of the highly dynamic actin filaments [139]. Yet, actin filaments rearrange in a matter of microseconds, while the current set-up only allows for snapshots on scale of seconds, minutes or hours. With further improvement in microscopy, we will therefore be able to study actin organization and dynamics in more detail. The improvement of fluorophores used for actin imaging can also be a valuable help to increase the detection of very fine actin filaments, as they often are lost during image pre-processing due to their weak intensity signals. Thus, advances in the field of microscopy and imaging will help bridging the gap between spatial and temporal scales, thus enabling a more accurate description of the actin cytoskeleton organization.

Cellular processes act on different temporal and spatial scales. For instance, our proposed framework sheds light onto cytoskeleton organization on a microsecond scale and quite restricted spatial scale of micrometres. Nevertheless, there is a need to connect these small-scale processes with processes on a larger scale. For example, plant growth and organ morphology act on scales of minutes and hours and are integrated over a larger spatial scale, such as cells, tissues or organs. The connection of these processes could be achieved by using machine learning approaches by combining imaging data on a cellular level, such as our proposed framework, and imaging of whole plants or organs to detect underlying patterns.

5.4 Limitations of the Network-Based Description of Shapes

For an accurate shape description, it is important to identify network properties which can be directly related to key shape characteristics. We used the closeness centrality to identify local shape features of pavement cells. Although we tested other centrality measures, we cannot exclude that there is another centrality measure that provides a better means for the detection of lobes and necks. Furthermore, we detect lobes and necks by identifying local minima and maxima of the closeness centrality along the contour, respectively. The detection of these local extrema could lead to errors due to variations in the closeness centrality values. To further improve the detection, we could introduce a threshold which defines whether the difference between the centrality value of the detected local extrema and the centrality values of the neighbouring nodes is significant. Yet another way could be to allow that a node is only connected to x nodes to the left and right from it.

Another way to improve the detection of lobes and necks is to combine the lobe detection with the shape description on tissue-level. For the creation of the polygonal graph, we identified the positions of tri-cellular junctions and defined them as the nodes of the

graph. However, we could also integrate the positional information of the junctions into the detection of lobes and necks. While we are already able to identify whether identified lobes are true lobes or tri-cellular junctions, we could also add tri-cellular junctions which were not detected as lobes.

The placement of nodes is currently approximated by calculating the optimal distance between nodes based on the image resolution and contour length. Therefore, nodes which are not exactly positioned in lobes, necks or tri-cellular junctions might be overlooked and not detected as local extrema. To determine the positions of tri-cellular junctions, we use the skeleton image of pavement cells. The positions of tri-cellular junctions are accurate as they are extracted directly from the underlying pavement cell contours. Using this information, we could place nodes along the contour while fixing the positions of nodes for tri-cellular junctions.

5.5 Outlook

The actin cytoskeleton framework facilitates the analysis of different cell phenotypes and thus is applicable in genetic or chemical screens which could be used to understand the genetic mechanisms of the cytoskeleton organization. While we focused on the description of 2D actin networks here, we could also extend the analysis to 3D actin networks. However, the quality of 3D imaging data, especially of large cells, is dependent on future advances of imaging techniques as actin filament have a highly dynamic behaviour. Moreover, it might be interesting to assess the segmentation quality of our proposed algorithm with other existing approaches for the extraction of filamentous structures using images as shown in Figure 2.10.
Furthermore, the extraction of actin filaments could be applied to the analysis of actin dynamics over time. This would require the spatial-temporal tracking of actin filaments to study changes in the actin network structure. Whilst some methods were proposed for the tracking of actin filament over time [137, 150] and the decomposition of actin networks into single filaments [41], no suitable framework for in-depth analysis of actin filament dynamics is available yet.

For GraVis there are several applications which include accurate quantification of key shape features of different genotypes. In addition, there should be a focus on investigating how properties of visibility graphs are associated with key cellular processes and structures. As we already demonstrated with the tissue-level shape description, our framework is also applicable to track temporal changes of cell shapes. Defining these shape changes across development could be used for genetic screens allowing to understand the genetic principles of morphogenesis. Moreover, to get further insights into the mechanism of shape formation on different scales, the shape of cells could be interrelated to shape of plant organs, such as leaves.

We demonstrated that our proposed frameworks are a first step to understand the organization of cytoskeletal components and the emergence of cell shapes. To get further ideas about how the cytoskeleton is involved in cell shape morphogenesis, both of these frameworks could be combined. GraVis detects the exact positions of lobe and necks in pavement cells. At the same time, we can extract the positional information and organization of the actin cytoskeleton. Through correlation of the positional information of the actin structures and precise lobe and neck coordinates, we could assess the involvment of actin structures in local cell shape morphology of lobes in pavement cells, as was proposed in many studies [91, 85, 116]. Moreover, we could extend this approach by including information of microtubules, thus obtaining a detailed view of the contributions of the different cytoskeletal components in shape morphogenesis.

Apart from combining our proposed frameworks, it should also be taken into consideration to combine the frameworks with quantitative genetics methods. The accurate and precise quantification of actin organization or cell shape is a fundamental principle for genome-wide association studies (GWAS) or quantitative trait loci (QTL) mapping. For instance, GWAS is an approach used to associate specific genetic variations with particular traits, typically between single-nucleotide polymorphisms (SNPs). For this, many different genomes are scanned to determine genetic markers. Here, we could use the quantitative information of actin organization or pavement cell shape of different mutants, such as shape defect mutants, or different treatments, such as with actin depolymerizing drugs to determine genetic markers. We could further use the quantitative information for QTL mapping, which is a statistical method to combine phenotypic and genotypic data to explain genetic variation in complex traits. Here, the precise location, interaction and number of specific regions of chromosomes are linked to certain phenotypes.

Bibliography

[1] Boudaoud A., A. Burian, D. Borowska-Wykret, M. Uyttewaal, R. Wrzalik, D. Kwiatkowska, and O. Hamant. FibrilTool, an ImageJ plug-in to quantify fibrillar structures in raw microscopy images. *Nature Protocols*, 9(2):457–463, 2014.

[2] K. Abley, P. B. De Reuille, D. Strutt, A. Bangham, P. Prusinkiewicz, A. F. M. Maree, V. A. Grieneisen, and E. Coen. An intracellular partitioning-based framework for tissue cell polarity in plants and animals. *Development*, 140(10):2061–2074, 2013.

[3] M. D. Abramoff, M. K. Garvin, and M. Sonka. Retinal imaging and image analysis. *IEEE Reviews in Biomedical Engineering*, 3:169–208, 2010.

[4] A. Akhmanova and M. O. Steinmetz. Control of microtubule organization and dynamics: two ends in the limelight. *Nature Reviews Molecular Cell Biology*, 16:711–726, 2015.

[5] M. Akkerman, E. J. R. Overdijk, J. H. N. Schel, A. M. C. Emons, and T. Ketelaar. Golgi body motility in the plant cell cortex correlates with actin cytoskeleton organization. *Plant and Cell Physiology*, 52(10):1844–1855, 2011.

[6] M. Alioscha-Perez, C. Benadiba, K. Goossens, S. Kasas, G. Dietler, R. Willaert, and H. Sahli. A robust actin filaments image analysis framework. *PLoS Computational Biology*, 12(8):e1005063, 2016.

[7] B. Altartouri, A. J. Bidhendi, T. Tani, J. Suzuki, C. Conrad, Y. Chebli, N. Liu, C. Karunakaran, G. Scarelli, and A. Geitmann. Pectin chemistry and cellulose crystallinity govern pavement cell morphogenesis in a multi-step mechanism. *Plant Physiology*, 2019.

[8] A. Altinok, M. E. Sargin, B. S. Manjunath, and K. Rose. Extracting dynamic microtubule features from image sequences. In CA Pacific Grove, editor, *2007 Conference Record of the Forty-First Asilomar Conference on Signals, Systems and Computers*, pages 1308–1312, 2007.

[9] J. C. Ambrose, T. Shoji, A. M. Kotzer, J. A. Pighin, and G. O. Wasteneys. The Arabidopsis CLASP gene encodes a microtubule-associated protein involved in cell expansion and division. *The Plant Cell*, 19:2763–2775, 2007.

[10] C. T. Anderson, A. Carroll, L. Akhmetova, and C. Somerville. Real-time imaging of cellulose reorientation during cell wall expansion in Arabidopsis roots. *Plant Physiology*, 152(2):787–796, 2009.

[11] W. J. Armour, D. A. Barton, A. M. K. Law, and R. L. Overall. Differential growth in periclinal and anticlinal walls during lobe formation in Arabidopsis cotyledon pavement cells. *The Plant Cell*, 27:2484–2500, 2015.

[12] V. Ayzenberg and S. F. Lourenco. Skeletal descriptions of shape provide unique perceptual information for object recognition. *Scientific Reports*, 9(1), 2019.

[13] F. Baluska, J. Jasik, H. G. Edelmann, T. Salajova, and D. Volkmann. Latrunculin B-induced plant dwarfism: plant cell elongation is F-actin-dependent. *Developmental Biology*, 231(1):113–124, 2001.

[14] F. Baluska, S. Vitha, P. W. Barlow, and D. Volkmann. Rearrangement of F-actin arrays in growing cells of intact maize root apex tissues: a major development switch occurs in the postmitotic transition region. *European Journal of Cell Biology*, 72:113–121, 1997.

[15] J. R. Banavar, T. J. Cooke, A. Rinaldo, and A. Maritan. Form, function, and evolution of living organisms. *PNAS*, 111(9):3332–3337, 2014.

[16] P. Bankhead, C. N. Scholfield, J. G. McGeown, and T. M. Curtis. Fast retinal vessel detection and measurement using wavelets and edge location refinement. *PLOS ONE*, 7(3):e32435, 2012.

[17] C. S. Bascom, P. K. Hepler, and M. Bezanilla. Interplay between ions, the cytoskeleton, and cell wall properties during tip growth. *Plant Physiology*, 176(1):28–40, 2017.

[18] T. I. Baskin and N. J. Bivens. Stimulation of radial expansion in *Arabidopsis* roots by inhibitors of actomyosin and vesicle secretion but not by various inhibitors of metabolism. *Planta*, 197:514–521, 1995.

[19] T. I. Baskin, J. E. Wilson, A. Cork, and R. E. Williamson. Morphology and microtubule organization in Arabidopsis roots exposed to oryzalin or taxol. *Plant Cell Physiology*, 35(6):935–942, 1994.

[20] S. Basu, C. Liu, and G. K. Rohde. localizing and extracting filament distributions from microscopy images. *Journal of Microscopy*, 258(1):13–23, 2015.

[21] K. Baumann. Auxin signalling: ABP1 finds its pair. *Nature Reviews Molecular Cell Biology*, 15:221–221, 2014.

[22] W. Baumgarten and M. J. B. Hauser. Computational algorithms for extraction and analysis of two-dimensional transportation networks. *Journal of Computational Interdisciplinary Sciences*, 3(1–2):107–116, 2012.

[23] S. J. Belongie, J. Malik, and J. Puzicha. Shape context: a new descriptor for shape matching and object recognition. *NIPS*, pages 831–837, 2000.

[24] S. A. Belteton, M. G. Sawchuk, B. S. Donohoe, E. Scarpella, and D. B. Szymanski. Reassessing the roles of PIN proteins and anticlinal microtubules during pavement cell morphogenesis. *Plant Physiology*, 176:432–449, 2018.

[25] T. N. Bibikova, E. Blancaflor, and S. Gilroy. Microtubules regulate tip growth and orientation in root hairs of *Arabidopsis thaliana*. *The Plant Journal*, 17:657–665, 1999.

[26] A. J. Bidhendi, B. Altartouri, F. P. Gosselin, and A. Geitmann. Mechanical stress initiates and sustains the morphogenesis of wavy leaf epidermis cells. *Cell Reports*, 28:1237–1250, 2019.

[27] A. J. Bidhendi and A. Geitmann. Relating the mechanics of the primary plant cell wall to morphogenesis. *Journal of Experimental Botany*, 67(2):449–461, 2016.

[28] A. J. Bidhendi and A. Geitmann. Geometrical details matter for mechanical modeling of cell morphogenesis. *Developmental Cell*, 50:117–125, 2019.

[29] E. Biot, M. Cortizo, J. Burguet, A. Kiss, M. Oughou, A. Maugarny-Cales, B. Goncalves, B. Adroher, P. Andrey, A. Boudaoud, and P. Laufs. Multiscale quantification of morphodynamics: MorphoLeaf software for 2D shape analysis. *Development*, 143:3417–3428, 2016.

[30] S. R. Bisgrove, W. E. Hable, and D. L. Kropf. +TIPs and microtubule regulation. The beginning of the plus end in plants. *Plant Physiology*, 136:3855–3863, 2004.

[31] E. B. Blancaflor. Cortical actin filaments potentially interact with cortical microtubules in regulating polarity of cell expansion in primary roots of maize (*Zea mays* L.). *Journal of Plant Growth Regulation*, 19:406–414, 2000.

[32] E. B. Blancaflor and P. H. Masson. Plant gravitropism. unraveling the ups and downs of a complex process. *Plant Physiology*, 133:1677–1690, 2003.

[33] L. Blanchoin, R. Boujemaa-Paterski, C. Sykes, and J. Plastino. Actin dynamics, architecture, and mechanics in cell motility. *Physiological Reviews*, 94(1):235–263, 2014.

[34] L. Blanchoin and C. J. Staiger. Plant formins: diverse isoforms and unique moelcular mechanism. *Biochimica et Biophysica Acta, Molecular Cell Research*, 1803:201–206, 2010.

[35] WoRMS Editorial Board. World Register of Marine Species. http://www.marinespecies.org at VLIZ (accessed on 01 July 2019).

[36] P. Bonacich. Pwer and centrality: a family of measures. *AJS: American Journal of Sociology*, 92(5):1170–1182, 1987.

[37] E. T. Bowman, K. Soga, and T. W. Drummond. *Particle shape characterization using Fourier Analysis CUED/D-Soils*. 2000.

[38] U. Brandes, D. Delling, M. Gaertler, R. Gorke, M. Hoefer, Z. Nikoloski, and D. Wagner. On modularity clustering. *IEEE Transactions on Knowledge and Data Engineering*, 20(2):172–188, 2008.

[39] D. Breuer, A. Ivakov, A. Sampathkumar, F. Holland, S. Persson, and Z. Nikoloski. Qunatitative analyses of the plant cytoskeleton reveal underlying organizational principles. *Journal of the Royal Society, Interface*, 11:20140362, 2014.

[40] D. Breuer and Z. Nikoloski. img2net: automated network-based analysis of imaged phenotypes. *Bioinformatics*, 30(22):3291–3292, 2014.

[41] D. Breuer and Z. Nikoloski. DeFiNe: an optimisation-based method for robust disentangling of filamentous networks. *Scientific Reports*, 5:18267, 2015.

[42] D. Breuer, J. Nowak, A. Ivakov, M. Somssich, S. Persson, and Z. Nikoloski. System-wide organization of actin cytoskeleton determines organelle transport in hypocotyl plant cells. *PNAS*, 114(28):E5741–5749, 2017.

[43] G. J. Brouhard and L. M. Rice. The contribution of alpha beta-tubulin curvature to microtubule dynamics. *Journal of Cell Biology*, 207(3):323–334, 2014.

[44] M. R. Bubb, A. M. Senderowicz, E. A. Sausville, K. L. Duncan, and E. D. Korn. Jasplakinolide, a cytotoxic natural product, induces actin polymerization and competitively inhibits the binding of phalloidin to F-actin. *Journal of Biological Chemistry*, 269:14869–14871, 1994.

[45] H. Buschmann, P. Green, A. Sambade, J. H. Doonan, and C. W. Lloyd. Cytoskeletal dynamics in interphase, mitosis and cytokinesis analysed through *Agrobacterium*-mediated transient transformation of tobacco BY-2 cells. *New Phytologist*, 190:258–267, 2011.

[46] A. E. Carpenter, T. R. Jones, M. R. Lamprecht, C. Clarke, I. H. Kang, O. Friman, D. A. Guertin, J. H. Chang, R. A. Lindquist, J. Moffat, P. Golland, and D. M. Sabatini. CellProfiler: image analysis software for identifying and quantifying cell phenotypes. *Genome Biology*, 7:R100, 2006.

[47] A. Carpita and M. McCann. *Biochemistry and Molecular Biology of Plants*, chapter The plant cell wall, pages 52–108. American Society of Plant Physiologists, 2000.

[48] K. Celler, M. Fujita, E. Kawamura, C. Ambrose, K. Herburger, A. Holzinger, and G. O. Wasteneys. *Cytoskeleton Methods and Protocols. Methods in Molecular Biology*, chapter Microtubules in plant cells: strategies and methods for immunofluorescence, transmission electron microscopy and live cell imaging, pages 155–184. Humana Press, New York, 2016.

[49] J. Chan, G. Calder, S. Fox, and C. Lloyd. Cortical microtubule arrays undergo rotary movements in *Arabidopsis* hypocotyl epidermal cells. *Nature Cell Biology*, 9(2):171–U157, 2007.

[50] J. Chan and E. Coen. Interaction between autonomous and microtubule guidance systems controls cellulose synthase trajectories. *Current Biology*, 30(5):941–947, 2020.

[51] C. S. Chen, M. Mrksich, S. Huang, G. M. Whitesides, and D. E. Ingber. Geometric control of cell life and death. *Science*, 276(5317):1425–1428, 1997.

[52] J. Chen and N. Wang. Tissue cell differentiation and multicellular evolution via cytoskeletal stiffening in mechanically stressed microenvironments. *Acta Mechanica Sinica*, 35:270–274, 2019.

[53] F. R. Chung. Spectral graph theory. In American Mathematical Society, editor, *Regional Conference Series in Mathematics*, volume 92, 1997.

[54] G. M. Cooper. *The cell: a molecular approach. 2nd edition.* Sunderland (MA): Sinauer Associates, 2000.

[55] R. L. Cosgriff. Identification of shapes. *Ohio State University Research Foundation Columbus*, pages 820–11, 1960.

[56] D. Cosgrove. Biophysical control of plant cell growth. *Annual Review of Plant Physiology*, 37:377–405, 1986.

[57] D. J. Cosgrove. Wall extensibility: its nature, measurement and relationship to plant cell growth. *New Phytologist*, 124(1):1–23, 1993.

[58] D. J. Cosgrove. Assembly and enlargement of the primary cell wall in plants. *Annual Review of Cell and Developmental Biology*, 13:171–201, 1997.

[59] D. J. Cosgrove and C. T. Anderson. Plant cellgrowth: do pectins drive lobe formation in *Arabidopsis* pavement cells? *Current Biology*, 30(11):R660–R662, 2020.

[60] M. Coue, S. L. Brenner, I. Spector, and E. D. Korn. Inhibition of actin polymerization by latrunculin A. *FEBS Letters*, 213:316–318, 1987.

[61] B. Crawford, R. Gera, J. House, T. Knuth, and R. Miller. Graph structure similarity using spectral graph theory. In *Studies in Computational Intelligence*, pages 209–221. Springer International Publishing, nov 2016.

[62] E. F. Crowell, V. Bischoff, T. Desprez, A. Rolland, Y. D. Stierhof, K. Schumacher, M. Gonneau, H. Hoefte, and S. Vernhettes. Pausing of Golgi bodies on microtubules regulates secretion of cellulose synthase complexes in *Arabidopsis*. *The Plant Cell*, 21:1141–1154, 2009.

[63] S. R. Cutler, D. W. Ehrhardt, J. S. Griffitts, and C. R. Somerville. Random GFP::cDNA fusions enable visualization of subcellular structures in cells of Arabidopsis at a high frequency. *PNAS*, 97:3718–3723, 2000.

[64] A. Das, A. Bucksch, C. A. Price, and J. S. Weitz. ClearedLeavesDB: an online database of cleared plant leaf images. *Plant Methods*, 10:8, 2014.

[65] S. Datta and S. Datta. Methods for evaluating clustering algorithms for gene expression data using a reference set of functional classes. *BMC Bioinformatics*, 7:397, 2006.

[66] M. J. Deeks, M. Fendrych, A. Smertenko, K. S. Bell, K. Oparka, F. Cvrckova, V. Zarsky, and P. J. Hussey. The plant formin AtFH4 interacts with both actin and microtubules, and contains a newly identified microtubule-binding domain. *Journal of Cell Science*, 123:1209–1215, 2010.

[67] M. J. Deeks and P. J. Hussey. Arp2/3 and 'the shape of things to come'. *Current Opinion in Plant Biology*, 6:561–567, 2003.

[68] B. Delaunay. Sur la sphere vide. a la memoire de georges voronoi. *Bulletin de l'Academie des Sciences de l'URSS. Classe des sciences mathematiques et na*, 6:793–800, 1934.

[69] J. Derksen, F. H. A. Wilms, and E. S. Pierson. The plant cytoskeleton: its significance in plant development. *Acta Botanica Neederlandica*, 39(1):1–18, 1990.

[70] A. Desai and T. J. Mitchison. Microtubule polymerization dynamics. *Annual Review of Cell and Developmental Biology*, 13:83–117, 1997.

[71] C. H. Dong, G. X. Xia, T. Hong, S. Ramachandran, B. Kost, and N. H. Chua. ADF proteins are involved in the control of flowering and regulate F-actin organization, cell expansion, and organ growth in *Arabidopsis*. *The Plant Cell*, 13:1333–1346, 2001.

[72] C. G. Dos Remedios, D. Chhabra, M. Kekic, I. V. Dedova, and M. Tsubakihara. Actin binding proteins: regulation of cytoskeletal microfilaments. *Physiological Reviews*, 83:433–473, 2003.

[73] J. X. Du, X. F. Wang, and G. J. Zhang. Leaf shape-based plant species recognition. *Applied Mathematics and Computation*, 185:883–893, 2007.

[74] S. R. Dubois and F. H. Glanz. An autoregressive model approach to two-dimensional shape classification. *IEEE Transactions on Pattern Analysis and Machine Intelligence*, PAMI-8(1):55–66, 1986.

[75] J. Elsner, M. Lipowczan, and D. Kwiatkowska. Differential growth of pavement cells of *Arabidopsis thaliana* leaf epidermis as revealed by microbead labeling. *American Journal of Botany*, 105(2):1–9, 2018.

[76] A. Endler and S. Persson. Cellulose synthases and synthesis in *Arabidopsis*. *Molecular Plant*, 4(2):199–211, 2011.

[77] R. C. Eng and A. Sampathkumar. Getting into shape: the mechanics behind plant morphogenesis. *Current Opinion in Plant Biology*, 46:25–31, 2018.

[78] K. L. Farquharson. Tracking pavement cells through space and time: microtubules define positions of lobe formation. *The Plant Cell*, 27:2317, 2015.

[79] C. Faulkner, J. Zhou, A. Evrard, G. Bourdais, D. MacLean, H. Haeweker, P. Eckes, and S. Robatzek. An automated quantitative image analysis tool for the identification of microtubule patterns in plants. *Traffic*, 18:683–693, 2017.

[80] P. Fayant, O. Girlanda, Y. Chebli, C. E. Aubin, I. Villemure, and A. Geitmann. Finite element model of polar growth in pollen tubes. *The Plant Cell*, 22:2579–2593, 2010.

[81] S. Ferson, F. J. Rohlf, and R. K. Koehn. Measuring shape variation of two-dimensional outlines. *Systematic Biology*, 34(1):59–68, 1985.

[82] F. Fotopoulou and E. Z. Psarakis. A visibility graph based shape decomposition technique. *Proceedings of the 9th International Conference on Computer Vision Theory and Applications*, VISAPP-2014:515–522, 2014.

[83] J. B. J. Fourier. Theorie analytique de la chaleur. *Firmin Didot, pere et fils, Paris*, 1822.

[84] S. Fox, P. Southam, F. Pantin, R. Kennaway, S. Robinson, G. Castorina, Y. E. Sanchez-Corrales, R. Sablowski, J. Chan, V. Grieneisen, A. F. M. Maree, A. Bangham, and E. Coen. Spatiotemporal coordination of cell division and growth during organ morphogenesis. *PLoS Biology*, 16(10):e2005952, 2018.

[85] M. J. Frank and L. G. Smith. A small, novel protein highly conserved in plants and animals promotes the polarized growth and division of maize leaf epidermal cells. *Current Biology*, 12:849–853, 2002.

[86] L. C. Freeman. A set of measures of centrality based on betweenness. *Sociometry*, 40(1):35–41, 1977.

[87] L. C. Freeman. Centrality in social networks: conceptual clarification. *Social Networks*, 1:215–239, 1979.

[88] D. L. Fritzsche. A systematic method for character recognition. *Ohio State University Research Foundation*, pages 1222–4, 1961.

[89] Y. Fu. The cytoskeleton in the pollen tube. *Current Opinion in Plant Biology*, 28:111–119, 2015.

[90] Y. Fu, Y. Gu, Z. Zheng, G. Wasteneys, and Z. Yang. *Arabidopsis* interdigitating cell growth requires two antagonistic pathways with opposing action on cell morphogenesis. *Cell*, 120:687–700, 2005.

[91] Y. Fu, H. Li, Z. Yang, M. A. Jones, J. J. Shen, and C. S. Grierson. The ROP2 GTPase controls the formation of cortical fine F-actin and the early phase of directional cell expansion during *Arabidopsis* organogenesis. *Plant Cell*, 14:777–794, 2002.

[92] Y. Fu, T. Xu, L. Zhu, M. Wen, and Z. Yang. A ROP GTPase signaling pathway controls cortical microtubule ordering and cell expansion in *Arabidopsis*. *Current Biology*, 19:1827–1832, 2009.

[93] Y. Gao, Y. Zhang, D. Zhang, X. Dai, M. Estelle, and Y. Zhao. Auxin binding protein 1 (ABP1) is not required for either auxin signaling or *Arabidopsis* development. *PNAS*, 112(7):2275–2280, 2015.

[94] M. K. Gardner, M. Zanic, and J. Howard. Microtubule catastrophe and rescue. *Current Opinion in Cell Biology*, 25(1):14–22, 2013.

[95] D. A. Geisler, A. Sampathkumar, M. Mutwil, and S. Persson. Laying down the bricks: logistic aspects of cell wall biosynthesis. *Current Opinion in Plant Biology*, 11:647–652, 2008.

[96] A. Geitmann and A. Nebenfuehr. Navigating the plant cell: intracellular transport logistics in the green kingdom. *Molecular Biology of the Cell*, 26:3373–3378, 2015.

[97] A. Geitmann and J. K. E. Ortega. Mechanics and modeling of plant cell growth. *Trends in Plant Science*, 14(9):467–478, 2009.

[98] B. C. Gibbon, D. R. Kovar, and C. J. Staiger. Latrunculin B has different effects on pollen germination and tube growth. *The Plant Cell*, 11:2349–2363, 1999.

[99] T. H. Giddings and L. A. Staehelin. *The Cytoskeletal Basis of Plant Growth and Form*, chapter Microtubule-mediated control of microfibril deposition: a re-examination of the hypothesis, pages 85–99. London: Academic Press, 1991.

[100] K. I. Goh, B. Kahng, and D. Kim. Universal behaviour of load distribution in scale-free networks. *Physical Review Letters*, 87:278701, 2001.

[101] P. B. Green. Mechanism for plant cellular morphogenesis. *Science*, 138(3548):1404–1405, 1962.

[102] K. T. Haas, R. Wightman, E. M. Meyerowitz, and A. Peaucelle. Pectin homogalacturonan nanofilament expansion drives morphogenesis in plant epidermal cells. *Science*, 367(6481):1003–1007, 2020.

[103] C. H. Haigler, L. Betancur, M. R. Stiff, and J. R. Tuttle. Cotton fiber: a powerful single-cell model for cell wall and cellulose research. *Frontiers in Plant Science*, 3:104, 2012.

[104] R. M. Haralick, S. R. Sternberg, and X. Zhuang. Image analysis using mathematical morphology. *IEEE Transactions on Pattern Analysis and Machine Intelligence*, PAMI-9(4):532–550, 1987.

[105] J. L. Henty, S. W. Bledsoe, P. Khurana, R. B. Meagher, and B. Day. *Arabidopsis* actin depolymerizing factor 4 modulates the stochastic dynamic behavior of actin filaments in the cortical array of epidermal cells. *The Plant Cell*, 23:3711–3726, 2011.

[106] J. L. Henty-Ridilla, J. Li, B. Day, and C. J. Staiger. ACTIN DEPOLYMERIZING FACTOR4 regulates actin dynamics during innate immune signaling in *Arabidopsis*. *The Plant Cell*, 26:340–352, 2014.

[107] P. K. Hepler, L. Vidali, and A. Y. Cheung. Polarized cell growth in higher plants. *Annual Review of Cell and Developmental Biology*, 17:159–187, 2001.

[108] T. Higaki, T. Sano, and S. Hasezawa. Actin microfilament dynamics and actin side-binding proteins in plants. *Current Opinion in Plant Biology*, 10:549–552, 2007.

[109] C. Hoffmann, D. Moes, M. Dieterle, K. Neumann, and F. Moreau. Live cell imaging approaches reveal actin cytoskeleton-induced self-association of the actin-bundling protein WLIM1. *Journal of Cell Science*, 127:583–598, 2014.

[110] J. Hoffmann, S. Donoughe, K. Li, M. K. Salcedo, and C. H. Rycroft. A simple developmental model recapitulates complex insect wing venation patterns. *PNAS*, 115(40):9905–9910, 2018.

[111] A. Holzinger and K. Blaas. *Cytoskeleton Methods and Protocols. Methods in Molecular Biology*, volume 1365, chapter Actin-Dynamics in Plant Cells: The Function of Actin-Perturbing Substances: Jasplakinolide, Chondramides, Phalloidin, Cytochalasins, and Latrunculins, pages 243–261. Humana Press, New York, 2016.

[112] J. Hossain and M. A. Armin. Leaf shape identification based plant biometrics. In *13th International conference on computer and information technology (ICCIT)*, pages 458–463, 2010.

[113] G. Hou, D. R. Mohamalawari, and E. B. Blancaflor. Enhanced gravitropismof roots with a disrupted cap actin cytoskeleton. *Plant Physiology*, 131:1360–1373, 2003.

[114] C. W. Hsu and C. J. Lin. A comparison of methods for multiclass support vector machines. *IEEE Transactions on Neural Networks*, 13(2):415–425, 2002.

[115] S. Huang, X. Qu, and R. Zhang. Plant villins: versatile actin regulatory proteins. *Journal of Integrative Plant Biology*, 57:40–49, 2015.

[116] P. J. Hussey, T. Ketelaar, and M. J. Deeks. Control of the actin cytoskeleton in plant cell growth. *Annual Review of Plant Biology*, 57:109–125, 2006.

[117] A. Ivakov and S. Persson. Plant cell shape: modulators and measurements. *Frontiers in Plant Science*, 4:439, 2013.

[118] E. Jacques, J. P. Verbelen, and K. Vissenberg. Review on shape formation in epidermal pavement cells of the *Arabidopsis* leaf. *Functional Plant Biology*, 41:914–921, 2014.

[119] M. Jiang and Q. Li. Automated extraction of microtubules and their plus-ends. In C. O. Breckenridge, editor, *Seventh IEEE Workshops on Applications of Computer Vision (WACV/MOTION'05)*, volume 1, pages 336–341, 2005.

[120] V. Kapoor, W. G. Hirst, C. Hentschel, S. Preibisch, and S. Reber. MTrack: automated detection, tracking, and analysis of dynamic microtubules. *Scientific Reports*, 9:3794, 2019.

[121] E. Kawamura and G. O. Wasteneys. MOR1, the *Arabidopsis thaliana* homologue of Xenopus MAP215, promotes rapid growth and shrinkage, and suppresses the pausing of microtubules in vivo. *Journal of Cell Science*, 121(24):4114–4123, 2008.

[122] H. J. Kim and B. A. Triplett. Cotton fiber growth in planta and in vitro. models for plant cell elongation and cell wal biogenesis. *Plant Physiology*, 127(4):1361–1366, 2001.

[123] J. Kim, J.H. Jung, J.L. Reyes, Y.S. Kim, S.Y. Kim, K.S. Chung, J.A. Kim, M. Lee, Y. Lee, V.N. Kim, N.H. Chua, and C.M. Park. microRNA-directed cleavage of ATHB15 mRNA regulates vascular development in Arabidopsis inflorescence stems. *Plant Journal*, 42(1):84–94, 2005.

[124] V. Kirik, U. Herrmann, C. Parupalli, J. C. Sedbrook, D. W. Ehrhardt, and M. Hülskamp. CLASP localizes in two discrete patterns on cortical microtubules and is required for cell morphogenesis and cell division in *Arabidopsis*. *Journal of Cell Science*, 120:4416–4425, 2007.

[125] J. Klotz and P. Nick. A novel actin-microtubule cross-linkin kinesin, NtKCH, functions in cell expansion and devision. *New Phytologist*, 193:576–589, 2012.

[126] B. Kost and N. H. Chua. The plant cytoskeleton: vacuoles and cell walls make the difference. *Cell*, 108:9–12, 2002.

[127] B. Kost, P. Spielhofer, and N. H. Chua. A GFP-mouse talin fusion protein labels plant actin filaments *in vivo* and visualizes the actin cytoskeleton in growing pollen tubes. *The Plant Journal*, 16(3):393–401, 1998.

[128] M. Krause, R. M. Alles, B. Burgeth, and J. Weickert. Fast retinal vessel analysis. *Journal of Real-Time Image Processing*, 11:413–422, 2016.

[129] J. H. Kroeger, R. Zerzour, and A. Geitmann. Regulator or driving force? the role of turgor pressure in oscillatory plant cell growth. *PLoS ONE*, 6(4):e18549, apr 2011.

[130] L. Lacasa, B. Luque, F. Ballesteros, J. Luque, and J. C. Nuno. From time series to complex networks: the visibility graph. *PNAS*, 105(13):4972–4975, 2008.

[131] A. Landherr, B. Friedl, and J. Heideman. A critical review of centrality measures in social networks. *Business & Information Systems Engineering*, 2(6):371–385, 2010.

[132] J. Le, E. L. Mallery, C. Zhang, S. Brankle, and D. B. Szymanski. *Arabidopsis* BRICK1/HSPC300 is an essential WAVE-complex subunit that selectively stabilizes the Arp2/3 activator SCAR2. *Current Biology*, 16:895–901, 2006.

[133] T. Lecuit and P. F. Lenne. Cell surface mechanics and the control of cell shape, tissue patterns and morphogenesis. *Nature Reviews Molecular Cell Biology*, 8:633–644, 2007.

[134] D. J. Lew. The morphogenesis checkpoint: how yeast cells watch their figures. *Current Opinion in Cell Biology*, 15:648–653, 2003.

[135] H. Li, D. Lin, P. Dhonukshe, S. Nagawa, D. Chen, J. Friml, B. Scheres, H. Guo, and Z. Yang. Phosphorylation switch modulates the interdigitated pattern of PIN1 localization and cell expansion in *Arabidopsis* leaf epidermis. *Cell Research*, 21:970–978, 2011.

[136] H. Li, J. J. Shen, Z. L. Zheng, Y. Lin, and Z. Yang. The Rop GTPase switch controls multiple developmental processes in Arabidopsis. *The Plant Cell*, 126:670–684, 2001.

[137] H. Li, T. Shen, M. B. Smith, I. Fujiwara, D. Vavylonis, and Huang X. Automated actin filament segmentation, tracking and tip elongation measurements based on open active contour models. *2009 IEEE International Symposium on Biomedical Imaging: From Nano to Macro*, pages 1302–1305, 2009.

[138] H. Li, T. Xu, D. Lin, M. Wen, M. Xie, J. Duclercq, A. Bielach, J. Kim, G. V. Reddy, J. Zuo, E. Benkova, J. Friml, H. Guo, and Z. Yang. Cytoskinin signaling regulates pavement cell morphogenesis in *Arabidopsis*. *Cell Research*, 23:290–299, 2013.

[139] J. Li, L. Blanchoin, and C. J. Staiger. Singaling to actin stochastic dynamics. *Annual Review of Plant Biology*, 66:415–440, 2015.

[140] J. Li, J. L. Henty-Ridilla, S. Huang, X. Wang, L. Blanchoin, and C. J. Staiger. Capping protein modulates the dynamic behavior of actin filaments in response to phosphatidic acin in *Arabidopsis*. *The Plant Cell*, 24:3742–3754, 2012.

[141] J. Li, B. H. Staiger, J. L. Henty-Ridilla, M. Abu-Abied, and E. Sadot. The availability of filament ends modulates actin stochastic dynamics in live plant cells. *Molecular Biology of the Cell*, 25:1263–1275, 2014.

[142] Y. Li, Y. Shen, C. Cai, C. Zhong, L. Zhu, M. Yuan, and H. Ren. The type II Arabidopsis formin14 interacts with microtubules and microfilaments to regulate cell division. *Plant Cell*, 22(8):2710–2726, 2010.

[143] J. J. Lindeboom, M. Nakamura, A. Hibbel, K. Shundyak, R. Gutierrez, T. Ketelaar, A. M. C. Emons, B. M. Mulder, V. Kirik, and D. W. Ehrhardt. A mechanism for reorientation of cortical microtubule arrays driven by microtubule severing. *Science*, 342:1245533, 2013.

[144] T. Lozano-Perez and M. A. Wesley. An algorithm for planning collision-free paths among polyhedral obstacles. *Communications of the ACM*, 22(10):560–570, 1979.

[145] M. Majda, P. Grones, I. M. Sintorn, T. Vain, P. Milani, P. Krupinski, B. Zagorska-Marek, C. Viotti, H. Joensson, E. J. Mellerowicz, O. Hamant, and S. Robert. Mechanochemical polarization of contiguous cell walls shapes plant pavement cells. *Developmental Cell*, 43:290–304, 2017.

[146] R. Malho. Expanding tip growth theory. *Trends in Plant Science*, 3:40–42, 1998.

[147] R. Malinkowski. Understanding of leaf development: the science of complexity. *Plants (Basel)*, 2:396–415, 2013.

[148] S. Mansoor and A. H. Paterson. Genomes for jeans: cotton genomics for engineering superior fiber. *Trends in Biotechnology*, 30(10):521–527, 2012.

[149] M. Marchiori and V. Latora. Harmony in the small-world. *Physica A: Statistical Mechanics and its Applications*, 285(3–4):539–546, 2000.

[150] S. B. Marston. A simple method for automatic tracking of actin filaments in the motility assay. *Journal of Muscle Research and Cell Motility*, 17:497–506, 1996.

[151] E. C. McKinney, M. K. Kandasamy, and R. B. Meagher. Small changes in the regulation of one *Arabidopsis* profilin isovariant, PRF1, alter seedling development. *The Plant Cell*, 13:1179–1191, 2001.

[152] C. Meier, T. Bouquin, M. E. Nielsen, D. Raventos, O. Mattson, A. Rocher, F. Schomburg, R. M. Amasino, and J. Mundy. Gibberellin response mutants identified by luciferase imaging. *The Plant Journal*, 25(5):509–519, 2001.

[153] H. Meinhardt and A. Gierer. Applications of a theory of biological pattern formation based on lateral inhibition. *Journal of Cell Science*, 15:321–346, 1974.

[154] A. Michelot, J. Berro, C. Guerin, R. Boujemaa-Paterski, and C. J. Staiger. Actin-filament stochastic dynamics mediated by ADF/cofilin. *Current Biology*, 17:825–833, 2007.

[155] V. Mirabet, P. Krupinski, O. Hamant, E. M. Meyerowitz, H. Joensson, and A. Boudaoud. The self-organization of plant microtubules inside the cell volume yields their cortical localization, stable alignment, and sensitivity to external cues. *PLoS Computational Biology*, 14(2):e1006011, 2018.

[156] B. Möller, Y. Poeschl, R. Plötner, and K. Bürstenbinder. PaCeQuant: a tool for high-throughput quantification of pavement cell shape characteristics. *Plant Physiology*, 175:998–1017, 2017.

[157] E. Mones, L. Vicsek, and T. Vicsek. Hierarchy measure for complex networks. *PLoS ONE*, 7(3):e33799, 2012.

[158] M. T. Morita. Directional gravity sensing in gravitropism. *Annual Review of Plant Biology*, 61:705–720, 2010.

[159] P. Myers, R. Espinosa, C. S. Parr, T. Jones, and G. S. Hammond. The Animal Diversity Web (Online). Accessed at https://animaldiversity.org (19.08.2019).

[160] S. Nagawa, T. Xu, D. Lin, P. Dhonukshe, X. Zhang, J. Friml, B. Scheres, Y. Fu, and Z. Yang. ROP GTPase-dependent actin microfilaments promote PIN1 polarization by localized inhibition of clathrin-dependent endocytosis. *PLoS Biology*, 10:e1001299, 2012.

[161] A. Nebenfuehr, L. A. Gallagher, T. G. Dunahay, J. A. Frohlick, A. M. Mazurkiewicz, J. B. Meehl, and L. A. Staehelin. Stop-and-go movements of plant Golgi stacks are mediated by the acto-myosin system. *Plant Physiology*, 121:1127–1141, 1999.

[162] M. Negri, P. Gamba, G. Lisini, and F. Tupin. Junction-aware extraction and regularization of urban road networks in high-resolution SAR images. *IEEE Transactions on Geoscience and Remote Sensing*, 44(10):2962–2971, 2006.

[163] J. C. Neto, G. E. Meyer, D. D. Jones, and A. K. Samal. Plant species identification using Elliptic Fourier leaf shape analysis. *Computers and Electronics in Agriculture*, 50(2):121–134, 2006.

[164] M. Newman. Communities, modules and large-scale structure in networks. *Nature Physics*, 8:25–31, 2012.

[165] M. E. J. Newman. A measure of betweenness centrality based on random walks. *Social Networks*, 27(1):39–54, 2005.

[166] E. Nogales and H. W. Wang. Structural intermediates in microtubule assembly and disassembly: how and why? *Current Opinion in Cell Biology*, 18(2):179–184, 2006.

[167] J. Nowak, K. Gennermann, S. Persson, and Z. Nikoloski. CytoSeg 2.0: automated extraction of actin filaments. *Bioinformatics*, page btaa035, 2020.

[168] B. Obara, V. Grau, and M. D. Fricker. A bioimage informatics approach to automatically extract complex fungal networks. *Bioinformatics*, 28(18):2374–2381, 2012.

[169] Y. Onoda, F. Schieving, and N. P. R. Anten. A novel method of measuring leaf epidermis and mesophyll stiffness shows the ubiquitous nature of the sandwich structure of leaf laminas in broad-leaved angiosperm species. *Journal of Experimental Botany*, 66:2487–2499, 2015.

[170] J. O'Rourke. Computational geometry column 18. *ACM SIGACT News*, 24.1:20–25, 1993.

[171] J. O'Rourke and A. P. C. S. J. O'Rourke. *Art gallery theorems and algorithms*. Oxford University Press, 1987.

[172] G. S. Ou, Z. L. Chen, and M. Yuan. Jasplakinolide reversibly disrupts actin filaments in suspension-cultured tobacco BY-2 cells. *Protoplasma*, 219:168–175, 2002.

[173] A. Paez-Garcia, J. A. Sparks, L. de Bang, and E. B. Blancaflor. *Concepts in Cell Biology - History and Evolution. Plant Cell Monographs*, volume 23, chapter Plant actin cytoskeleton: new functions from old scaffold, pages 103–137. Springer, Cham, 2018.

[174] R. Palin and A. Geitmann. The role of pectin in plant morphogenesis. *Biosystems*, 109(3):397–402, 2012.

[175] M. Palmieri and J. Z. Kiss. Disruption of the F-actin cytoskeleton limits statolith movement in *Arabidopsis* hypocotyls. *Journal of Experimental Botany*, 56:2539–2250, 2005.

[176] E. Paluch and C. P. Heisenberg. Biology and physics of cell shape changes in development. *Current Biology*, 19:R790–R799, 2009.

[177] E. Panteris and B. Galatis. The morphogenesis of lobed plant cells in the mesophyll and epidermis: organization and distinct roles of cortical microtubules and actin filaments. *New Phytologist*, 167:721–732, 2005.

[178] A. R. Paredez, C. R. Somerville, and D. W. Ehrhardt. Visualization of cellulose synthase demonstrates functionsl association with microtubules. *Science*, 312(5779):1491–1495, 2006.

[179] G. E. Peng, S. R. Wilson, and O. D. Weiner. A pharmacological cocktail for arresting actin dynamics in living cells. *Molecular Biology of the Cell*, 22(21):3986–3994, 2011.

[180] V. V. Peremyslov, A. I. Prokhnevsky, and V. V. Dolja. Class XI myosins are required for development, cell expansion, and F-actin organization in *Arabidopsis*. *The Plant Cell*, 22:1883–1897, 2010.

[181] K. M. Peterson and K. U. Torii. Long-term, high-resolution confocal time lapse imaging of Arabidopsis cotyledon epidermis during germination. *Journal of Visualized Experiments*, 70:e4426, 2012.

[182] J. Petrasek and K. Schwarzerova. Actin and microtubule cytoskeleton interactions. *Current Opinion in Plant Biology*, 12(6):728–734, 2009.

[183] L. J. Pillitteri and J. Dong. Stomatal development in Arabidopsis. *The Arabidopsis Book*, 11:e0162, 2013.

[184] M. Poll. *Fauna van Belgie = Faune de Belgique*, chapter Poissons marins, page 452. Le Patrimoine du Musée Royal d'Histoire Naturelle de Belgique/Musée Royal d'Histoire Naturelle de Belgique: Brussel, 1947.

[185] T. D. Pollard, L. Blanchoin, and R. D. Mullins. Molecular mechanisms controlling actin filament dynamics in nonmuscle cells. *Annual Review of Biophysics and Biomolecular Structure*, 29:545–576, 2000.

[186] T. D. Pollard and J. A. Cooper. Actin and actin-binding proteins. a critical evaluation of mechanisms and functions. *Annual Review of Biochemistry*, 55:987–1035, 1986.

[187] T. D. Pollard and J. A. Cooper. Actin, a central player in cell shape and movement. *Science*, 27:1208–1212, 2009.

[188] C. Poppe, R. P. Hangarter, R. A. Sharrock, F. Nagy, and E. Schaefer. The light-induced reduction of the gravitropic growth-orientation of seedlings of *Arabidopsis thaliana* (L.) Heynh. is a photomorphogenic response mediated synergistically by the far-red-absorbing forms of phytochromes A and B. *Planta*, 199:511–514, 1996.

[189] S. Preibisch, S. Saalfeld, and P. Tomancak. Globally optimal stitching of tiles 3D microscopic image acquisitions. *Bioinformatics*, 25:1463–1465, 2009.

[190] C. A. Price, O. Symonova, Y. Mileyko, T. Hilley, and J. S. Weitz. Leaf extraction and analysis framework graphical user interface: segmenting and analyzing the structure of leaf veins and areoles. *Plant Physiology*, 155:236–245, 2011.

[191] Y. M. Qin and Y. X. Zhu. How cotton fibres elongate: a tale of linear cell-growth mode. *Current Opinion in Plant Biology*, 14:106–111, 2011.

[192] J. Qiu and F. F. Li. Quantitative morphological analysis of curvilinear network for microscopic image based on individual fibre segmentation (IFS). *Journal of Microscopy*, 256(3):153–165, 2014.

[193] J. L. Qiu, R. Jilk, M. D. Marks, and D. B. Szymanski. the *Arabidopsis* SPIKE1 gene is required for normal cell shape control and tissue development. *The Plant Cell*, 14:101–118, 2002.

[194] X. Qu, K. M. Peterson, and K. U. Torii. Stomatal development in time: the past and the future. *Current Opinion in Genetics & Development*, 45:1–9, 2017.

[195] S. Ramachandran, H. Christensen, Y. Ishimaru, C. H. Dong, C. M. Wen, A. L. Cleary, and N. H. Chua. Profilin plays a role in cell elongation, cell shape maintenance and flowering in *Arabidopsis*. *Plant Physiology*, 124:1637–1647, 2000.

[196] J. Riedl, A. H. Crevenna, K. Kessenbrock, J. H. Yu, D. Neukirchen, M. Bista, F. Bradke, D. Jenne, T. A. Holak, Z. Werb, M. Sixt, and R. Wedlich-Soldner. Lifeact: a versatile marker to visualize F-actin. *Nature Methods*, 5:605–607, 2008.

[197] C. Ringli, N. Baumberger, A. Diet, B. Frey, and B. Keller. *ACTIN*2 is essential for bulge site selection and tip growth during root hair development in *Arabidopsis*. *Plant Physiology*, 129:1464–1472, 2002.

[198] A. H. K. Roeder, A. Cunha, C. K. Ohno, and E. M. Meyerowitz. Cell cycle regulates cell type in the *Arabidopsis* sepal. *Development*, 139:4416–4427, 2012.

[199] H. Rogge, N. Artelt, N. Endlich, and K. Endlich. Automated segmentation and quantification of actin stress fibres undergoing experimentally induced changes. *Journal of Microscopy*, 268(2):129–140, 2017.

[200] P. Ronceray, C. P. Broedersz, and M. Lenz. Fiber networks amplify active stress. *PNAS*, 113(11):2827–2832, 2016.

[201] G. Sabidussi. The centrality index of a graph. *Psychometrika*, 31:581–603, 1966.

[202] L. Sack and C. Scoffoni. Leaf venation: structure, function, development, evolution, ecology and applications in the past, present and future. *New Phytologist*, 198(4):983–1000, 2013.

[203] M. Sahaf and E. Sharon. The rheology of a growing leaf: stress-induced changes in the mechanical properties of leaves. *Journal of Experimental Botany*, 67:5509–5515, 2016.

[204] C. Saito, M. T. Morita, T. Kato, and M. Tasaka. Amyloplasts and vacuolar membrane dynamics in the living graviperceptive cell of the Arabidopsis inflorescence stem. *The Plant Cell*, 17:548–558, 2005.

[205] A. Sampathkumar, R. Gutierrez, H. E. McFarlane, M. Bringmann, Lindeboom J., A. M. Emons, L. Samuels, T. Ketelaar, D. W. Ehrhardt, and S. Persson. Patterning and lifetie of plasma membrane-localized cellulose synthase is dependent on actin organization in Arabidopsis interphase cells. *Plant Physiology*, 162:675–688, 2013.

[206] A. Sampathkumar, P. Krupinski, R. Wightman, P. Milani, A. Berquand, A. Boudaoud, O. Hamant, H. Jönsson, and E. M. Meyerowitz. Subcellular and supracellular mechanical stress prescribes cytoskeleton behavior in Arabidopsis cotyledon pavement cells. *eLife*, 3:e01967, 2014.

[207] A. Sampathkumar, J. J. Lindeboom, S. Debolt, R. Gutierrez, D. W. Ehrhardt, T. Ketelaar, and S. Persson. Live cell imaging reveals structural associations between the actin and microtubule cytoskeleton in *Arabidopsis*. *The Plant Cell*, 23:2302–2313, 2011.

[208] Y. E. Sánchez-Corrales, M. Hartley, J. van Rooij, A. F. M. Marée, and V. A. Grieneisen. Morphometrics of complex cell shapes: lobe contribution elliptic Fourier analysis (LOCO-EFA). *Development*, 145:dev156778, 2018.

[209] A. Sapala, A. Runions, A. L. Routier-Kierzkowska, L. Gupta, M. D. andHong, H. Hofhuis, S. Verger, G. Mosca, C. B. Li, A. Hay, O. Hamant, A. H. K. Roeder, M. Tsiantis, P. Prusinkiewicz, and R. S. Smith. Why plants make puzzle cells, and how their shape emerges. *eLife*, 7:e32794, 2018.

[210] J. Schindelin, I. Arganda-Carreras, and E. Frise. Fiji: an open-source platform for biological-image analysis. *Nature Methods*, 9(7):676–682, 2012.

[211] R. Schneider, A. Sampathkumar, and S. Persson. Quantification of cytoskeletal dynamics in time-lapse recordings. *Current Protocols in Plant Biology*, 4(2):e20091, 2019.

[212] D. Seetapun, B. T. Castle, A. J. McIntyre, P. T. Tran, and D. J. Odde. Estimating the microtubule GTP cap size in vivo. *Current Biology*, 22(18):1681–1687, 2012.

[213] J. V. Shah. Cells in tight spaces: the role of cell shape in cell function. *Journal of Cell Biology*, 191(2):233–236, 2010.

[214] L. G. Shapiro. Decomposition of two-dimensional shapes by graph-theoretic clustering. *IEEE Transactions on Pattern Analysis and Machine Intelligence*, PAMI-1(1):10–20, 1979.

[215] S. L. Shaw, R. Kamyar, and D. W. Ehrhardt. Sustained microtubule treadmilling in *Arabidopsis* cortical arrays. *Science*, 300(5626):1715–1718, 2003.

[216] M. B. Sheahan, C. J. Staiger, R. J. Rose, and D. W. McCurdy. A green fluorescent protein fusion to actin-binding domain 2 of Arabidopsis fimbrin highlights new features of a dynamic actin cytoskeleton in live plant cells. *Plant Physiology*, 136:3968–3978, 2004.

[217] F. Y. Shih and A. J. Kowalski. Automatic extraction of filaments in Halpha solar images. *Solar Physics*, 218:99–122, 2003.

[218] T. Shoji, N. N. Narita, K. Hayashi, J. Asada, T. Hamada, S. Sonobe, K. Nakajima, and T. Hashimoto. Plant-specific microtubule-associated protein SPIRAL2 is required for anisotropic growth in Arabidopsis. *Plant Physiology*, 136:3933–3944, 2004.

[219] V. R. Simon and L. A. Pon. Actin-based organelle movement. *Experientia*, 52:1117–1122, 1996.

[220] A. P. Smertenko, M. J. Deeks, and P. J. Hussey. Strategies of actin reorganisation in plant cells. *Journal of Cell Science*, 123:3019–3028, 2010.

[221] L. G. Smith. Cytoskeletal control of plant cell shape: getting the fine points. *Current Opinion in Plant Biology*, 6:63–73, 2003.

[222] Y. Song, G. Li, J. Nowak, X. Zhang, D. Xu, X. Yang, G. Huang, W. Liang, L. Yang, C. Wang, V. Bulone, Z. Nikoloski, J. Hu, S. Persson, and D. Zhang. The rice actin-binding protein RMD regulates light-dependent shoot gravitropism. *Plant Physiology*, 181:630–644, 2019.

[223] I. Spector, F. Braet, N. R. Shochet, and M. R. Bubb. New anti-actin drugs in the study of the organization and function of the actin cytoskeleton. *Microscopy Research and Technique*, 47:18–37, 1999.

[224] I. Spector, N. R. Shochet, D. Blasberger, and Y. Kashman. Latrunculins - novel marinemacrolides that disrupt microfilament organization and affect cell growth: I. comparison with Cytochalasin D. *Cell Motility and the Cytoskeleton*, 13:127–144, 1989.

[225] J. J. Staal, M. D. Abramoff, M. Niemeijer, M. A. Viergever, and B. van Ginneken. Ridge based vessel segmentation in color images of the retina. *IEEE Transactions on Medical Imaging*, 23:501–509, 2004.

[226] L. Staff, L. Hurd, P. andd Reale, C. Seoighe, A. Rockwood, and C. Gehring. The hidden geometries if the *Arabidopsis thaliana* epidermis. *PLOS ONE*, 7(9):e43546, 2012.

[227] C. J. Staiger. Signaling to the actin cytoskeleton in plants. *Annual Review of Plant Physiology and Plant Molecular Biology*, 51:257–288, 2000.

[228] C. J. Staiger, M. B. Sheahan, P. Khurana, X. Wang, D. W. McCurdy, and L. Blanchoin. Actin filament dynamics are dominated by rapid growth and severing activity in the *Arabidopsis* cortical array. *Journal of Cell Biology*, 184:269–280, 2009.

[229] M. A. Stephens. *Breakthroughs in StatisticsStatistics. Springer Series in Statistics (Perspectives in Statistics)*, chapter Introduction to Kolmogorov (1933) on the empirical determination of a distribution. Springer, New York, NY, 1992.

[230] K. Stephenson and M. Zelen. Rethinking centrality: methods and examples. *Social Networks*, 11(1):1–37, 1989.

[231] M. R. Stiff and C. H. Haigler. Cotton fibre tips have diverse morphologies and show evidence of apical cell wall synthesis. *Scientific Reports*, 6:27883, 2016.

[232] D. B. Szymanski. Plant cells taking shape: new insights into cytosplasmic control. *Current Opinion in Plant Biology*, 12:735–744, 2009.

[233] D. Takemoto and A. R. Hardham. The cytoskeleton as a regulator and target of biotic interactions in plants. *Plant Physiology*, 136:3864–3876, 2004.

[234] C. Thomas. Bundling actin filaments from membranes: some novel players. *Frontiers in Plant Science*, 3:188, 2012.

[235] S. C. Tiwari and T. A. Wilkins. Cotton (*Gossypium hirsutum*) seed trichomes expand via diffuse growing mechanism. *Canadian Journal of Botany*, 73:746–757, 1995.

[236] K. U. Torii. Two-dimensional spatial patterning in developmental systems. *Trends in Cell Biology*, 22(8):438–446, 2012.

[237] R. Toth, C. Gerding-Reimers, M. J. Deeks, S. Menninger, R. M. Gallegos, I. A. N. Tonaco, K. Huebel, P. J. Hussey, H. Waldmann, and G. Coupland. Prieurianin/endosidin 1 is an actin stabilizing small molecule identified from chemical genetic screen for circadian clock effectors in *Arabidopsis thaliana*. *Plant Journal*, 71:338–352, 2012.

[238] A. M. Turing. The chemical basis of morphogenesis. *Philosophical Transactions of the Royal Society of London. Series B, Biological Sciences*, 237(641):37–72, 1952.

[239] R. V. Vőfély, J. Gallagher, G. D. Psiano, M. Bartlett, and S. A. Braybrook. Data from: Of puzzles and pavements: a quantitative exploration of leaf epidermal cell shape. *Dryad Digital Repositiory*, 2018.

[240] R. V. Vőfély, J. Gallagher, G. D. Psiano, M. Bartlett, and S. A. Braybrook. Of puzzles and pavements: a quantitative exploration of leaf epidermal cell shape. *New Phytologist*, 221(1):540–552, 2018.

[241] M. Wada. Chloroplast movement. *Plant Science*, 210:177–182, 2013.

[242] T. Wakatsuki, B. Schwab, N. C. Thompson, and E. L. Elson. Effects of cytochalasin D and latrunculin B on mechanical properties of cells. *Journal of Cell Science*, 114:1025–1036, 2001.

[243] H. W. Wang and E. Nogales. Nucleotide-dependent bending flexibility of tubulin regulates microtubule assembly. *Nature*, 435:911–915, 2005.

[244] J. Wang, H. Y. Wang, P. M. Zhao, L. B. Han, G. L. Jiao, Y. Y. Zheng, S. J. Huang, and G. X. Xia. Overexpression of a profilin (GhPFN2) promotes the progression of developmental phases in cotton fibers. *Plant Cell Physiology*, 51(8):1276–1290, 2010.

[245] P. Wang, T. J. Hawkins, and P. J. Hussey. Connecting membranes to the actin cytoskeleton. *Current Opinion in Plant Biology*, 40:71–76, 2017.

[246] P. Wang and P. J. Hussey. Interactions between plant endomembrane systems and the actin cytoskeleton. *Frontiers in Plant Science*, 6:422, 2015.

[247] Z. Wang, Z. Chi, D. Feng, and Q. Wang. Leaf image retrieval with shape features. In *International conference on advances in visual information systems*, pages 477–487, 2000.

[248] G. O. Wasteneys. Progress in understanding the role of microtubules in plant cells. *Current Opinion in Plant Biology*, 7:651–660, 2004.

[249] G. O. Wasteneys and M. E. Galway. Remodeling the cytoskeleton for growth and form: an overview with some new views. *Annual Review of Plant Biology*, 54:691–722, 2003.

[250] G. O. Wasteneys, J. Willingale-Theune, and D. Menzel. Freeze shattering: a simple and effective method for permeabilizing higher plant cell walls. *Journal of Microscopy*, 188:51–61, 1997.

[251] R. C. Wilson and P. Zhu. A study of graph spectra for comparing graphs and trees. *Pattern Recognition*, 41(9):2833–2841, 2008.

[252] T. C. Wu, S. A. Belteton, J. Pack, D. B. Szymanski, and D. M. Umulis. LobeFinder: a convex hull-based method for quantitative boundary analyses of lobes plant cells. *Plant Physiology*, 171:2331–2342, 2016.

[253] X. Xiao, V. F. Geyer, H. Bowne-Anderson, J. Howard, and I. F. Sbalzarini. Automatic optimal filament segmentation with sub-pixel accuracy using generalized linear models and B-spline level-sets. *Medical Image Analysis*, 32:157–172, 2016.

[254] T. Xu, M. Wen, S. Nagawa, Y. Fu, J. G. Chen, M. J. Wu, C. Perrot-Rechenmann, J. Friml, A. M. Jones, and Z. Yang. Cell surface- and Rho GTPase-based auxin signaling controls cellular interdigitation in *Arabidopsis*. *Cell*, 143:99–110, 2010.

[255] K. Yamamoto and J. Z. Kiss. Disruption of the actin cytoskeleton results inthe promotion of gravitropism in inflorescence stems and hypocotyls of Arabidopsis. *Plant Physiology*, 128:669–681, 2002.

[256] M. Yanagisawa, A. S. Desyatova, S. A. Belteton, E. L. Mallery, J. A. Turner, and D. B. Szymanski. Patterning mechanisms of cytoskeletal and cell wall systems during leaf trichome morphogenesis. *Nature Plants*, 1:15014, 2015.

[257] M. Yanagisawa, C. Zhang, and D. B. Szymanski. ARP2/3-dependent growth in the plant kingdom: SCARs for life. *Frontiers in Plant Science*, 4:166, 2013.

[258] Z. Yang. Small GTPases: versatile signaling switches in plants. *The Plant Cell*, 14:S375–S388, 2002.

[259] Y. Yu, S. Wu, J. Nowak, G. Wang, L. Han, Z. Feng, A. Mendrinna, Y. Ma, H. Wang, X. Zhang, J. Tian, L. Dong, Z. Nikoloski, S. Persson, and Z. Kong. Live-cell imaging of the cytoskeleton in elongating cotton fibres. *Nature Plants*, 5:498–504, 2019.

[260] Z. Yuan, F. Li, Z. Peng, and C. Bo. Description of shape characteristics through Fourier and wavelet analysis. *Chinese Journal of Aeronautics*, 27(1):160–168, 2014.

[261] C. Zhang, L. E. Halsey, and D. B. Szymanski. The development and geometry of shape change in Arabidopsis thaliana cotyledon pavement cells. *BMC Plant Biology*, 11:27, 2011.

[262] D. Zhang and G. Lu. Review of shape representation and description techniques. *Pattern Recognition*, 37:1–19, 2004.

[263] Z. Zhang, Y. Nishimura, and P. Kanchanawong. Extracting microtubule networks from superresolution single-molecule localization microscopy data. *Molecular Biology of the Cell*, 28(2):333–345, 2016.

[264] Z. Zhang, S. Xia, and P. Kanchanawong. An integrated enhancement and reconstruction strategy for the quantitative extraction of actin stress fibers from fluorescence micrographs. *BMC Bioinformatics*, 18:268, 2017.

[265] Z. Zhang, Y. Zhang, H. Tan, Y. Wang, G. Li, W. Liang, Z. Yuan, J. Hu, H. Ren, and D. Zhang. RICE MORPHOLOGY DETERMINANT encodes thetype II formin FH5 and regulates rice morphogenesis. *The Plant Cell*, 23:681–700, 2011.

[266] C. Zhao, S. S. F. Chan, W. K. Cham, and L. M. Chu. Plant identification using leaf shapes - a pattern counting approach. *Pattern Recognition*, 48:3203–3215, 2015.

[267] R. Zhong and Z. H. Ye. Secondary cell walls: Biosynthesis, patterned deposition and transcriptional regulation. *Plant Cell Physiology*, 56(2):195–214, 2015.

Appendix

1. Breuer D, **Nowak J**, Ivakov A, Somssich M, Persson S and Nikoloski Z (2017). System-wide organization of actin cytoskeleton determines organelle transport in hypocotyl plant cells.
   PNAS, **114**(28): E5741-5749.

2. Yu Y, Wu S, **Nowak J**, Wang G, Han L, Feng Z, Mendrinna A, Ma Y, Wang H, Zhang X, Tian J, Dong L, Nikoloski Z, Persson S and Kong Z (2019). Live-cell imaging of the cytoskeleton in elongating cotton fibres.
   Nature Plants, **5**: 498-504.

3. Song Y, Li G, **Nowak J**, Zhang X, Xu D, Yang X, Huang G, Liang W, Yang L, Wang C, Bulone V, Nikoloski Z, Hu J, Persson S and Zhang D (2019). The rice actin-binding protein RMD regulates light-dependent shoot gravitropism.
   Plant Physiology, **181**: 630-644.

4. **Nowak J**, Gennermann K, Persson S and Nikoloski Z (2020). CytoSeg 2.0: automated extraction of actin filaments.
   Bioinformatics, btaa035.

System-wide organization of actin cytoskeleton determines organelle transport in hypocotyl plant cells

David Breuer[a,b,1], Jacqueline Nowak[a,b,c], Alexander Ivakov[c,d], Marc Somssich[c], Staffan Persson[c,e,2], and Zoran Nikoloski[a,b,2]

[a]Systems Biology and Mathematical Modeling, Max Planck Institute of Molecular Plant Physiology, 14476 Potsdam, Germany; [b]Bioinformatics, Institute of Biochemistry and Biology, University of Potsdam, 14476 Potsdam, Germany; [c]ARC Centre of Excellence in Plant Cell Walls, School of Biosciences, University of Melbourne, Parkville, VIC 3010, Australia; [d]ARC Centre of Excellence for Translational Photosynthesis, College of Medicine, Biology and Environment, Australian National University, Canberra, Acton, ACT 2601, Australia; and [e]Plant Cell Walls, Max Planck Institute of Molecular Plant Physiology, 14476 Potsdam, Germany

Edited by Natasha V. Raikhel, Center for Plant Cell Biology, Riverside, CA, and approved May 25, 2017 (received for review April 26, 2017)

The actin cytoskeleton is an essential intracellular filamentous structure that underpins cellular transport and cytoplasmic streaming in plant cells. However, the system-level properties of actin-based cellular trafficking remain tenuous, largely due to the inability to quantify key features of the actin cytoskeleton. Here, we developed an automated image-based, network-driven framework to accurately segment and quantify actin cytoskeletal structures and Golgi transport. We show that the actin cytoskeleton in both growing and elongated hypocotyl cells has structural properties facilitating efficient transport. Our findings suggest that the erratic movement of Golgi is a stable cellular phenomenon that might optimize distribution efficiency of cell material. Moreover, we demonstrate that Golgi transport in hypocotyl cells can be accurately predicted from the actin network topology alone. Thus, our framework provides quantitative evidence for system-wide coordination of cellular transport in plant cells and can be readily applied to investigate cytoskeletal organization and transport in other organisms.

actin | cytoskeleton | Golgi | image processing | networks

The cell interior is a heterogeneous and crowded space comprising a large range of molecules and organelles (1, 2). Because diffusion through this complex environment is not sufficient to match varying demands for cell maintenance and growth, intricate cellular transport schemes have evolved (3, 4). Transport of cellular components across large distances relies substantially on the cytoskeleton (4–7). Moreover, in plant cells, many organelles move rapidly due to actomyosin-based cytoplasmic streaming (8–10). For instance, Golgi transport relies on the actomyosin system, and an impaired actin cytoskeleton leads to Golgi aggregation and reduced secretion and endocytosis (10–12). Although many molecular features of actin-based transport in plant cells have been elucidated (13, 14), quantitative measures of the structure of the actin cytoskeleton, and how this structure relates to organelle transport, remain elusive. This is largely due to the difficulties in accurately segmenting the actin cytoskeleton and organelle movement, in particular in growing plant cells.

Theoretical models have been used to analyze the interplay between cytoplasmic streaming and actin organization, demonstrating the emergence of self-organized, rotational streaming patterns (3, 15). However, these studies neglected the discrete, filamentous structure of the cytoskeleton. Theoretical investigations that have considered discrete cytoskeletal structures revealed different regimes of transport, depending on the contribution from diffusion or motor-protein–driven transport along random networks of segments (16); the impact of motor-protein movements on cytoplasm in lattice networks (17); and the effect of length, orientation, and polarity of random filament segments on transport rates (18). The studies that do incorporate biological data have suggested that plant cytoskeletal networks, approximated as grids, may support efficient transport processes in hypocotyl cells (19, 20) and that organelle movement depends on local actin structures in root epidermal cells (10). A detailed study of leaf trichome growth demonstrated the importance of organized actin networks for efficient and targeted distribution of new cell wall material (21). However, a global, system-wide view of actin-based organelle transport remains elusive and is complicated by differences between cell types and developmental stages.

Here, we developed a network-based framework that accurately segments the actin cytoskeleton from three developmental stages of hypocotyl plant cells and combined it with an automated tracking of Golgi transport. This approach allowed us to analyze the four aspects of the actin cytoskeletal transport system, including its structure, design principles, dynamics, and control (22). We found that the actin cytoskeleton maintains properties that support efficient transport over time in growing, partially and fully elongated hypocotyl cells, despite rapid reorganization. We also show that Golgi wiggling behavior is reminiscent of

Significance

In the crowded interior of a cell, diffusion alone is insufficient to master varying transport requirements for cell sustenance and growth. The dynamic actin cytoskeleton is an essential cellular component that provides transport and cytoplasmic streaming in plant cells, but little is known about its system-level organization. Here, we resolve key challenges in understanding system-level actin-based transport. We present an automated image-based, network-driven framework that accurately incorporates both actin cytoskeleton and organelle trafficking. We demonstrate that actin cytoskeleton network properties support efficient transport in both growing and elongated hypocotyl cells. We show that organelle transport can be predicted from the system-wide cellular organization of the actin cytoskeleton. Our framework can be readily applied to investigate cytoskeleton-based transport in other organisms.

Author contributions: D.B., S.P., and Z.N. designed research; D.B. and J.N. performed research; D.B., J.N., and M.S. contributed new reagents/analytic tools; D.B. and J.N. analyzed data; D.B., J.N., A.I., S.P., and Z.N. wrote the paper; and A.I. and M.S. recorded data.

The authors declare no conflict of interest.

This article is a PNAS Direct Submission.

Freely available online through the PNAS open access option.

[1]To whom correspondence should be addressed. Email: breuer@mpimp-golm.mpg.de.

[2]S.P. and Z.N. contributed equally to this work.

This article contains supporting information online at www.pnas.org/lookup/suppl/doi:10.1073/pnas.1706711114/-/DCSupplemental.

optimized search strategies that might indicate efficient uptake and deposition of Golgi-related cell material. In addition, we demonstrated that features of Golgi transport can be predicted from properties of the system-wide organization of the actin cytoskeleton. Altogether, our framework opens up a systems perspective to dissect and understand the transport functionality of the actin cytoskeleton.

Results

A Pipeline to Extract and Represent the Actin Cytoskeleton as a Network. Because the actin cytoskeleton is composed of discrete and interconnected filaments, it can be efficiently represented in a network-based framework (19, 23, 24) with nodes representing crossings or end points of actin filaments (AFs) and weighted edges capturing AF segments. We extracted network representations from partially elongated *Arabidopsis thaliana* (*Arabidopsis*) hypocotyl cells, around 3 mm from the apical hook, that expressed FABD-GFP, using spinning-disc confocal microscopy data (Fig. 1*F* for pipeline; *Materials and Methods*). To study actin-based transport at different cell developmental stages, we further analyzed fully elongated as well as growing hypocotyl cells, around 5 mm and 1 mm from the apical hook, respectively (Fig. S1 and below). The recorded images were corrected for drift and bleaching (Fig. 1*A*), manually cropped to the cellular region of interest, and filtered to enhance tube-like structures of the cytoskeleton with a parameter v_{width} (Fig. 1*B*). AFs were segmented by applying an adaptive median threshold of block size, v_{thres} (Fig. 1*C*). The binary images were skeletonized to obtain AF center lines and spurious fragments smaller than v_{size} pixels or below v_{int} of the average fragment intensity were removed (Fig. 1*D*). Networks were obtained by identifying the nodes, adding edges between pairs of nodes directly connected via the skeleton, and assigning edge weights reflecting features of AF segments, e.g., average thickness (Fig. 1*E*).

To test whether our network-based framework captured relevant biological features of the actin cytoskeleton, we compared our automated segmentations against synthetic images of known cytoskeleton-like structures (Fig. 1*G*) as well as manually segmented cytoskeleton images as a gold standard (Fig. 1*H*). Because the accuracy of the network representation relies

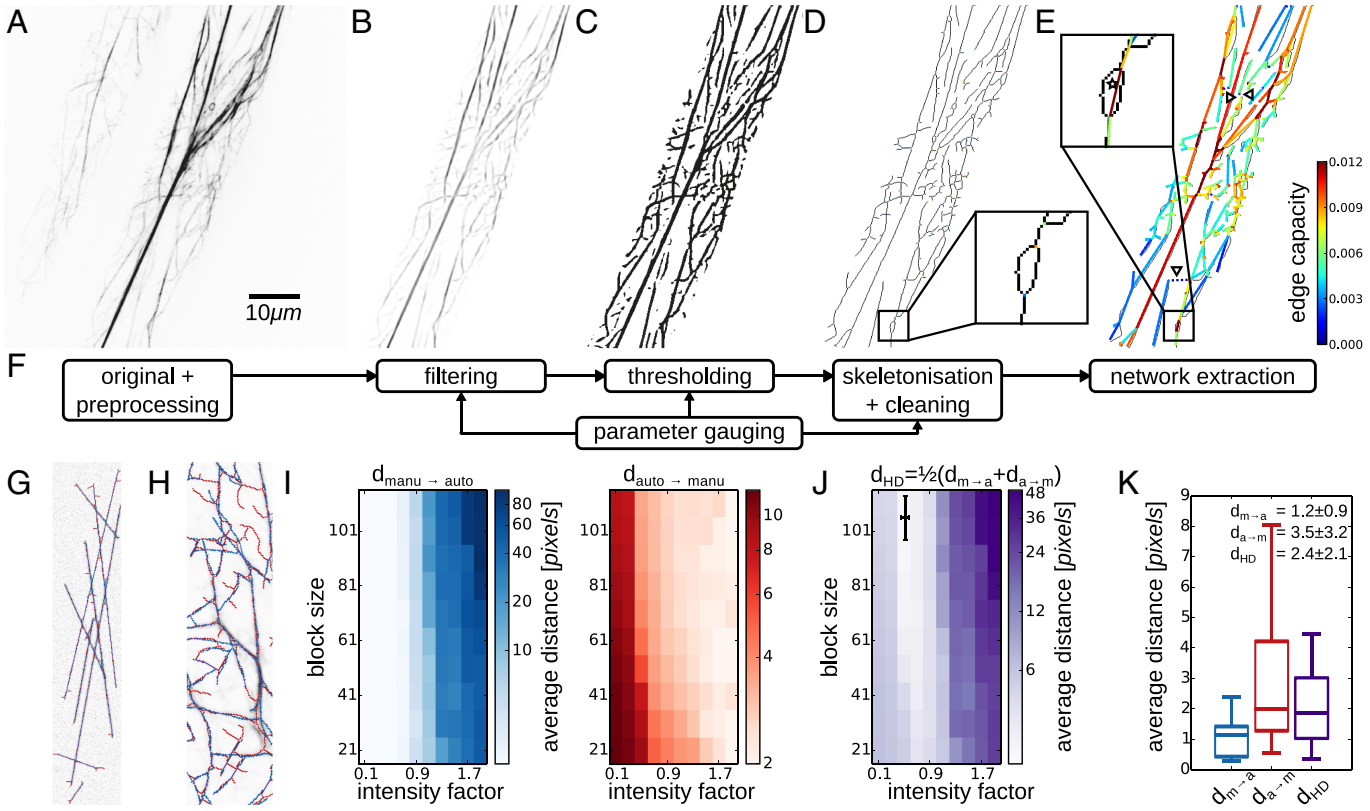

Fig. 1. Automated extraction and validation of networks from actin cytoskeletal image data. (*A*) Grayscale confocal image of two partially elongated *Arabidopsis* hypocotyl cells after registration and background subtraction ("original + preprocessing"). The same cell was used as example throughout the paper. (*B*) Cytoskeleton image with improved signal-to-noise ratio after cropping of the largest cell and application of tubeness filter ($v_{\mathrm{width}} = 1.8$; "filtering"). (*C*) Binary cytoskeleton image after application of adaptive median threshold ($v_{\mathrm{thres}} = 101$; "thresholding"). (*D*) Skeletonized cytoskeletal structures after removal of spurious fragments of small size or low intensity ($v_{\mathrm{size}} = 27$ pixels and $v_{\mathrm{int}} = 0.5$; "skeletonization + cleaning"). Positions of network nodes are marked by colored pixels (*Inset*). (*E*) Overlay of skeleton image and extracted cytoskeletal network with edges color coded by their capacity, reflecting average filament thickness ("network extraction"). Multiple filaments may contribute to an edge (compare *Inset* and star). Edges were added to connect the network (compare dotted lines and triangles). (*F*) Overview of automated pipeline for network-based representation of the actin cytoskeleton incorporating image processing (*A–D*), network extraction (*E*), and parameter gauging (*G–K*). (*G*) Overlay of synthetic filaments (blue) and automated segmentation (red) of a synthetic cytoskeleton image (gray). (*H*) Overlay of manual (blue) and automated (red) segmentation of a biological cytoskeleton image (gray). (*I*) Four image processing parameters were varied to determine their optimal values for 20 images and 20 images of synthetic and biological cytoskeletons, respectively, which were segmented manually for comparison ("parameter gauging"). Segmentation quality was measured by the average of the smallest distance, $d_{\mathrm{manu}\to\mathrm{auto}}$ (blue), from the pixels of the manual segmentation to those of the automated segmentation and vice versa, $d_{\mathrm{auto}\to\mathrm{manu}}$ (red). Shown are sections of the parameter space, averaged over all 40 studied images, for fixed $(v_{\mathrm{width}}, v_{\mathrm{int}}) = (1.8, 101)$ and varying block size v_{thres} and size threshold v_{size}. (*J*) Minimization of the Haussdorf distance $d_{\mathrm{HD}} = \frac{1}{2}\left(d_{\mathrm{manu}\to\mathrm{auto}} + d_{\mathrm{auto}\to\mathrm{manu}}\right)$ (purple) to avoid both over- and undersegmentation yielded $(v^*_{\mathrm{width}}, v^*_{\mathrm{thres}}, v^*_{\mathrm{size}}, v^*_{\mathrm{int}}) = (1.8, 101, 27, 0.50) \pm (0.2, 8.0, 8.9, 0.06)$ (mean ± SD). (*K*) Distribution of average distances between manual and automated segmentations for the optimal parameters with $d_{\mathrm{manu}\to\mathrm{auto}} = 1.2 \pm 0.9$ pixels, $d_{\mathrm{auto}\to\mathrm{manu}} = 3.5 \pm 3.2$ pixels, and $d_{\mathrm{HD}} = 2.4 \pm 2.1$ pixels, respectively.

on four parameters (v_{width}, v_{thres}, v_{size}, and v_{int}), we performed extensive gauging by varying these parameters in a wide range of values (Fig. 1 *I* and *J*) and identified those ensuring best agreement between manual and automated segmentations measured by the Haussdorf distance, i.e., the average minimum distance between pixels of the two segmentations (25, 26). Parameter gauging yielded an optimal average of $d_{\mathrm{HD}} = 2.4 \pm 2.1$ pixels (Fig. 1 *J* and *K*; mean ± SD), comparable to contending approaches (*SI Materials and Methods*). Thus, whereas errors in the automated segmentation occur, our parameter optimization ensures an optimal compromise between over- and undersegmentation across different recordings.

Our approach is directly applicable to 3D image data. However, our focus in the main text on 2D networks is justified by the cylindrical shell geometry of the cortical cytoskeleton (19, 27) as well as the size of the transported Golgi, which may bridge gaps between cortical AFs that are not resolved in 2D images (28–30). Moreover, we show that our findings remain valid for 3D image data (Fig. S2 and below). Thus, our approach yields an accurate and mathematically powerful network representation of the cytoskeleton in hypocotyl plant cells from image data.

The Network Representations Capture Biologically Relevant Features of the Actin Cytoskeleton. To ensure that our framework captured known changes in the actin cytoskeleton, we determined differences in cytoskeletal organization between partially elongated hypocotyl cells of plants treated with Latrunculin B (LatB; Fig. 2*A*), a drug that inhibits actin polymerization (31), and control cells (Fig. 2*B*; seven cells from seven different seedlings per treatment). To quantify actin network phenotypes, we computed the number of connected components after removal of edges with capacities below the 50th percentile as a measure of fragmentation (Fig. 2*D* and ref. 32; mathematical definitions and interpretations of all studied network properties are given in Table S1). Fragmentation was lower in networks of control than of LatB-treated cells (Fig. 2*E*; independent two-sample t test P value $P_t < 10^{-50}$), indicating that large connected patches of AFs were absent in LatB-treated cells, consistent with visual inspection. Similarly, the average edge capacity was higher in control than in LatB-treated cells ($P_t < 10^{-38}$), reflecting a reduction in actin bundling in the LatB-treated cells. Finally, these findings were corroborated by the assortativity (32), which quantifies whether two adjacent nodes are of similar degree and reflects the network heterogeneity. We found stronger heterogeneity for control than for LatB-treated cells ($P_t < 10^{-50}$), suggesting regions of bundled actin that are surrounded by AFs in the control cells.

To further assess the filamentous structure of the actin cytoskeleton, we compared the arc length of filament segments to their Euclidean length and found a strong correlation (Fig. 2*F*; Pearson correlation coefficient $c_P = 0.998$ and P value $P_P < 10^{-50}$). Consequently, filament bending, i.e., the ratio of the two lengths, was small, $B = 1.2 \pm 0.2$, in particular for long filament segments (Fig. 2*F*, *Inset*). This limited bending of longer filament segments is plausible because actin bundles, typically resulting in longer filament segments, exhibit greater stiffness compared with AFs (33, 34). Furthermore, we found that filament segments were preferentially oriented in parallel to the major cell axis in control cells, but not in LatB-treated cells (Fig. 2*G*). To demonstrate the robustness of our findings, we showed that the differences in network properties between control and treatment were not affected by removal of a random fraction of edges, simulating effects of erroneous network extraction (Fig. S3).

Next, we compared cytoskeletal networks in hypocotyl cells at different developmental stages, i.e., in growing and fully elongated cells, and found notable differences (Fig. S1). In particular, in contrast to both partially and fully elongated hypocotyl cells, the actin cytoskeleton in untreated growing hypocotyl cells showed stronger fragmentation and weaker bundling than in their LatB-treated counterparts. These differences are in agreement with the more even distribution and more strongly branched structure of the actin cytoskeleton in growing hypocotyl cells (35, 36) (Fig. S1), as well as the continuous gradient in cell elongation rates along the hypocotyl in dark-grown *Arabidopsis* seedlings (37). Moreover, our findings from 2D image data were corroborated by analyses of 3D image data and networks (Fig. S2). Therefore, our results show that the extracted network representations of the actin cytoskeleton enable automated phenotyping of cytoskeletal structures.

The Actin Cytoskeleton Supports Efficient Transport. A major function of the plant actin cytoskeleton is to mediate transport of a range of organelles and compartments. To assess the transport efficiency of actin networks in partially elongated hypocotyl cells, we computed a number of seminal network properties and compared them against ensembles of two types of randomized null model networks (each network was randomized 20 times; Fig. 2*C* for first null model that shuffles node positions and edges and Fig. S3 for second null model that shuffles edge properties only). We determined the average path length (32), which reflects the reachability of a network, and compared it against an ensemble of networks from the first null model (Fig. 2*H*). We found that the average path length of the extracted networks was smaller than that of the null model networks (Fig. 2*I*; $P_t < 10^{-50}$; Fig. S3 for analysis of robustness of this finding against removal of edges). This difference indicates that the actin cytoskeleton is tuned toward shorter path lengths. Similarly, the coefficients of variation (CVs) of the shortest path lengths in the extracted networks were smaller than expected from the null model networks ($P_t < 10^{-50}$), indicating that also fluctuations in the path length between any two nodes are maintained at a low level. Another classical transport-related network property is the algebraic connectivity (32), which reflects the redundancy of paths between any two nodes and thus captures the robustness of the transportation network against disruptions. The algebraic connectivity of the extracted networks was higher than expected by chance ($P_t < 10^{-14}$). In contrast, the LatB-disrupted actin cytoskeletons did not show any significant differences in their transport-related network properties compared with the null model networks (Fig. S3). These findings support the hypothesis that transport efficiency is a biological design principle of the intact actin cytoskeleton (19).

To investigate the structural origin of this transport efficiency, we reconsidered the assortativity (32) of the cytoskeleton and found that it was higher in the extracted networks than expected by chance ($P_t < 10^{-50}$). Similarly, we found that the CV of the angles between AF segments and the major cell axis was smaller in the extracted networks than expected by chance ($P_t < 10^{-50}$). Together these findings suggest that the formation of connected patches of aligned actin bundles is a functionally relevant feature of the cytoskeleton.

To ensure that our results were robust, we used an additional and more restricted null model, which shuffles only edge properties. Whereas the first null model is more flexible, the second one excludes potential artifacts that could arise from an increased number of edge crossings or a more homogeneous distribution of node positions compared with the extracted networks (Fig. S3). Our findings from the first null model were consistently confirmed by the second one. Hence, differences in the studied network properties between extracted and null model networks are not an artifact of the randomization procedures.

Despite organizational differences of the actin cytoskeleton in hypocotyl cells at different developmental stages, the actin network in partially elongated as well as fully elongated and growing hypocotyl cells showed properties of efficient transport (Fig. S1). For example, both reachability and robustness of the actin networks were better than expected by chance. Again, our findings

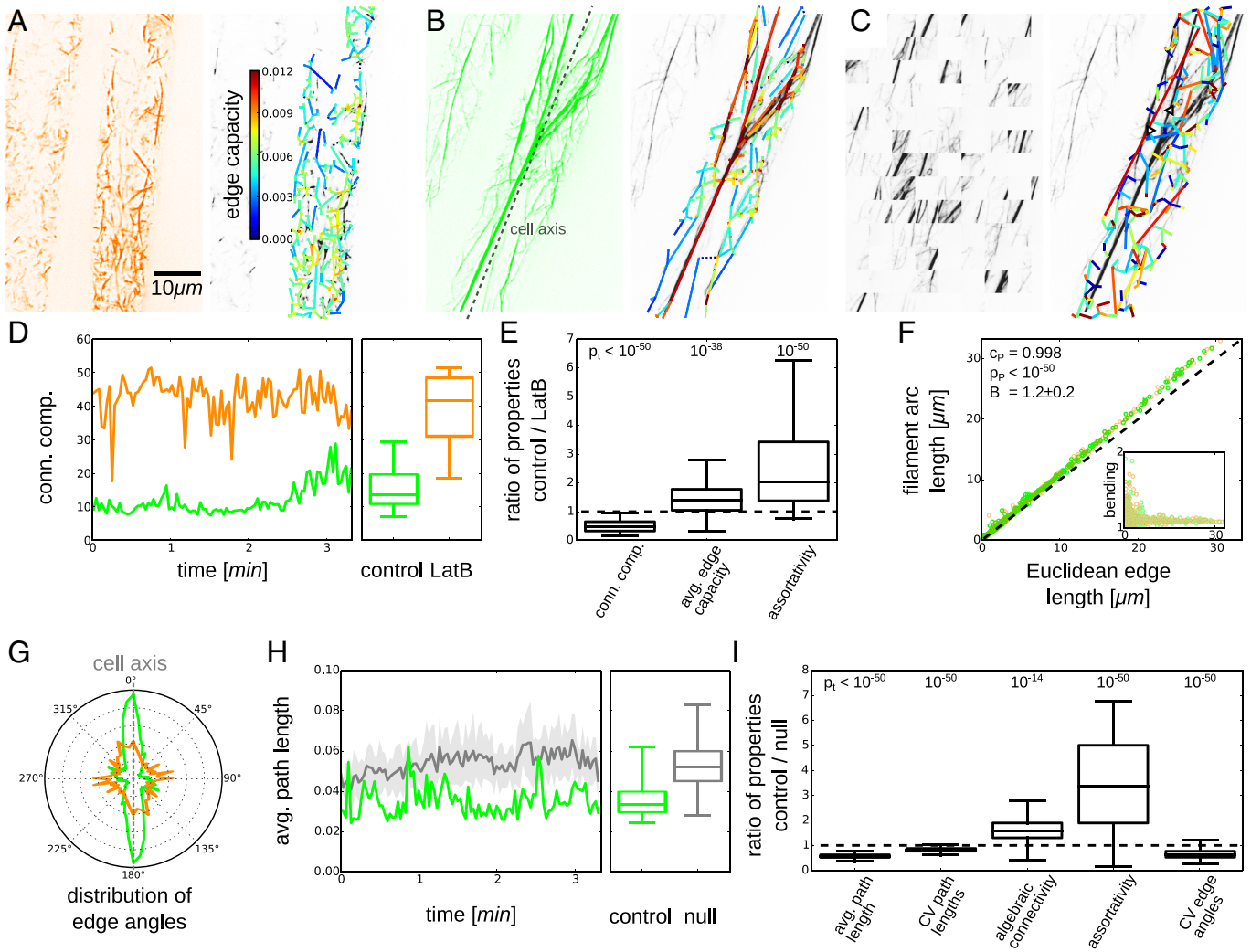

Fig. 2. Phenotyping of actin cytoskeleton using the extracted networks captures biological signals and reveals transport efficiency. Shown are results for partially elongated hypocotyl cells of plants treated with the actin-disrupting drug LatB (orange), untreated control plants (green), and ensembles of 20 randomized networks (gray). (*A*) Cellular recording (*Left*) and extracted actin network (*Right*) of a LatB-treated cell with edge colors representing edge capacities. (*B*) Cellular recording (*Left*) and extracted actin network (*Right*) of an untreated control cell. (*C*) Artistic interpretation of the randomization procedure (*Left*) and a randomized network (*Right*) of the control cell (*B*) with occasional edge crossings (e.g., triangles). (*D*) Time series and box plots of the number of connected components after removal of edges with capacities below the 50th percentile ("fragmentation") for a control and a LatB-treated cell. (*E*) Ratios of different properties of networks extracted from seven control and seven LatB-treated cells. The number of connected components was lower and the average edge capacity ("bundling") and the degree assortativity ("heterogeneity") were higher for control than for LatB-treated cells (independent two-sample t test P values $P_t < 0.05$ were considered significant). (*F*) Scatter plots of the arc length a_F of the filament segments vs. the Euclidean length a_E of the corresponding edges showed strong correlation for control and LatB-treated cells (Pearson correlation coefficient $c_P = 0.998$ and P value $P_P < 10^{-50}$). *F*, *Inset* displays relative lengths $B = a_E^{-1} a_F$ ("bending") with an average of $B = 1.2 \pm 0.2$ (mean $\pm$ SD). (*G*) Distribution of edge angles, weighted by edge capacities, relative to the major cell axis showed a prevalence of AFs parallel to the cell axis in the control cells but not in LatB-treated cells. (*H*) Time series and box plots of the average path length ("reachability") for one control cell and 20 randomized networks of the first null model for each time step (mean $\pm$ SD). (*I*) The extracted actin networks of the seven control cells showed significantly lower average path lengths, CV of the path lengths ("dispersal"), and CV of the edge angles ("contortion") than their counterparts from the first null model. The algebraic connectivities ("robustness") and assortativities (heterogeneity) of the actin networks were higher than expected from the first null model.

remained valid when studying actin networks extracted from 3D image data (Fig. S2).

A potential issue, shared by all current approaches that extract transport-related networks from image data, is the unknown edge directionality. Individual AFs usually allow unidirectional movement of motor proteins only, and actin bundles in root hairs and other tip growing cells are typically composed of parallel AFs (9, 38, 39). In contrast, our analyses of cytoskeletal transport capacity rely on the assumption of bidirectional transport along edges. Indeed, our data showed that $<50\%$ of actin edges exhibit predominantly unidirectional movement of close-by Golgi, irrespective of the actin bundle thickness (see Fig. 4 and Fig. S4), partially justifying the assumption of bidirectional transport. This deviation from the expected unidirectional movement along bundles of parallel AFs may be partially due to noise-induced tracking errors that may lead to apparent bidirectional movement, especially during phases of Golgi pausing (11, 40). Moreover, in the computation of edge directionality a given Golgi may be associated with multiple edges and neighboring actin bundles may exhibit different orientations (10, 21) (details in Fig. S4). Finally, given the low Reynolds numbers of the cytoplasm (1), cytoplasmic streaming may carry temporarily detached Golgi (41) irrespective of the underlying actin bundle or its orientation (Fig. S5). In summary, our analyses indicate that transport efficiency

is a central design principle of the actin cytoskeleton in hypocotyl plant cells.

Automated Quantification of Golgi Movement. To quantify actin-based cellular transport, we studied partially elongated hypocotyl cells dually labeled with FABD-GFP and tdTomato-CesA6 (tdT-CesA6), used as a proxy for Golgi movement (42, 43). We analyzed the flow of Golgi through automated tracking (44, 45) in image series from control and LatB-treated cells (Fig. 3 *A* and *B*). Golgi bodies moved with velocity $v = 0.36 \pm 0.26\,\mathrm{s}^{-1}\cdot\mu\mathrm{m}$ in control cells (Fig. 3*C*), which is higher than $v = 0.04 \pm 0.03\,\mathrm{s}^{-1}\cdot\mu\mathrm{m}$ in LatB-treated cells, consistent with previous studies (10, 11). The Golgi movement was predominantly parallel to the major cell axis in control cells but not in LatB-treated cells (Fig. 3*D*), correlating with the orientation of actin bundles (compare with Fig. 2*G*). Thus, our automated tracking captures known features of Golgi movement and may therefore be suitable for further, more detailed analyses of Golgi behavior.

Golgi Bodies Exhibit Wiggling, Which Does Not Change Over Time or with Distance to the Actin Cytoskeleton. The movement of Golgi bodies is characterized as saltatory or stop and go (11, 30),

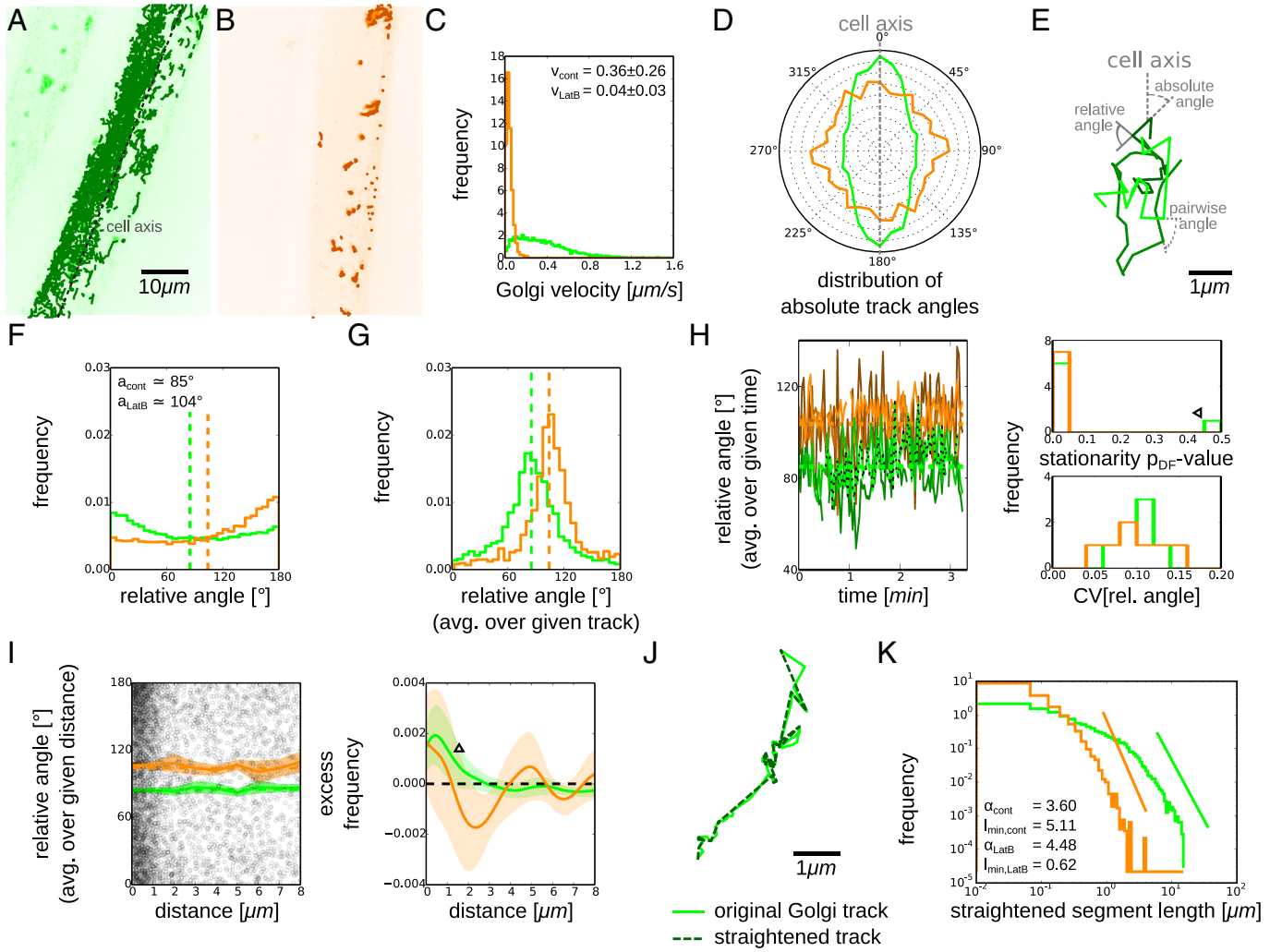

Fig. 3. Quantification of Golgi movement indicates stability and efficiency of wiggling behavior. Shown are Golgi dynamics in partially elongated hypocotyl cells of plants treated with the actin-disrupting drug LatB (orange) and untreated control plants (green). (*A*) Overlay of cellular recording of Golgi and Golgi tracks from a control cell. (*B*) Overlay of cellular recording of Golgi and Golgi tracks from a LatB-treated cell. (*C*) Distributions of Golgi velocities in LatB-treated cells, $v = 0.04 \pm 0.03\,\mathrm{s}^{-1}\cdot\mu\mathrm{m}$, and control cells, $v = 0.36 \pm 0.26\,\mathrm{s}^{-1}\cdot\mu\mathrm{m}$ (mean ± SD). (*D*) Distributions of absolute angles for control and LatB-treated cells. (*E*) Schematic of different angles used to study movement of Golgi bodies. Shown are the absolute angle between a Golgi track segment and the major cell axis (dashed gray angle) and the relative angle between two consecutive segments of a given Golgi track (solid gray angle), as well as the pairwise angle between two segments of two different Golgi tracks at a given time step (dotted gray angle). (*F*) Distributions of relative angles were broad with $a = 85° \pm 55°$ and $a = 104° \pm 55°$ for control and LatB-treated cells, respectively (dashed lines). (*G*) Distributions of relative angles, averaged over a given track, showed unimodal distributions with peaks around 85° and 104° for control and LatB-treated cells, respectively (dashed lines). (*H*) Time series of relative angles, averaged over a given time step, for each of the studied control and LatB-treated cells (*Left*). All time series were stationary; i.e., they showed no increasing or decreasing trend (*H*, *Upper Right*; augmented Dickey–Fuller unit root-test *P* values $P_{DF} < 0.05$), except one (see triangle). The fluctuations of the time series were small (*H*, *Lower Right*; CV $[a] = 0.10 \pm 0.03$). (*I*) Distributions of relative angles in dependence of distance of the track segments from the cytoskeleton (*Left*; circles show results for control cells; solid lines and shaded areas show mean ± SD). Excess of Golgi at a given distance from the cytoskeleton for control and LatB-treated cells (*I*, *Right*; compare solid lines and triangle) is given by the difference between the frequency of actual Golgi and the frequency of Golgi distributed randomly and uniformly across the cell area (dashed black line). (*J*) Example of an original Golgi track (solid light green) and the corresponding straightened track (dashed dark green), where each new track segment represents a largely straight run of the Golgi with relative angles below 90°. (*K*) Distributions of segment lengths of straightened Golgi tracks followed truncated power laws with exponents $\alpha = 3.60$ and $\alpha = 4.48$ and bounds $l_{min} = 5.11$ and $l_{min} = 0.62$ for control and LatB-treated cells, respectively.

whereby Golgi switch between periods of directed movement and undirected "wiggling" behavior (Fig. 3*E*). Whereas it has been suggested that Golgi wiggling is not specific to individual Golgi bodies (10), it is yet unclear whether Golgi wiggling changes over time or depends on the distance of the Golgi from the actin cytoskeleton. To quantify these characteristics, we computed the angles between consecutive Golgi track segments (referred to as "relative angles"; Fig. 3*E*) and refer to movement with relative angles above 90° as wiggling behavior (Fig. S6 shows another measure of wiggling). The observed distributions of relative angles across the studied cells were broad, demonstrating that both largely unidirectional movement and wiggling behavior were present (Fig. 3*F*). For LatB-treated cells, the average relative angle $a = 104^\circ \pm 55^\circ$ was larger than for control cells with $a = 85^\circ \pm 55^\circ$ and wiggling was thus more common. The distributions of relative angles averaged across a given track (Fig. 3*G*) peaked at around 90° for both untreated and LatB-treated cells, showing that the majority of Golgi tracks contained both periods of directed movement and wiggling behavior. Hence, our findings confirm that wiggling behavior is not specific to individual Golgi.

To test whether the prevalence of Golgi wiggling changes over time, we calculated the distribution of average relative angles over time (Fig. 3*H*, *Left*). We found that Golgi motility did not change during the course of the recordings (Fig. 3*H*, *Upper Right*). Moreover, the prevalence of Golgi wiggling showed only very minor fluctuations within and across time series (Fig. 3*H*, *Lower Right*; $\mathrm{CV}\,[a] = 0.10 \pm 0.03$), indicating that a constant fraction of Golgi exhibited wiggling behavior over time. Our data therefore suggest that Golgi wiggling is a common and stable cellular phenomenon. To study the effect of the distance between actin cytoskeleton and Golgi on wiggling, we computed the relative angles between consecutive track segments at a given distance from the cytoskeletal center line (Fig. 3*I*, *Left*). The frequency of Golgi was dependent on the distance to the AFs (Fig. 3*I*, *Right*), with high Golgi densities up to $2\,\mu\mathrm{m}$ from the AFs. Surprisingly, the prevalence of Golgi wiggling did not depend on the distance from the AFs (or on their thickness, Fig. S6). Moreover, although Golgi movement may vary substantially between cells, the features of Golgi movement studied here were highly consistent across cells (Fig. S6).

Movement Patterns of Golgi Resemble Search Strategies and Might Optimize Uptake and Delivery. We note that the Golgi wiggling resembles the searching behavior of foraging animals (46, 47) or microbial motion (48) that has been suggested to optimize search efficiency. This type of motion is characterized by random reorientations (Fig. 3*D*) and step sizes l that follow a power-law distribution $P(l) = \frac{\alpha-1}{l_{\min}}\left(\frac{l}{l_{\min}}\right)^{-\alpha}$. Because our image series provide snapshots with fixed time intervals, to quantify the distribution of Golgi step sizes, we considered track segments with relative angles below 90° as one step and replaced them by a single segment capturing the net displacement (Fig. 3*J*). Indeed, the distributions of step sizes of these straightened tracks followed truncated power laws with exponents $\alpha = 3.60$ and $\alpha = 4.48$ for control and LatB-treated cells, respectively [Fig. 3*K*; in particular, truncated power laws yielded higher likelihoods than exponential distributions (49)]. These exponents are larger than those typically reported for foraging animals or bacteria, $1 < \alpha < 3$ (46–48), but might indicate search strategies in small areas with a limited number of targets (50) or in the presence of obstacles or preferred areas (51–53), e.g., other organelles or delivery sites. Again, these findings were highly consistent across cells (Fig. S6).

Despite obvious differences in mechanisms underlying Golgi movement and animal foraging there may be similar goals. Namely, it is plausible that Golgi-derived material may need to be exchanged between parts of the plasma membrane, the endoplasmatic reticulum (ER), and other compartments. Assuming that these sites are not globally coordinated by the cell, the switching of Golgi between directed movement and wiggling behavior may therefore provide an efficient search strategy. This is compatible with proposed models of Golgi movement (30), such as the "vacuum cleaner" model (Golgi move through the cell and pick up products from the ER) or the "recruitment" model (Golgi pause in the vicinity of active ER sites to facilitate trafficking). Our findings might therefore indicate a connection between Golgi wiggling and the optimization of uptake and delivery of Golgi-related material throughout the cell.

The Golgi search behavior is compatible with the movement of Golgi along the actin structures. Whereas, at a given time step, the majority of Golgi stayed at the same AF, some faster Golgi moved to different AFs (Fig. S5). Moreover, it remains unclear whether Golgi bodies are transported through the cell by direct interactions with motor proteins or indirectly via cytoplasmic streaming (54). By investigating the relative movement of different Golgi at a given time step (referred to as "pairwise angles"; Fig. 3*E*), we found substantial antiparallel movement of close-by Golgi (Fig. S5). Taking into account the low Reynolds numbers of the cytoplasm (1), this antiparallel movement contradicts the assumption of indirect, cytoplasmic-streaming–induced movement and instead supports myosin-based transport of a substantial fraction of Golgi bodies. In conclusion, our data suggest that switching of Golgi to adjacent AFs is myosin dependent, whereas switching to nonadjacent AFs is due to cytoplasmic streaming that may carry the Golgi over large distances.

Local and Global Actin Network Architecture May Be Used to Predict Direction and Velocity of Golgi Movement. Our previous analyses assumed that the capacity of a given actin network edge, i.e., its average thickness, reflects its potential to transport cellular cargo (Fig. 2). To test this hypothesis, we studied the Golgi flow on two levels: First, we computed pairwise correlations between the properties of Golgi flow and actin structures, as modeled by our extracted networks. Second, we combined different edge properties of the actin networks to predict features of Golgi flow (e.g., direction and velocity), using a multiple–linear-regression approach. To this end, for the extracted actin networks (Fig. 4 *A* and *B*), we determined the local edge capacities and global edge properties that incorporate information about the importance of any given edge in the network context. Namely, we studied edge degree (measuring the total thickness of adjacent edges), the edge page rank (measuring the probability that cargo that randomly traverses the network is found at the given edge), the edge path betweenness (measuring the likelihood that the given edge lies on a shortest path through the network), and the edge flow betweenness [measuring the total maximum flow between any two nodes through the given edge (32); see Table S1 for mathematical definitions and explanations]. In parallel, from the Golgi tracks at each time step, we constructed an auxiliary Golgi flow network by copying the structure of the actin network and assigning new edge weights in the Golgi flow network according to various features of Golgi movement in the vicinity of the respective edge [e.g., the number of Golgi (Fig. 4*E*) or the direction and velocity of close-by Golgi (Fig. 4*F*)].

To investigate the relationship between actin structure and Golgi dynamics in partially elongated hypocotyl cells, we first computed the correlation between the determined edge properties of actin and Golgi flow networks. For instance, we studied the dependence of the Golgi direction and velocity on the actin edge rank. The correlation between the two properties varied over time and across cells (Fig. 4*G*). Across all studied partially elongated cells, this correlation was significant for control cells with $c_P = 0.384$, whereas no significant correlation was found for the LatB-treated cells with $c_P = -0.023$. These findings are compatible with the severely reduced flow (Fig. 3*C*) and increased

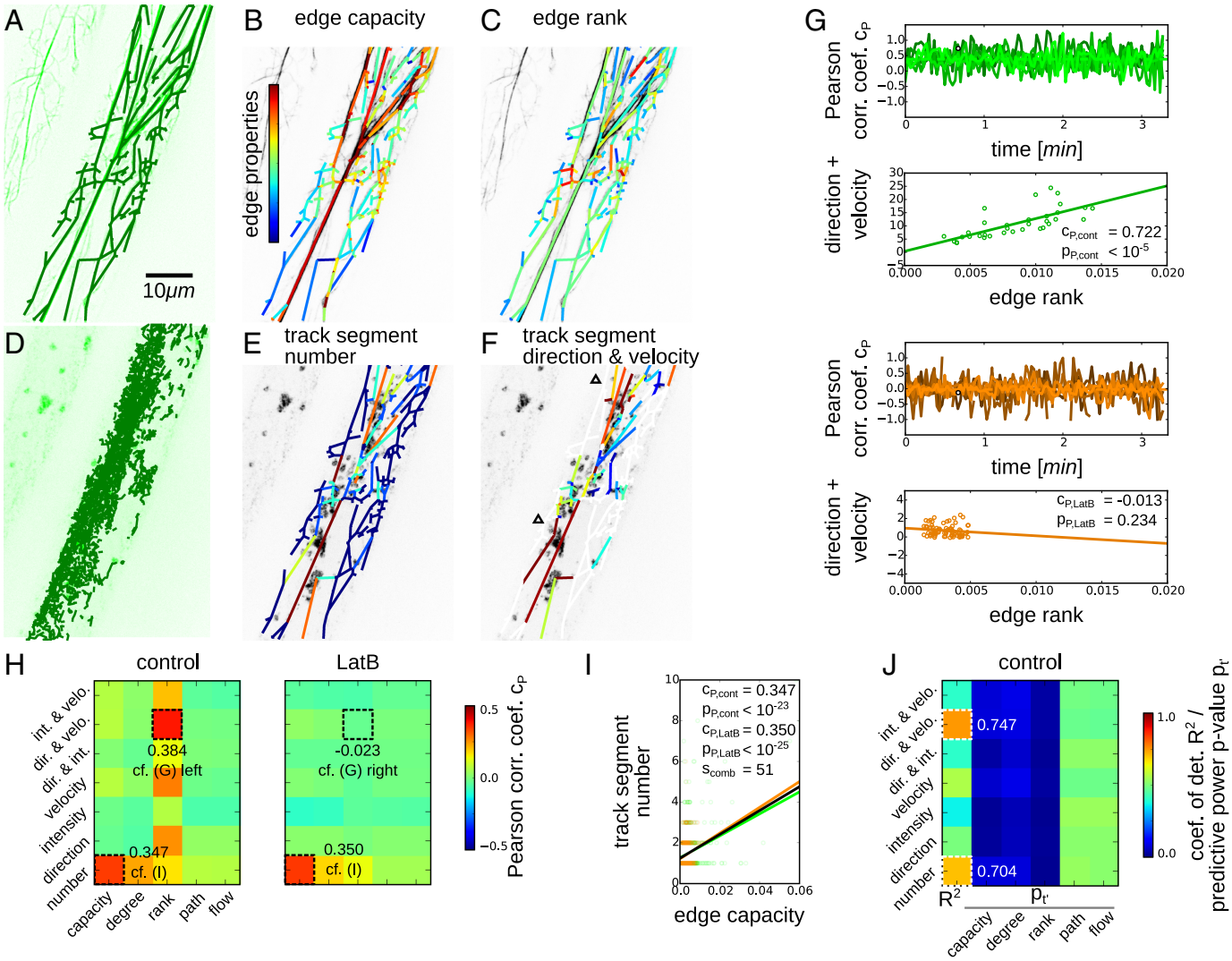

Fig. 4. Analysis of cellular organization of actin cytoskeleton enables prediction of Golgi dynamics. Shown are results for partially elongated hypocotyl cells of plants treated with the actin-disrupting drug LatB (orange) and untreated control cells (green). (*A*) Overlay of cellular recording of actin cytoskeleton and extracted actin network. (*B*) Extracted actin network with edge colors representing their capacities, i.e., average thicknesses. (*C*) Extracted actin network with edge colors representing their edge ranks. (*D*) Overlay of cellular recording of Golgi and Golgi tracks throughout the recording. (*E*) Golgi flow network with edge colors representing the numbers of close-by Golgi, i.e., track segments with starting points within 8 pixels from a given edge. (*F*) Golgi flow network with edge colors representing the direction and velocity of close-by Golgi track segments (no Golgi were assigned to white edges, e.g., triangles). (*G*) Time series of Pearson correlation coefficients c_P between Golgi track segment direction and velocity and actin edge rank (*Upper*) and exemplary scatter plots for one time point for a control and a LatB-treated cell, respectively (*Lower*; compare to open circles in *Upper*). (*H*) Heat maps of Pearson correlation coefficients c_P between different edge properties of actin and Golgi flow networks for control (*Left*) and LatB-treated (*Right*) cells. For control cells and LatB-treated cells, there was a significant correlation between the actin edge capacity and the Golgi number (compare to *I*). Correlations between the actin edge rank and Golgi direction and velocity were significant for the control cells with $c_P = 0.384$ but not for the LatB-treated cells with $c_P = -0.023$ (compare to *G*). (*I*) Scatter plots of the number of Golgi close to an edge and the respective edge capacity showed positive correlations with $c_P = 0.347$ for control and $c_P = 0.350$ for LatB-treated cells. The slope of a linear regression for the combined data was $s = 51$ (black). (*J*) Heat map of coefficients of determination R^2 for multiple linear regressions of the Golgi flow network edge properties (first column) and the respective predictive power *P* values $P_{t'}$ of the actin edge properties that were used as predictors (last five columns; one-sample two-sided *t* test *P* values $P_{t'}$ measure whether inclusion of the respective predictor improves the prediction) for the control cells. Coefficients of determination were highest for direction- and velocity-related Golgi properties ($R^2 > 0.7$). The actin capacity, degree, and rank were more reliable predictors ($P_{t'} < 0.05$) than edge flow and path betweenness ($P_{t'} \geq 0.05$).

wiggling behavior of Golgi (Fig. 3*F*) in LatB-treated cells. We further evaluated the correlations between all pairs of edge properties, averaged across the studied cells and time points (Fig. 4*H*). Some pairs of properties, such as Golgi direction and velocity and actin edge rank discussed above, were correlated for the control cells ($|c_P| > 0.2$) but not for the LatB-treated cells ($|c_P| \leq 0.2$; Fig. 4*G*). Only the number of Golgi close to a given edge was correlated with the respective edge capacity and edge degree for both control and LatB-treated cells (Fig. 4*I*). These findings show that although the flow of Golgi is severely altered by the LatB treatment, Golgi still agglomerate in the vicinity of the actin stubs (Fig. 3*I*). However, for most pairs of actin and Golgi flow network edge properties, there was no or only weak correlation ($|c_P| \leq 0.2$). Hence, whereas in particular, edge flow and path betweenness have been suggested to predict transport in real-world networks (55–57), they were not predictive of Golgi transport along the actin cytoskeleton in hypocotyl plant cells. This deviation may be due to different transport requirements in particular regions of the cell, especially during hypocotyl elongation growth (37, 58).

Because pairwise correlations were of moderate value, we then used multiple linear regression to see whether certain aspects of Golgi flow could be predicted from a combination of actin edge properties. Indeed, the number of Golgi close to an actin edge (Fig. 4*K*; coefficient of determination $R^2 = 0.704$) and the Golgi direction and velocity ($R^2 = 0.747$) were accurately predicted from the edge properties of the underlying actin cytoskeletal network. Moreover, edge capacity, edge degree, and edge rank of the actin network had higher predictive power (one-sample two-sided t test P values $P_{t'} < 0.05$ for most Golgi flow properties) than the edge path and flow betweenness ($P_{t'} \geq 0.05$). As edge capacity and edge degree reflect (semi)local actin bundling, their observed high predictive power supports the finding that actin bundling is correlated with Golgi density and velocity (Fig. S5) (10). As indicated above, the edge rank measures the (global) importance of an edge in the network context and corresponds to the probability that cargo that randomly switches between adjacent filament segments is found at the given edge, whereby thicker filaments are frequented with higher probabilities. This assumption of random movement is compatible with the wiggling of Golgi (Fig. 3).

Interestingly, these correlations between actin structures and Golgi movement were very similar for growing and fully elongated hypocotyl cells (Fig. S1). Our results were confirmed by analysis of 3D data of actin cytoskeleton and Golgi (Fig. S2). Therefore, the system-wide organization of the actin cytoskeleton in hypocotyl cells shapes, and may be used to predict, the dynamic flow of Golgi.

Finally, we note that our imaging setup captured only the outer periclinal cell side, for both 2D and 3D data. Because 3D imaging of the complete, quickly rearranging plant cytoskeleton is not yet feasible, we modeled the cylindrical geometry of the cortical cytoskeleton by periodically extending the original, 2D extracted network. Whereas cytoskeletal structures on different cell sides generally differ (e.g., refs. 59 and 60 for actin and ref. 61 for microtubules), it is parsimonious and avoids an unbiological plane-like cytoskeletal geometry. Indeed, taking into account this cylindrical geometry moderately but significantly improved the predictive power of our regression-based analyses of Golgi movement (Fig. S4). Taken together, our data show that Golgi transport in hypocotyl cells is not merely determined by the local structure of the cortical cytoskeleton, but also depends on larger architectural contexts, as well as its cylindrical geometry.

Concluding Remarks

Although the molecular details of actin monomers and filaments as well as actin-associated proteins are relatively well studied, quantifying actin-based transport in a larger cellular context remains challenging. To address this gap, we introduced an accurate image-based network representation of the actin cytoskeleton to facilitate automated and unbiased quantification of cytoskeletal phenotypes and functions. We used this framework to establish that system-level properties of the actin cytoskeleton determine key features of Golgi transport in *Arabidopsis* hypocotyl cells.

Our approach of integrating cytoskeletal network structures with tracking data of organelles is directly transferable to various biological systems and functions: In plants, in addition to the analysis of different cell types, transport of mitochondria (4, 10) and photodamage avoidance movement of chloroplasts (62) represent interesting test grounds. In animals, it has been shown that cytoplasmic streaming in fruit fly oocytes (63) and transport of lysosomes in monkey kidney cells depend on microtubules (7). Although these are interesting local correlations of cytoskeletal features and organelle transport, we expect broader, system-level understanding of these processes by the application of interdisciplinary approaches such as ours. Our automated framework paves the way for quantitative assessment of the actin cytoskeleton and trafficking in, for example, large-scale chemical and genetic screens. Moreover, our findings indicate that network-based models could be used to predict potential exchange sites of Golgi-related material. Altogether, the presented combination of experimental imaging techniques and theoretical network-based analyses provides an important step toward a systems understanding and, ultimately, control of cytoskeleton-based transport.

Materials and Methods

Plant Material and Experimental Setup. We used *Arabidopsis* Columbia-0 35S:FABD-GFP and pCesA6:tdT-CesA6 dual-labeled, 3-d-old, and dark-grown seedlings (12, 36) to study actin cytoskeleton and Golgi bodies (*SI Materials and Methods* and Movie S1). For drug and control treatment, seedlings were floated on distilled water with and without 150 nM LatB, respectively. Image series of partially elongated hypocotyl cells around 1 mm below the apical hook were captured using a spinning-disk confocal microscope with a spatial resolution of 0.133 pixel$^{-1}\cdot\mu$m and a time interval of 2 s between subsequent 2D images (64). In a slightly modified imaging setup, both growing and fully elongated cells around 1 mm and 5 mm below the apical hook, respectively, were imaged for comparison. Additionally, 3D image stacks were obtained using the same setup with 1 μm between three subsequent z slices.

Extraction and Randomization of Actin Networks. We corrected the potential drift of the seedlings using Fiji-StackReg rigid body stack registration (45, 65), compensated photobleaching by normalizing mean intensities, and improved the signal-to-noise ratio by using the Fiji-BackgroundSubtraction filter with a radius of 50 pixels (66) (*SI Materials and Methods*; see mathbiol.mpimp-golm.mpg.de/CytoSeg/ for open-source code and examples). To represent the actin cytoskeleton as a network in 2D and 3D, we enhanced filamentous structures of width v_{width} with a 2D tubeness filter (67), applied an adaptive median threshold with block size v_{thres} (68), skeletonized the resultant binary image (69), and removed all spurious connected components smaller than v_{size} pixels or with average intensities below v_{int} of the average component intensity. We identified the nodes of the network as crossings or endpoints of filaments. We added an edge between two nodes if they were directly connected by a skeleton line and assigned different edge weights such as its capacity, i.e., the average intensity along the respective filament per unit length. We gauged the four imaging parameters, using synthetic images of known cytoskeleton-like structures and manual segmentations of cytoskeleton images as a gold standard. To assess the biological relevance of the studied actin network properties, we used a first null model that distributes the nodes of the original network randomly and uniformly across the cell area (2D) or volume (3D) and shuffles edges such that their Euclidean length is preserved. A second null model shuffles only the edge properties of the original network (19).

Quantification of Golgi Movement. We automatically tracked the movement of Golgi in 2D and 3D, using Fiji-TrackMate (*SI Materials and Methods*). We detected the Golgi as particles of around 5 pixels in radius (44, 45). We then linked the Golgi in different frames, using the linear assignment problem tracker with a maximum linkage distance of 24 pixels, a maximum gap-closing distance of 24 pixels, and a maximum frame gap number of 4. To correlate actin structures with Golgi movement, we constructed auxiliary Golgi flow networks by copying the actin network. Each edge of the Golgi flow network was then assigned different weighting factors, e.g., the number of track segments within a cutoff distance of 8 pixels or the average velocity of close-by Golgi.

ACKNOWLEDGMENTS. D.B. was funded by an International Max Planck Research School scholarship. S.P. was funded by the Max Planck Society, an Australian Research Council Future Fellowship grant (FT160100218), an R@MAP Professorship at University of Melbourne, and a Dyason travel grant. S.P. and Z.N. acknowledge an International Research and Research Training Fund (Research Network and Consortia) grant.

1. Luby-Phelps K (2000) Cytoarchitecture and physical properties of cytoplasm: Volume, viscosity, diffusion, intracellular surface area. *Int Rev Cytol* 192:189–221.
2. Ellis RJ (2001) Macromolecular crowding: An important but neglected aspect of the intracellular environment. *Curr Opin Struct Biol* 11:114–119.
3. Goldstein RE, van de Meent JW (2015) A physical perspective on cytoplasmic streaming. *Interface Focus* 5:20150030.
4. Wang P, Hussey PJ (2015) Interactions between plant endomembrane systems and the actin cytoskeleton. *Front Plant Sci* 6:422.

5. Kim H, Park M, Kim SJ, Hwang I (2005) Actin filaments play a critical role in vacuolar trafficking at the Golgi complex in plant cells. *Plant Cell* 17:888–902.
6. Cheung AY, de Vries SC (2008) Membrane trafficking: Intracellular highways and country roads. *Plant Physiol* 147:1451–1453.
7. Bálint S, Verdeny Vilanova I, Sandoval Álvarez A, Lakadamyali M (2013) Correlative live-cell and superresolution microscopy reveals cargo transport dynamics at microtubule intersections. *Proc Natl Acad Sci USA* 110:3375–3380.
8. Volkmann D, Baluska F (1999) Actin cytoskeleton in plants: From transport networks to signaling networks. *Microsc Res Tech* 47:135–154.
9. Tominaga M, et al. (2000) The role of plant villin in the organization of the actin cytoskeleton, cytoplasmic streaming and the architecture of the transvacuolar strand in root hair cells of Hydrocharis. *Planta* 210:836–843.
10. Akkerman M, Overdijk EJ, Schel JH, Emons AMC, Ketelaar T (2011) Golgi body motility in the plant cell cortex correlates with actin cytoskeleton organization. *Plant Cell Physiol* 52:1844–1855.
11. Nebenführ A, et al. (1999) Stop-and-go movements of plant Golgi stacks are mediated by the acto-myosin system. *Plant Physiol* 121:1127–1142.
12. Sampathkumar A, et al. (2013) Patterning and lifetime of plasma membrane-localized cellulose synthase is dependent on actin organization in Arabidopsis interphase cells. *Plant Physiol* 162:675–688.
13. Staiger CJ, Baluška F, Volkmann D, Barlow P (2000) *Actin: A Dynamic Framework for Multiple Plant Cell Functions* (Springer, Amsterdam), 1st Ed.
14. Shimmen T, Yokota E (2004) Cytoplasmic streaming in plants. *Curr Opin Cell Biol* 16:68–72.
15. Woodhouse FG, Goldstein RE (2013) Cytoplasmic streaming in plant cells emerges naturally by microfilament self-organization. *Proc Natl Acad Sci USA* 110:14132–14137.
16. Neri I, Kern N, Parmeggiani A (2013) Modeling cytoskeletal traffic: An interplay between passive diffusion and active transport. *Phys Rev Lett* 110:098102.
17. Houtman D, et al. (2007) Hydrodynamic flow caused by active transport along cytoskeletal elements. *Europhys Lett* 78:18001.
18. Ando D, Korabel N, Huang KC, Gopinathan A (2015) Cytoskeletal network morphology regulates intracellular transport dynamics. *Biophys J* 109:1574–1582.
19. Breuer D, et al. (2014) Quantitative analyses of the plant cytoskeleton reveal underlying organizational principles. *J R Soc Interface* 11:20140362.
20. Breuer D, Nikoloski Z (2014) img2net: Automated network-based analysis of imaged phenotypes. *Bioinformatics* 30:3291–3292.
21. Yanagisawa M, et al. (2015) Patterning mechanisms of cytoskeletal and cell wall systems during leaf trichome morphogenesis. *Nat Plants* 1:15014.
22. Kitano H (2002) Systems biology: A brief overview. *Science* 295:1662–1664.
23. Gardel ML, et al. (2004) Elastic behavior of cross-linked and bundled actin networks. *Science* 304:1301–1305.
24. Banerjee N, Park J (2015) Modeling and simulation of biopolymer networks: Classification of the cytoskeleton models according to multiple scales. *Korean J Chem Engineer* 32:1207–1217.
25. Mayerich D, Bjornsson C, Taylor J, Roysam B (2012) NetMets: Software for quantifying and visualizing errors in biological network segmentation. *BMC Bioinformatics* 13:S7.
26. Xu T, et al. (2015) SOAX: A software for quantification of 3D biopolymer networks. *Sci Rep* 5:9081.
27. Clark AG, Dierkes K, Paluch EK (2013) Monitoring actin cortex thickness in live cells. *Biophys J* 105:570–580.
28. Boevink P, et al. (1998) Stacks on tracks: The plant Golgi apparatus traffics on an actin/ER network. *Plant J* 15:441–447.
29. Dupree P, Sherrier DJ (1998) The plant Golgi apparatus. *Biochim Biophys Acta* 1404:259–270.
30. Nebenführ A, Staehelin LA (2001) Mobile factories: Golgi dynamics in plant cells. *Trends Plant Sci* 6:160–167.
31. Wakatsuki T, Schwab B, Thompson NC, Elson EL (2001) Effects of cytochalasin D and latrunculin B on mechanical properties of cells. *J Cell Sci* 114:1025–1036.
32. Newman M (2009) *Networks: An Introduction* (Oxford Univ Press, Oxford), 1st Ed.
33. Claessens MM, Bathe M, Frey E, Bausch AR (2006) Actin-binding proteins sensitively mediate F-actin bundle stiffness. *Nat Mater* 5:748–753.
34. Breuer D, Nikoloski Z (2015) DeFiNe: An optimisation-based method for robust disentangling of filamentous networks. *Sci Rep* 5:18267.
35. Fu Y, Li H, Yang Z (2002) The rop2 GTPase controls the formation of cortical fine f-actin and the early phase of directional cell expansion during Arabidopsis organogenesis. *Plant Cell* 14:777–794.
36. Sheahan MB, Staiger CJ, Rose RJ, McCurdy DW (2004) A green fluorescent protein fusion to actin-binding domain 2 of Arabidopsis fimbrin highlights new features of a dynamic actin cytoskeleton in live plant cells. *Plant Physiol* 136:3968–3978.
37. Gendreau E, et al. (1997) Cellular basis of hypocotyl growth in Arabidopsis thaliana. *Plant Physiol* 114:295–305.
38. Fu Y, Wu G, Yang Z (2001) Rop GTPase–dependent dynamics of tip-localized F-actin controls tip growth in pollen tubes. *J Cell Biol* 152:1019–1032.
39. Thomas C, et al. (2009) Actin bundling in plants. *Cell Motil Cytoskeleton* 66:940–957.
40. Crowell EF, et al. (2009) Pausing of Golgi bodies on microtubules regulates secretion of cellulose synthase complexes in Arabidopsis. *Plant Cell* 21:1141–1154.
41. Tominaga M, et al. (2003) Higher plant myosin XI moves processively on actin with 35 nm steps at high velocity. *EMBO J* 22:1263–1272.
42. Paredez AR, Somerville CR, Ehrhardt DW (2006) Visualization of cellulose synthase demonstrates functional association with microtubules. *Science* 312:1491–1495.
43. Luo Y, et al. (2015) V-ATPase activity in the TGN/EE is required for exocytosis and recycling in Arabidopsis. *Nat Plants* 1:15094.
44. Jaqaman K, et al. (2008) Robust single-particle tracking in live-cell time-lapse sequences. *Nat Methods* 5:695–702.
45. Schindelin J, et al. (2012) Fiji: An open-source platform for biological-image analysis. *Nat Methods* 9:676–682.
46. Viswanathan GM, et al. (1999) Optimizing the success of random searches. *Nature* 401:911–914.
47. Humphries NE, Weimerskirch H, Queiroz N, Southall EJ, Sims DW (2012) Foraging success of biological Lévy flights recorded in situ. *Proc Natl Acad Sci USA* 109:7169–7174.
48. Matthäus F, Jagodic M, Dobnikar J (2009) E. coli superdiffusion and chemotaxis-search strategy, precision, and motility. *Biophys J* 97:946–957.
49. Clauset A, Shalizi CR, Newman M (2009) Power-law distributions in empirical data. *SIAM Rev* 51:661–703.
50. Zhao K, et al. (2015) Optimal Lévy-flight foraging in a finite landscape. *J R Soc Interface* 12:20141158.
51. Sutantyo DK, Kernbach S, Levi P, Nepomnyashchikh VA (2010) Multi-robot searching algorithm using Lévy flight and artificial potential field. *IEEE SSRR* 1:1–6.
52. Viswanathan GM, Da Luz MG, Raposo EP, Stanley HE (2011) *The Physics of Foraging: An Introduction to Random Searches and Biological Encounters* (Cambridge Univ Press, New York), 1st Ed.
53. Hills TT, Kalff C, Wiener JM (2013) Adaptive Lévy processes and area-restricted search in human foraging. *PLoS One* 8:e60488.
54. Buchnik L, Abu-Abied M, Sadot E (2014) Role of plant myosins in motile organelles: Is a direct interaction required? *J Integr Plant Biol* 57:23–30.
55. Borgatti SP (2005) Centrality and network flow. *Soc Networks* 27:55–71.
56. Jiang B, Zhao S, Yin J (2008) Self-organized natural roads for predicting traffic flow: A sensitivity study. *J Stat Mech* 2008:P07008.
57. Kazerani A, Winter S (2009) Can betweenness centrality explain traffic flow? *Proceedings of the 12th AGILE International Conference on Geographic Information Science*, eds Sester M, Bernard L, Paelke V (Leibniz Universität Hannover, Hannover, Germany), pp 1702–1717.
58. Geisler DA, Sampathkumar A, Mutwil M, Persson S (2008) Laying down the bricks: Logistic aspects of cell wall biosynthesis. *Curr Opin Plant Biol* 11:647–652.
59. Jacques E, Verbelen JP, Vissenberg K (2014) Review on shape formation in epidermal pavement cells of the Arabidopsis leaf. *Funct Plant Biol* 41:914–921.
60. Armour WJ, Barton DA, Law AM, Overall RL (2015) Differential growth in periclinal and anticlinal walls during lobe formation in Arabidopsis cotyledon pavement cells. *Plant Cell* 27:2484–2500.
61. Peaucelle A, Wightman R, Höfte H (2015) The control of growth symmetry breaking in the Arabidopsis hypocotyl. *Curr Biol* 25:1746–1752.
62. Kasahara M, et al. (2002) Chloroplast avoidance movement reduces photodamage in plants. *Nature* 420:829–832.
63. Ganguly S, Williams LS, Palacios IM, Goldstein RE (2012) Cytoplasmic streaming in Drosophila oocytes varies with kinesin activity and correlates with the microtubule cytoskeleton architecture. *Proc Natl Acad Sci USA* 109:15109–15114.
64. Sampathkumar A, et al. (2011) Live cell imaging reveals structural associations between the actin and microtubule cytoskeleton in Arabidopsis. *Plant Cell* 23:2302–2313.
65. Thévenaz P, Ruttimann UE, Unser M (1998) A pyramid approach to subpixel registration based on intensity. *IEEE Trans Image Process* 7:27–41.
66. Sternberg SR (1983) Biomedical image processing. *IEEE Comput Soc* 16:22–34.
67. Sato Y, et al. (1998) Three-dimensional multi-scale line filter for segmentation and visualization of curvilinear structures in medical images. *Med Image Anal* 2:143–168.
68. van der Walt S, et al. (2014) scikit-image: Image processing in Python. *PeerJ* 2:e453.
69. Haralick RM, Sternberg SR, Zhuang X (1987) Image analysis using mathematical morphology. *IEEE Trans Pattern Anal Mach Intell* 4:532–550.
70. van Rossum G, Drake FL (2011) *Python Language Reference Manual* (Network Theory, Godalming, UK), 1st Ed.
71. Dhondt S, et al. (2012) Quantitative analysis of venation patterns of Arabidopsis leaves by supervised image analysis. *Plant J* 69:553–563.
72. Baumgarten W, Hauser MJ (2012) Computational algorithms for extraction and analysis of two-dimensional transportation networks. *J Comput Interdiscip Sci* 3:107–16.
73. Cooper GM (2000) *The Cell: A Molecular Approach* (ASM, Boston), 2nd Ed.
74. Dirnberger M, Kehl T, Neumann A (2014) NEFI: Network extraction from images. *Sci Rep* 5:15669.
75. Obara B, Grau V, Fricker MD (2012) A bioimage informatics approach to automatically extract complex fungal networks. *Bioinformatics* 28:2374–2381.
76. Obara B, Fricker M, Gavaghan D, Grau V (2012) Contrast-independent curvilinear structure detection in biomedical images. *IEEE Trans Image Process* 21:2572–2581.
77. Mayerich DM, Keyser J (2008) Filament tracking and encoding for complex biological networks. *Proceedings of the 2008 ACM Symposium on Solid and Physics Modeling*, eds Haines E, McGuire M (ACM, New York), pp 353–358.
78. Meijering E (2010) Neuron tracing in perspective. *Cytometry A* 77:693–704.
79. Caldarelli G, Capocci A, De Los Rios P, Munoz MA (2002) Scale-free networks from varying vertex intrinsic fitness. *Phys Rev Lett* 89:258702.
80. Cover TM, Hart PE (1967) Nearest neighbor pattern classification. *IEEE Trans Inf Theory* 13:21–27.
81. Belsley DA (2006) *Encyclopedia of Statistical Sciences* (Wiley Online Library, Bethesda), 2nd Ed.
82. Dijkstra EW (1959) A note on two problems in connexion with graphs. *Numer Math* 1:269–271.
83. Berger F, Keller C, Klumpp S, Lipowsky R (2015) External forces influence the elastic coupling effects during cargo transport by molecular motors. *Phys Rev E* 91:022701.
84. Klumpp S, Lipowsky R (2005) Cooperative cargo transport by several molecular motors. *Proc Natl Acad Sci USA* 102:17284–17289.
85. Staiger CJ, et al. (2009) Actin filament dynamics are dominated by rapid growth and severing activity in the Arabidopsis cortical array. *J Cell Biol* 184:269–280.

LETTERS
https://doi.org/10.1038/s41477-019-0418-8
nature plants

Live-cell imaging of the cytoskeleton in elongating cotton fibres

Yanjun Yu[1,2,7], Shenjie Wu[3,7], Jacqueline Nowak[4,5,6,7], Guangda Wang[1,2], Libo Han[1,2], Zhidi Feng[1,2], Amelie Mendrinna[4], Yinping Ma[1,2], Huan Wang[1,2], Xiaxia Zhang[1,2], Juan Tian[1,2], Li Dong[1,2], Zoran Nikoloski[5,6], Staffan Persson[4*] and Zhaosheng Kong[1,2*]

Cotton (*Gossypium hirsutum*) fibres consist of single cells that grow in a highly polarized manner, assumed to be controlled by the cytoskeleton[1–3]. However, how the cytoskeletal organization and dynamics underpin fibre development remains unexplored. Moreover, it is unclear whether cotton fibres expand via tip growth or diffuse growth[2–4]. We generated stable transgenic cotton plants expressing fluorescent markers of the actin and microtubule cytoskeleton. Live-cell imaging revealed that elongating cotton fibres assemble a cortical filamentous actin network that extends along the cell axis to finally form actin strands with closed loops in the tapered fibre tip. Analyses of F-actin network properties indicate that cotton fibres have a unique actin organization that blends features of both diffuse and tip growth modes. Interestingly, typical actin organization and endosomal vesicle aggregation found in tip-growing cell apices were not observed in fibre tips. Instead, endomembrane compartments were evenly distributed along the elongating fibre cells and moved bi-directionally along the fibre shank to the fibre tip. Moreover, plus-end tracked microtubules transversely encircled elongating fibre shanks, reminiscent of diffusely growing cells. Collectively, our findings indicate that cotton fibres elongate via a unique tip-biased diffuse growth mode.

Cotton (*Gossypium hirsutum*) fibres are highly specialized, unicellular seed trichomes that develop through four distinct stages: fibre initiation, fibre elongation, secondary cell wall synthesis and maturation[5,6]. The fibre cells undergo highly polarized growth, with the length-to-diameter ratio reaching 1,000 to 3,000[5]. During growth, the cotton fibres produce an astounding amount of cellulose that accounts for more than 95% of the dry weight of mature fibres[5]. Therefore, in addition to their importance for the textile industry[7], cotton fibres provide an excellent model to investigate polar cell elongation and cellulose biosynthesis[5,6]. Reverse genetic studies revealed that many genes encoding proteins associated with the cytoskeleton are essential for fibre elongation and cell wall synthesis[1,8–12]. In addition, comparative transcriptomic and genomic analyses, as well as genetic studies of natural fibre mutants, have demonstrated that the cytoskeleton has greatly contributed to domestication and cotton fibre traits across locations in Asia, Africa and the Americas[13–15]. Consequently, many cytoskeleton-related genes were positively selected during cotton domestication; for example, several profilin-encoding genes, the *FORMIN HOMOLOGY INTERACTING PROTEIN1* (*FIP1*) gene and the gene encoding a type XI-K myosin (GhXIK; Gh_A13G1707) were selected for cotton fibre elongation[16–18]. It is therefore of great importance to study and understand how the cytoskeleton functions in cotton fibre development.

Difficulties in generating stable transformants, and subsequent live-cell imaging, of cotton fibres have impaired visualization and analyses of the cytoskeleton. Although immunolabelling of fixed, cultured cotton fibres has been used to study cytoskeletal features during fibre development[1], it is difficult to discern how the fixation protocols affect the organization of the cytoskeleton, and the spatio-temporal behaviour of the cytoskeleton during cotton fibre growth remains unexplored. Most plant cells expand via diffuse growth, in which cell expansion and cell wall synthesis take place relatively evenly across the entire cell surface. By contrast, some specialized cell types, such as pollen tubes and root hairs, exhibit tip growth, in which cell expansion and wall deposition occur at the cell apex[19,20]. Due to their highly elongated morphology, cotton fibre cells have often been regarded as tip-growing cells[2,3]. However, a diffuse growth mode has been proposed due to the presence of transversely arranged microtubules perpendicular to the growth axis of elongating cotton fibres and flax phloem fibres[4,9,21–24]. This discrepancy prompted scientists to propose a linear cell growth hypothesis for fibre elongation, in which the fibre shank expands via diffuse growth and the fibre apex via tip growth[2]. The dispute, however, remains unresolved, and it is therefore not clear whether cotton fibre cells elongate via diffuse growth, tip growth or linear growth.

To investigate the spatial organization and dynamics of the actin cytoskeleton in fibre cells, we introduced the actin filament (F-actin) reporter *ABD2–GFP* into cotton via stable transformation. Homozygous transgenic T3 progeny lines, which were indistinguishable from wild-type plants and expressed detectable levels of the F-actin reporter *ABD2-GFP*, were selected for subsequent live-cell imaging (Supplementary Fig. 1a,b). We observed intact and dynamic F-actin networks in various cell types of the transgenic lines (Supplementary Fig. 1c). Together, these results indicate that ABD2–GFP can be produced in stable transgenic cotton lines and that the ABD2–GFP labelling did not disturb the growth and development of the cotton plants.

To explore the organization of the actin cytoskeleton during cotton fibre development, we acquired *z*-stack images of living fibre cells at various developmental stages. Notably, the actin cytoskeleton forms a continuous cortical network in growing cotton fibres

[1]State Key Laboratory of Plant Genomics, Institute of Microbiology, Academy of Seed Design, Chinese Academy of Sciences, Beijing, China. [2]University of Chinese Academy of Sciences, Beijing, China. [3]Cotton Research Institute, Shanxi Academy of Agricultural Sciences, Yucheng, China. [4]School of Biosciences, University of Melbourne, Melbourne, Victoria, Australia. [5]Systems Biology and Mathematical Modeling, Max Planck Institute of Molecular Plant Physiology, Potsdam, Germany. [6]Bioinformatics, Institute of Biochemistry and Biology, University of Potsdam, Potsdam, Germany. [7]These authors contributed equally: Yanjun Yu, Shenjie Wu, Jacqueline Nowak. *e-mail: Staffan.persson@unimelb.edu.au; zskong@im.ac.cn

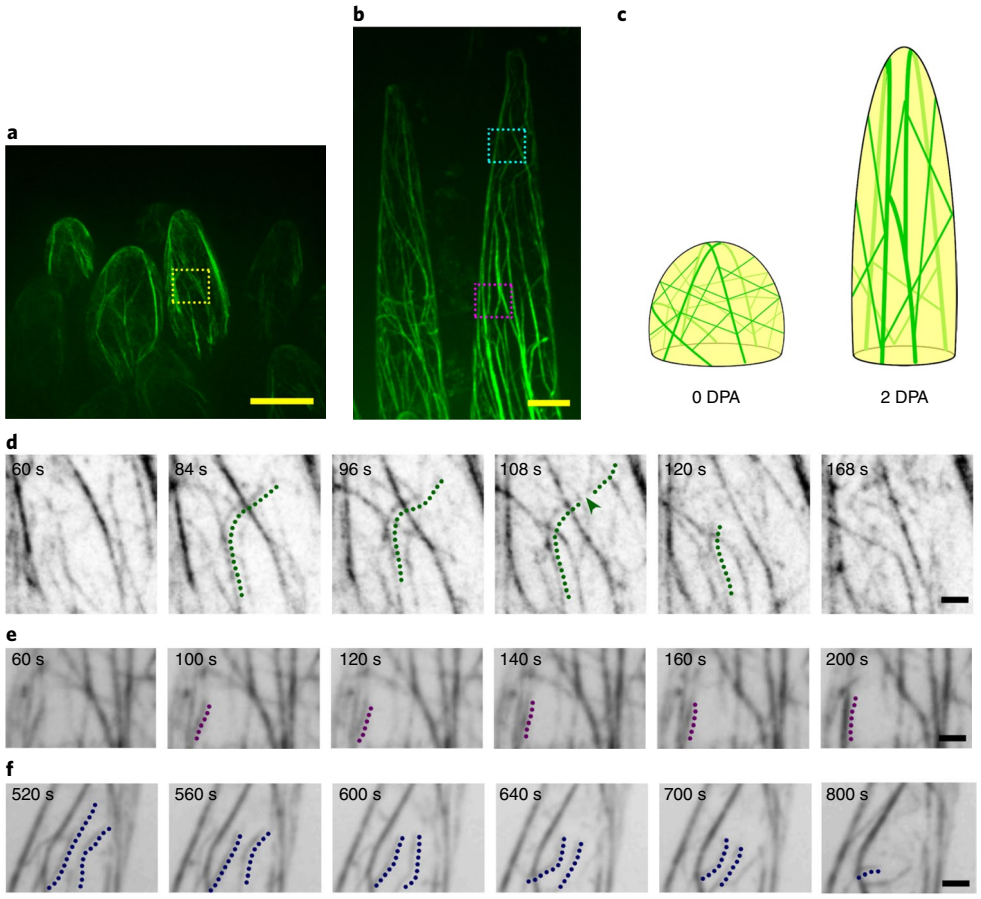

Fig. 1 | F-actin architectures and dynamics in cotton fibre cells at different developmental stages. a, A maximum projection of 21 *z*-slices (0.5 µm step size) illustrating F-actin architecture and dynamics in fibre initials. Scale bar, 10 µm. **b**, A maximum projection of 19 *z*-slices (0.5 µm step size) showing the F-actin architecture and dynamics in elongating cotton fibre cells. Scale bar, 10 µm. **c**, Illustrations showing the features of the spatial F-actin architectures in fibre cells at different developmental stages: left, at the initiating stage; right, at the elongating stage. **d**, 4D F-actin images (21 *z*-slices, 0.5 µm step size; 24 time series) of a close-up view indicated by the dotted yellow box in **a**, illustrating a severing event (green arrowhead). Scale bar, 2 µm. **e**, 4D F-actin images (19 *z*-slices, 0.5 µm step size; 24 time series) of a close-up view indicated by the dotted purple box in **b**, illustrating a bundling event. Scale bar, 2 µm. **f**, 4D F-actin images of a close-up view indicated by the dotted cyan box in **b**, illustrating a de-polymerization event. Scale bar, 2 µm. Representative images for fibres of 0 DPA (**a**,**d**) and 2 DPA (**b**,**e**,**f**) are shown based on data from six plants in three independent experiments.

(Supplementary Fig. 2a,b and Supplementary Video 1). To obtain a better understanding of the F-actin architecture, we reconstructed three-dimensional (3D) image stacks of the ABD2–GFP fluorescence through optical sectioning of fibre cells at different developmental stages (Supplementary Fig. 2c–h). Fibre initials at the day of anthesis (day zero post anthesis, 0 DPA) contained a dome-shaped, fine cortical network, encircling the cavity of fibre cells (Supplementary Fig. 2c,d and Supplementary Video 2). Elongating fibre cells displayed a barrel-shaped F-actin structure and longitudinally aligned actin bundles (Supplementary Fig. 2e–h and Supplementary Video 2). These results demonstrate that the actin cytoskeleton preferentially assembles into cortical networks during cotton fibre elongation.

To gain insight into the spatio-temporal behaviour of the actin cytoskeleton during cotton fibre elongation, we monitored the F-actin dynamics at different developmental stages (Fig. 1a,b and Supplementary Videos 3 and 4). In fibres at 0 DPA, we observed uniformly distributed, fine actin filaments assembled into a dome-shaped F-actin cage at the cell cortex of protruding fibre initials, with only few actin bundles (Fig. 1a,c and Supplementary Video 3). During subsequent fibre elongation, the dome-shaped F-actin meshwork underwent dynamic remodelling. At 2 DPA, the F-actin network assembled axially into bundles to form extended, hollow F-actin barrels at the cortex of the elongating fibre cells (Fig. 1b,c and Supplementary Video 4). The barrel-shaped structure of the actin network comprised a backbone of longitudinally aligned actin cables and a fine F-actin meshwork linking the actin cables. Collectively, our live-cell observations indicate that the actin cytoskeleton undergoes substantial rearrangements during fibre growth (Fig. 1c).

We next monitored and measured parameters that underpin the actin dynamics, such as severing, bundling and de-polymerization (Fig. 1d–f), in fibre initials (0 DPA) and in rapidly elongating fibre cells (2 DPA; Supplementary Fig. 3a–g and Supplementary Table 1). While the F-actin amount was comparable at the two developmental stages, the severing frequency was significantly lower in the elongating cells (Supplementary Fig. 3a,b). Notably, the F-actin density, skewness, length, shrinkage and elongation rates were significantly higher at 2 DPA than at 0 DPA (Supplementary Fig. 3c–g). These characteristics are in accordance with the increased number of F-actin bundles that we observed during fibre elongation.

To compare different features of the actin cytoskeleton organization between cells that use either diffuse or tip growth as their main expansion mode, we imaged different cell types of cotton plant expressing the ABD2–GFP marker and compared the actin features to those of cotton fibres. We chose to image elongating etiolated

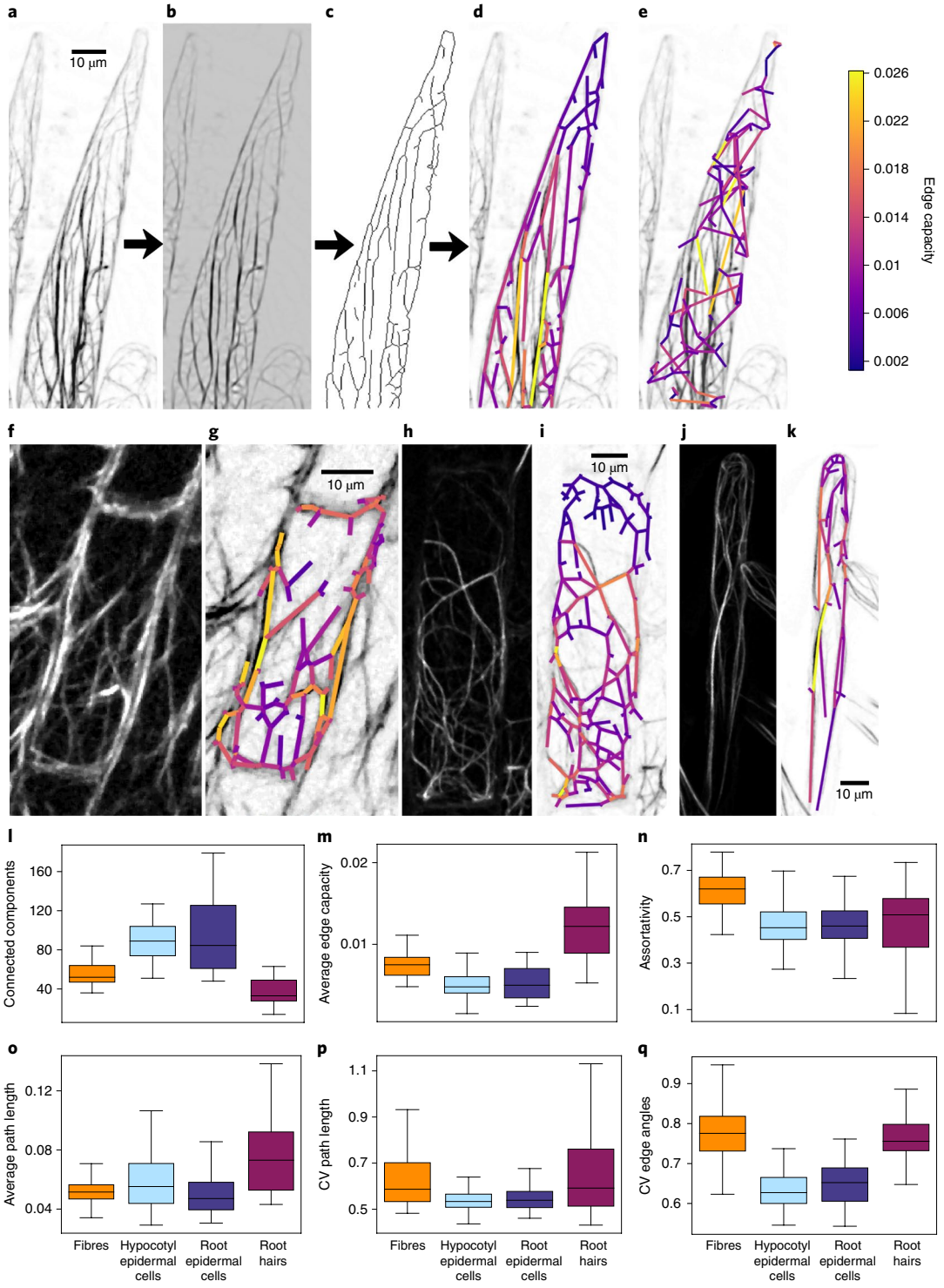

Fig. 2 | Automated network extraction analysis shows that the F-actin organization in cotton fibres blends features of that in tip- and diffuse-growth cells. a–**e**, Automated extraction of networks from actin cytoskeletal image data from cotton fibres. **a**, A greyscale confocal image of cotton fibre after bleach correction, background subtraction and stack registration. **b**, Enhanced tube-like structures after application of a tubeness filter. **c**, A skeletonized cytoskeleton image after elimination of small or low-intensity objects. **d**, A greyscale cytoskeleton image with the extracted network overlaid, with the edges colour-coded according to their capacity. **e**, A greyscale cytoskeleton image with a randomized network overlaid. The edge capacities are indicated as per the colour scheme to the far right. **f**–**k**, Single-frame and greyscale cytoskeleton images with the extracted network overlaid, with the edges colour-coded according to their capacity from different cell types: elongating cotton hypocotyl epidermal cells (**f**,**g**), elongating cotton root epidermal cells (**h**,**i**) and cotton root hairs (**j**,**k**). For each cell type (**a**,**f**,**h**,**i**), representative images of 12 fibre cells from five independent replicates were imaged and networks were extracted. **l**–**q**, Different properties of extracted networks from cotton fibres (orange), elongating hypocotyl epidermal cells (light blue), elongating root epidermal cells (dark blue) and root hairs (magenta). We then calculated the properties from 250, 161, 150 and 132 extracted networks of cotton fibres, elongating cotton hypocotyl epidermal cells, elongating cotton root epidermal cells and cotton root hairs, respectively. The properties are indicated on the *y* axes of the graphs. The box plots are shown with median (horizontal line), 25th and 75th percentiles (box edges) and 1.5× interquartile range (whiskers).

hypocotyl cells and root epidermal cells of the elongation zone as examples of cells that grow through diffuse growth, and root hair cells that expand via tip growth (Fig. 2a–k). The actin cytoskeleton was imaged, processed and segmented as described in Breuer et al.[25] (Fig. 2a–d). The resulting binary images were compared to the original images to ensure that we captured the majority of the F-actin[25], and were skeletonized to obtain networks that are defined by nodes (F-actin intersections or end-points), edges (F-actin that connects the nodes) and weights (F-actin bundling)[25] (Fig. 2d,e). We next calculated properties for the extracted networks (that is, actin organization) and assessed the similarity of their network properties.

In terms of transport-related network properties, we first looked at the number of connected components, which estimates the overall connectedness of the actin network (Fig. 2l). The cotton fibres exhibited a significantly larger number of connected components than that of root hairs (independent two-sample *t*-test *P* value $P_t < 10^{-39}$), but significantly smaller than that of elongating hypocotyl cells ($P_t < 10^{-41}$) and root epidermal cells ($P_t < 10^{-46}$, Fig. 2l). Furthermore, the average edge capacity was significantly larger in cotton fibres than in elongating hypocotyls ($P_t < 10^{-48}$) and root epidermal cells ($P_t < 10^{-35}$), but significantly smaller than in root hairs ($P_t < 10^{-44}$; Fig. 2m). To determine the network heterogeneity, which estimates the degree of clustering of F-actin and bundles, we calculated the assortativity of the networks. We found that the cotton fibres showed a significantly higher degree of clustering than all of the other cell types (elongating hypocotyls, $P_t < 10^{-53}$; root epidermal cells, $P_t < 10^{-51}$; root hairs, $P_t < 10^{-26}$; Fig. 2n). The average shortest path length quantifies the reachability from one point to another in the actin network. This metric was similar in cotton fibres and both elongating hypocotyls ($P_t < 10^{-3}$) and root epidermal cells ($P_t < 10^{-3}$), but significantly smaller than that of root hairs ($P_t < 10^{-26}$, Fig. 2o). Therefore, our results indicate a disposition towards short path length in cotton fibres. Moreover, cotton fibres showed a significantly larger coefficient of variation of the shortest path lengths than elongating hypocotyls ($P_t < 10^{-16}$) and root epidermal cells ($P_t < 10^{-12}$), but were similar to root hairs ($P_t < 0.2$) with respect to this property (Fig. 2p). These results indicate that different points in the actin networks of cotton fibres may be reached at almost the same cost, as measured by the path length in the actin cytoskeleton. The estimation of the coefficient of variation of the edge angles quantifies the degree of actin bundles, as the actin bundles typically are organized along the longitudinal axis of cells[25]. Here, we found that elongating hypocotyls ($P_t < 10^{-72}$) and root epidermal cells ($P_t < 10^{-57}$) displayed a significantly reduced coefficient of variation of the edge angles as compared to cotton fibres and root hairs (Fig. 2q). Our results show that some of the actin network properties of cotton fibres are similar to elongating hypocotyls while other properties align better with root hairs. Therefore, the cotton fibre actin cytoskeleton exhibits a network organization that is distinct from both diffusely growing cells and tip-growing cells.

Diffuse growth is supported by the organization of cortical microtubules, which orient the deposition of nascent cellulose microfibrils to steer anisotropic growth of plant cells[26,27]. To explore the spatial organization and dynamics of the microtubule cytoskeleton in fibre cells, an mCherry-tagged microtubule plus-end tracking protein, EB1b, which has been used extensively to track growing microtubules[28,29], was transformed into cotton. Stable transgenic lines, which were indistinguishable from wild-type plants and displayed stable and bright mCherry fluorescence in various cell types, were selected for subsequent live-cell imaging (Supplementary Fig. 4 and Supplementary Videos 5 and 6). We acquired time-lapse images in living fibre cells at different developmental stages. Notably, mCherry–EB1b dynamics suggested a haphazard cortical microtubule array in the dome-shaped fibre initials (Fig. 3a and Supplementary Video 7). Strikingly, in elongating fibre cells (2 DPA), the mCherry–EB1b dynamics were largely occurring

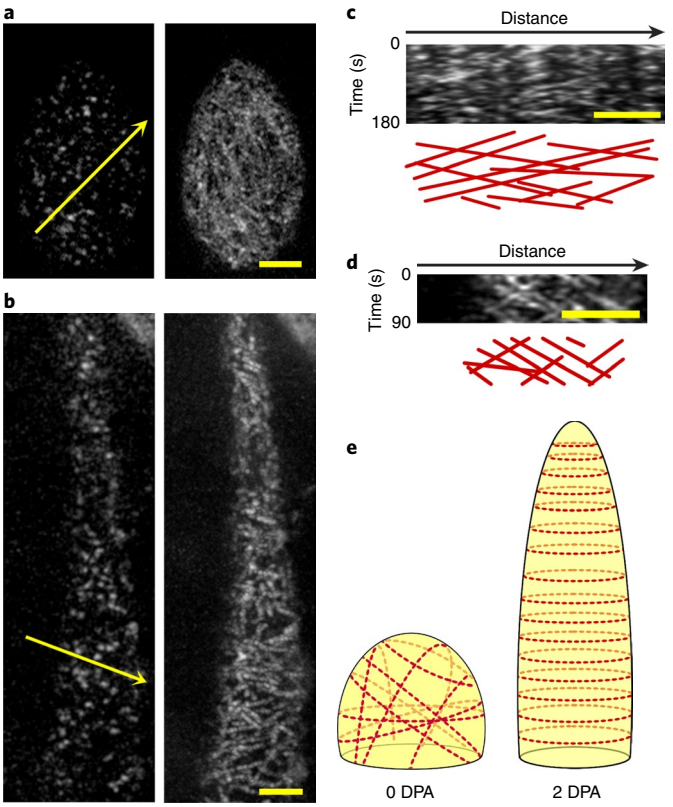

Fig. 3 | Microtubule array organization, tracked by the plus-end tracking protein EB1b, in cotton fibre cells during development. a, A single-frame mCherry–EB1b image illustrating plus-ends of growing microtubules in cotton fibre initials at 0 DPA (left) and the maximum projection of 60 frames of time-lapse mCherry–EB1b images illustrating cortical microtubule networks surrounding the fibre initial (right). The yellow arrow indicates the area and direction for kymograph analysis in **c**. **b**, A single-frame mCherry–EB1b image illustrating plus-ends of growing microtubules in elongating cotton fibre cells at 2 DPA (left) and the maximum projection of 30 frames of time-lapse mCherry–EB1b images illustrating transverse cortical microtubule arrays encircling the elongating fibre cell (right). The yellow arrow indicates the area and direction for kymograph analysis in **d**. **c**,**d**, Kymograph analysis displays the polarity of new microtubules in fibre initials (**c**) and elongating fibre cells (**d**). The red lines track the directions of EB1b particle movements in schematic kymographs. **e**, Illustrations showing the features of cortical microtubule arrays in fibre cells at different developmental stages: at the initiating stage (left) and at the elongating stage (right). Scale bars, 10 μm. Representative images for fibres at 0 DPA (**a**,**c**) and 2 DPA (**b**,**d**) are shown based on data from eight plants in three independent experiments.

transversely to the fibre growth axis, indicative of a transversely oriented microtubule array (Fig. 3b and Supplementary Video 8). Such microtubule organization is characteristic of diffuse-growing cells[30,31]. Kymograph analysis revealed that microtubules grew and shrank in a bi-directional mode in fibre cells during development, with a higher density in fibre initials than that in elongating fibres (Fig. 3c,d and Supplementary Videos 7 and 8). A microtubule-depleted zone (MDZ) was observed at the apex of elongating trichome branches, which is assumed to extend as a tip-biased diffuse mode[32,33]. Thus, we investigated whether MDZ occurs at the apex of elongating fibres. However, EB1b proved to be insufficient as a marker to acquire 3D reconstruction images of high quality at the fibre cell apex. We therefore performed immunostaining of microtubules of the fibres and observed clear MDZ at the fibre

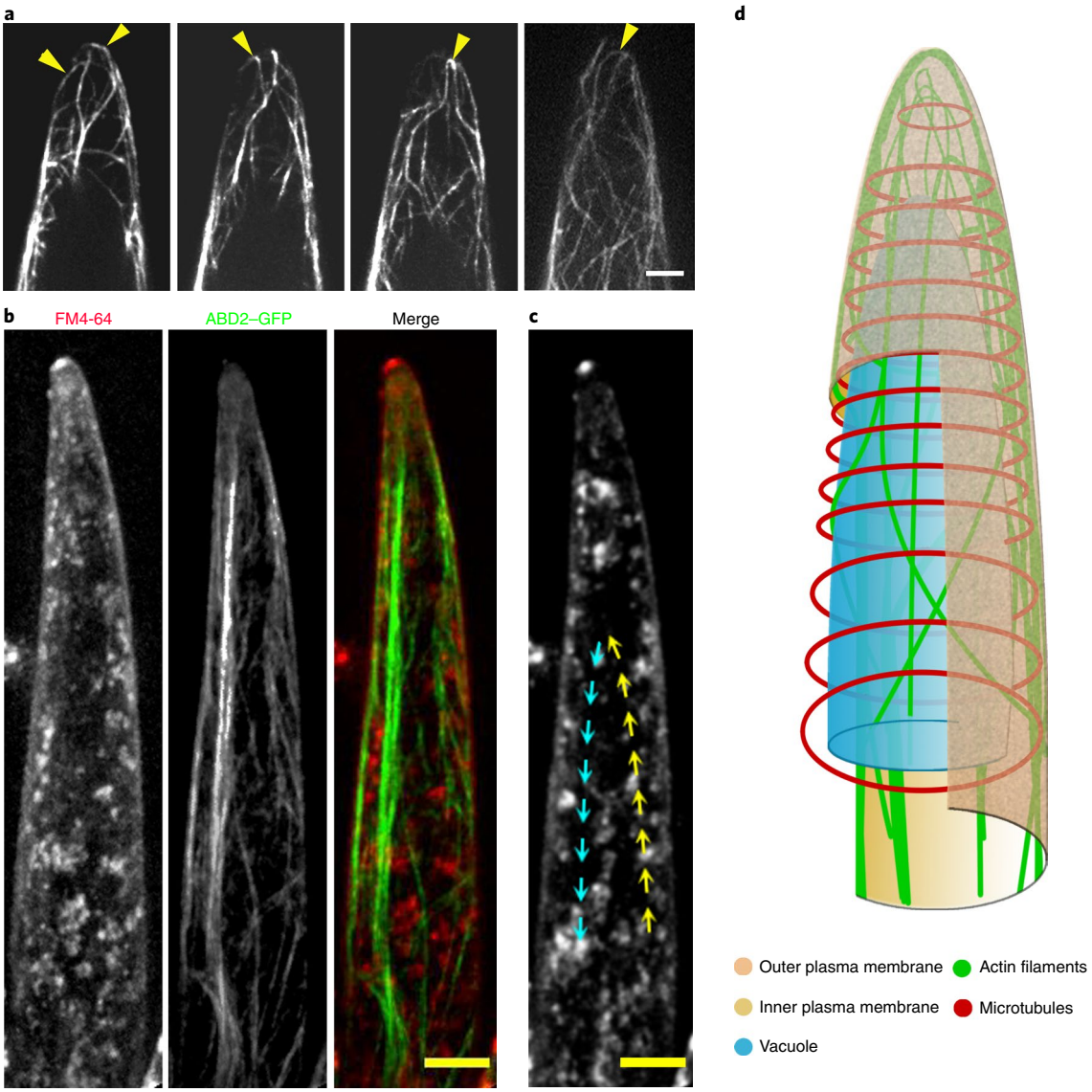

Fig. 4 | Apical F-actin, cytoplasmic trafficking features and a proposed tip-biased diffuse mode for fibre elongation. a, Time-lapse images (43 *z*-slices, 0.2 µm step size; 60 time series) illustrating F-actin architecture and dynamics in the tip areas of elongating cotton fibre cells. The arrowheads indicate closed F-actin strand loops that appear attached to the plasma membrane. Scale bar, 5 µm. **b**, A maximum projection of *z*-slices from a 4D images series (15 *z*-slices, 0.5 µm step size; 360 time series) illustrating that endosomal vesicles (stained by FM4-64) are evenly distributed along elongating cotton fibre cells. Scale bar, 10 µm. **c**, Vesicles (FM4-64) undergo back and forth movements from the fibre shank to the fibre tip. The arrows track one single vesicle that undergoes movement via cytoplasmic streaming. The yellow arrows indicate movement towards the tip; the cyan arrows indicate movement backwards. Scale bar, 10 µm. **d**, The proposed model showing the unique, tip-biased diffuse growth mode of cotton fibre elongation. Representative images in **a**–**c** are shown based on data from five plants in three independent experiments.

apices (Supplementary Fig. 6 and Supplementary Video 9). We next attempted to also track the microtubules in older cotton fibres. However, cotton fibres within the boll have an adhesive cotton fibre middle lamella that fuses adjacent fibres into thick bundles containing hundreds of fibres[34]. Elongating fibre tips usually twist together and turn inward towards the seed, making it difficult to find visible fibre tips outside the boll, and almost impossible to find separated fibres, after 3 DPA[34]. After much effort, we failed to acquire fluorescent signals of the microtubules in fibre shanks at later elongation stages due to the relatively dim signal of mCherry–EB1. Instead, we also here performed microtubule immunostaining of cotton fibres at late growth stages. We observed transverse microtubule arrays that aligned perpendicularly to the elongating fibre axis at 8 DPA and 12 DPA (Supplementary Fig. 5). Taken together, these results support that the cotton fibre probably expands via a tip-biased diffuse growth mode, as microtubules are transversely arranged along the fibre shank and largely absent at the apex.

The actin organization at the cell tip is critical for defining the mode of tip-growing cells[19,35,36]. To get further indications of how cotton fibres expand, we therefore explored the spatio-temporal dynamics of the actin cytoskeleton in the tapering tips of elongating fibre cells. Interestingly, analysis of 4D image series revealed that the actin cytoskeleton displayed a highly polarized, but continuous network that spanned from the fibre shank to the tip: actin cables traversed the shank and linked to fine F-actin structures at the tip (Fig. 4a and Supplementary Video 10). In particular, actin filaments were clearly visible and formed curved cortical structures that extended across the fibre apex (Fig. 4a and Supplementary Video 10).

Notably, this actin structure differs from cells that grow via typical tip growth, such as pollen tubes, which have an actin fringe in the sub-apical region and an actin-free zone at the pollen tube apex[19,35,37,38]. This actin fringe assembles de novo in the sub-apex of the pollen tube and is separated from the actin cytoskeleton in the shank[19,35,37,38]. In addition, we did not observe any isolated actin structures, such as the cortical actin cap at the apex of elongating leaf trichomes[32,33] that is thought to be associated with the tip-sharpening process of trichomes[32]. In fact, unlike the pointed tips of *Arabidopsis* leaf trichomes, cotton fibres have tapered but blunt tips.

Apart from the typical actin organization in tip-growing cell apices, tip growth is also characterized by the aggregation of endosomal vesicles at the apical region[19,37]. Thus, we analysed vesicle behaviour in elongating fibres using FM4-64 lipophilic dye as a membrane marker. Strikingly, endomembrane compartments were evenly distributed along the elongating fibre cells and moved, presumably via cytoplasmic streaming, bi-directionally along the fibre shank to and from the fibre tip (Fig. 4b,c and Supplementary Videos 11 and 12). This behaviour is distinctly different from that of the reverse fountain pattern observed for vesicle transport in pollen tubes[39,40]. Collectively, our live-cell observations indicate that cotton fibre elongation occurs via a unique, tip-biased diffuse growth mode (Fig. 4d).

In conclusion, our findings uncover organizing principles and the dynamic behaviour of the cytoskeleton during cotton fibre elongation. The stable transgenic cotton lines expressing ABD2–GFP and mCherry–EB1b markers offer unique opportunities to explore cytoskeletal dynamics in this economically important crop species. On the basis of multiple lines of evidence, including microtubule array arrangements and dynamics, F-actin organization and dynamics and cytoplasmic streaming, we propose that cotton fibres probably elongate via a tip-biased, but diffuse growth mode. Our findings provide significant insight into the cellular mechanism of cotton fibre cell elongation and offer inroads for genetic improvement of cotton fibre quality.

Methods

Plant material. The *G. hirsutum* (accession R15) was used as the wild-type control and the recipient of the *35S::ABD2–GFP* construct[32]. The *G. hirsutum* (accession C7) was used as a control and recipient of the *promEB1b::mCherry–EB1b* construct. Cotton transformation was performed as described previously[11]. Both the wild-type and the transgenic cotton plants were grown in the field under normal farming practices in Beijing. Flowers were tagged on the day of anthesis, and fibres were dissected from ovules in bolls at various DPA for live-cell imaging.

Plasmid construction. As described in the previous study[41], the Phusion DNA polymerase with high fidelity (New England Biolabs) was used to amplify all of the required gene products for the *promEB1b::mCherry–EB1b* construct, Fusion PCR was applied to get the *promEB1b::mCherry–EB1b* fusion fragment, and Gateway-based technology was applied to get the expression construct. In detail, the promoter of the *EB1b* gene (At5G62500), containing the 1,369 base pairs upstream from the initiation ATG, was amplified from genomic DNA with primers of P_{EB1b}-F and P_{EB1b}-R (containing the overhang of a mCherry fragment); the mCherry-encoding sequence was amplified with primers of mCherry-F (containing the overhang of the *EB1b* promoter fragment) and mCherry-R (containing overhangs of the 'glycine·alanine' linker-encoding sequence and the *EB1b*-encoding fragment); the *EB1b*-coding sequence was amplified with primers of gEB1b-F and gEB1b-R. The above-mentioned three PCR fragments were further linked together by Fusion PCR using primers of P_{EB1b}-F (containing overhangs of the 'glycine·alanine' linker-encoding sequence and the *EB1b*- encoding fragment) and gEB1b-R. The resulting PCR fragment was subsequently cloned into the pENTR/D-Topo vector to get the Entry clone, and was then delivered into pGWB1 by recombination reaction to get the final *promEB1b::mCherry–EB1b* construct. Primers are listed in Supplementary Table 2.

Spinning-disc confocal microscopy and image analyses. Live-cell imaging was carried out under a spinning disk confocal microscope (UltraView VoX, Perkin Elmer), which was equipped with the Yokogawa Nipkow CSU-X1 spinning disk scanner, the Hamamatsu EMCCD 9100-13 and the Nikon TiE inverted microscope containing the Perfect Focus System. Acquired images were processed and analysed using Volocity (Perkin Elmer), ImageJ (http://rsbweb.nih.gov/ij), as described previously[32,41]. The F-actin severing frequency was defined as the number of severing events per 100 μm² per second. The elongation rate and shrinkage rate were measured as described previously[42,43]. F-actin skewness and density were measured according to previous approaches[44]. The maximum projection of the time-lapsed stack was used to record the global dynamics of the cytoskeleton in fast-growing fibre cells.

Automated network extraction and analysis of network properties. Actin cytoskeleton images of hypocotyls and root hairs in the transgenic cotton were imaged using a spinning-disc microscope as described previously[30]. We used a previously reported framework to automatically process and extract networks from the actin cytoskeleton images[25]. We calculated seminal network properties including: the number of connected components, assortativity, edge capacity, average shortest path length, and the coefficients of variation of the shortest path lengths and edge angles[30,40]. The calculated properties were compared between the different cell types and against an ensemble of randomized null model networks using an independent two-sample *t*-test and we used the Bonferroni adjustment for multiple testing corrections.

Immunostaining of microtubules in elongating fibre cells. Cotton fibres were collected from growing cotton bolls at 2 DPA, 8 DPA and 12 DPA, and fixed for 40 min with 4% (w/v) paraformaldehyde and 0.1% (v/v) glutaraldehyde in PME buffer (50 mM PIPES, 2 mM $MgSO_4$ and 5 mM EGTA, pH 6.9) containing 0.05% (v/v) Triton X-100 and 0.3 M mannitol. After three washes in PME buffer, fibres were carefully cut off the ovules and placed onto Poly-Prep slides (Sigma-Aldrich), and then incubated with 1% (w/v) cellulase R-10 (Yakult Pharmaceutical Industry Co.) and 0.1% (w/v) pectolase Y-23 (Yakult Pharmaceutical Industry Co.) in PME buffer supplemented with 1 mM phenylmethylsulfonyl fluoride at room temperature (6 min for fibres at 8 DPA and 8 min for fibres at 12 DPA). Fibres were washed once in PME buffer and twice in PBS (pH 6.9), and then incubated in PBS containing 1% (w/v) bovine serum albumin and 0.1% primary antibody (anti-α-tubulin antibody DM1A, Sigma-Aldrich) at 4 °C overnight, washed with PBS three times, and then incubated with the secondary antibody ((TRITC) AffiniPure goat anti-mouse IgG (H + L), EarthOx)) in the dark for 2 h at 37 °C. Slides were washed twice with PBS to remove residual antibodies, mounted with 50% (v/v) glycerol and sealed for imaging.

Reporting Summary. Further information on research design is available in the Nature Research Reporting Summary linked to this article.

Data availability

All data are available from the corresponding authors upon request.

Received: 9 March 2018; Accepted: 18 March 2019;
Published online: 30 April 2019

References

1. Wang, J. et al. Overexpression of a profilin (GhPFN2) promotes the progression of developmental phases in cotton fibres. *Plant Cell Physiol.* **51**, 1276–1290 (2010).
2. Qin, Y. M. & Zhu, Y. X. How cotton fibres elongate: a tale of linear cell-growth mode. *Curr. Opin. Plant Biol.* **14**, 106–111 (2011).
3. Stiff, M. R. & Haigler, C. H. Cotton fibre tips have diverse morphologies and show evidence of apical cell wall synthesis. *Sci. Rep.* **6**, 27883 (2016).
4. Tiwari, S. C. & Wilkins, T. A. Cotton (*Gossypium hirsutum*) seed trichomes expand via diffuse growing mechanism. *Can. J. Bot.* **73**, 746–757 (1995).
5. Haigler, C. H., Betancur, L., Stiff, M. R. & Tuttle, J. R. Cotton fibre: a powerful single-cell model for cell wall and cellulose research. *Front. Plant Sci.* **3**, 104 (2012).
6. Kim, H. J. & Triplett, B. A. Cotton fibre growth in planta and in vitro. Models for plant cell elongation and cell wall biogenesis. *Plant Physiol.* **127**, 1361–1366 (2001).
7. Mansoor, S. & Paterson, A. H. Genomes for jeans: cotton genomics for engineering superior fibre. *Trends Biotechnol.* **30**, 521–527 (2012).
8. Han, L. B. et al. The dual functions of WLIM1a in cell elongation and secondary wall formation in developing cotton fibres. *Plant Cell* **25**, 4421–4438 (2013).
9. Kong, Z. et al. Kinesin-4 functions in vesicular transport on cortical microtubules and regulates cell wall mechanics during cell elongation in plants. *Mol. Plant* **8**, 1011–1023 (2015).
10. Li, X. B., Fan, X. P., Wang, X. L., Cai, L. & Yang, W. C. The cotton ACTIN1 gene is functionally expressed in fibres and participates in fibre elongation. *Plant Cell* **17**, 859–875 (2005).
11. Lv, F. et al. GhCFE1A, a dynamic linker between the ER network and actin cytoskeleton, plays an important role in cotton fibre cell initiation and elongation. *J. Exp. Bot.* **66**, 1877–1889 (2015).
12. Wang, H. Y. et al. Down-regulation of GhADF1 gene expression affects cotton fibre properties. *Plant Biotechnol. J.* **7**, 13–23 (2009).

13. Bao, Y. et al. Parallel up-regulation of the profilin gene family following independent domestication of diploid and allopolyploid cotton (*Gossypium*). *Proc. Natl Acad. Sci. USA* **108**, 21152–21157 (2011).
14. Thyssen, G. N. et al. A Gly65Val substitution in an actin, GhACT_LI1, disrupts cell polarity and F-actin organization resulting in dwarf, lintless cotton plants. *Plant J.* **90**, 111–121 (2017).
15. Jiang, Y. et al. Genetic fine mapping and candidate gene analysis of the *Gossypium hirsutum* Ligon lintless-1 (Li1) mutant on chromosome 22(D). *Mol. Genet. Genom.* **290**, 2199–2211 (2015).
16. Wang, M. et al. Asymmetric subgenome selection and *cis*-regulatory divergence during cotton domestication. *Nat. Genet.* **49**, 579–587 (2017).
17. Zhang, T. et al. Sequencing of allotetraploid cotton (*Gossypium hirsutum* L. acc. TM-1) provides a resource for fiber improvement. *Nat. Biotechnol.* **33**, 531–537 (2015).
18. Fang, L. et al. Genomic analyses in cotton identify signatures of selection and loci associated with fibre quality and yield traits. *Nat. Genet.* **49**, 1089–1098 (2017).
19. Cheung, A. Y. & Wu, H. M. Structural and signaling networks for the polar cell growth machinery in pollen tubes. *Annu. Rev. Plant Biol.* **59**, 547–572 (2008).
20. Smith, L. G. & Oppenheimer, D. G. Spatial control of cell expansion by the plant cytoskeleton. *Annu. Rev. Cell Dev. Biol.* **21**, 271–295 (2005).
21. Preuss, M. L. et al. A plant-specific kinesin binds to actin microfilaments and interacts with cortical microtubules in cotton fibres. *Plant Physiol.* **136**, 3945–3955 (2004).
22. Seagull, R. Changes in microtubule organization and wall microfibril orientation during *in vitro* cotton fibre development: an immunofluorescent study. *Can. J. Bot.* **64**, 1373–1381 (1986).
23. Preuss, M. L., Delmer, D. P. & Liu, B. The cotton kinesin-like calmodulin-binding protein associates with cortical microtubules in cotton fibres. *Plant Physiol.* **132**, 154–160 (2003).
24. Ageeva, M. V. et al. Intrusive growth of flax phloem fibres is of intercalary type. *Planta* **222**, 565–574 (2005).
25. Breuer, D. et al. System-wide organization of actin cytoskeleton determines organelle transport in hypocotyl plant cells. *Proc. Natl Acad. Sci. USA* **114**, E5741–E5749 (2017).
26. Lei, L., Li, S. D. & Gu, Y. Cellulose synthase complexes: composition and regulation. *Front. Plant Sci.* **3**, 75 (2012).
27. Gutierrez, R., Lindbloom, J., Paredez, A., Emons, A. M. & Ehrhardt, D. W. Organization of cellulose synthase trafficking and motility in the plasma membrane by the cortical microtubule array. *Nat. Cell Biol.* **11**, 797–806 (2009).
28. Zhang, Q., Fishel, E., Bertroche, T. & Dixit, R. Microtubule severing at crossover sites by katanin generates ordered cortical microtubule arrays in *Arabidopsis*. *Curr. Biol.* **23**, 2191–2195 (2013).
29. Chan, J., Sambade, A., Calder, G. & Lloyd, C. *Arabidopsis* cortical microtubules are initiated along, as well as branching from, existing microtubules. *Plant Cell* **21**, 2298–2306 (2009).
30. Baskin, T. I. & Gu, Y. Making parallel lines meet transferring information from microtubules to extracellular matrix. *Cell Adhes. Migr.* **6**, 404–408 (2012).
31. Wasteneys, G. O. & Ambrose, J. C. Spatial organization of plant cortical microtubules: close encounters of the 2D kind. *Trends Cell Biol.* **19**, 62–71 (2009).
32. Tian, J. et al. Orchestration of microtubules and the actin cytoskeleton in trichome cell shape determination by a plant-unique kinesin. *eLife* **4**, e09351 (2015).
33. Yanagisawa, M. et al. Patterning mechanisms of cytoskeletal and cell wall systems during leaf trichome morphogenesis. *Nat. Plants* **1**, 15014 (2015).
34. Singh, B., Cheek, H. D. & Haigler, C. H. A synthetic auxin (NAA) suppresses secondary wall cellulose synthesis and enhances elongation in cultured cotton fibre. *Plant Cell Rep.* **28**, 1023–1032 (2009).
35. Qu, X. et al. Organization and regulation of the actin cytoskeleton in the pollen tube. *Front. Plant Sci.* **5**, 786 (2014).
36. Qu, X. et al. Organizational innovation of apical actin filaments drives rapid pollen tube growth and turning. *Mol. Plant* **10**, 930–947 (2017).
37. Li, S. et al. LlFH1-mediated interaction between actin fringe and exocytic vesicles is involved in pollen tube tip growth. *New Phytol.* **214**, 745–761 (2017).
38. Liu, X. et al. Profilin regulates apical actin polymerization to control polarized pollen tube growth. *Mol. Plant* **8**, 1694–1709 (2015).
39. Fu, Y. The cytoskeleton in the pollen tube. *Curr. Opin. Plant Biol.* **28**, 111–119 (2015).
40. Dong, H. J., Pei, W. K. & Ren, H. Y. Actin fringe is correlated with tip growth velocity of pollen tubes. *Mol. Plant* **5**, 1160–1162 (2012).
41. Liu, T. et al. Augmin triggers microtubule-dependent microtubule nucleation in interphase plant cells. *Curr. Biol.* **24**, 2708–2713 (2014).
42. Henty, J. L. et al. *Arabidopsis* actin depolymerizing factor4 modulates the stochastic dynamic behavior of actin filaments in the cortical array of epidermal cells. *Plant Cell* **23**, 3711–3726 (2011).
43. Li, J. et al. Capping protein modulates the dynamic behavior of actin filaments in response to phosphatidic acid in *Arabidopsis*. *Plant Cell* **24**, 3742–3754 (2012).
44. Henty-Ridilla, J. L., Li, J., Day, B. & Staiger, C. J. ACTIN DEPOLYMERIZING FACTOR4 regulates actin dynamics during innate immune signaling in *Arabidopsis*. *Plant Cell* **26**, 340–352 (2014).

Acknowledgements

We thank G.-X. Xia (Institute of Microbiology, Chinese Academy of Sciences) for providing valuable assistance and insightful suggestions about the project. We also thank D. Delmer (University of California, Davis) for critical comments and valuable suggestions on the manuscript. We are grateful to L. Su (Institute of Microbiology, Chinese Academy of Sciences) for providing technical assistance in microscopy We also appreciate the technical support of the UltraView Vox system from L. Jiao in Perkin Elmer. This study was supported by the National Key Research and Development Program of China 2016YFD0100505 and 2016YFD0100306, by the National Science Foundation of China under grant no. 31371676, by the startup fund of 'One Hundred Talents' programme of the Chinese Academy of Sciences, by the National Natural Science Foundation of China (31601350), by the National Major Project for Developing New GM Crops (2016ZX08005) and by the grants from the State Key Laboratory of Plant Genomics. S.P. was funded by a R@MAP Professorship at University of Melbourne, by a Future Fellowship grant (FT160100218) and by an IRRTF-RNC grant via University of Melbourne.

Author contributions

Y.Y. performed live-cell imaging on cytoskeleton dynamics, prepared figures and videos, and generated stable transgenic cotton plants expressing the mCherry–EB1b reporter. S.W. conducted stable cotton transformation for the ABD2–GFP reporter, and field experiments for the screening and propagation of the cotton marker lines. J.N. analysed F-actin network properties of cotton fibres, hypocotyls and root hairs. G.W. analysed microtubule and F-actin dynamics, prepared figures and videos, developed the code for generating the progressively increasing mCherry–EB1b series and designed the working model. Z.F. made the mCherry–EB1b expression vector. A.M., L.H., Y.M., H.W., X.Z., J.T. and L.D. provided essential technical assistance. Z.N. provided guidance in the analysis of network properties. S.P. supervised the analysis of network properties. Z.K. conceived the project, interpreted the data and wrote the manuscript with the input of other authors. Z.K., S.P., Z.N. and J.N. revised the article.

Competing interests

The authors declare no competing interests.

Additional information

Supplementary information is available for this paper at https://doi.org/10.1038/s41477-019-0418-8.

Reprints and permissions information is available at www.nature.com/reprints.

Correspondence and requests for materials should be addressed to S.P. or Z.K.

Publisher's note: Springer Nature remains neutral with regard to jurisdictional claims in published maps and institutional affiliations.

The Rice Actin-Binding Protein RMD Regulates Light-Dependent Shoot Gravitropism[1][OPEN]

Yu Song,[a] Gang Li,[b] Jacqueline Nowak,[c,d,e] Xiaoqing Zhang,[a] Dongbei Xu,[a] Xiujuan Yang,[b] Guoqiang Huang,[a] Wanqi Liang,[a] Litao Yang,[a] Canhua Wang,[a] Vincent Bulone,[b] Zoran Nikoloski,[c,d] Jianping Hu,[f] Staffan Persson,[a,e] and Dabing Zhang[a,b,2,3]

[a]The University of Adelaide-Shanghai Jiao Tong University Joint Laboratory for Plant Science and Breeding, School of Life Sciences and Biotechnology, Shanghai Jiao Tong University, 200240 China
[b]School of Agriculture, Food and Wine, University of Adelaide, Urrbrae, South Australia 5064, Australia
[c]Systems Biology and Mathematical Modeling Group, Max Planck Institute of Molecular Plant Physiology, 14476 Potsdam-Golm, Germany
[d]Bioinformatics Group, Institute of Biochemistry and Biology, University of Potsdam, 14476 Potsdam-Golm, Germany
[e]Department of Energy Plant Research Laboratory, Michigan State University, East Lansing, Michigan 48824
[f]School of Biosciences, University of Melbourne, Parkville Victoria 3010, Melbourne, Australia

ORCID IDs: 0000-0002-1744-5220 (G.L.); 0000-0002-2881-7384 (J.N.); 0000-0002-6103-5704 (G.H.); 0000-0002-9938-5793 (W.L.); 0000-0002-4515-5722 (L.Y.); 0000-0003-2671-6763 (Z.N.); 0000-0002-4635-4299 (J.H.); 0000-0002-6377-5132 (S.P.); 0000-0002-1764-2929 (D.Z.).

Light and gravity are two key determinants in orientating plant stems for proper growth and development. The organization and dynamics of the actin cytoskeleton are essential for cell biology and critically regulated by actin-binding proteins. However, the role of actin cytoskeleton in shoot negative gravitropism remains controversial. In this work, we report that the actin-binding protein Rice Morphology Determinant (RMD) promotes reorganization of the actin cytoskeleton in rice (*Oryza sativa*) shoots. The changes in actin organization are associated with the ability of the rice shoots to respond to negative gravitropism. Here, light-grown *rmd* mutant shoots exhibited agravitropic phenotypes. By contrast, etiolated *rmd* shoots displayed normal negative shoot gravitropism. Furthermore, we show that RMD maintains an actin configuration that promotes statolith mobility in gravisensing endodermal cells, and for proper auxin distribution in light-grown, but not dark-grown, shoots. *RMD* gene expression is diurnally controlled and directly repressed by the phytochrome-interacting factor-like protein OsPIL16. Consequently, overexpression of *OsPIL16* led to gravisensing and actin patterning defects that phenocopied the *rmd* mutant. Our findings outline a mechanism that links light signaling and gravity perception for straight shoot growth in rice.

Light and gravity are two key determinants for plant growth and development, as they drive the establishment of the above- and below-ground developmental axes of a plant. This is especially important at the seedling establishment stage, a time when plants are sensitive to light and gravity (Gommers and Monte, 2018). However, how plants coordinate light and gravity perception and signaling is not well understood.

"Gravitropism" is the process by which plants adjust their growth in response to gravity, ensuring that shoots grow upward and roots grow downward. Gravitropism consists of gravisensing, signal initiation, and transduction, and asymmetric cell growth (Blancaflor and Masson, 2003). In root columella cells and shoot endodermal cells, starch-filled amyloplasts are considered as statoliths. (Blancaflor and Masson, 2003; Morita, 2010). Statoliths sediment according to the gravity vector to propagate gravitropic signals that are converted into biochemical and physiological outputs; for example, redistribution of auxin (Kiss, 2000). Although the root gravitropic response is relatively

[1]This work was supported by the National Key Research and Development Program of China (grant no. 2016YFD0100804), the National Natural Science Foundation of China (grant no. 31430009), the Innovative Research Team, Ministry of Education, and 111 Project (grant no. B14016), the Science and Technology Commission of Shanghai Municipality (grant no. 13JC1408200), the China Scholarship Council (CSC grant no. 201506230050), the Australian Research Council Future Fellowship (grant no. FT160100218 to S.P.), and the University of Melbourne International Research and Research Training Fund-Research Network and Consortia (grant to S.P.).

[2]Author for contact: zhangdb@sjtu.edu.cn.
[3]Senior author.
The author responsible for distribution of materials integral to the findings presented in this article in accordance with the policy described in the Instructions for Authors (www.plantphysiol.org) is: Dabing Zhang (zhangdb@sjtu.edu.cn).

D.Z., S.P., Y.S., J.H., and V.B. designed the project; Y.S., G.L., J.N., X.Z., D.X., X.Y., and G.H. performed the experiments; Y.S., G.L., J.N., Z.N., X.Z., D.X., X.Y., G.H., W.L., C.W., L.Y., D.Z., and S.P. analyzed the data; Y.S., D.Z., S.P., J.H., J.N., and Z.N. co-wrote the article; all authors discussed the results and commented on the article.
[OPEN]Articles can be viewed without a subscription.
www.plantphysiol.org/cgi/doi/10.1104/pp.19.00497

well understood, the molecular mechanisms that underpin shoot negative gravitropic responses remain ill-defined. However, studies of shoot negative gravitropic mutants have shed some light on this process. For example, mutations in the transcription factors (TFs) *SCARECROW* and *SHORT-ROOT*, which are essential for the development of endodermis, caused agravitropic responses in Arabidopsis (*Arabidopsis thaliana*) stems (Fukaki et al., 1998). Shoot gravitropism3 (SGR3), a syntaxin, together with SNARE protein ZIG (ZIG-ZAG), forms a SNARE complex, which positively mediates shoot negative gravitropism via vesicle transport (Yano et al., 2003). In Arabidopsis, hypocotyls of starch excess (*sex1*) mutant displayed increased gravity response, and the amyloplasts were twice as big as those of wild type in the endodermal cells (Vitha et al., 2007). However, root gravitropic response, as well as amyloplast sedimentation in root columella cells, of sex1 was similar to that of wild type (Vitha et al., 2007). Similarly, inflorescence stems of *shoot gravitropism 1* (*sgr3*), *sgr5*, and *sgr6* exhibited defective gravitropic response, but gravitropic responses of hypocotyls and roots were normal (Tasaka et al., 1999), indicating that gravitropic responses occur via different mechanisms in distinct organs (Mirza et al., 1984; Hobbie and Estelle, 1995; Fukaki et al., 1996, 1998; Yamauchi et al., 1997; Morita et al., 2006).

The gravitropic response system interacts with the response pathways of other environmental signals. For example, light and gravitropism intersect in plant shoots. In Arabidopsis, dark-grown hypocotyls show strong negative gravitropism, but light-grown hypocotyls display random growth orientation under red or far-red light conditions (Poppe et al., 1996). Light inhibition of negative gravitropism in hypocotyls is mediated by phytochromes (Poppe et al., 1996; Robson and Smith, 1996). For example, the tomato (*Solanum lycopersicum*) mutant of *LAZY-2* (*LZ2*, not yet cloned) grew downward in a phytochrome-dependent manner when exposed to white light, but displayed normal gravitropic response in the dark (Gaiser and Lomax, 1993; Behringer and Lomax, 1999). In addition, phytochrome-interacting factors (PIFs) positively regulate shoot negative gravitropism by controlling endodermal amyloplast development in Arabidopsis etiolated hypocotyls (Kim et al., 2011). Despite these findings, molecular mechanisms on how plants coordinate light and gravity perception and signal transduction are not well defined.

An intact and dynamic actin cytoskeleton is thought to be important for plants to respond to gravity; however, pharmaceutical treatment and mutant analyses have yielded conflicting results (Yamamoto and Kiss, 2002; Hou et al., 2003; Palmieri and Kiss, 2005). In Arabidopsis shoots, pharmacological disruption of the F-actin cytoskeleton formation by Latrunculin B (LatB) led to increased gravitropic response (Yamamoto and Kiss, 2002). However, other studies have questioned the need for an intact F-actin network for graviperception in inflorescence stems (Hou et al., 2003; Saito et al., 2005), and Lat-B treatment caused reduced amyloplast mobility in Arabidopsis endodermal cells (Palmieri and Kiss, 2005). Previously, we showed that the actin cytoskeleton in rice (*Oryza sativa*) is controlled by Rice Morphology Determinant (RMD, also called "BUI1"), a type-II formin protein specifying rice morphology by regulating actin nucleation and organization (Zhang et al., 2011). RMD also regulates actin dynamics and auxin homeostasis during root cell elongation and growth (Li et al., 2014), as well as pollen tube development (Li et al., 2018), and it is required for crown root angle in response to P starvation (Huang et al., 2018). Here, we show that RMD promotes shoot negative gravitropism by regulating actin organization and amyloplast sedimentation in the endodermis of light-grown shoots. *RMD* gene expression is controlled by the diurnally active phytochrome-interacting factor-like protein OsPIL16. We have thus uncovered a mechanism by which RMD is involved in controlling shoot negative gravitropism in a light-dependent manner.

RESULTS

RMD Is Required for Rice Shoots to Grow Upright in the Light

Our previous studies indicated that the actin-binding protein RMD is a vital regulator of rice morphology (Yang et al., 2011; Zhang et al., 2011). A prominent phenotype of the *rmd* mutants is that their shoots tend to be bent rather than straight as observed in wild type (Yang et al., 2011; Zhang et al., 2011). This observation indicates a function of RMD during rice seedling establishment and vertical growth maintenance. To quantify the shoot bending of *rmd* mutant seedlings, we measured the shoot deviation from straight growth in two null alleles of *RMD*, *rmd-1* and *rmd-2* (Zhang et al., 2011). Mean values of the angle (θ) between the direction of growth and the longitudinal axis were compared. In light conditions, >85% of *rmd-2* displayed a clear agravitropic phenotype, 37.65% at 0° to 20°, 39.51% at 20° to 40°, and 8.02% at 40° to 60° (Fig. 1A; Supplemental Fig. S1). By contrast, etiolated *rmd-1* and *rmd-2* seedlings grew their shoots straight upward just like that of wild type (Fig. 1B). These observations indicated that the shoot phenotype of *rmd* mutants is light-specific. Further, an *rmd-2* mutant complemented by an estradiol-inducible *pLex::RMD-RFP* transgene (Li et al., 2014) showed no shoot bending phenotype when grown in the light on estradiol-containing media (Supplemental Fig. S2A), confirming that the shoot-bending phenotype in the mutant is due to the lack of a functional RMD.

To investigate whether the shoot bending of *rmd* mutants was due to differential cell elongation, we performed semisection assays to analyze cell length of wild-type and *rmd-2* shoots. In light-grown *rmd-2* sheaths, cell lengths at the inward side of the bent

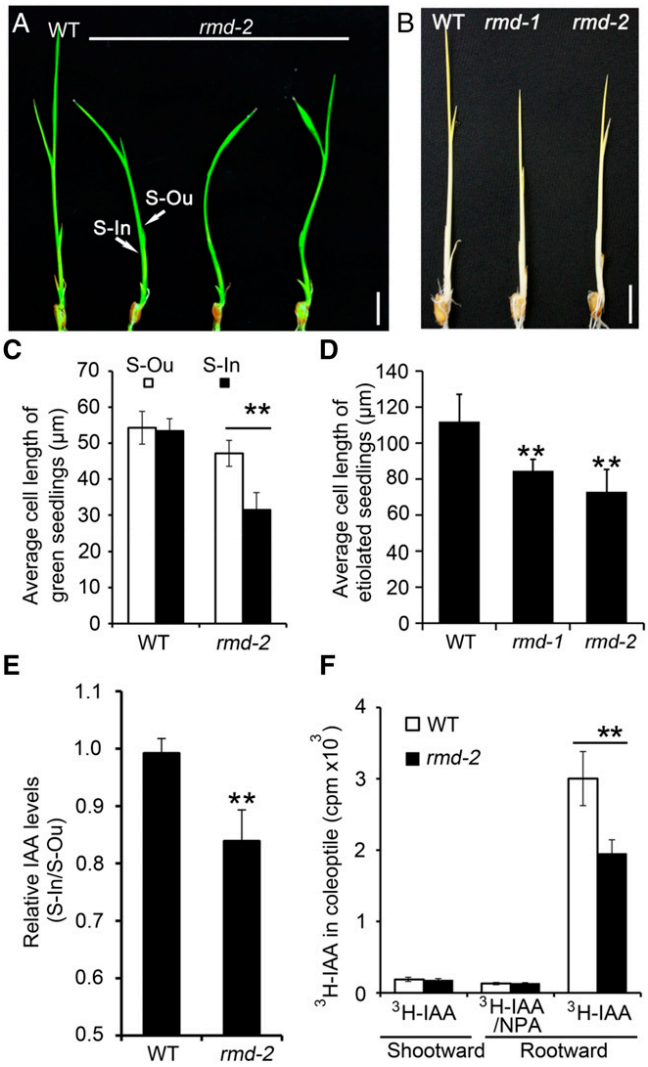

Figure 1. The *rmd* mutant displays light-dependent agravitropic growth and aberrant auxin homeostasis in the shoot. A, Shoots of 5-d–old seedlings after germination under light/dark cycle. Scale bar = 1 cm. B, Shoots of 3-d–old seedlings after germination in darkness. Scale bar = 1 cm. C, S-Ou (outer side of leaf sheaths) and S-In (inner side of leaf sheaths) cell length in light-grown wild-type (WT; $n > 120$ cells from 10 shoots) and *rmd-2* ($n > 141$ cells from 12 shoots) seedlings. Results are presented as means ± SD. Student's *t* test: $^{**}P < 0.01$. D, Cell length of sheaths in etiolated wild-type ($n = 45$), *rmd-1* ($n = 48$), and *rmd-2* ($n = 40$) shoots. Data were analyzed by conducting both *t* test and ANOVA. Results are presented as means ± SD. $^{**}P < 0.01$. E, The ratio between IAA levels in S-In versus S-Ou in shoots without apex. Results are presented as means ± SD. Student's *t* test: $^{**}P < 0.01$. F, Coleoptile auxin polar transport assays. NPA (1-N-Naphthylphthalamic acid; 10 μM) was applied to inhibit auxin transport ($n = 3$). Results are presented as means ± SD. Student's *t* test: $^{**}P < 0.01$.

region were significantly shorter (~34%) than those at the outward bending side. On the contrary, no significant differences in cell lengths were found between opposite sides of wild-type sheaths (Fig. 1C). Despite the lack of a shoot-bending phenotype in dark-grown *rmd-2*, cell lengths were overall shorter in the mutant than in the wild type (Fig. 1D), consistent with the fact that *rmd* mutants have shorter hypocotyls (Zhang et al., 2011). These results suggested that the shoot-bending phenotype in *rmd* is due to asymmetric cell elongation in light-grown shoots.

RMD Is Required for Auxin Transport and Distribution in the Shoot

The downward growth of the *rmd* mutant seedlings is comparable to that of the prostrate growth of the maize (*Zea mays*) *lazy1* (*la1*) mutant, that is affected in polar auxin distribution (Dong et al., 2013). With the purpose of determining whether auxin homeostasis is perturbed in *rmd* shoots, which might result in the observed asymmetric cell elongation, we measured indole-3-acetic acid (IAA) levels in tissues from the inward and outward sides of the bending region in shoots. Results showed that the IAA level from the inward side was lower (2.78 pg/mg) than that of the outward side (3.31 pg/mg) in light-grown *rmd-2* shoots, whereas no differences in IAA levels were observed from the two opposite shoot sides in wild type (Fig. 1E).

To directly measure the polar auxin transport capacity of the plant, we compared rootward IAA transport in coleoptiles between wild type and *rmd-2* mutants. We found that rootward polar auxin transport was 1.95 ± 10^3 cpm (counts per minute) in *rmd-2* mutants, and significantly reduced from the 3×10^3 cpm in wild type (Fig. 1F). It is well established that auxin export activity relies on PIN auxin efflux carriers (Ding et al., 2011). Therefore, we next analyzed OsPIN1b localization in the shoot using transgenic lines expressing an OsPIN1b-YFP fusion protein under the control of the native *OsPIN1b* promoter (*ProOsPIN1b*::OsPIN1b-YFP). In leaf sheaths of light-grown plants, we observed that OsPIN1b-YFP was detected in the basal plasma membrane of the cells in wild type, but some were clearly distributed to the lateral sides of *rmd-2* (Supplemental Fig. S2B). By contrast, OsPIN1b displayed very similar localization patterns in etiolated shoot cells of *rmd-2* and wild-type seedlings (Supplemental Fig. S2C). These data indicated that RMD is important for polar OsPIN1b localization, and proper auxin homeostasis, in light-grown rice shoots. The altered auxin distribution in the *rmd* shoots may cause the asymmetrical cell elongation and bent phenotype of light-grown shoots.

The Light-Dependent Phenotype in *rmd* Is Associated with Reduced Gravitropic Response

We hypothesized that the inability of the light-grown *rmd* seedlings to grow straight up was associated with a defect in the gravitropic response. To test this hypothesis, we first selected 2-d–old light-grown wild-type and *rmd-2* mutants to analyze gravitropic responses. At this stage the seedlings do not have any true leaves, which may complicate interpretations. The

results revealed that *rmd-2* displayed a reduced level of the gravitropic response (Supplemental Fig. S3, A and B). Next, we analyzed shoot negative gravitropism of *rmd-2* by reorienting 5-day–old seedlings 90° from their previous growth position at different light conditions. Light-grown *rmd-2* seedlings displayed markedly a reduced shoot gravitropic response after gravity stimulation compared with wild type (Fig. 2, A and B). By contrast, etiolated *rmd-2* mutants exhibited a normal shoot gravitropic response (Fig. 2, C and D).

Endodermal amyloplasts are thought to act as statoliths in shoot negative gravitropism (Morita, 2010). To test whether amyloplast behavior is affected in the *rmd* mutants, we checked the localization of amyloplasts in the endodermal cells using histological analyses. Under light, amyloplasts were distributed at the base of the endodermal cells, in accordance with the gravity vector, in wild-type seedlings (Supplemental Fig. S4A), but exhibited uneven distribution in *rmd-2* (Supplemental Fig. S4A). Indeed, some amyloplasts were visible along the sides, or displaced to the central part, of the endodermal cells in the light-grown *rmd-2* mutants (Supplemental Fig. S4A). This result indicated that RMD promotes amyloplast sedimentation in shoot endodermal cells, which differs from the role of RMD in buffering amyloplast movement in root columella

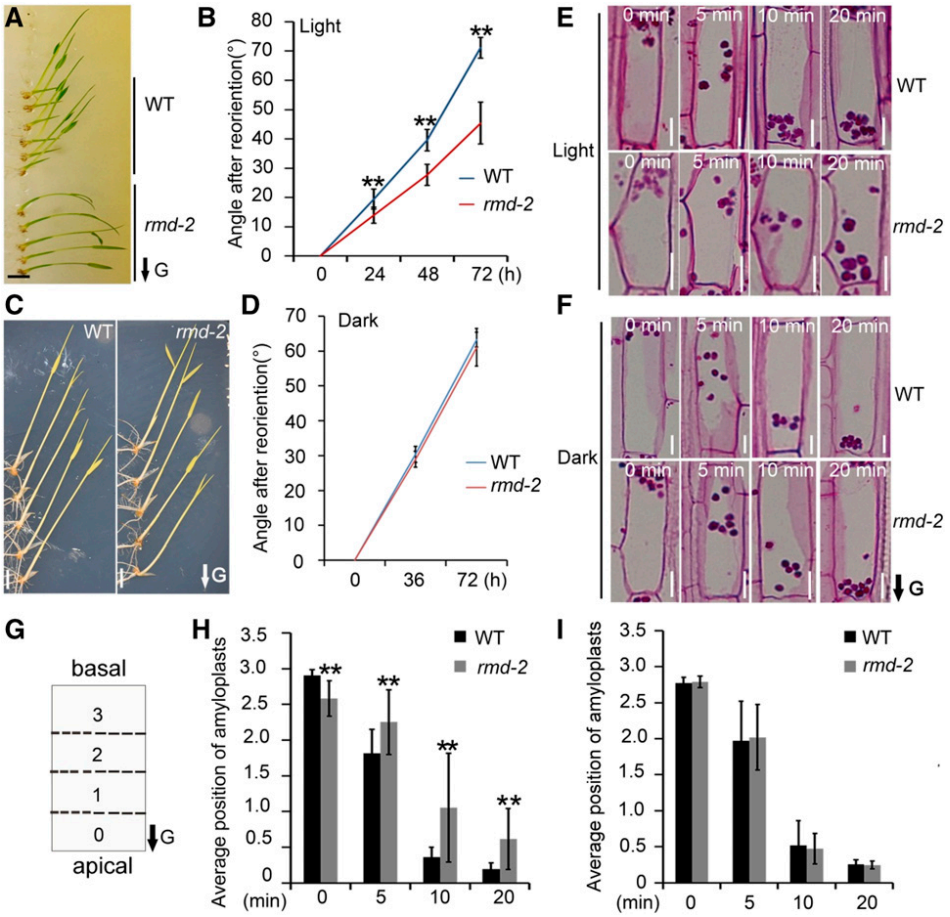

Figure 2. The curved growth of *rmd* shoot is caused by reduced gravisensing under light. A, Seventy-two hours after 5-d–old wild-type (WT) and *rmd-2* seedlings grown under light/dark cycle were reoriented for 90°. Scale bar = 1 cm. B, Kinetic comparison of shoot curved angle between wild type ($n = 14$) and *rmd-2* ($n = 16$) under gravistimulation. Values are means ± SD. Student's *t* test: $^{**}P < 0.01$. C, Seventy-two hours after 5-d–old etiolated wild type ($n = 15$) and *rmd-2* ($n = 15$) were reoriented for 90°. The arrow indicates gravity direction. Scale bar = 1 cm. D, Measurement of curve angle of wild-type ($n = 15$) and *rmd-2* ($n = 15$) etiolated seedlings 72 h after seedlings were reoriented. Values are means ± SD. Student's *t* test. E and F, Comparison of the kinetics of amyloplast sedimentation in shoot endodermal cells between wild type and *rmd* in light-grown (E) and etiolated (F) seedlings. Amyloplasts were stained by periodic acid-Schiff kit after 0, 5, 10, and 20 min of the gravistimulation. Scale bars = 10 μm. The arrow indicates gravity direction. G, Schematic position of amyloplasts in endodermal cells. Each cell is divided into four equal segments, numbered 0–3. Amyloplasts moved from basal to apical after seedlings were inverted and their positions were scored. The arrow indicates gravity direction. H, Average position of amyloplasts (defined in G) in light-grown wild type ($n = 86$ from four shoots) and *rmd-2* ($n = 86$ from four shoots) seedlings at different time points after seedlings were reoriented. Values are means ± SD. Student's *t* test: $^{**}P < 0.01$. I, Average position of amyloplasts (defined in G) in dark-grown wild type ($n = 74$ from four shoots) and *rmd-2* ($n = 74$ from four shoots) seedlings at different time points after seedlings were reoriented. Values (defined in G) are means ± SD.

cells during gravisensing (Huang et al., 2018). The amyloplasts were distributed along the basal part of the endodermal cells in both etiolated *rmd-2* and wild-type plants, consistent with the lack of bent phenotypes of the *rmd* mutants (Supplemental Fig. S4B). These results indicated that the gravitropic defect of *rmd* was associated with amyloplast behavior.

Changes in the gravity vector trigger changes in the localization of amyloplasts (Kiss, 2000). To investigate the dynamics of amyloplasts in *rmd* plants during shoot negative gravitropic response, we performed histochemical analyses to check amyloplast relocalization after seedlings were reoriented. After turning 5-d–old light-grown wild type rice seedlings upside-down, we found that most amyloplasts moved to the basal side of endodermal cells already 10 min after the turn (Fig. 2, E, G, and H). However, the majority of amyloplasts in *rmd-2* failed to reach the basal region of the endodermal cells and instead remained at the central part 10 min after the turn (Fig. 2, E, G, and H). After 20 min, although some of the amyloplasts in *rmd-2* did reach the base of the endodermal cells, many of them still remained scattered in the cells (Fig. 2, E, G, and H). In dark-grown seedlings, however, the dynamics of amyloplasts were very similar in wild type and *rmd-2* after the seedlings were reoriented (Fig. 2, F, G, and I). Thus, we propose that RMD affects shoot negative gravitropism in light-grown rice seedlings and impacts the redistribution and dynamics of amyloplasts in the endodermal cell layers.

Organization of the Actin Cytoskeleton Is Disturbed in the Shoot Endodermis of Light-Grown *rmd* Mutants

Given our previous report that RMD is localized to the chloroplast surface in leaf cells (Zhang et al., 2011) and on the surface of statoliths in root columella cells (Huang et al., 2018), we predicted that the RMD protein may be physically associated with amyloplasts in the shoot. To test this hypothesis, we performed confocal microscopy on rescued *rmd-2* lines that contained the RMD-GFP fusion under the control of the native promoter of *RMD* (Huang et al., 2018; Fig. 3A). Consistent with our previous results (Huang et al., 2018), we found that a functional RMD-GFP localized to distinct organelles, reminiscent of amyloplasts, inside the endodermal cells of rice shoots (Fig. 3, B and C), indicating that RMD was mainly localized to amyloplasts in shoot endodermis.

RMD binds to actin filaments (AFs) in vitro and affects actin organization in roots and pollen tubes (Yang et al., 2011; Zhang et al., 2011; Li et al., 2018). To first assess whether the actin cytoskeleton is important for shoot gravitropism, we transferred germinated wild-type rice seeds to half-strength Murashige and Skoog (MS) liquid medium supplemented with 1 μM of LatB, an actin polymerization inhibitor (Baluška et al., 2001). Light-grown wild-type seedlings grown on LatB showed bent shoot growth or twisted shoots

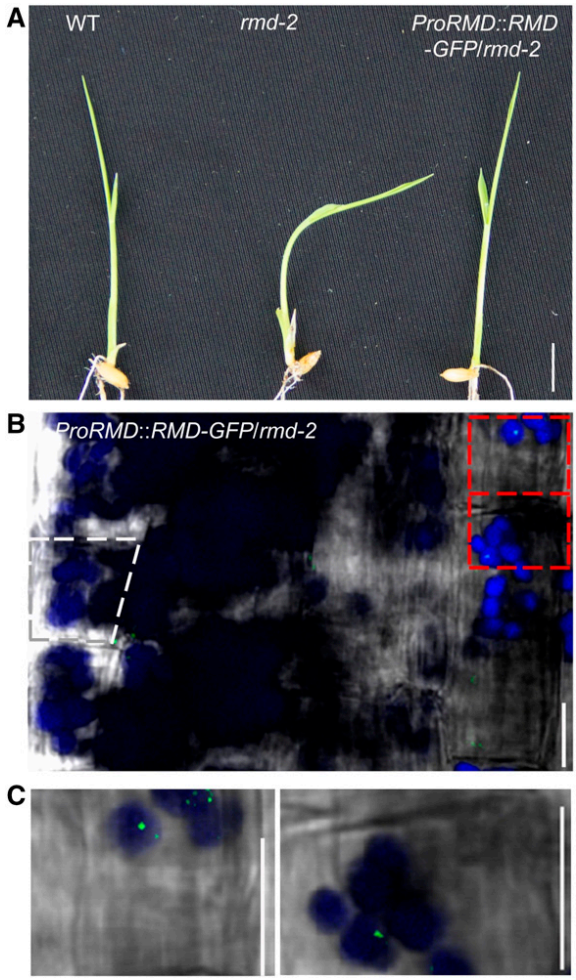

Figure 3. The RMD protein is associated with amyloplasts in the shoot. A, Complementation of the *rmd-2* mutant by *ProRMD::RMD-GFP*. B, Intracellular localization of RMD-GFP in shoot endodermal cells. Cy5 (cyan) signals are autofluorescence of amyloplasts. The dotted gray circle indicated the cortex cell. At least 10 lines were checked. C, A magnified view of the area enclosed in the dotted red circle of (B). Scale bars = 1 cm (A) and 10 μm (B and C). WT, wild type.

(Supplemental Fig. S5A), and thus phenocopied the growth of the *rmd* mutants. By contrast, the majority of dark-grown wild-type seedlings grown on LatB-containing medium exhibited normal vertical growth, with less than ~30% seedlings displaying abnormal growth patterns (Supplemental Fig. S5B). LatB-grown wild-type seedlings contained unevenly distributed amyloplasts at the distal end of light-grown endodermal cells (Supplemental Fig. S5C). For LatB-treated etiolated seedlings, we found normal amyloplast sedimentation at the base of the endodermis in vertical growth seedlings. However, amyloplasts displacement to the central part of endodermal cells was observed in bending etiolated seedlings (Supplemental Fig. S5D). These results demonstrate that the abnormal gravitropic perception in *rmd* might be connected to the role of RMD in actin organization under light.

We next reasoned that RMD may influence amyloplast distribution and dynamics through its impact on organization of the actin cytoskeleton in the endodermis. To investigate if actin organization was changed in the *rmd* mutants from wild type in endodermal cells, we stained shoot endodermal cells with AlexaFluor488-phalloidin. Confocal microscopy showed sparser AF abundance and abnormal amyloplast distribution in light-grown *rmd-2* endodermal cells compared with wild type (Fig. 4A). In the dark, however, actin organization mainly appeared surrounding the amyloplasts both in wild-type and *rmd-2* endodermal cells (Fig. 4B). Moreover, the amyloplasts were predominantly located at the base of the cells (Fig. 4B). To further investigate these differences under light conditions, we extracted actin networks from actin cytoskeletal image data of light-grown wild type and *rmd-2* (Fig. 4, C and D) and analyzed network properties that provide measurements of the actin organization (Breuer et al., 2017). The results showed that the number of connected actin components was lower in *rmd-2* than in wild type (independent *t* test, *P* value: $P < 10^{-4}$), and the average edge capacity ("bundling") of actin in *rmd-2* shoot endodermal cells was higher than in the wild type ($P < 10^{-4}$; Fig. 4E), indicating that there are fewer AFs in the mutant. Furthermore, the average shortest path length and diameter of actin in *rmd-2* were bigger than in the wild type ($P < 10^{-7}$ and $P < 10^{-3}$, respectively; Fig. 4, E and F), suggesting that the actin-filament network in the mutant was less compact and nodes were in closer proximity to each other. These properties indicate that the wild-type actin network is more coherent and better suited for effective transport than that of the *rmd* mutants (Breuer et al., 2017).

RMD Is Diurnally Expressed and Regulated by Light Signaling Components

Because the RMD-mediated shoot negative gravitropic response is light-dependent, we next asked what the molecular link between light signaling, gravitropism, and RMD-mediated actin cytoskeleton organization might be. We first performed reverse transcription quantitative PCR (RT-qPCR) analysis of *RMD* and found that *RMD* transcript levels were substantially higher in light-grown than in etiolated seedlings (Supplemental Fig. S6A). Additionally, we sampled plants grown in the field every 4 h, and found that the abundance of the *RMD* transcript was oscillatory, with the highest level at 4 PM and lowest level at 4 AM (Supplemental Fig. S6B). This gene expression pattern was corroborated by data from the Rice Expression Profile Database (RDB, http://ricexpro.dna.affrc.go.jp/; Sato et al., 2011).

In Arabidopsis, hypocotyl growth orientation is controlled by phytochrome-mediated inhibition of negative gravitropism through PIFs (Lariguet and Fankhauser, 2004; Kim et al., 2011), which are nuclear proteins that integrate light and other signals, such as

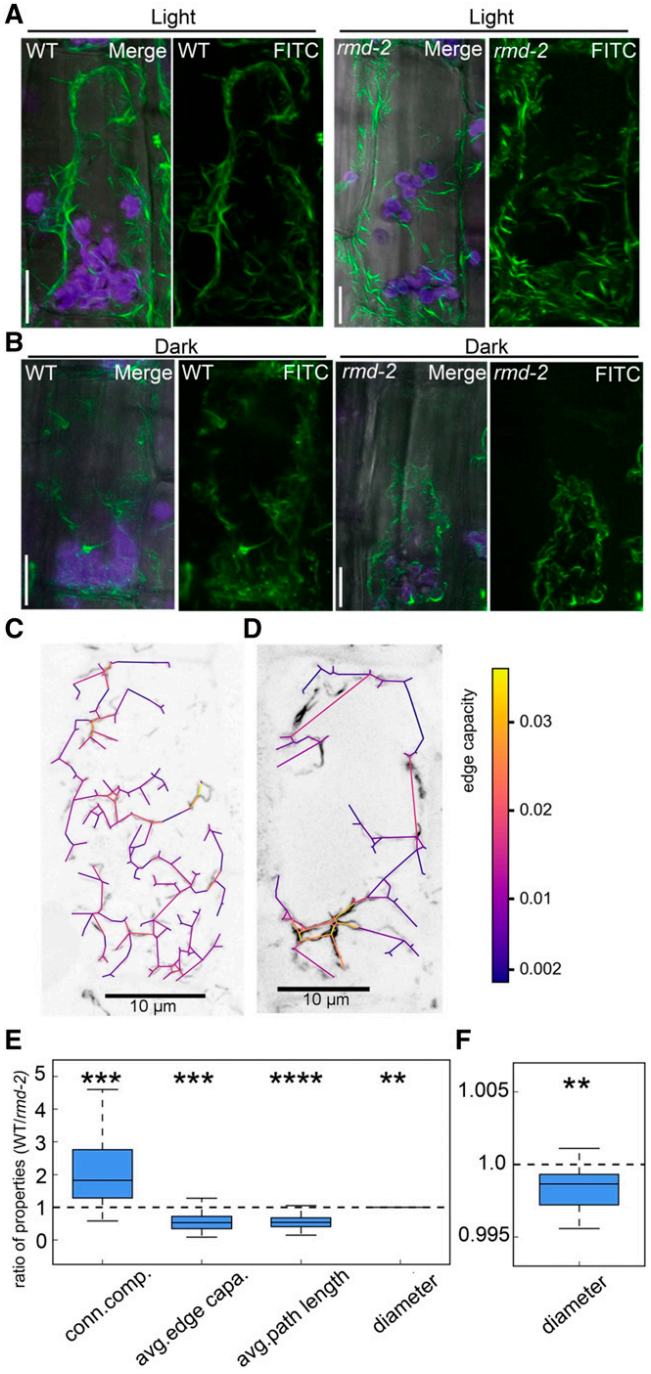

Figure 4. Disturbed actin cytoskeleton in shoot endodermis of light-grown *rmd* mutants. A and B, F-actin organization in shoot endodermal cells of light-grown (A) and etiolated (B) seedlings. Images were merged from Fluorescein isothiocyanate (FITC; green, F-actin) and Cy5 (cyan, amyloplasts) channels. Scale bars = 10 μm. C and D, Z-projected actin cytoskeleton with extracted network overlaid for (A) wild type ($n = 14$) and (B) *rmd-2* mutant ($n = 15$). The color bar represents edge-capacity values. E and F, Ratio of the indicated property values between wild type (WT; $n = 14$) and *rmd-2* ($n = 15$; E) and a magnified boxplot for diameter (F). Boxplots are shown with median (horizontal line), 25th and 75th percentiles (box edges), and 1.5× interquartile range (whiskers). Values are means ± SD. Student's *t* test: $^{**}P < 0.01$, $^{***}P < 0.001$, and $^{****}P < 0.0001$.

hormones and the circadian clock, to regulate gene expression (Leivar and Monte, 2014). To test whether *RMD* expression is controlled by PIF-related proteins, we first analyzed cis-regulatory elements of the *RMD* promoter (2 kb upstream of start codon), using the online analytical tool MatInspector (Cartharius et al., 2005), and identified three predicted PIF-binding elements (PBE: −1,576 bp, G-box: −849 bp and −639 bp; Fig. 5A). We therefore speculated that *RMD* could be regulated by PILs (PIF homologs in rice) through their binding to the *RMD* promoter. To test this hypothesis, and due to low level expression of one member, we cloned five *PIL* genes among the six members in the rice genome, including *OsPIL11*, *OsPIL13*, *OsPIL14*, *OsPIL15*, and *OsPIL16*, by RT-qPCR from rice cDNAs and placed each gene under the *CaMV35S* promoter. We also fused ~2 kb of the *RMD* promoter with the gene of firefly luciferase (LUC), and cotransformed *35S*::*OsPILs* with *pRMD*::LUC into *Nicotiana benthamiana*, using renilla luciferase (REN) as an internal control. Luciferase activity measurements showed that *LUC* expression was activated by OsPIL15, but repressed by OsPIL16 (Fig. 5B). Interestingly, OsPIL15 and OsPIL16 are homologous, and share a 33% protein sequence similarity (Supplemental Fig. S6C).

Because PIFs regulate downstream genes by binding to G-boxes and PBE-boxes in the promoter of the target genes (Kidokoro et al., 2009), we performed yeast one-hybrid (Y1H) and chromatin immunoprecipitation (ChIP)-qPCR assays to assess whether OsPIL15 and OsPIL16 could bind to these boxes within the *RMD* promoter. Y1H assays showed that OsPIL16 interacted

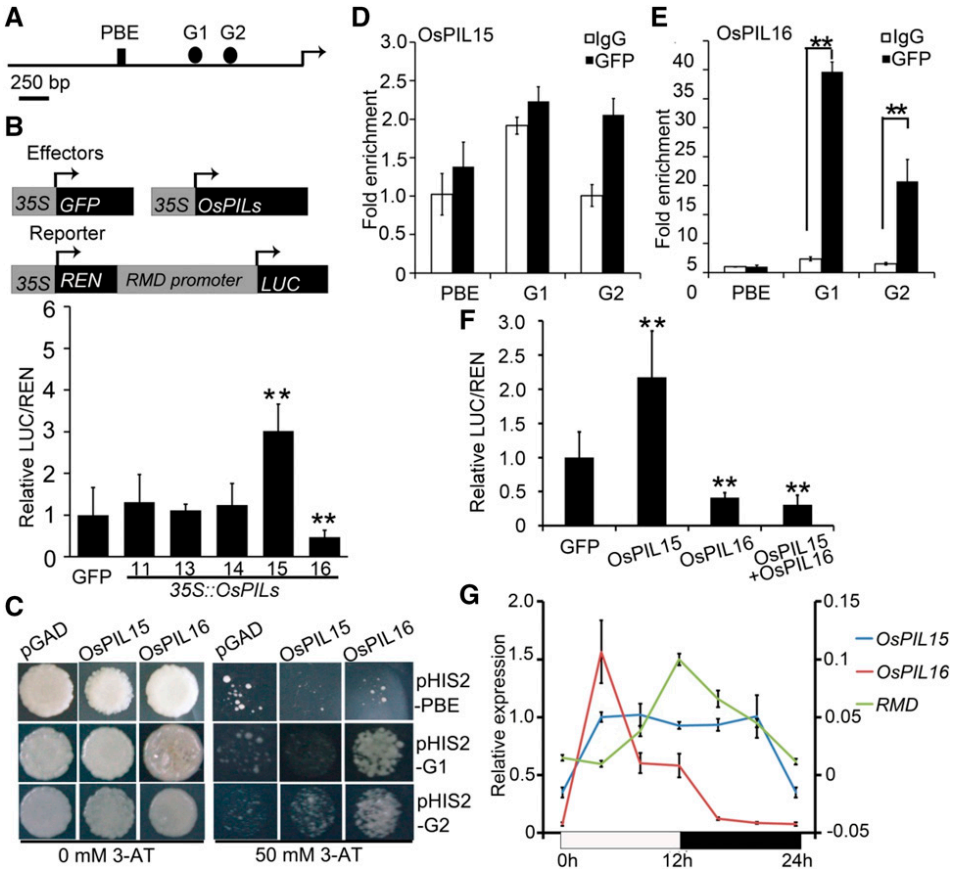

Figure 5. Regulation of *RMD* expression by OsPIL15 and OsPIL16. A, Cis-acting elements in the promoter of *RMD*. CACATG; G1 and G2, G-box, CACGTG. B, OsPIL15 activates *RMD* promoter activity and OsPIL16 inhibits *RMD* promoter activity in *N. benthamiana* leaf cells. Effectors are 35S::*OsPILs* and *35S*::*GFP* (control), and *pRMD*::*LUC* is the reporter. Renilla is the internal control whereby LUC activity was normalized to REN activity. Data were analyzed by conducting both *t* test and ANOVA. Data represent means ± SD ($n \geq 5$). $^{**}P < 0.01$. C, Y1H analysis. Interactions between OsPIL16 and G1 and G2, and between OsPIL15 and G2 in the promoter of *RMD*, are shown. D and E, ChIP-qPCR results showing binding of OsPIL15 (D) and OsPIL16 (E) to the *RMD* promoter fragments containing the PBE-box and G-box. Student's *t* test *P* values: $^{**}P < 0.01$. F, Co-expression of OsPIL15 and OsPIL16 inhibit *RMD* promoter activity in *N. benthamiana* leaf cells. Effectors are 35S::*OsPIL15*, 35S::*OsPIL16*, 35S::*OsPIL15*+*OsPIL16*, and *35S*::*GFP* (control), and *pRMD*::*LUC* is the reporter. Renilla is the internal control whereby LUC activity was normalized to REN activity. Data were analyzed by conducting both *t* test and ANOVA. Data represent means ± SD ($n \geq 5$). $^{**}P < 0.01$. G, RT-qPCR analysis of the diurnal expression pattern of *RMD* (right axis), *OsPIL15* (left axis), and *OsPIL16* (left axis) in growth chamber. Plants were placed in the 12-h/12-h light/dark cycle. Results are presented as means ± SD. Plants were placed in the 12-h/12-h light/dark cycle.

strongly with G1 and weakly with G2, while OsPIL15 interacted weakly with G2 (Fig. 5C). To investigate whether these PILs also bind to the *RMD* promoter in vivo, we generated rice transgenic lines expressing OsPIL15-GFP and OsPIL16-GFP (Supplemental Fig. S7, A and B). ChIP-qPCR assays using GFP antibodies on the nuclear protein–DNA complex extracted from the transgenic lines showed clear enrichment of the G1- and G2-boxes for OsPIL16, and slight enrichment of the G2-box for OsPIL15 (Fig. 5, D and E). Additional analysis of truncated *pRMD* constructs with the deletion of the above cis-elements showed that G1 and G2 were essential for OsPIL16's suppression of *RMD's* promoter activity, and that G2 was critical for OsPIL15 to activate *RMD's* promoter (Supplemental Fig. S7, C–E). Given that OsPIL15 activates and OsPIL16 represses *RMD* expression, we next assessed whether the *RMD* expression is induced or suppressed when both TFs are present. To do this, we coexpressed 35S-driven OsPIL15 and OsPIL16 and *pRMD*::LUC in *N. benthamiana* leaf cells and analyzed the promoter activity by dual-Luciferase (Dual-LUC) assay. These results clearly show that the *RMD* promoter activity was repressed (Fig. 5F), indicating that OsPIL16 has a stronger effect on *RMD* expression than OsPIL15.

As *RMD* exhibits diurnal expression, we also checked the expression of *OsPIL15* and *OsPIL16* using data from the RDB (http://ricexpro.dna.affrc.go.jp/). *OsPIL16* displayed an opposite expression pattern to that of *RMD*, whereas *OsPIL15* did not show significant diurnal expression, which we confirmed by RT-qPCR analyses (Fig. 5G). These data suggest that OsPIL15 might drive a basal expression of *RMD* during both day and night, but that OsPIL16 inhibits the *RMD* expression during the night when OsPIL16 is present. Due to the *RMD* promoter activity results, inverse expression relationship (Supplemental Fig. S6, A and D), and the strong interaction between *OsPIL16* and *RMD*, we chose to characterize the functional interactions of OsPIL16 and *RMD* in greater detail.

OsPIL16 Negatively Regulates *RMD* Gene Expression through Its bHLH Domain

OsPIL16 has two putative conserved motifs, an N-terminal PIL-motif possibly for the interaction with phytochromes and a C-terminal basic helix-loop-helix (bHLH) domain for DNA-binding (Nakamura et al., 2011; Supplemental Fig. S7F). To establish which region in OsPIL16 is responsible for repressing *RMD* expression, we fused each of these two motifs, or the full-length *OsPIL16* to the *binding domain* of GAL4, and performed transcriptional activation tests in yeast (Hao et al., 2010). The full-length OsPIL16, the PIL-containing OsPIL16-N, and the bHLH domain-containing OsPIL16-C conferred weak, strong, and no transcriptional activity in yeast, respectively (Supplemental Fig. S7G). Thus, we hypothesized that the bHLH domain of OsPIL16 might be responsible for repressing *RMD* transcriptional level. To test this hypothesis, we transiently coexpressed *OsPIL16* or *OsPIL16-C* with *pRMD*::*LUC* in *N. benthamiana*. Both constructs displayed reduced LUC activity compared with the control (Supplemental Fig. S7H). These data supported the conclusion that OsPIL16 represses *RMD* expression in rice through its C-terminal bHLH domain.

OsPIL16 Regulates Rice Growth and Shoot Gravitropism

If OsPIL16 is a negative regulator of *RMD* expression, overexpression (OE) of *OsPIL16* should mimic the *rmd* mutant phenotype to some degree. To this end, we generated transgenic rice plants expressing *35S*::*OsPIL16* and selected three independent lines that showed substantial reduction in *RMD* expression compared to the wild type (Supplemental Fig. S6, E and F). Similar to *rmd*, *OsPIL16* OE lines showed delayed shoot and root growth (Zhang et al., 2011; Li et al., 2014), and more transverse AFs in shoots (Supplemental Fig. S8, A–H). Quantification of the fluorescence intensity of the AlexaFluor488-phalloidin-labeled actin showed slightly weaker fluorescence signals in *OsPIL16*-OE lines than wild type in light, but not much difference in dark-grown seedlings (Supplemental Fig. S8, D and H), suggesting that OsPIL16 regulates actin cytoskeleton abundance via its repression of *RMD* in light.

We next checked whether *OsPIL16*-OE transgenic lines displayed an aberrant gravitropic response. The light-grown *OsPIL16*-OE transgenic lines displayed a reduced level of gravitropic response compared with wild type (Fig. 6, A and B), but this defect was less pronounced in etiolated seedlings (Fig. 6, C and D). Ten minutes after the light-grown seedlings were turned upside down, a large proportion of amyloplasts still remained in the middle of the shoot endodermal cells in *OsPIL16*-OE lines, which was in stark contrast to the wild type (Fig. 6, E, G, and H). However, most amyloplasts in the *OsPIL16*-OE lines finally reached the base of the cells in 20 min (Fig. 6, E, G, and H). Again, amyloplast sedimentation occurred at the same pace in etiolated wild-type and *OsPIL16*-OE seedlings (Fig. 6, F, G, and I). Together these results revealed striking similarities in phenotypic behavior of the *OsPIL16*-OE lines and the *rmd* mutant, providing strong evidence that *RMD* is negatively regulated by the light signaling component OsPIL16 and that this regulation is important for gravisensing in light-grown rice plants.

DISCUSSION

Shoot negative gravitropism is essential for plant architecture and yield (Li et al., 2007; Wu et al., 2013; Zhang et al., 2018). Seedling establishment is exquisitely sensitive to environmental cues and, after emergence from the soil, it is especially affected by the

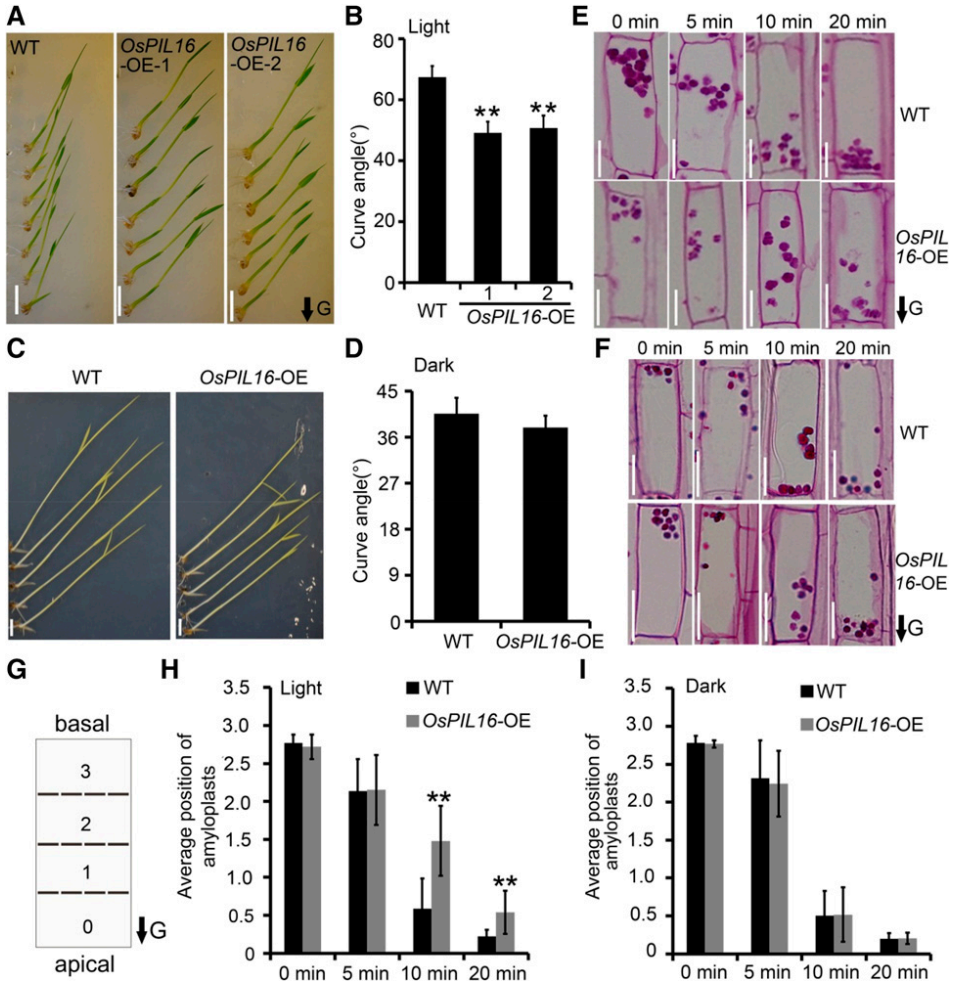

Figure 6. Analysis of gravitropism in *OsPIL16* OE lines. A, Five-days–old light-grown seedlings of wild type (WT) and *OsPIL16* OE lines 72 h after seedlings were turned 90°. Scale bars = 1 cm. Arrow indicates direction of gravity. B, Measurement of the angle of curves in shoots after gravistimulation. Data were analyzed by conducting both *t* test and ANOVA. Values are means ± SD. $n = 14$. $^{**}P < 0.01$. C, Five-d–old etiolated wild type and *OsPIL16*-OE 72 h after gravistimulation. Scale bars = 1 cm. D, Measurement of the angle of curves in etiolated wild type ($n = 13$) and *OsPIL16*-OE ($n = 13$) seedlings 72 h after gravistimulation. Values are means ± SD. E and F, Comparison of the kinetics of amyloplasts sedimentation in shoot endodermal cells in light-grown (E) and etiolated (F) wild type and *OsPIL16*-OE. Scale bars = 20 μm. Arrow indicates gravity direction. G, Schematic position of amyloplasts in endodermal cells. Each cell is divided into four equal segments numbered 0 to 3. Amyloplasts moved from basal to apical side after seedlings were inverted and their positions were scored. Arrow indicates direction of gravity. H, Average position of amyloplasts in light-grown wild type ($n = 84$ from four shoots) and *OsPIL16*-OE ($n = 84$ from four shoots) at different time points after seedlings were reoriented. Values (defined in G) are means ± SD. Student's *t* test: $^{**}P < 0.01$. I, Average position of amyloplasts in etiolated wild type ($n = 78$ from four shoots) and *OsPIL16*-OE ($n = 74$ from four shoots) at different time points after seedlings were reoriented. Values (defined in G) are means ± SD.

balance between the light/dark cycle and gravity (Gommers and Monte, 2018). In this work, we outline a mechanism for how plant shoots regulate their actin cytoskeleton to respond to gravitropic changes during the day to optimize seedling development.

AFs have long been suggested to be involved in shoot gravitropism through their ability to modulate amyloplast movement, but conflicting results have been reported (Yamamoto and Kiss, 2002; Hou et al., 2003; Palmieri and Kiss, 2005). Nevertheless, recent studies have indicated that AFs may act as tension sensors in the cell (Okamoto et al., 2015). In this study, we show that RMD is required for the organization of AFs, which impacts amyloplast behavior in shoot endodermal cells. RMD thus promotes negative gravitropism in rice shoots. Notably, even though *rmd* shoot endodermal and root columella cells had an impaired actin cytoskeleton, the amyloplasts sedimented faster in the columella cells and slower in the endodermal cells as compared to the control (Huang et al., 2018; Fig. 2). Hence, depending on the cellular context, RMD contributes differently to the gravitropic outputs. We speculate that this difference may be caused by the weak and ring-like F-actin surrounding amyloplasts in

root columella cells, but more abundant actin arrays in the shoot endodermal cells (Fig. 4). Indeed, previous studies showed that LatB-induced disruption of the actin cytoskeleton limited amyloplast dynamics in shoot endodermal cells, but induced settlement in root columella cells (Palmieri and Kiss, 2005). This again indicates a distinct role of F-actin in amyloplast dynamics during the gravitropic response in roots and shoots. The organ-specific gravitropic responses therefore suggest that the molecular mechanisms of gravitropic response vary between plant above- and below-ground organs. Furthermore, it is also plausible that vacuoles in shoot endodermal cells function as negative regulators of amyloplast sedimentation in shoot endodermal cells (Saito et al., 2005).

Interestingly, RMD only modulates shoot negative gravisensing in light-grown seedlings, linking the function of RMD to light signaling. Several studies have investigated the relationship between AFs and light, which is perhaps best described in the context of chloroplast movement under different light conditions (Wada and Kong, 2018). We hypothesize that, in light-grown plants, RMD promotes actin organization to support amyloplast distribution and as a result, gravisensing. This hypothesis agrees well with the localization of RMD to the amyloplast in the endodermis (Fig. 7). Similarly, E3 ligase protein SGR9 also localized on the surface of amyloplasts in the endodermis and positively modulated gravity sensing in Arabidopsis shoots (Nakamura et al., 2011). We therefore speculate that there is a possible link between RMD and protein-turnover components, such as E3 ligases; however, this remains to be elucidated. We previously presented in vitro biochemical data that RMD promotes AF formation and bundling (Zhang et al., 2011), and revealed the localization of RMD on chloroplast surface (via the phosphatase and tensin domain) in leaf cells (Zhang et al., 2011) and on the surface of statoliths in root

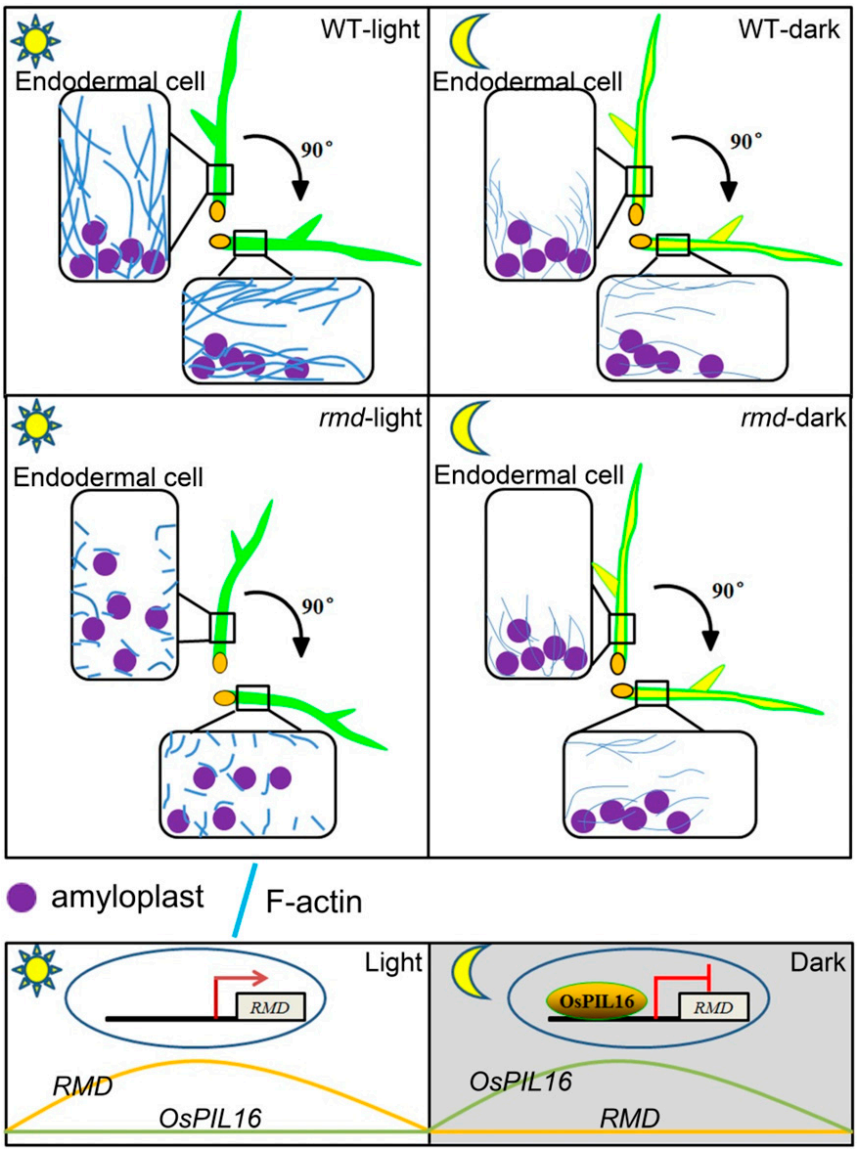

Figure 7. Schematic model for RMD function in light-mediated shoot negative gravitropism. In the dark and in the absence of phytochrome activity, OsPIL16 accumulates in the nucleus and inhibits *RMD* expression, changing actin organization in the endodermis to allow shoot negative gravitropism in etiolated seedlings. Upon exposure to light, the level of OsPIL16 is reduced, which allows expression of *RMD* and subsequent RMD-induced reorganization of the actin cytoskeleton that facilitates amyloplast dynamics in endodermal cells. In the absence of RMD, the endodermis fails to rearrange the actin organization, which reduces amyloplast sedimentation and consequently leads to abnormal shoot gravisensing in the light. WT, wild type.

columella cells (Huang et al., 2018). In this context, we postulate that RMD is anchored to amyloplasts via its phosphatase and tensin domain and that the formin domains of RMD orchestrate changes in AF organization in shoot endodermal cells.

In Arabidopsis, the light-mediated negative gravitropism of hypocotyls is inhibited by phytochromes through PIFs (Kim et al., 2011). However, the molecular mechanism and downstream components involved in this process are still not clear. In rice, Phytochrome A is important for the light-modulated root gravitropic response (Takano et al., 2001), indicating that gravisensing may also be modulated by light in rice shoots and that this phytochrome-mediated modulation of gravitropic response may be conserved in plants. Here, we provide evidence that the *RMD* gene is a direct target of the phytochrome interacting factor-like proteins OsPIL15 and OsPIL16, which regulate the expression of *RMD* during the diurnal cycle in rice. Specifically, OsPIL15 may maintain a "basal level" of *RMD* expression throughout the diurnal cycle as this TF is continuously on. By contrast, *OsPIL16* is only expressed during the night and strongly represses *RMD* expression and thus orchestrates changes in the actin cytoskeleton. OsPIL16 binds to the G-box of the *RMD* promoter through its C-terminal bHLH domain. Notably, despite OsPIL16 being a repressor of *RMD* expression, the N-terminal PIL-motif in OsPIL16 is a transcriptional activator, indicating that OsPIL16 may act as an activator or repressor depending on the circumstance. Similarly, the N terminus of AtPIF7 acts as a transcriptional activator in Arabidopsis, whereas its C-terminal bHLH domain repressed *DREB1* expression under circadian control (Kidokoro et al., 2009). Transcriptional activation via PIFs was also demonstrated in Arabidopsis (Moon et al., 2008; Sakuraba et al., 2014), indicating that PIFs have dual functions possibly depending on the promoter context. Interestingly, our analysis of 112 actin-related genes in rice (Supplemental Table S1), including those that encode formin, myosin, and actin-depolymerizing factors, revealed that the expression of 23 of them are diurnally regulated and 17 out of these 23 genes contain G-boxes in their promoters (Supplemental Fig. S9, A and B). Among these genes, we selected five members and conducted expression pattern analysis by RT-qPCR. Our results showed that these five genes indeed exhibited diurnal regulation (Supplemental Fig. S10, A–E). In addition, transferring dark-grown seedlings into light conditions impacted the transcriptional level of these genes (Supplemental Fig. S10F). These data further substantiate a close connection between light signaling and the actin cytoskeleton. In Arabidopsis, PIF1 share 19% protein sequence similarity of OsPIL15 and 24% of OsPIL16, required for photomorphogenesis and chlorophyll synthesis (Shen et al., 2005; Soy et al., 2014), but it is not clear whether Arabidopsis PIF1 plays a role in gravitropism and actin cytoskeleton patterning.

Based on our data, we propose a model in which rice shoot negative gravitropism is connected to light signaling via AFs (Fig. 7). In the dark, OsPIL16 accumulates and acts as a transcriptional repressor of *RMD*, and perhaps other actin-related genes, to change the organization of the actin cytoskeleton. When exposed to light, the level of OsPIL16 is possibly reduced, at least judging from transcript abundance, and *RMD* is consequently increased to modulate actin organization. As a result, amyloplast localization and movement are properly controlled in endodermal cells. In the absence of RMD, or when OsPIL16 is overexpressed, and thus *RMD* repressed, the actin cytoskeleton organization changes in light, which leads to aberrant amyloplast localization and movement, and abnormal shoot gravisensing (Fig. 7). In summary, our study has uncovered a mechanism underlying the intersection of light perception and gravitropism in plants.

MATERIALS AND METHODS

Plant Growth

All rice (*Oryza sativa*) plants are in the 9522 background (ssp. *japonica*). The two alleles, *rmd-1* and *rmd-2*, were generated by ^{60}Coray treatment from 9522. *rmd-1* contains a T-to-C transition and a four-nucleotide (AAGG) deletion in the 11th exon, leading to premature termination at the 1,465th amino acid. *rmd-2* has a four-nucleotide (ATGG) deletion in the 4th exon, leading to premature terminations at the 392nd amino acid. Rice seedlings were grown on 1% (w/v) agar in growth chambers under a 12-h light/12-h dark cycle at 30°C light/28°C dark. *Nicotiana benthamiana* plants were grown in growth chambers at 23°C with a 16-h light/8-h dark cycle. Seedlings were photographed using a model no. E995 Digital Camera (Nikon).

Generation of Rice Transgenic Lines

The *rmd-1* and *rmd-2* mutants, and *pLex*::*RMD-RFP* and *ProRMD*::*RMD-GFP* transgenic lines used in this study were described in Zhang et al. (2011), Li et al. (2014), and Huang et al. (2018). *ProOsPIN1b*::*OsPIN1b-YFP* was created by inserting the *PIN1b* cDNA (*AK102343*) into *Spe*I and *Sma*I sites of pA7-YFP, followed by the insertion of *OsPIN1b-YFP* into *Sma*I and *Eco*RI sites of *pCAMBIA1301*. The ~3-kb promoter of *OsPIN1b* was cloned from BAC *OSJNBa0055K09* and inserted into *Bst*EII and *Eco*RV sites of *pCAMBIA1301-OsPIN1b-YFP*. *ProOsPIN1b*::*OsPIN1b-YFP*/*rmd-2* was obtained by crossing *ProOsPIN1b*::*OsPIN1b-YFP*/*9522* with *rmd-2*. The *OsPIL15*-overexpressing construct was created by inserting the 1,911-bp *OsPIL16* cDNA into the *Nco*I and *Bgl*II sites of *pCAMBIA1301*. The *OsPIL16*-overexpressing construct was created by inserting the 1,512-bp *OsPIL16* cDNA into the *Bgl*II and *Spe*I sites of *pCAMBIA1301*. The final constructs were transformed into wild-type rice callus by *Agrobacterium tumefaciens*-mediated transformation. Primers used to create *pCAMBIA1301-OsPIN1b-YFP*-and *OsPIL16*-overexpressing lines are listed in Supplemental Table S2.

Gravitropism Assay

After sterilizing with 70% (v/v) ethanol for 2 min and then washing five times with double-distilled water, rice seeds were placed on three layers of filter paper in plates containing half-strength liquid MS at 28°C. Two-d–old seedlings without true leaf outgrowth, or a 5-d–old seedling with one true leaf, were used for quantification. At these stages, the gravitropic set-point angle (GSA) was at the base of the seedlings (Fig. 2A). As shown in Figure 1A, except for S-shape and twisted *rmd* mutants, the base of *rmd* bending seedlings was straight, and we thus selected this type of mutant for the analysis. The seedlings were transferred to a new agar plate and kept for 3 h of vertical growth before being turned 90° and grown under dim and nondirectional light. The gravitropic curvature was determined by measuring the angle of the reoriented shoots using the software ImageJ (National Institutes of Health).

Histochemical Analysis

For histochemical analysis, 5-d–old seedlings grown in the soil were selected. Tissue was cut close by the GSA and quickly fixed in 10% (v/v) formaldehyde, 5% (v/v) acetic acid, and 50% (v/v) ethanol in vertical position for 30 min in 0.2-mL tubes under vacuum. After fixation, samples were dehydrated in 30%, 50%, 70%, 80%, 95%, 100%, and 100% (v/v) ethanol for 30 min at each concentration. Samples were infiltrated and embedded in Technovit 7100 resin embedding kit (Heraeus Kulzer). Infiltration solution was prepared by dissolving 1 g of Hardener I into 100 mL of Basic resin. Then samples were pre-infiltrated in a mixed solution of 100% ethanol and infiltration solution (v/v = 1:1) for 2 h. After this, samples were transferred into infiltration solution and kept overnight. The embedding solution was prepared just before use, by mixing Hardener II and the infiltration solution at a ratio of 1:15. Samples in the embedding solution were kept at 37°C until solidifying. Sections (5 μm) were made using a semi-thin microtome (Leica Microsystems), and stained with 0.5% (w/v) toluidine blue. The periodic acid-Schiff kit (Sigma-Aldrich) was used to stain amyloplasts for amyloplast sedimentation analysis (Wu et al., 2013). Photos were taken with an Ni-E Optical Microscope (Nikon). For each time point, the amyloplast positions in at least 70 endodermal cells were examined from four different shoots.

Pharmacological Treatments

LatB (10 mM; Sigma-Aldrich) and estradiol (50 mM; Sigma-Aldrich) were kept as stock solutions in dimethyl sulfoxide. The desired concentration of LatB and estradiol was obtained by diluting each chemical in water (Yamamoto and Kiss, 2002). After germination, seeds were put on top of the three layers of filter paper in a bottle containing half-stength liquid MS with LatB or estradiol, without being immersed into the liquid medium. Seedlings were photographed using a model no. E995 Digital Camera (Nikon).

F-Actin Staining

F-actin staining and fluorescence quantification was performed as described in Zhang et al. (2011) and Yang et al. (2011) with slight modification. Shoots were cut from ~5-d–old rice seedlings. Tissue was cut close to the GSA. Then samples were incubated for 1 h in PEM buffer (100 mM of Piperazine-1,4-bisethanesulfonic acid, 10 mM of EGTA, 5 mM of $MgSO_4$, and 0.3 M of mannitol at pH = 6.9) that contains 2% (v/v) glycerol (Sigma-Aldrich) and 6.6 μM of Alexa Fluor 488-phalloidin (Invitrogen), and then observed in 50% (v/v) glycerol (Sigma-Aldrich) with a model no. A1R Laser Scanning Confocal Microscope (Nikon). At least 10 cells from three different lines were examined.

Microscopic Analysis

Confocal microscopy was conducted with a model no. A1R Laser Scanning Confocal Microscope (Nikon). Fluorescence signals for GFP and amyloplast autofluorescence were detected with 500- to 510-nm and 640- to 700-nm settings respectively, with the excitation wavelength of 488 nm. Images were extracted with an NIS-Elements Viewer 4.20 (Nikon) and processed with the software Adobe Photoshop CS6 (Adobe).

Dual-LUC Assay

Dual-LUC assay was performed using *N. benthamiana* plants. With the exception of *OsPIL12*, all of the rice PILs (*OsPIL11*, *13*, *14*, *15*, and *16*) were successfully cloned. Effectors were constructed by cloning full-cDNAs of *OsPILs* into *Hin*dIII and *Xba*I sites of the pGreenII-0000 vector, under the control of *35S* promoter, and *35S*::*OsPIL16C* was constructed by inserting a 510-bp C-terminal sequence of *OsPIL16* into *Hin*dIII and *Eco*RI sites of the same vector. For co-expression of OsPIL15 and OsPIL16, the whole length of the *35S* promoter and *OsPIL15* were amplified and cloned into *Xba*I sites of the pGreenII-0000 vector. Reporters *pGreen-pRMD::LUC*, *pGreen-pRMDδI::LUC*, *pGreen-pRMDδII::LUC*, and *pGreen-pRMDδIII::LUC* were constructed by fusing firefly LUC with the truncated *RMD* promoters, followed by insertion of the final construct into *Hin*dIII and *Nco*I sites of the pGreenII-0800 vector. REN was the internal control.

Effectors and reporters were cotransformed into *Agrobacterium* (strain GV3101) with the helper plasmid pSoup-19. *Agrobacterium* was resuspended with MS medium (pH = 5.8) and adjusted to OD_{600} = 0.6 before MES (pH = 5.6, 10-μM final concentration) and acetosyringone (200-μM final concentration) were added. After incubation for ~3 h at room temperature, the *Agrobacterium* mixture (reporter: effector ratio at 2:8) was infiltrated into young *N. benthamiana* leaves with a 1-mL syringe. Plants were kept under weak light conditions for 48 h.

LUC and REN activities were tested using dual-LUC assay reagents (Promega) according to the manufacturer's instructions. LUC/REN values were measured in a Turner 20/20 Luminometer (Promega). At least five biological replicates were measured for each sample. The primer sequences used to perform Dual-LUC assay are listed in Supplemental Table S2.

Y1H Assay

Fragments of the *RMD* promoter that contain PBE-box (163 bp) or G-boxes (164 bp, 189 bp) were amplified and cloned into *Sac*I and *Sac*II sites of the pHIS2 vector (Clontech). Full-length cDNAs of *OsPIL15* and *OsPIL16* were amplified and inserted into *Nde*I and *Bam*HI sites of pGADT7 (Clontech). Yeast strain Y187 was used to perform Y1H. Y187 was incubated in a YPD medium (yeast extract 10 g/L, peptone 20 g/L, and dextrose 16 g/L medium) at 30°C overnight. Constructed pHIS2 and pGADT7 plasmids were prepared with cDNA, and cotransformed into yeast strain by incubating with 100 mM of DTT, 0.2 M of lithium acetate, and 40% (w/v) polyethylene glycol at 45°C for 30 min. Protein–DNA interactions among OsPIL15, OsPIL16, and various *RMD* promoter fragments were analyzed in SD/-Trp/-Leu/-His medium containing 0 mM or 50 mM of 3-amino-11, 2, 4-triazole. Primer sequences used in the Y1H assay are listed in Supplemental Table S2.

ChIP qPCR Assay

The ChIP assay was performed using a protocol described in Bowler et al. (2004). Two-week–old *35S*::*OsPIL15-GFP* or *35S*::*OsPIL16-GFP* transgenic seedlings were used to isolate chromatin. Seedlings (200 g) were cut into pieces in 50 mL of EB1 buffer (10 mM of Tris-HCl at pH = 8.0, 0.4 M of Suc, 0.1 mM of Phenylmethanesulfonyl fluoride, and 5 mM ofβ-Mercaptoethanol [β-ME]) containing 1% (v/v) formaldehyde and then kept under vacuum for 30 min, after which 0.125 M of Gly was added to stop cross-linking and samples were washed with water 8–10 times to eliminate elution buffer (EB1). Then, samples were ground in 30 mL of EB1 buffer without formaldehyde, and filtered at 2,880 g through four layers of Miracloth (EMD Millipore) for 20 min. After the supernatant was discarded, samples were resuspended in 1 mL of EB2 solution (10 mM of Tris-HCl at pH = 8.0, 0.25 M of Suc, 10 mM of $MgCl_2$, 1% [v/v] TritonX-100, 5 mM of β-ME, 0.1 mM of PMSF, and protease inhibitor), centrifuged at 20,000*g* for 5 min, and resuspended with 300 μL of EB3 (10 mM of Tris-HCl at pH = 8.0, 1.7 M of Suc, 2 mM of $MgCl_2$, 0.15% [v/v] TritonX-100, 5 mM of β-ME, 0.1 mM of PMSF, and protease inhibitor) before gentle transfer into a new tube containing EB3 solution in the same volume. Samples were centrifuged at 16,000*g* for 1 h and resuspended in 250 μL of nuclei lysis buffer (1% [w/v] SDS, 50 mM of Tris-HCl at pH = 8.0, 10 mM of EDTA, 0.1 mM of PMSF, and protease inhibitor), and then stored at −20°C. Chromatins that are 500 bp to 1 kb were obtained by sonication, after which the supernatants that contained complexes of nuclear protein and nucleic acid were collected.

For immunoprecipitation, firstly we added 900 μL of ChIP dilution buffer (16.7 mM of Tris-HCl at pH = 8.0, 1.2 mM of EDTA, 167 mM of NaCl, 1% [v/v] Triton X-100, 0.1 mM of PMSF, and protease inhibitor) into 100-μL complex to dilute SDS, then added 40 μL of Protein A/G agarose/salmon sperm DNA beads, shaken slightly at 4°C for 1 h. After collecting supernatants, we continued to add IgG and GFP antibody, and samples were incubated and agitated gently overnight at 4°C. Then we collected immunoprecipitate by adding protein A agarose beads and agitating gently for 1 h at 4°C. The immunoprecipitated protein–DNA complexes were eluted with 0.1 M of $NaHCO_3$ containing 1% (w/v) SDS. We reversed the cross-link by incubation at 65°C with 250 mM of NaCl. For extracting DNA, first we incubated samples with 20 μL of 1 M Tris-HCl at pH = 6.5, 10 μL of 0.5 M EDTA, and 1.5 μL of 14 mg/mL proteinase K at 45°C for 1 h. Then we obtained DNA by phenol/chloroform extraction and ethanol precipitation. For qPCR reactions, the recovered DNA was used as a template, with three biological replicates. The primers used in the ChIP-qPCR assay are listed in Supplemental Table S2.

Transcriptional Activity Detection in Yeast

For transcriptional activity assay in yeast, *OsPIL16*, *OsPIL16N*, and *OsPIL16C* were introduced into pGBKT7 by inserting full-length (the 330-bp N-terminal region or the 510-bp C-terminal region) *OsPIL16* into the restriction sites *Nde*I and *Eco*RI. Y1H assays were performed following the manufacturer's instructions (Clontech). Yeast strain AH109 was used to perform the assay. pGBKT7-OsPIL16, pGBKT7-OsPIL16N, pGBKT7-OsPIL16C, and pGBKT7 were transformed into yeast strain AH109 individually, just as mentioned in "Y1H Assay." To test the transcriptional activity conferred by OsPIL16 on the promoter, yeast colonies were kept at 28°C for 2–3 d in SD-Trp and SD-Trp-His medium. Primers used for Y1H constructs are listed in Supplemental Table S2.

Assays to Measure IAA Level and Polar Transport

Inside or outside shoot segments from 5-d–old seedlings were collected for quantification of endogenous free auxin. IAA levels were measured as described in Barbez et al. (2012) with slight modification. Materials were grinded with 1 mL of cold P buffer (50 mM, pH = 7.0) and free IAA was extracted with methanol. Analysis was done by gas chromatography–mass spectrometry. Data presented are the means of three independent lots with 30–50 seedlings in each lot.

IAA polar transport was measured according to the method described in Lin et al. (2009). One-d–old coleoptiles were kept in darkness in MS liquid medium containing phytogel and 0.1 μM of ^{3}H-labeled IAA (American Radiolabeled Chemicals) at 28°C room temperature. N-1-naphthylphthalamic acid was used as a negative control to block IAA transport; shootward IAA transport was also used as a negative control. After incubation for ~3 h, 5 mm of nonsubmerged coleoptiles were excised and transferred into 2 mL of scintillation liquid (0.03% [w/v] 1,4-bis[5-phenyloxazol-2-yl] benzene, 0.3% [w/v] 2,5-diphenyloxazole, 80% [w/v] methylbenzene, 20% [v/v] glycol ether), then incubated for 18 h, before radioactivity was measured by a liquid scintillation counter (LS650; Beckman).

RNA Extraction and mRNA Expression Analysis

For RT-qPCR analysis, total RNA was isolated with the TRIZOL Reagent (Invitrogen). cDNA was synthesized from 4 μg of total RNA with M-MLV reverse transcriptase (Primescript RT Reagent Kit; Takara). RT-qPCR was performed using CFX384 (Bio-Rad) with the SYBR FAST qPCR Master Mix (KAPA Bio). Rice *Ubiquitin* mRNA was used as an internal control. For RT-qPCR assays, cDNA was denatured at 95°C for 10 min, followed by 45 cycles of 10^{-s} 95°C, 15^{-s} 58°C, and 15^{-s} 72°C. All results were presented as the means of three biological replicates. Primers used for gene expression analysis are listed in Supplemental Table S2.

Phylogenetic Analysis and Expression Profiling

Full-length amino acid sequences of PIL family members in Arabidopsis and rice were used to construct the phylogenetic tree using the software ClustalW (https://www.genome.jp/tools-bin/clustalw) for amino acid alignment, and the software MEGA 6.0 (https://www.megasoftware.net/) and the neighbor-joining tree method with a Poisson model, partial deletion, and bootstrap (1,000 replicates) were used for tree construction (Hall, 2013).

Accession numbers used to construct phylogenetic trees are as follows: *AtPIF1*, AT2G20180; *ATPIL1*, AT2G46970; *AtPIF3*, AT1G09530; *AtPIF4*, AT2G43010; *AtPIF5*, AT3G59060; *AtPIF6*, AT3G62090; *AtPIF7*, AT5G61270; *AtPIF8*, AT4G00050; *OsPIL11*, Os12g0610200; *OsPIL12*, Os03g0639300; *OsPIL13*, Os03g0782500; *OsPIL14*, Os07g0143200; *OsPIL15*, Os01g0286100; and *OsPIL16*, Os05g0139100.

The GENESIS software platform (http://genesis-sim.org/) was used to profile gene expression (Sturn et al., 2002). Gene expression data were downloaded from the RDB (http://ricexpro.dna.affrc.go.jp/; Sato et al., 2011). An expression image was calculated and imported in the software after loading the data. We set the upper maximum value as 1.0, and lower maximum value as −1.0. The operating procedure is based on the GENESIS manual written by Sturn et al. (2002).

Quantitative Analysis of the Actin Cytoskeleton

Actin networks extracted from images were analyzed using the automated extraction pipeline described in Breuer et al. (2017). Shoots of ~5-d–old rice seedlings were selected, from which we cut away the epidermis layers. Endodermal cell layers were quickly transformed into and were kept vertically in PEM buffer that contains 2% (v/v) glycerol (Sigma-Aldrich) and 6.6 μM of Alexa Fluor 488-phalloidin (Invitrogen). Samples were incubated for 1 h. After that, we imaged the actin cytoskeleton in wild-type and *rmd-2* endodermal rice cells as described in the "F-Actin Staining" and "Microscopic Analysis" sections and processed the images using a Fiji pipeline (National Institutes of Health) by correcting for bleaching, uneven illuminated background, and drifting of cells (Schindelin et al., 2012). Because the images consisted of multiple slices that were taken at different focal distances, we used the maximum intensity Z-projection to combine them into a composite image.

Afterward, we selected the region of interest and enhanced tube-like structures, before binarizing the image with an adaptive threshold and skeletonizing the binarized cytoskeleton, i.e. representing it as a one-pixel–wide skeleton. From the resulting skeleton, we identified nodes (end-points and crossings) that were connected with an edge if they were directly connected. The resulting networks were finally weighted according to their average AF thickness and selected network-based properties were calculated.

Aside from the properties analyzed in Breuer et al. (2017), e.g. the number of connected components, average edge capacity, and average shortest path length, we also computed the diameter of the extracted networks and normalized the extracted values by the expected diameter following Moore's bound $D_{\exp} = \log_{\Delta} n$, where Δ is the maximum degree and n is the largest number of edges. An independent two-sample t test was used to compare the calculated properties of wild-type and *rmd-2* mutant networks. We used 14 replicates for the wild type and 15 replicates for the *rmd-2* mutant. From each image we extracted the actin cytoskeleton network and calculated the above-mentioned properties.

Statistical Analyses

Statistical analyses were performed with the software SPSS 22.0 (IBM). For the two groups' comparison, we used one-tailed Student's t test. For multiple comparisons, both the Student's t test and ANOVA followed by the posthoc test least-significant difference method were performed, which are mentioned in the figure legends. Values are means ± SD. At least three biological replicates are shown (P values: one asterisk shows significance at $P < 0.05$, two asterisks show significance at $P < 0.01$, three asterisks show significance at $P < 0.001$, and four asterisks show significance at $P < 0.0001$).

Accession Numbers

Sequence data used in this article can be found from the National Center for Biotechnology Information database under the following accession numbers: *OsPIL15*, Os01g0286100; *OsPIL16*, Os05g0139100; *Osmyosin-1*, LOC_Os07g37560; *OsOpaque10*, LOC_Os03g49630; *OsARP8*, LOC_Os04g57210; *OsFH3*, LOC_Os10g02980; *OsFH5*, LOC_Os07g40510; *OsFH6*, LOC_Os08g17820; *OsFH13*, LOC_Os07g39920; *OsFH15*, LOC_Os09g34180; *OsADF1*: LOC_Os02g44470; *OsADF2*: LOC_Os03g56790; *OsADF3*: LOC_Os03g60580; and *OsADF11*: LOC_Os12g43340.

Supplemental Data

The following supplemental materials are available.

Supplemental Figure S1. Growth direction of 4-d–old light-grown wild-type and rmd-2 shoots at intervals at 20°.

Supplemental Figure S2. Complementation of *rmd* by the estradiol-inducible *RMD* transgene and localization of OsPIN1b-YFP.

Supplemental Figure S3. Shoot negative gravitropism assay 2 d after germination.

Supplemental Figure S4. Distribution of amyloplasts wild-type and *rmd* seedlings.

Supplemental Figure S5. The effect of LatB on shoot gravitropism in plants.

Supplemental Figure S6. Expression patterns of *RMD* and *OsPIL16*, and phylogenetic analysis of PIL family proteins.

Supplemental Figure S7. OsPIL15 and OsPIL16 directly regulate *RMD* expression.

Supplemental Figure S8. OE lines of *OsPIL16* exhibit aberrant development and actin organization.

Supplemental Figure S9. Expression of rice genes putatively involved in actin cytoskeleton regulation and their promoter analysis.

Supplemental Figure S10. Diurnal expression patterns and light-induced expression of selected actin-related genes.

Supplemental Table S1. Accession number, annotation, and expression data downloaded from the Rice Expression Profile Database (RiceXPro) of 112 actin-related genes.

Supplemental Table S2. Sequences of primers used in this study.

ACKNOWLEDGMENTS

The authors thank Mingjiao Chen and Zhijing Luo (Shanghai Jiao Tong University) for performing rice cultivation, Gwen Mayo (Adelaide Microscopy) for assistance in the microscopy work, Dan Peet (the University of Adelaide) for providing the LUC luminometer, and Hongquan Yang for providing pGreenII-0000 and pGreenII-0800 vectors.

Received April 25, 2019; accepted July 30, 2019; published August 15, 2019.

LITERATURE CITED

Baluška F, Jasik J, Edelmann HG, Salajová T, Volkmann D (2001) Latrunculin B-induced plant dwarfism: Plant cell elongation is F-actin-dependent. Dev Biol **231:** 113–124

Barbez E, Kubeš M, Rolčík J, Béziat C, Pěnčík A, Wang B, Rosquete MR, Zhu J, Dobrev PI, Lee Y, et al (2012) A novel putative auxin carrier family regulates intracellular auxin homeostasis in plants. Nature **485:** 119–122

Behringer FJ, Lomax TL (1999) Genetic analysis of the roles of phytochromes A and B1 in the reversed gravitropic response of the *lz-2* tomato mutant. Plant Cell Environ **22:** 551–558

Blancaflor EB, Masson PH (2003) Plant gravitropism. Unraveling the ups and downs of a complex process. Plant Physiol **133:** 1677–1690

Bowler C, Benvenuto G, Laflamme P, Molino D, Probst AV, Tariq M, Paszkowski J (2004) Chromatin techniques for plant cells. Plant J **39:** 776–789

Breuer D, Nowak J, Ivakov A, Somssich M, Persson S, Nikoloski Z (2017) System-wide organization of actin cytoskeleton determines organelle transport in hypocotyl plant cells. Proc Natl Acad Sci USA **114:** E5741–E5749

Cartharius K, Frech K, Grote K, Klocke B, Haltmeier M, Klingenhoff A, Frisch M, Bayerlein M, Werner T (2005) MatInspector and beyond: Promoter analysis based on transcription factor binding sites. Bioinformatics **21:** 2933–2942

Ding Z, Galván-Ampudia CS, Demarsy E, Łangowski Ł, Kleine-Vehn J, Fan Y, Morita MT, Tasaka M, Fankhauser C, Offringa R, et al (2011) Light-mediated polarization of the PIN3 auxin transporter for the phototropic response in *Arabidopsis*. Nat Cell Biol **13:** 447–452

Dong Z, Jiang C, Chen X, Zhang T, Ding L, Song W, Luo H, Lai J, Chen H, Liu R, et al (2013) Maize LAZY1 mediates shoot gravitropism and inflorescence development through regulating auxin transport, auxin signaling, and light response. Plant Physiol **163:** 1306–1322

Fukaki H, Fujisawa H, Tasaka M (1996) *SGR1, SGR2, SGR3*: Novel genetic loci involved in shoot gravitropism in *Arabidopsis thaliana*. Plant Physiol **110:** 945–955

Fukaki H, Wysocka-Diller J, Kato T, Fujisawa H, Benfey PN, Tasaka M (1998) Genetic evidence that the endodermis is essential for shoot gravitropism in *Arabidopsis thaliana*. Plant J **14:** 425–430

Gaiser JC, Lomax TL (1993) The altered gravitropic response of the *lazy-2* mutant of tomato is phytochrome regulated. Plant Physiol **102:** 339–344

Gommers CMM, Monte E (2018) Seedling establishment: A dimmer switch-regulated process between dark and light signaling. Plant Physiol **176:** 1061–1074

Hall BG (2013) Building phylogenetic trees from molecular data with MEGA. Mol Biol Evol **30:** 1229–1235

Hao YJ, Song QX, Chen HW, Zou HF, Wei W, Kang XS, Ma B, Zhang WK, Zhang JS, Chen SY (2010) Plant NAC-type transcription factor proteins contain a NARD domain for repression of transcriptional activation. Planta **232:** 1033–1043

Hobbie L, Estelle M (1995) The *axr4* auxin-resistant mutants of *Arabidopsis thaliana* define a gene important for root gravitropism and lateral root initiation. Plant J **7:** 211–220

Hou G, Mohamalawari DR, Blancaflor EB (2003) Enhanced gravitropism of roots with a disrupted cap actin cytoskeleton. Plant Physiol **131:** 1360–1373

Huang G, Liang W, Sturrock CJ, Pandey BK, Giri J, Mairhofer S, Wang D, Muller L, Tan H, York LM, et al (2018) Rice actin binding protein RMD controls crown root angle in response to external phosphate. Nat Commun **9:** 2346

Kidokoro S, Maruyama K, Nakashima K, Imura Y, Narusaka Y, Shinwari ZK, Osakabe Y, Fujita Y, Mizoi J, Shinozaki K, et al (2009) The phytochrome-interacting factor PIF7 negatively regulates *DREB1* expression under circadian control in Arabidopsis. Plant Physiol **151:** 2046–2057

Kim K, Shin J, Lee SH, Kweon HS, Maloof JN, Choi G (2011) Phytochromes inhibit hypocotyl negative gravitropism by regulating the development of endodermal amyloplasts through phytochrome-interacting factors. Proc Natl Acad Sci USA **108:** 1729–1734

Kiss JZ (2000) Mechanisms of the early phases of plant gravitropism. CRC Crit Rev Plant Sci **19:** 551–573

Lariguet P, Fankhauser C (2004) Hypocotyl growth orientation in blue light is determined by phytochrome A inhibition of gravitropism and phototropin promotion of phototropism. Plant J **40:** 826–834

Leivar P, Monte E (2014) PIFs: Systems integrators in plant development. Plant Cell **26:** 56–78

Li G, Liang W, Zhang X, Ren H, Hu J, Bennett MJ, Zhang D (2014) Rice actin-binding protein RMD is a key link in the auxin-actin regulatory loop that controls cell growth. Proc Natl Acad Sci USA **111:** 10377–10382

Li G, Yang X, Zhang X, Song Y, Liang W, Zhang D (2018) Rice morphology determinant-mediated actin filament organization contributes to pollen tube growth. Plant Physiol **177:** 255–270

Li P, Wang Y, Qian Q, Fu Z, Wang M, Zeng D, Li B, Wang X, Li J (2007) *LAZY1* controls rice shoot gravitropism through regulating polar auxin transport. Cell Res **17:** 402–410

Lin H, Wang R, Qian Q, Yan M, Meng X, Fu Z, Yan C, Jiang B, Su Z, Li J, et al (2009) DWARF27, an iron-containing protein required for the biosynthesis of strigolactones, regulates rice tiller bud outgrowth. Plant Cell **21:** 1512–1525

Mirza JI, Olsen GM, Iversen TH, Maher E (1984) The growth and gravitropic responses of wild-type and auxin-resistant mutants of *Arabidopsis thaliana*. Physiol Plant **60:** 516–522

Moon J, Zhu L, Shen H, Huq E (2008) PIF1 directly and indirectly regulates chlorophyll biosynthesis to optimize the greening process in *Arabidopsis*. Proc Natl Acad Sci USA **105:** 9433–9438

Morita MT (2010) Directional gravity sensing in gravitropism. Annu Rev Plant Biol **61:** 705–720

Morita MT, Sakaguchi K, Kiyose S, Taira K, Kato T, Nakamura M, Tasaka M (2006) A C2H2-type zinc finger protein, SGR5, is involved in early events of gravitropism in Arabidopsis inflorescence stems. Plant J **47:** 619–628

Nakamura M, Toyota M, Tasaka M, Morita MT (2011) An *Arabidopsis* E3 ligase, SHOOT GRAVITROPISM9, modulates the interaction between statoliths and F-actin in gravity sensing. Plant Cell **23:** 1830–1848

Okamoto K, Ueda H, Shimada T, Tamura K, Kato T, Tasaka M, Morita MT, Hara-Nishimura I (2015) Regulation of organ straightening and plant posture by an actin–myosin XI cytoskeleton. Nat Plants **1:** 15031

Palmieri M, Kiss JZ (2005) Disruption of the F-actin cytoskeleton limits statolith movement in *Arabidopsis* hypocotyls. J Exp Bot **56:** 2539–2550

Poppe C, Hangarter RP, Sharrock RA, Nagy F, Schäfer E (1996) The light-induced reduction of the gravitropic growth-orientation of seedlings of *Arabidopsis thaliana* (L.) Heynh. is a photomorphogenic response mediated synergistically by the far-red-absorbing forms of phytochromes A and B. Planta **199:** 511–514

Robson PR, Smith H (1996) Genetic and transgenic evidence that phytochromes A and B act to modulate the gravitropic orientation of *Arabidopsis thaliana* hypocotyls. Plant Physiol **110:** 211–216

Saito C, Morita MT, Kato T, Tasaka M (2005) Amyloplasts and vacuolar membrane dynamics in the living graviperceptive cell of the Arabidopsis inflorescence stem. Plant Cell **17:** 548–558

Sakuraba Y, Jeong J, Kang MY, Kim J, Paek NC, Choi G (2014) Phytochrome-interacting transcription factors PIF4 and PIF5 induce leaf senescence in *Arabidopsis*. Nat Commun **5:** 4636

Sato Y, Antonio BA, Namiki N, Takehisa H, Minami H, Kamatsuki K, Sugimoto K, Shimizu Y, Hirochika H, Nagamura Y (2011) RiceXPro: A platform for monitoring gene expression in *japonica* rice grown under natural field conditions. Nucleic Acids Res **39:** D1141–D1148

Schindelin J, Arganda-Carreras I, Frise E, Kaynig V, Longair M, Pietzsch T, Preibisch S, Rueden C, Saalfeld S, Schmid B, et al (2012) Fiji: An open-source platform for biological-image analysis. Nat Methods **9:** 676–682

Shen H, Moon J, Huq E (2005) PIF1 is regulated by light-mediated degradation through the ubiquitin-26S proteasome pathway to optimize photomorphogenesis of seedlings in Arabidopsis. Plant J **44:** 1023–1035

Soy J, Leivar P, Monte E (2014) PIF1 promotes phytochrome-regulated growth under photoperiodic conditions in *Arabidopsis* together with PIF3, PIF4, and PIF5. J Exp Bot **65:** 2925–2936

Sturn A, Quackenbush J, Trajanoski Z (2002) Genesis: Cluster analysis of microarray data. Bioinformatics **18:** 207–208

Takano M, Kanegae H, Shinomura T, Miyao A, Hirochika H, Furuya M (2001) Isolation and characterization of rice phytochrome A mutants. Plant Cell **13:** 521–534

Tasaka M, Kato T, Fukaki H (1999) The endodermis and shoot gravitropism. Trends Plant Sci **4:** 103–107

Vitha S, Yang M, Sack FD, Kiss JZ (2007) Gravitropism in the *starch excess* mutant of *Arabidopsis thaliana*. Am J Bot **94:** 590–598

Wada M, Kong SG (2018) Actin-mediated movement of chloroplasts. J Cell Sci **131:** jcs210310

Wu X, Tang D, Li M, Wang K, Cheng Z (2013) Loose Plant Architecture1, an INDETERMINATE DOMAIN protein involved in shoot gravitropism, regulates plant architecture in rice. Plant Physiol **161:** 317–329

Yamamoto K, Kiss JZ (2002) Disruption of the actin cytoskeleton results in the promotion of gravitropism in inflorescence stems and hypocotyls of Arabidopsis. Plant Physiol **128:** 669–681

Yamauchi Y, Fukaki H, Fujisawa H, Tasaka M (1997) Mutations in the *SGR4, SGR5* and *SGR6* loci of *Arabidopsis thaliana* alter the shoot gravitropism. Plant Cell Physiol **38:** 530–535

Yang W, Ren S, Zhang X, Gao M, Ye S, Qi Y, Zheng Y, Wang J, Zeng L, Li Q, et al (2011) *BENT UPPERMOST INTERNODE1* encodes the class II formin FH5 crucial for actin organization and rice development. Plant Cell **23:** 661–680

Yano D, Sato M, Saito C, Sato MH, Morita MT, Tasaka M (2003) A SNARE complex containing SGR3/AtVAM3 and ZIG/VTI11 in gravity-sensing cells is important for *Arabidopsis* shoot gravitropism. Proc Natl Acad Sci USA **100:** 8589–8594

Zhang N, Yu H, Yu H, Cai Y, Huang L, Xu C, Xiong G, Meng X, Wang J, Chen H, et al (2018) A core regulatory pathway controlling rice tiller angle mediated by the *LAZY1*-dependent asymmetric distribution of auxin. Plant Cell **30:** 1461–1475

Zhang Z, Zhang Y, Tan H, Wang Y, Li G, Liang W, Yuan Z, Hu J, Ren H, Zhang D (2011) *RICE MORPHOLOGY DETERMINANT* encodes the type II formin FH5 and regulates rice morphogenesis. Plant Cell **23:** 681–700

Bioinformatics, 2020, 1–2
doi: 10.1093/bioinformatics/btaa035
Advance Access Publication Date: 23 January 2020
Applications Note

Bioimage informatics

CytoSeg 2.0: automated extraction of actin filaments

Jacqueline Nowak [1,2,3,*], Kristin Gennermann[2], Staffan Persson[1,†] and Zoran Nikoloski[2,3,†]

[1]School of Biosciences, University of Melbourne, Parkville, VIC 3010, Australia, [2]Bioinformatics, Institute of Biochemistry and Biology, University of Potsdam, 14476 Potsdam, Germany and [3]Systems Biology and Mathematical Modeling, Max Planck Institute of Molecular Plant Physiology, 14476 Potsdam, Germany

*To whom correspondence should be addressed.
†The authors wish it to be known that, in their opinion, the last two authors should be regarded as Joint Last Authors.

Associate Editor: Jonathan Wren

Received on May 24, 2019; revised on December 23, 2019; editorial decision on January 13, 2020; accepted on January 19, 2020

Abstract

Motivation: Actin filaments (AFs) are dynamic structures that substantially change their organization over time. The dynamic behavior and the relatively low signal-to-noise ratio during live-cell imaging have rendered the quantification of the actin organization a difficult task.

Results: We developed an automated image-based framework that extracts AFs from fluorescence microscopy images and represents them as networks, which are automatically analyzed to identify and compare biologically relevant features. Although the source code is freely available, we have now implemented the framework into a graphical user interface that can be installed as a Fiji plugin, thus enabling easy access by the research community.

Availability and implementation: CytoSeg 2.0 is open-source software under the GPL and is available on Github: https://github.com/jnowak90/CytoSeg2.0.

Contact: nowakj@student.unimelb.edu.au

Supplementary information: Supplementary data are available at *Bioinformatics* online.

1 Introduction

The actin cytoskeleton underpins many cellular processes, such as cytoplasmic streaming, cell wall organization and trafficking of vesicles inside the cell (Derksen *et al.*, 1990). Together with microtubules, the actin filaments (AFs) provide the backbone of the cytoskeleton.

Plant AFs have been visualized via immunolabeling in fixed samples or through fluorescently tagged cytoskeleton-binding proteins, such as GFP-fABD2, Lifeact or mTalin (Kost *et al.*, 1998; Riedl *et al.*, 2008; Sheahan *et al.*, 2004; Wick *et al.*, 1981; Wilsen *et al.*, 2006). Measurements of the organization and behavior of the AFs have therefore been steadily improving (Yoneda *et al.*, 2007). Although automated frameworks for the analysis of microtubule organization and dynamics are well-established (Faulkner *et al.*, 2017; Kapoor *et al.*, 2019), it has proven more challenging to device-automated frameworks to quantify features of the actin cytoskeleton, mainly due to its rapid dynamics. Nevertheless, several automated frameworks for AF analyses are available, including measurements of length, orientation and intensity distribution of filaments (Alioscha-Perez *et al.*, 2016; Rogge *et al.*, 2017; Zhang *et al.*, 2017).

Recently, we published an automated framework which extracts networks from segmented AFs (Breuer *et al.*, 2017). We used transport-related network properties to quantify the organization of the actin cytoskeleton and showed that AFs in *Arabidopsis thaliana* hypocotyls are optimized for efficient transport. Moreover, our framework can be used to compare the actin cytoskeleton organization between different organisms and different cell types (Yu *et al.*, 2019) but can also be used for other types of biological systems (see Supplementary Material).

Yet, the framework was provided as plain code that needed manual adjustments for individual experiments. Therefore, we present a graphical user interface (GUI) called CytoSeg 2.0 that facilitates easy use of the published algorithms and individualized gauging of parameters. The GUI was developed as a plugin for Fiji, which is widely used image processing software for biologists (Schindelin *et al.*, 2012).

2 Implementation and functionality

The CytoSeg 2.0 GUI is built as a macro for the Fiji imaging software. The code can be downloaded from Github (https://github.com/jnowak90/CytoSeg2.0) and should be extracted in the plugins folder of the Fiji application, which makes the GUI visible in the Fiji plugins menu. To use the GUI, both Fiji and Python 3 have to be installed with related plugins and modules (listed on the Github page).

The GUI is built for the analysis of fluorescently tagged actin cytoskeleton image stacks from living cells in TIFF format. However, it is also possible to use the GUI for immunolabeled AFs

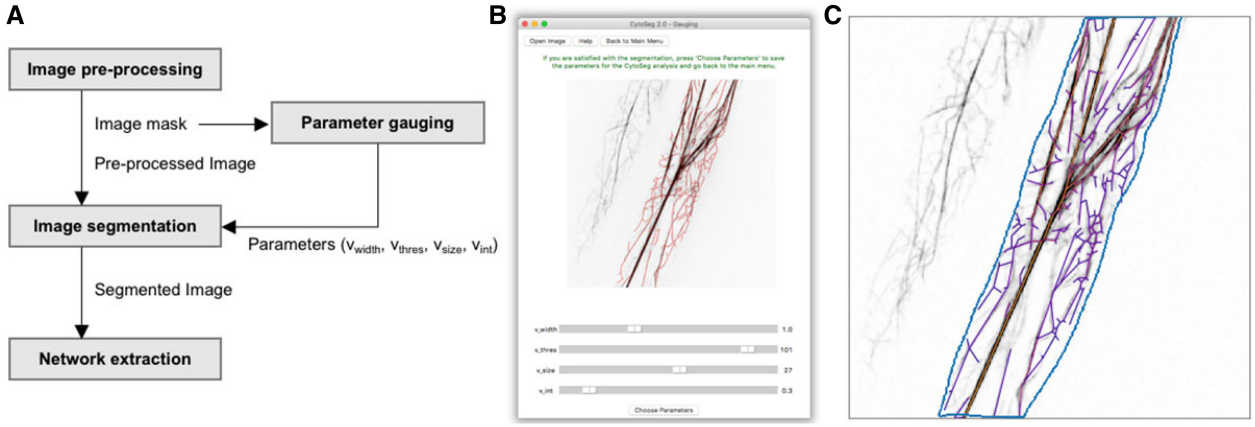

Fig. 1. Overview of the CytoSeg 2.0 workflow. (**A**) Scheme of the four different steps of the image processing pipeline. (**B**) GUI for the parameter gauging and resulting segmented actin cytoskeleton (red). (**C**) Pre-processed image with the selected region of interest (blue) and overlayed extracted network (purple/orange). (Color version of this figure is available at *Bioinformatics* online.)

or other types of filamentous structures (see Supplementary Material). The user can select a single image stack (e.g. image stack of different time points) or a folder of images/movies as input. Large image files should be used with caution due to long running times. Demo images of control and LatB-treated actin cytoskeletons are provided on the Github page.

The pipeline of CytoSeg 2.0 is partitioned into four steps: image pre-processing, parameter gauging, image segmentation and network extraction (Fig. 1A). The user can select whether to choose a complete analysis which includes all four steps, or a specific step of this series. During the pre-processing, the image is corrected for cell drift (stack registration), loss of fluorescence due to long light exposure (bleach correction) and uneven illuminated background (background subtraction). Maximum intensity Z-projected images are then used to manually select the region of interest, stored as an image mask (Fig. 1C). The mask is necessary for both the parameter gauging and the image segmentation. The segmentation of the image into actin cytoskeleton and background is dependent on four parameters: v_{width} (filament width), v_{thres} (adaptive median threshold), v_{size} (size of smallest components) and v_{int} (average filament intensity). To find the parameters for the optimal segmentation of the actin cytoskeleton, we added a GUI for the gauging of the parameters (Fig. 1B).

Here, the user can change the four parameters by dragging the corresponding sliders. The resulting segmented, and skeletonized actin cytoskeleton is then highlighted (red, Fig. 1B), and changes can be made until optimal segmentation is achieved. The selected parameters can be saved and will be stored for future analysis. To make sure that the selected parameters can be used for multiple images of the same experiment, several images should be tested during the gauging process.

Once the gauged parameters are selected, they can be used for the image segmentation. The segmented image is obtained by using a Gaussian filter (v_{width}), adaptive thresholding (v_{width}, v_{thres}), removal of small particles (v_{size}) and removal of filaments below a certain threshold (v_{int}).

Networks are then extracted from the segmented image by defining crossings or endpoints of the skeleton as nodes, connected by edges if they can be directly reached on the skeleton. Furthermore, the edges are weighted according to their edge capacity which is defined by the weight and length of the underlying filament (Fig. 1C). Apart from the extracted networks, the algorithm also creates randomized networks that maintain the edge length distribution and number of nodes.

The resulting extracted and random networks, as well as a table of calculated transport-related network properties (average edge capacity, assortativity, number of connected components, average path length, algebraic connectivity and edge angles) are saved in a new folder for every image and can be used for further analysis, such as for comparison of network properties between different conditions, alteration of properties over time or testing for statistical significance.

Funding

Z.N. is supported by the German Federal Ministry of Research and Education project SHAPENET, No. 031L0177A. S.P. was funded by two Australian Research Council [DP19001941 and FT160100218] and an IRRTF grant from the University of Melbourne.

Conflict of Interest: none declared.

References

Alioscha-Perez,M. *et al.* (2016) A robust actin filaments image analysis framework. *PLoS Comput. Biol.*, **12**, e1005063.

Breuer,D. *et al.* (2017) System-wide organization of actin cytoskeleton determines organelle transport in hypocotyl plant cells. *Proc. Natl. Acad. Sci. USA*, **114**, E5741–E5749.

Derksen,J. *et al.* (1990) The plant cytoskeleton: its significance in plant development. *Acta Bot. Neerl.*, **39**, 1–18.

Faulkner,C. *et al.* (2017) An automated quantitative image analysis tool for the identification of microtubule patterns in plants. *Traffic*, **18**, 683–693.

Kapoor,V. *et al.* (2019) MTrack: automated detection, tracking and analysis of dynamic microtubules. *Sci. Rep.*, **9**, 3794.

Kost,B. *et al.* (1998) A GFP-mouse talin fusion protein labels plant actin filaments *in vivo* and visualizes the actin cytoskeleton in growing pollen tubes. *Plant J.*, **16**, 393–401.

Riedl,J. *et al.* (2008) Lifeact: a versatile marker to visualize F-actin. *Nat. Methods*, **5**, 605–607.

Rogge,H. *et al.* (2017) Automated segmentation and quantification of actin stress fibres undergoing experimentally induced changes. *J. Microsc.*, **268**, 129–140.

Sheahan,M.B. *et al.* (2004) A green fluorescent protein fusion to actin-binding domain 2 of *Arabidopsis fimbrin* highlights new features of a dynamic actin cytoskeleton in live plant cells. *Plant Physiol.*, **136**, 3968–3978.

Schindelin,J. *et al.* (2012) Fiji: an open-source platform for biological-image analysis. *Nat. Methods*, **9**, 676–682.

Wick,S.M. *et al.* (1981) Immunofluorescence microscopy of organized microtubule arrays in structurally stabilized meristematic plant cells. *J. Cell Biol.*, **89**, 685–690.

Wilsen,K.L. *et al.* (2006) Imaging the actin cytoskeleton in growing pollen tubes. *Sex. Plant Reprod.*, **19**, 51–62.

Yoneda,A. *et al.* (2007) Recent progress in living cell imaging of plant cytoskeleton and vacuole using fluorescent-protein transgenic lines and three-dimensional imaging. *Protoplasma*, **230**, 129–139.

Yu,Y. *et al.* (2019) Live-cell imaging of the cytoskeleton in elongating cotton fibres. *Nat. Plants*, **5**, 498–504.

Zhang,Z. *et al.* (2017) An integrated enhancement and reconstruction strategy for the quantitative extraction of actin stress fibers from fluorescence micrographs. *BMC Bioinformatics*, **18**, 268.